

Dissertation
submitted to the
Combined Faculty of Natural Sciences and Mathematics
of the Ruprecht-Karls-Universität of Heidelberg, Germany
for the degree of
Doctor of Natural Sciences

Put forward by
Jindra Sophie Gensior
born in Grevenbroich, Germany
Oral examination: the 19th of July, 2021

The influence of the
galactic gravitational potential
on
star formation and the interstellar medium

Referees: Prof. Dr. Ralf Klessen
apl. Prof. Dr. Henrik Beuther

Zusammenfassung

Empirisch gesehen hängt die Sternentstehungsrate einer Galaxie nur von ihrer molekularen Gasmasse ab. Neuere Beobachtungen zeigen jedoch, dass die Sternentstehung in stellaren Sphäroiden systematisch unterhalb dieser Skalierungsbeziehungen liegt. Es wurde vorgeschlagen, dass die globale galaktische Umgebung die Gasdynamik so beeinflussen kann, dass die Sternentstehung stark unterdrückt wird. Dies wird mit einer Reihe von hydrodynamischen Simulationen isolierter Galaxien untersucht, welche ein neues Sternentstehungsmodell beinhalten, das den Einfluss der galaktischen Dynamik auf die Sternentstehung erfasst. Der von den Simulationen abgedeckte Parameterraum reicht von Scheibengalaxien bis zu Sphäroiden, deren anfängliche Gasanteile von 1-20 Prozent variieren. Dies ermöglicht eine ausführliche Untersuchung der Auswirkungen von unterschiedlichen Gravitationspotentialen auf die Gaseigenschaften und die Sternentstehungsrate, und wie diese mit dem Gasanteil zusammenhängen. Die Scherung, die durch das tiefe Gravitationspotential eines Sphäroids entsteht, erzeugt Turbulenz im Gas, was zu einer dynamischen Unterdrückung der Fragmentierung und Sternentstehung führt. Die dynamische Unterdrückung der Sternentstehung steigt mit höheren stellaren Oberflächendichten und niedrigerem Gasanteil. Dies impliziert, dass die Physik der Sternentstehung den Baryonenkreislauf bei niedrigen Rotverschiebungen und hohen Galaxienmassen begrenzen und regulieren kann.

Abstract

Empirically, the star formation rate of a galaxy depends only on its molecular gas mass. However, recent observations indicate that star formation in stellar spheroids systematically falls below these scaling relations. It has been suggested that the global galactic environment can affect the gas dynamics such that star formation is heavily suppressed. This is investigated using a suite of hydrodynamic simulations of isolated galaxies, which includes a new sub-grid model that captures the influence of galactic dynamics on star formation. The parameter space covered by the simulations ranges from disc galaxies to spheroids, with initial gas fractions varying from 1-20 per cent. This enables a detailed exploration of how differences in the gravitational potential affect the gas properties and star formation rate, as well as how it interlinks with the gas fraction. The shear generated by the deep gravitational potential of spheroids is found to drive turbulence in the gas, leading to a dynamical suppression of fragmentation and star formation. This dynamical suppression of star formation is enhanced at higher stellar surface densities and lower gas fractions. This implies that the physics of star formation can limit and regulate the baryon cycle at low redshifts and high galaxy masses.

Contents

List of Figures	v
List of Tables	vii
Acronyms and Abbreviations	ix
Preface	xi
1 Introduction and Background	1
1.1 Galaxies	2
1.2 Galactic Star Formation	5
1.3 The Baryon Cycle of Galaxies	14
1.4 The Interstellar Medium and Cloud-scale Star Formation	15
1.5 This Thesis	28
2 Heart of Darkness: the influence of galactic dynamics on quenching star formation in galaxy spheroids	29
2.1 Introduction	30
2.2 Modelling Star Formation in Galaxy Simulations	33
2.3 Method	36
2.4 Comparison of Star Formation Models with a Constant or Varying Star Formation Efficiency	41
2.5 Effect of the Gravitational Potential on Interstellar Medium properties	49
2.6 Discussion	59
2.7 Summary and Conclusions	64
3 The WISDOM of Power Spectra: quantifying how the galactic gravitational potential impacts the central gas reservoirs of galaxies	67
3.1 Introduction	68
3.2 Methods	70
3.3 Power Spectra	79
3.4 Discussion	85
3.5 Summary and Conclusions	93

4	The Elephant in the Bathtub: when the physics of star formation regulate the baryon cycle of galaxies	95
4.1	Introduction	96
4.2	Simulations	99
4.3	Results	101
4.4	When the Elephant steps into the Bathtub: Predicting the Onset of Dynamical Suppression	105
4.5	Discussion	109
5	Conclusions	113
5.1	Summary	113
5.2	Discussion	116
5.3	Outlook	118
	Acknowledgements	121
	Images from the World Wide Web	123
	Bibliography	125
A	Appendix: Heart of Darkness	159
A.1	Resolution Test	159
A.2	Choice of Star Formation Thresholds	161
B	Appendix: WISDOM of Power Spectra	165
B.1	KinMS	165
B.2	Parameter Tests	167
B.3	Additional Simulations	173
B.4	WISDOM Power Spectrum Slope (non-)Correlations	175
C	Appendix: Elephant in the Bathtub	177
C.1	Validation of the Multi-linear Regression	178
C.2	Gas Density Distributions	178

List of Figures

1.1	The Hubble classification scheme for galaxies	3
1.2	The Schmidt-Kennicutt relation and the star formation suppression of early-type galaxies	7
1.3	The baryon cycle of galaxies	14
2.1	Schematic of the cloud-scale identification algorithm	36
2.2	Radial gradient of the angular velocity for galaxies of different morphologies	41
2.3	Radially-resolved Schmidt-Kennicutt relation, contrasting galaxies evolved with a constant and dynamics-dependent star formation efficiency	42
2.4	Radial profiles of the turbulent velocity dispersion, contrasting galaxies evolved with a constant and dynamics-dependent star formation efficiency .	43
2.5	Radial profiles of the virial parameter, contrasting galaxies evolved with a constant and dynamics-dependent star formation efficiency	45
2.6	Radial profiles of the turbulent pressure, contrasting galaxies evolved with a constant and dynamics-dependent star formation efficiency	46
2.7	Gas surface density projections, contrasting galaxies evolved with a constant and dynamics-dependent star formation efficiency	47
2.8	Radial profiles of the gas surface density, contrasting galaxies evolved with a constant and dynamics-dependent star formation efficiency	48
2.9	Radial profiles of the turbulent velocity dispersion, comparing different gravitational potentials	50
2.10	Radial profiles of the virial parameter, comparing different gravitational potentials	52
2.11	Cumulative distribution of the virial parameter at stellar birth, comparing different gravitational potentials	53
2.12	Radial profiles of the turbulent pressure, comparing different gravitational potentials	54
2.13	Gas surface density projection, comparing different gravitational potentials .	56
2.14	Radially-resolved Schmidt-Kennicutt relation, comparing different gravitational potentials	57
2.15	Star formation main sequence and offset thereof of the simulations and the xCOLDGASS galaxies	58
3.1	Circumnuclear regions of the simulations	71

3.2	Gas surface density maps of the WISDOM galaxies	76
3.3	Surface density power spectra of the simulations	79
3.4	Power spectrum slopes as a function of central stellar surface density: simulations	81
3.5	Power spectra of the WISDOM galaxies	83
3.6	Power spectrum slopes as a function of central stellar surface density: observations	84
3.7	Power spectrum slopes as a function of the sensitivity limit of the observations	85
3.8	Power spectrum slopes as a function of the gas-to-stellar mass ratio of the observations	86
3.9	Power spectrum slopes as a function of the specific star formation rate of the observations	87
3.10	Power spectrum slopes as a function of the central gas surface density of the observations	88
3.11	Power spectrum slopes as a function of the central gas-to-stellar surface density ratio of the observations	89
3.12	Power spectrum slopes as a function of the central stellar surface density: simulations and observations	90
4.1	Radial profiles of the turbulent velocity dispersion, comparing the effect of different gas fractions	102
4.2	Star formation main sequence and offset thereof, comparing the effect of different gas fractions	104
4.3	Region of redshift and stellar mass parameter space affected by dynamical suppression	108
A.1	Resolution test: radial profile of the virial parameter	160
A.2	Resolution test: cumulative distribution of the virial parameter	160
A.3	Resolution test: cumulative distribution of the virial parameter at stellar birth	161
A.4	Threshold tests: radial profiles of the virial parameter	162
A.5	Threshold tests: cumulative distribution of the virial parameters	163
A.6	Threshold tests: cumulative distribution of the virial parameters at stellar birth	163
A.7	Threshold tests: Schmidt-Kennicutt relation	164
B.1	Gas surface density maps with <code>KinMS</code>	165
B.2	Power spectrum slopes as a function of central stellar surface density: simulations (<code>KinMS</code>)	166
B.3	Beam size test: power spectrum slopes as a function of central stellar surface density	167
B.4	Inclination test: power spectrum slopes as a function of central stellar surface density	169
B.5	Surface density threshold test: power spectrum slopes as a function of central stellar surface density	170

B.6	Power spectra of the unmasked simulations	172
B.7	Power spectrum slopes as a function of the centre masking	173
B.8	Power spectrum slopes as a function of central stellar surface density: additional simulations	174
C.1	Validation of the multi-linear regression	177
C.2	Probability distribution functions of the volumetric gas density	178
C.3	Gas surface density projection, comparing the effect of different gas fraction	180

List of Tables

1.1	Analytic star formation efficiency models	24
2.1	Initial conditions of the Gensior et al. (2020) simulations	39
3.1	Physical properties of the WISDOM galaxies	74
3.2	Properties of the zeroth moment map of the WISDOM galaxies	78
3.3	Power spectrum fitting results: simulations	80
3.4	Power spectrum fitting results: observations	82
4.1	Initial conditions of the Gensior and Kruijssen (2021) simulations	100
A.1	Initial conditions for the supplementary star formation threshold tests	162
B.1	Beam size test: power spectrum slopes – central stellar surface density correlation coefficients	168
B.2	Inclination test: power spectrum slopes – central stellar surface density correlation coefficients	170
B.3	Surface density threshold test: power spectrum slopes – central stellar surface density correlation coefficients	171
B.4	Initial conditions for supplementary simulations with large central stellar surface densities	173
B.5	Correlation test: power spectrum slope and assorted properties for the WISDOM galaxies	176

List of Abbreviations

- AGN:** Active galactic nucleus
ALMA: Atacama large millimetre/sub-millimetre array
CMZ: Central molecular zone; the central ~ 500 pc of the Milky Way
ETG: Early-type galaxy (elliptical, spheroid, lenticular)
GMC: Giant molecular cloud
ISM: Interstellar medium
LTG: Late-type galaxy (spiral)
MHD: magneto-hydrodynamic
PHANGS: Physics at high angular resolution in nearby galaxies
PDF: Probability distribution function
SFE: Star formation efficiency; unless otherwise specified measured per free-fall time, ϵ_{ff}
SFMS: Star formation main sequence; correlation between star formation rate and stellar mass for star forming galaxies
SFR: Star formation rate
SK: Schmidt-Kennicutt; proportionality relation between star formation rate and gas surface density
SMBH: super-massive black hole
SN: Supernova
sSFR: Specific star formation rate; star formation rate normalised by stellar mass
WISDOM: mm-Wave Interferometric Survey of Dark Object Masses

Preface

The research presented in this thesis has been carried out at the Astronomisches Rechen-Institut, a part of the Centre for Astronomy of Heidelberg University, between October 2017 and May 2021.

The aim of this thesis is to determine how the interstellar medium and star formation activity of a galaxy are affected by its morphology. Chapter 2 presents a suite of hydrodynamic simulations of isolated galaxies, whose morphology ranges from disc galaxy to spheroid and includes the development of a new sub-grid star formation model that captures the impact of galactic dynamics on star formation. In Chapter 3, the ability of the gravitational potential to drive turbulence in the interstellar medium is studied by computing the density power spectra of the Chapter 2 simulations and comparing them to observations. Finally, Chapter 4 extends the work of Chapter 2 and makes it applicable to the galaxy population at large, using an additional set of simulations that constrain the role of the gas fraction.

The contents of Chapter 2 and Chapter 4 have been published by Oxford University Press in the international, peer-reviewed journal *Monthly Notices of the Royal Astronomical Society* as Gensior et al. (2020) and Gensior and Kruijssen (2021), respectively. Chapter 3 is based on a manuscript in preparation (Gensior, Davis, Bureau, Kruijssen) which will be submitted to an international journal after this thesis is submitted. My contribution to the articles and manuscript presented in this thesis is that of the principal author. All research has been carried out in collaboration with other authors and a more detailed description of my contribution prefaces each relevant chapter.

Full references to publications included in this thesis are given below:

- Chapter 2: Jindra Gensior et al. (June 2020). “Heart of darkness: the influence of galactic dynamics on quenching star formation in galaxy spheroids”. *MNRAS* 495.1, 199–223. arXiv: 2002.01484 [astro-ph.GA]
- Chapter 4: Jindra Gensior and J. M. Diederik Kruijssen (Jan. 2021). “The elephant in the bathtub: when the physics of star formation regulate the baryon cycle of galaxies”. *MNRAS* 500.2, 2000–2011. arXiv: 2011.01235 [astro-ph.GA]

Chapter 1

Introduction and Background

Humankind has a long history of gazing at the night sky, trying to understand the Universe. Cave paintings and stone carvings indicate that pre-historic humans might have had a basic understanding of some astrophysical phenomena as early as several thousand years BC (Sweatman and Coombs, 2018). We have come a long way since those early days of stargazing and vastly improved our theoretical understanding in many areas. We have realised that stars are fundamental to our existence. They are a link across many astrophysical phenomena from galaxy formation and evolution to planet formation and astrobiology (McKee and Ostriker, 2007; Krumholz, 2014).

However, beyond the fact that stars form out of collapsing clouds of gas, many questions remain open. For example, what sets the efficiency with which gas is converted into stars – local processes within or around the cloud, the galactic environment¹, or both? How does the physics of star formation on cloud-scales relate to the star formation observed for galaxies globally? What causes a galaxy to cease star formation?

The disparity of the spatial and temporal scales involved in the star formation process is enormous. On the spatial side ranging from < 0.01 pc for the cores in which individual stars form, to tens of kpc for individual galaxies, or tens and hundreds of Mpc if considering cosmological effects. The timescales range from Myr to a Hubble time and vastly exceed human lifetimes, making observations of the process impossible. Thus, a complete understanding and theory of star formation remains elusive, making it one of the major unsolved problems of contemporary astrophysics.

This thesis aims to address some of the above questions, using numerical simulations of galaxies that model star formation based on recent advances in cloud-scale star formation theory. The remainder of this introduction is structured as follows. First, Section 1.1 gives an overview over galaxies, their classification and properties, then Section 1.2 discusses galaxy-integrated star formation and its cessation. Section Section 1.3 discusses the baryon cycle of galaxies. Finally, Section 1.4 zooms in on smaller scales, focussing on the interstellar medium and cloud-scale star formation theory.

¹In this thesis galactic environment will refer to the conditions within a galaxy. If environment is denoted to mean the position of a galaxy in the field, a group or a cluster this will be explicitly stated.

1.1 Galaxies

Galaxies are like people. The better
you get to know them the more
peculiar they often seem to become.

S. van den Bergh, *Galaxy Morphology
and Classification*

A cornerstone for our modern understanding of galaxy formation in a cold dark matter with a non-zero cosmological constant (Λ CDM) cosmological formalism is the model by White and Rees (1978). Structure formation within the universe proceeds from the growth of density perturbations that become gravitationally unstable and collapse when the density contrast to the surrounding matter becomes large enough. These structures grow hierarchically through merging, and form a complex web with the most massive gravitationally bound objects at the intersections. Gas follows the gravity of the dark matter halo, and provided it can cool efficiently within it, it begins to collapse and forms stars, and thus galaxies (e.g. Mo et al., 2010). This hierarchical growth is observed in numerical simulations of structure formation (e.g. Springel et al., 2005b), which have been found to reproduce the observed clustering of galaxies.

This paradigm of structure formation defines our understanding of a galaxy: a gravitationally bound system of gas and stars which sits within a larger and more massive dark matter halo. Massive galaxies also appear to host super-massive black holes (SMBHs) in their centres (e.g. Lynden-Bell, 1969; Kormendy and Richstone, 1995). The accretion discs of some nearby ones can now be directly observed (see Event Horizon Telescope Collaboration et al., 2019). Galaxies have long been classified based on the stellar morphology and structure they show in optical images. The earliest attempt at this was undertaken by Wolf (1908), but the classification proposed by Hubble (1926) is the one still in use today (albeit somewhat modified, e.g. Conselice, 2014). The original Hubble (1926) classification scheme, shown in Figure 1.1 like it was first visualised by Hubble (1936), divides galaxies into ellipticals and spirals. The stars in elliptical galaxies are arranged in a spheroid, with dispersion-dominated kinematics. By contrast, spirals consist of a rotation-supported stellar disc and a nuclear spheroidal component. They are classified by the size of their stellar bulge, and how tightly wound and resolved their spiral arms are, as well as sub-divided based on whether they possess a central stellar bar or not. Lenticular galaxies (S0) form an intermediate category between spiral and elliptical galaxies in the Hubble (1936) tuning fork. They also consist of a central spheroid embedded in a stellar disc, where the disc does not show signatures of spiral arms. However, it has been suggested based on visual and dynamical measurements that lenticulars form a parallel branch to the spirals and can also be classified by the size of their stellar bulge² (e.g. van den Bergh, 1976; Cappellari et al., 2011b; Conselice, 2014). For completeness, it should be mentioned that there are also galaxies with irregular morphologies (caused by mergers, e.g. Toomre and Toomre, 1972) and dwarfs (galaxies with stellar masses $< 10^9 M_{\odot}$, e.g. Geha et al., 2012) that do

²The terms bulge and spheroid will be used synonymously throughout this thesis.

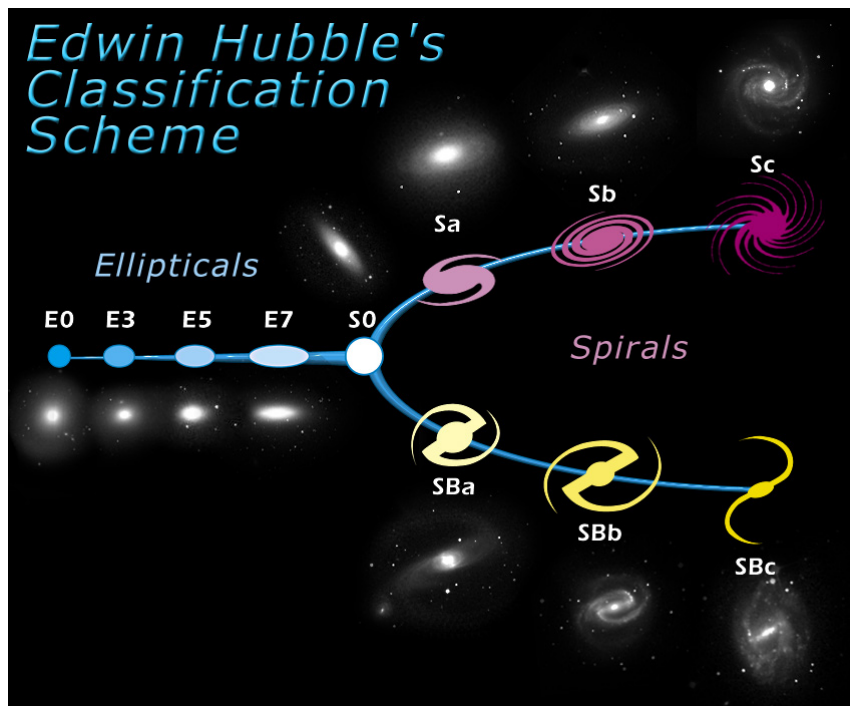


Figure 1.1: The Hubble classification scheme for galaxies, forming the iconic tuning fork. Early-type galaxies (i.e. ellipticals and lenticulars/S0) are classified by their increasing ellipticity and the absence of a spiral structure within a stellar disc (S0). The split in the tuning fork occurs for late-type galaxies (i.e. spirals), which are divided into barred and non-barred galaxies, and ordered along the tuning fork by the size of the nuclear region and how tightly wound their spiral arms are. Image credit: STScI

not fit within this classification scheme, but they are not within the focus of this thesis. Rather, I will focus on (more) massive galaxies which can be divided by how bulge- or disc-dominated they are. Ellipticals and lenticulars are commonly grouped together under the term early-type galaxies (ETGs), while spirals and irregulars fall under the umbrella term late-type galaxies (LTGs). Despite the nomenclature, they do not form an evolutionary sequence from early- to late-types.

The morphology of a galaxy is related to its optical colour. ETGs tend to be redder than LTGs (e.g. Holmberg, 1958; Roberts and Haynes, 1994). Galaxies form a bimodal distribution in colour-absolute magnitude (and therefore mass) space (e.g. Baldry et al., 2004), divided into a ‘blue cloud’ and ‘red sequence’, that has been in place at least since redshift 3–4 (e.g. Brammer et al., 2011; Whitaker et al., 2011; Muzzin et al., 2013). Since the colour is determined from the integrated light of all stars within the galaxy, it depends on the age of the stellar populations and thus on the star formation history of the galaxy. Young stellar populations appear bluer, whereas evolved ones are red. The implication of the colour-magnitude bimodality is that, on average, LTGs are actively star forming and occupying the blue cloud, while early-types are quiescent and have old stellar populations

(e.g. Roberts and Haynes, 1994; Kauffmann et al., 2003; Blanton and Moustakas, 2009) and are therefore commonly described as ‘red and dead’.

There are different formation pathways proposed for the different galaxy types. Theory predicts that disc-dominated, rotation supported LTGs form when the specific angular momentum of the gas accreting onto a halo is conserved (Fall and Efstathiou, 1980; Mo et al., 1998). Failure to reproduce disc-dominated galaxies in (early) numerical simulations resulted from gas cooling too efficiently and forming a dense central spheroid (e.g. Katz et al., 1996; Balogh et al., 2001) highlighted the importance of feedback from stars and active galactic nuclei (AGN) that heats and expels gas from the galactic disc and thus prevents this runaway bulge formation (e.g. Somerville and Davé, 2015; Naab and Ostriker, 2017, and references therein). The gas and dust reservoir within galaxies, referred to as interstellar medium (ISM), will be discussed in more detail in Section 1.4. The most pertinent ISM component for star formation is cold molecular gas (e.g. Wong and Blitz, 2002, see Section 1.2.1.1). LTGs in the local Universe have gas-to-stellar mass ratios of ~ 10 per cent (e.g. Saintonge et al., 2017; Tacconi et al., 2020) and had substantially larger gas fractions (up to 50 per cent) at high redshift (e.g. Geach et al., 2011; Tacconi et al., 2013, 2018; Tacconi et al., 2020).

Major mergers have long been shown to produce dispersion-dominated stellar spheroids (e.g. Toomre, 1977; Barnes, 1988; Mihos and Hernquist, 1996). However, a dominant disc component can be reformed through a gas-rich merger (e.g. Robertson et al., 2004, 2006; Hopkins et al., 2009; Martig et al., 2009). This highlights that a key requirement for forming ETGs is a mechanism that can prevent accretion of gas, through feedback or other mechanisms (e.g. Somerville and Davé, 2015; Naab and Ostriker, 2017). This will be discussed in more detail in Section 1.2.2. Contrary to the "red and dead" stereotype, a significant fraction of ETGs contain cold gas and dust. Atomic hydrogen (HI) is detected in > 50 per cent of ETGs (e.g. Oosterloo et al., 2010; Yıldız et al., 2020), dust detection rates range from 50 to 75 per cent (e.g. Knapp et al., 1989; Colbert et al., 2001; Kokusho et al., 2019) and approximately 25 per cent of ETGs host molecular gas (H_2 ³) reservoirs (e.g. Combes et al., 2007; Welch et al., 2010; Young et al., 2011; Davis et al., 2019). While some ETGs have a molecular gas fraction of 5–10 per cent, the majority has gas fractions $\lesssim 1$ per cent (Young et al., 2011; Davis et al., 2019). The origin of the molecular gas in ETGs appears to be diverse. It is likely a mix between molecular gas retained through the morphological transformation from spiral to ETG, stellar mass loss, cooling from the hot halo and gas-rich minor mergers depositing gas in a kinematically misaligned disc (e.g. Davis et al., 2013b; Babyk et al., 2019; Davis et al., 2019). The implications of the presence of molecular gas, as a seed for star formation, in ETGs will be explored further in Section 1.2 and several chapters of this thesis.

³It is difficult to observe H_2 directly, because the molecule does not have a dipole moment and the rovibrational transitions only get excited at high temperatures. The most commonly used observational proxy is carbon monoxide (CO; e.g. Carroll and Ostlie, 2006).

1.2 Galactic Star Formation

Observational star formation relations are the fundamental probe that theory and numerical simulations need to match (if they are not hard-coded into them in the first place). There are some uncertainties associated with the observations, for example due to differences in various tracers of the star formation rate (SFR) and their calibration (e.g. Kennicutt, 1998a; Kennicutt and Evans, 2012; Calzetti, 2013) and the conversion of the observed gas luminosities into a molecular gas mass (e.g. Bolatto et al., 2013, and references therein). Nonetheless, over time some tight global scaling relations have been observed. In the following sections the scaling relations between SFR and gas density (Section 1.2.1.1), SFR and galaxy stellar mass (Section 1.2.1.2) will be reviewed, leading into a discussion of possible mechanisms to quench, i.e. shut down star formation, in galaxies (Section 1.2.2).

1.2.1 Empirical Star Formation Scaling Relations

1.2.1.1 The Schmidt-Kennicutt relation

In his seminal work, Schmidt (1959) proposed that the global SFR of a galaxy depends only on the density of its gas:

$$\dot{\rho}_{\text{SFR}} \propto \rho^n, \quad (1.2.1)$$

where Schmidt (1959) argued that $n \approx 2$ matched the most observational constraints at the time. This sparked a large effort into empirically determining the exponent of the Schmidt law, as well as a debate into whether a global law for star formation exists at all or whether a threshold for star formation or other criteria are required (e.g. Kennicutt, 1989, and references therein). Nearly four decades after Schmidt's paper, Kennicutt (1998b) observed a tight relation between the total (atomic plus molecular) gas surface density and SFR surface density:

$$\Sigma_{\text{SFR}} = A \Sigma_{\text{g}}^N, \quad (1.2.2)$$

with $N = 1.4 \pm 0.15$. The tightness of this relation across 5 decades in Σ_{g} and 6 decades in Σ_{SFR} for a sample consisting of 61 star forming disc galaxies as well as 36 starbursts⁴ provides compelling evidence for the presence of a global star formation relation. More recent investigations with improved measurements of SFR and gas and larger sample sizes remain in good agreement with the original Schmidt (1959)-Kennicutt (1998b) $N \approx 1.4$ relation (e.g. Kennicutt and Evans, 2012; de los Reyes and Kennicutt, 2019).

However, starting from Wong and Blitz (2002), there has been a growing body of evidence that the global SFR of galaxies correlates more strongly with their molecular gas content, rather than the total gas (e.g. Wong and Blitz, 2002; Bigiel et al., 2008; Schruba et al., 2011; Leroy et al., 2013). For example, Bigiel et al. (2008) demonstrate that the radial profiles of the SFR traces that of H_2 , while that of HI differs significantly. The SFR drops sharply below total gas surface densities of 9–10 $\text{M}_{\odot} \text{pc}^{-2}$, where the ISM is atomic-dominated (e.g. Wong and Blitz, 2002; Bigiel et al., 2008). Even though these

⁴Starbursts are galaxies with an enhanced star formation rate and appear particularly luminous in the infrared (e.g. Kennicutt and Evans, 2012).

studies do not find any relation between Σ_{SFR} and Σ_{HI} , more recently the volumetric HI density has been observed to be a good tracer of the volumetric global SFR (Bacchini et al., 2019, 2020).

The molecular star formation relation exhibits a linear scaling of SFR with H_2 surface density (e.g. Bigiel et al., 2008; Schruba et al., 2011; Leroy et al., 2013; Bolatto et al., 2017). The depletion time is defined as $t_{\text{dep,mol}} = \Sigma_{\text{H}_2}/\Sigma_{\text{SFR}}$, i.e. the time required to convert the entirety of the current molecular gas reservoir into stars at the current SFR (assumed constant). For a linear scaling relation between gas surface density and SFR, it implies that all galaxies will have the same depletion time, or alternatively that there is a uniform conversion efficiency of molecular gas into stars. The depletion time measured for nearby spiral galaxies is ~ 2 Gyr (e.g. Bigiel et al., 2008; Leroy et al., 2008).

Dense gas is defined as gas a few orders of magnitude denser than CO. In extragalactic observations it is commonly traced through emission from the molecule HCN, whereas a dust extinction threshold is used in Milky Way clouds. Dense gas has been proposed as another good (if not fundamental) tracer of the star formation rate by Gao and Solomon (2004). They argue that star formation solely takes place in dense gas, evidenced by the tighter correlation between the HCN luminosity and the infrared (IR) luminosity (L_{IR} ; the SFR tracer), compared to CO and L_{IR} . Since CO traces all molecular gas, including dense gas emitting in HCN, the CO- L_{IR} relationship is a corollary of that between HCN and L_{IR} (Gao and Solomon, 2004). Later work shows that the slightly super-linear positive correlation between HCN and IR luminosity also extends down to massive, dense clumps in the Milky Way. This further suggests that the dense gas fraction determines the SFR and implies that starbursts can be understood as having an enhanced fraction of dense gas (Wu et al., 2010, see also Lada et al., 2010, 2012).

This thesis is motivated by the deviations that galaxies show from these (global) star formation relations. Specifically, the sub-set of ETGs that contains molecular gas but appears to form stars at a lower rate than LTGs. An absence or suppression of star formation in lenticulars had already been noticed in the early days of extragalactic star formation studies (e.g. Schommer and Bothun, 1983; Kennicutt, 1989). More recently Saintonge et al. (2011) showed that the depletion time in the COLDGASS sample of 222 galaxies with $M_* > 10^{10} M_{\odot}$ increases with increasing stellar mass (see also Bolatto et al., 2017). Since the depletion time is the ratio of SFR to gas density, its inverse can be regarded as a proxy for how efficiently gas is converted into stars. Thus, long depletion times imply less efficient star formation. In a follow up study, Saintonge et al. (2012) demonstrate that galaxies with a larger central stellar surface density (a proxy for the dominance of the spheroidal component of galaxies) exhibit longer depletion times than later galaxy types at comparable stellar mass. Davis et al. (2014) find that the SFR in ETGs is systematically suppressed by a factor of ~ 3 below the relation of Kennicutt (1998b) and Bigiel et al. (2008). This is shown in Figure 1.2 (Figure 5 in Davis et al., 2014). van de Voort et al. (2018) specifically target 6 ETGs that have undergone a gas-rich minor merger recently. Although mergers usually precede a starburst episode, the SFR of these objects lies 1–2 orders of magnitude below the Kennicutt (1998b) relation for LTGs of similar gas surface densities (van de Voort et al., 2018).

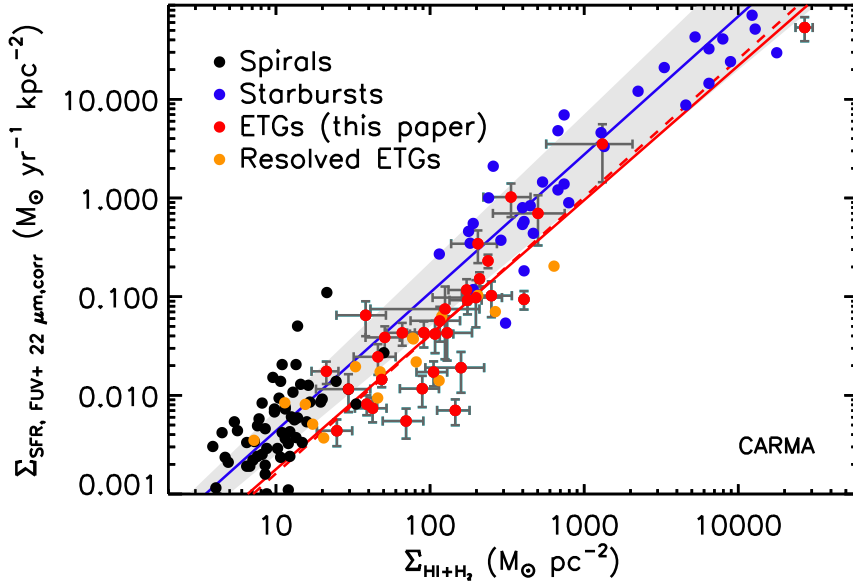


Figure 1.2: Star formation rate surface density as a function of total gas surface density for the spiral (black) and starburst (blue) galaxies from Kennicutt (1998b), the resolved early-type galaxies (ETGs; orange) from Martig et al. (2013) and the ETGs (red) from Davis et al. (2014). The blue line shows the original Kennicutt (1998b) relation, and while the red line shows the best fit to the ETGs, highlighting their suppressed SFR. Figure reproduced from Davis et al. (2014).

It has been hypothesised that the SFR of ETGs might appear suppressed when comparing the molecular or total gas scaling relations, but that their dense gas fractions might be such that they should fall on the HCN- L_{IR} relation. Indeed, Krips et al. (2010) find that the 3 out of 4 ETGs they detected in HCN fall on the low-SFR end of the Gao and Solomon (2004) relation. Crocker et al. (2012) detect HCN in 12 out of 18 ETGs. These ETGs are considerably more scattered in L_{IR} -HCN/ ^{12}CO space than the Gao and Solomon (2004) sample, and even at high dense gas fractions of 5–10 per cent have a lower L_{IR} by an order of magnitude or more. This could in part be caused by the HCN-to- ^{12}CO ratio not being a good tracer of the dense gas fraction in ETGs (Crocker et al., 2012). Given the scarcity of data it is currently not possible to draw a meaningful conclusion for the relation between dense gas (fraction) and star formation for ETGs as a whole.

However, SFR suppression is not exclusively seen in ETGs. The central molecular zone (CMZ) is the bulge-dominated region of the Milky Way, encompassing the central 500 pc. The SFR of the CMZ also falls below the predictions of the Schmidt-Kennicutt (SK) relation (e.g. Longmore et al., 2013; Kruijssen et al., 2014). Resolved (at the scale of \sim kpc) HCN observations of more than 30 nearby late-type galaxies show a similar behaviour. The SFR shows an anti-correlation with the stellar surface density, while the dense gas fraction is correlated with the stellar surface density (e.g. Usero et al., 2015; Bigiel et al., 2016; Gallagher et al., 2018; Querejeta et al., 2019). Specifically, Usero et al. (2015) find that the

star formation rate in galaxy centres is suppressed by a factor of 6-8 compared to the discs. The offset from the SK relation seems to depend on morphology, too. Analysing 28 galaxies from the ALMA-MaNGA QUEnching and STar formation (ALMaQUEST Lin et al., 2020) survey, Ellison et al. (2021a) find that the offset below the SK relation correlates with the Sérsic (1963) index. The larger the Sérsic index, the more bulge-dominated a galaxy (an index of 4 corresponds to the light profile of an elliptical, while 1 corresponds to a disc). Ellison et al. (2021a) find that the offset from the SK relation is $\gtrsim 0.5$ dex for galaxies with $N_{\text{Sersic}} > 3$.

These discrepancies between a large observed dense gas fraction, but a suppressed SFR at high stellar surface densities highlight that simple, solely density-dependent star formation models cannot accurately capture the complexity of the star formation process. Instead the efficiency of star formation seems to depend on the environment. This will be further explored Section 1.4.2.2.

1.2.1.2 The Star Formation Main Sequence

Star-forming galaxies fall along a tight empirical relation between their global SFR and stellar mass, M_* (e.g. Daddi et al., 2007; Elbaz et al., 2007; Noeske et al., 2007b; Schiminovich et al., 2007; Pannella et al., 2009; Magdis et al., 2010; Peng et al., 2010; Rodighiero et al., 2010, 2011; Wuyts et al., 2011; Whitaker et al., 2012; Speagle et al., 2014; Whitaker et al., 2014; Renzini and Peng, 2015; Saintonge et al., 2016; Janowiecki et al., 2020; Leslie et al., 2020). This relationship of increasing SFR with increasing M_* was dubbed the star formation main sequence (SFMS) by Noeske et al. (2007b). The SFMS is established up to redshift $z \approx 6$ (e.g. Speagle et al., 2014) for a variety of star formation tracers (see discussion in Speagle et al., 2014; Renzini and Peng, 2015). It has a (sub-)linear slope in $\log M_* - \log \text{SFR}$ space, which somewhat depends on the selection criteria (see e.g. Whitaker et al., 2012, who recover a linear relation for their data when only fitting blue galaxies). The normalisation of the SFMS changes with time, for example dropping by a factor of 20–30 since $z \sim 2$ (e.g. Daddi et al., 2007; Whitaker et al., 2012; Leslie et al., 2020), which is likely a reflection of the cosmic star formation history (e.g. Madau and Dickinson, 2014). The slope of the relation is time dependent as well (e.g. Speagle et al., 2014; Whitaker et al., 2014; Leslie et al., 2020). Nonetheless, the relation is fairly tight at all times, with an observed scatter of $\lesssim 0.3$ dex (e.g. Noeske et al., 2007b; Whitaker et al., 2012; Speagle et al., 2014).

Many studies have found the shape of the SFMS to deviate from a single power law, flattening at high galaxy stellar masses (e.g. Elbaz et al., 2011; Lee et al., 2015; Schreiber et al., 2015; Saintonge et al., 2016; Tomczak et al., 2016; Popesso et al., 2019; Cook et al., 2020; Leslie et al., 2020). The mass above which the relation flattens varies between the studies from $\log M_*/M_\odot \geq 9.5$ (Leslie et al., 2020) to $\log M_*/M_\odot \geq 10.5$ (Schreiber et al., 2015), and possibly as a function of redshift (Tomczak et al., 2016). It also becomes less pronounced at $z \gtrsim 2$ (e.g. Schreiber et al., 2015; Leslie et al., 2020). The general interpretation is that the inclusion of galaxies which are already in the process of quenching causes the flattening. Specifically, there have been two main physical interpretations put forward to explain this behaviour:

Firstly, that the increase in the abundance of bulge-dominated galaxies with decreasing redshift (e.g. Bundy et al., 2006, 2010; Buitrago et al., 2013) leads to lower average SFR (e.g. Schreiber et al., 2015; Popesso et al., 2019; Leslie et al., 2020). It has been shown that the SFR is anti-correlated with the bulge-fraction or more generally decreases from late- to early-type morphology at fixed stellar mass (e.g. Wuyts et al., 2011; Abramson et al., 2014; Catalán-Torrecilla et al., 2017; Janowiecki et al., 2020; Leslie et al., 2020). A dependence of the SFMS on morphology is also found for resolved relations (e.g. González Delgado et al., 2016; Maragkoudakis et al., 2017; Medling et al., 2018; Pan et al., 2018; Ellison et al., 2021a), where galaxies with a more dominant spheroid component tend to be offset below the SFMS. The offset of galaxies below the SFMS, that fall either within the transition region (green valley) or quiescent in the red cloud, is also directly related to the bulge mass fraction of the galaxy (e.g. Cook et al., 2020). However, Cook et al. (2020) show that the trend persists even after decomposing galaxies into bulge and disc regions and considering the SFR and the disc mass only (under the assumption that this is the star-forming component). This suggests that another mechanism not directly related to morphology is required to explain the low SFRs at high galaxy masses.

The second interpretation for the flattening of the SFMS is related to the lack of cold gas in massive galaxies. Saintonge et al. (2016) find that both the atomic and molecular gas fractions steadily decrease with increasing stellar mass. This implies that the SFR decrease is a simple consequence of cutting off the gas supply of a galaxy, rather than issues of converting the atomic into molecular gas. The most massive galaxies in the flattening part of the SFMS will exhaust their gas reservoir within one depletion time of 1–2 Gyr and not accrete sufficient quantities of new gas to sustain their current SFRs, thus quenching slowly (e.g. Noeske et al., 2007a; Saintonge et al., 2016; Popesso et al., 2019). However, low gas fractions also do not seem to be a necessary condition for quiescence. Janowiecki et al. (2020) define an atomic and a molecular gas main sequence in analogy with the SFMS and find that galaxies with gas reservoirs on or above these gas main sequences (even for molecular gas) can have SFRs suppressed an order of magnitude below the SFMS.

From the discussion of empirical star formation relations, two main drivers of the SFR have emerged. The star formation efficiency (SFE) appears to be linked to the galactic environment. As discussed in Section 1.2.1.1 and above, star formation in ETGs and galaxy bulges is suppressed compared to LTGs. This implies that the SFR carries some dependence on galaxy morphology. At the same time, the amount of gas in a galaxy also influences its star formation activity. What remains unclear are the specific physical mechanisms that govern the entire process, and especially leads galaxies to become quenched. This will be discussed in more detail in the following Section.

1.2.2 How do galaxies quench?

Before discussing which mechanisms might drive a galaxy into quiescence, we first have to define what it means to be quenched. Unfortunately, quenching is a very fuzzy concept in both the qualitative and quantitative description (e.g. Man and Belli, 2018; Donnari et al., 2019; Iyer et al., 2020). Qualitatively, quenching on one hand means the process by which an actively star-forming galaxy significantly reduces, if not terminates, its star

formation. On the other hand, it gets used simultaneously to refer to the maintenance of this quiescent state until the present day. This can involve drastically different timescales, and thus it is still debated whether a single quenching mechanism can do both (e.g. Man and Belli, 2018). Quantitatively, there are three main approaches taken in the literature to define something as quenched or quiescent⁵ (see e.g. Donnari et al., 2019, and discussion therein). The first is to use a cut in specific SFR (sSFR). The sSFR is defined as the SFR normalised by M_* , which can also be interpreted as the ratio of current to prior star formation. This maximum sSFR threshold for quiescence can be fixed based on a strong bimodality in the stellar mass-SFR plane (e.g. Fontana et al., 2009; McGee et al., 2011; Wetzel et al., 2012), usually an $\text{sSFR} = 10^{-11}$ yr is used. Alternatively the sSFR cut-off can be time-dependent, particularly if a large redshift range is considered to account for the variation in star formation across cosmic time (e.g. Pacifici et al., 2016; Jian et al., 2018; Carnall et al., 2020; Iyer et al., 2020). Secondly, one can impose a minimum offset from the SFMS, usually $> 2\sigma$; e.g. Morselli et al., 2017; Cook et al., 2020 or alternatively a flat 1 dex suppression (e.g. Fang et al., 2018). The third method selects quenched galaxies based on the region they occupy in the plane of restframe U-V, V-J colour (e.g. Williams et al., 2009; Whitaker et al., 2011). Finally, there exists a sub-set of galaxies that are classified as ‘post-starburst’ (PSB), because their spectra show signatures of A-type, but not the most massive O- and B-type stars, in combination with instantaneous star formation rates below the SFMS. This is indicative of PSBs having undergone a short starburst < 1 Gyr ago and rapidly quenching afterwards. PSBs constitute less than a per cent of the galaxy population at $z \sim 0$, but they were more numerous in the past (~ 5 per cent at $z \sim 2$) and could be responsible for building up to 38 per cent of the red sequence at $z > 0.7$ (e.g. Wild et al., 2009, 2016). Intriguingly, PSBs appear to host large fractions of molecular gas. Therefore, PSBs require a rapid quenching mechanism that additionally allows them to retain substantial amounts of molecular gas while suppressing the SFR (e.g. French et al., 2015; Rowlands et al., 2015; Suess et al., 2017; Smercina et al., 2018; Yesuf and Ho, 2020).

Summarising the above, in order to drastically reduce the star formation activity in a galaxy the quenching mechanism must achieve one or more of the following:

1. prevent the accretion of cold gas onto a galaxy,
2. remove cold gas from the galaxy, either by heating or expelling it,
3. influence the SFE, such that the SFR becomes suppressed even if cold, molecular gas is present within the galaxy.

Peng et al. (2010) distinguished between *environmental quenching*, which acts primarily on satellites (e.g. Peng et al., 2012; Wetzel et al., 2013), and *mass quenching*, mechanisms for massive galaxies. In the context of environmental quenching, environment refers to the surroundings of a galaxy. For completeness it should be mentioned that the environmental

⁵Depending on the definition of quenching, these terms mean the same thing (and the literature tends to use them interchangeably). However, in light of the double definition of quenching it would probably behoove us to use quenching to refer to the initial process of shutting down the star formation and quiescence to the maintenance of the quenched state afterwards.

effects that can quench satellites are ram-pressure stripping of a galaxies ISM (e.g. Gunn and Gott, 1972; Abadi et al., 1999), strangulation (removal of the outer gaseous envelope of a galaxy falling into the cluster, star formation will cease once the remaining gas reservoir is exhausted e.g. Larson et al., 1980; Balogh et al., 2000), and galaxy harassment (many interactions with other cluster members, e.g. Farouki and Shapiro, 1981; Moore et al., 1996). However, the focus of this thesis lies on centrals and isolated galaxies and thus I will review the mechanisms which can affect those galaxies in more detail below.

Cosmological Starvation falls into the first category of the quenching list. It prevents the accretion of gas onto halos. Physically it is motivated by the varied accretion histories of dark matter halos (e.g. McBride et al., 2009), some of which experience starvation following a growth phase (e.g. Diemand et al., 2007). If the dark matter halo accretion rate $d \ln M_{\text{DM}}/dt$ drops below 0.4 Gyr^{-1} , the gas accretion rate will follow suit and cause a drop in sSFR below the SFMS within a few hundred Myr (Feldmann et al., 2016). Cosmological starvation was proposed by Feldmann and Mayer (2015) to explain the existence of massive, quiescent ETGs at $z > 2$ that must have formed most of their stars at even higher redshift (e.g. Straatman et al., 2014) and quenched within a few hundred Myr (e.g. Schawinski et al., 2014). This mechanism does not completely shut off gas accretion (and by extension star formation) and is not expected to work well in galaxy groups and clusters which exhibit a higher dark matter halo density.

Halo Quenching also prevents the accretion of cold gas onto galaxies. Numerical simulations predict that once the dark matter halo of a galaxy exceeds a halo mass of $\sim 10^{12} M_{\odot}$, the gas accreted onto it will be shocked to the virial temperature of the halo (Birnboim and Dekel, 2003, see also e.g. Kereš et al., 2005; Dekel and Birnboim, 2006; Ocvirk et al., 2008; Kereš et al., 2009; Davé et al., 2017). If the gas is then incapable of cooling and new gas continues getting shock heated, this effectively prevents gas in the circumgalactic medium (CGM) from condensing onto the galaxies. However, even if external accretion no longer takes place, stellar mass loss from asymptotic giant branch stars can replenish a galaxies ISM and could thus allow for star formation again. In addition, it has been shown that cold streams from the cosmic web can penetrate the shock heated halo and deliver cool gas to the galaxy (e.g. Dekel et al., 2009).

Gravitational heating refers the transfer of gravitational potential energy from infalling satellites or gas clumps to kinetic energy of the halo gas through dynamical friction (e.g. Dekel and Birnboim, 2008; Khochfar and Ostriker, 2008; Johansson et al., 2009). Gravitational heating is a way to sustain a hot CGM without requiring AGN feedback. It is focussed on sustaining a hot intracluster medium in particular (e.g. Khochfar and Ostriker, 2008) and might act in support of halo quenching.

AGN feedback can come in two distinct modes, dubbed ‘quasar’ and ‘radio’ mode respectively. Quasar mode is ejective, powering strong outflows that remove gas from the galaxy (e.g. Sanders et al., 1988; Di Matteo et al., 2005; McCarthy et al., 2011). By contrast, in radio mode the AGN feedback heats the gas, thus making it unavailable for star formation without needing to eject it from the galaxy (e.g. Bower et al., 2006; Croton et al., 2006). The addition of AGN feedback allowed the big cosmological simulations of the last decade to match the knee in the observed galaxy mass function (e.g. Vogelsberger

et al., 2014; Schaye et al., 2015; Pillepich et al., 2018) that simple estimations based on previous dark matter only simulations (e.g. Springel et al., 2005b) failed to predict. The tight correlation between bulge mass and SMBH mass (e.g. Magorrian et al., 1998; Kormendy and Ho, 2013), in conjunction with the strong dependence of quiescence on bulge dominance, has been interpreted as an observational indication for the importance of AGN feedback (e.g. Bluck et al., 2014, 2019). However, no observational evidence has conclusively proven AGN feedback to be the powerhouse that quenches star formation and then keeps it quiescent. Furthermore, AGN feedback offers no explanation for the suppressed SFRs in PSBs and ETGs that host molecular gas reservoirs but do not show signs of recent AGN activity (e.g. Davis et al., 2014; Rowlands et al., 2015; Suess et al., 2017).

Stellar feedback in form of supernovae (SN) and stellar winds during a starburst episode has been discussed as the other potential driver of ejective galactic winds (e.g. Chevalier and Clegg, 1985; Heckman et al., 1990; Veilleux et al., 2005). Low SFEs in dwarf galaxies can be accounted for with SN regulation (e.g. Dekel and Silk, 1986; Governato et al., 2010; Shen et al., 2014). Stellar feedback is also a pre-requisite for reproducing late-type galaxies that match observations (e.g. Guedes et al., 2011; Stinson et al., 2013; Hopkins et al., 2014; Agertz and Kravtsov, 2015). However, above halo masses of $\sim 10^{12} M_{\odot}$, stellar feedback fails to regulate and thus quench star formation. Neither superbubble feedback, which takes into account the increase in the effectiveness of feedback due to clustering of SNe, (e.g. Keller et al., 2016), nor radiation pressure driven winds (e.g. Aumer et al., 2013; Roškar et al., 2014) can generate realistic quiescent massive galaxies.

Morphological Quenching was coined by Martig et al. (2009). It is the only quenching mechanism that addresses the third point on the list: suppressing the SFR in the presence of a molecular gas reservoir. Briefly, the idea is that the deep gravitational potential of a spheroid stabilises the gas disc against gravitational instability, thus preventing star formation. This is based on the stability analysis originally conducted by Toomre (1964). A thin disc (of gas or stars) is stable against axisymmetric instabilities if

$$Q = \frac{\kappa\sigma}{\epsilon G\Sigma} > 1, \quad (1.2.3)$$

where κ is the epicyclic frequency, σ the velocity dispersion, Σ the surface density of the disc, $\epsilon = \pi$ for a gas disc and 3.36 for a stellar disc. This condition can also be expressed as a length scale, $\lambda_T = \pi G\Sigma_g/\Omega^2$. On scales larger than λ_T , differential rotation (shear) prevents the formation of instabilities. The stability of a gas disc embedded in a stellar disc is more aptly characterised using an effective Q parameter (observationally, e.g. Wong and Blitz, 2002; Leroy et al., 2008). This effective Toomre parameter (Jog and Solomon, 1984b; Elmegreen, 1995; Martig et al., 2009) is defined as:

$$Q_{\text{eff}}^{-1} = \alpha_{\text{gas}}Q_{\text{gas}}^{-1} + \alpha_{*}Q_{*}^{-1}, \quad (1.2.4)$$

where the coefficients α_{gas} and α_{ast} depend on the velocity dispersion of the gas and stars, as well as the shape of the gravitational potential, and are of order unity for LTGs. A thin stellar disc can enhance the self-gravity within gravitational perturbations, lowering the

effective Toomre Q and thus allowing the gas to fragment into clouds even if the gas disc on its own would be stable (e.g. Jog and Solomon, 1984a). Martig et al. (2009) argue that the impact of the spheroidal component on the stability of the gas disc is twofold. Firstly, for lenticulars and ellipticals $Q_* \gg 1$, helping to stabilise the gas rather than triggering its collapse. Secondly they suggest that the spheroidal potential will enhance κ and induce a high velocity dispersion through shear, thereby leading to $Q_{\text{gas}} > 1$.

How effective morphological quenching is in suppressing star formation in ETGs remains somewhat ambiguous. Numerical simulations indicate that a dominant spheroidal component is not always sufficient in suppressing star formation. Simulating a massive isolated galaxy embedded in a hot CGM halo, Su et al. (2019) find that the SFR is only marginally affected by the presence of a massive bulge. The temporarily quiescent galaxy in Martig et al. (2009) becomes star-forming again following a merger and Martig et al. (2013) only see a suppression of star formation below the SK relation for an ETG with a gas fraction of 1.3 per cent. While Ceverino et al. (2010) attribute the quiescent state of their simulations at $z \sim 1.3$ to morphological quenching, the simulated galaxies have gas fractions a factor of $\sim 2-5$ below the observational limits at this redshift. This indicates that morphological quenching might require a low gas fraction to operate. While the strong correlation between bulge mass and quiescence (e.g. Bluck et al., 2014, 2019) can also be interpreted as evidence for morphological quenching, more direct evidence is rare. The increase in Q towards the centre of $z \sim 2$ star-forming galaxies has been interpreted as the early-onset of morphological quenching by Genzel et al. (2014). Yet, analysing galaxies on the SFMS at $0.5 < z < 0.8$, Freundlich et al. (2019) find no trend between the SFR and morphological indicators for bulge-dominance. This contrasts with findings in the local Universe (e.g. Saintonge et al., 2011; Ellison et al., 2021a), which Freundlich et al. (2019) argue could be due to an average gas-to-stellar mass ratio of 0.28. By contrast a stack of $z > 1.4$ ETGs, with an average gas fraction of 9 per cent, has an sSFR suppressed by a factor of 30, which Gobat et al. (2018) attribute to morphological quenching. Distinctly different radial sSFR profiles for bulges and discs, where bulges show a centrally suppressed sSFR might be another indicator of morphological quenching in action (e.g. Méndez-Abreu et al., 2019).

Although it does not fall under the mantle of morphological quenching as defined by Martig et al. (2009), shear from bars has been proposed as another possibility of quenching star formation in gas rich spiral galaxies. Simulations those objects confirm that the formation of a bar can suppress the SFR by an order of magnitude within a Gyr (see Khoperskov et al., 2018, and references therein).

In summary, it is likely that there is no single quenching mechanism that can explain all quiescent galaxies everywhere. Instead, it is likely a combination of some of the mechanisms introduced in this section. However, morphological quenching remains the popular choice to invoke for galaxy samples that exhibit suppressed SFRs but still host molecular gas reservoirs at all redshifts (e.g. Davis et al., 2014; Suess et al., 2017; Kim et al., 2018; Smercina et al., 2018; Janowiecki et al., 2020). This thesis explores the effect of morphological quenching in depth in Chapters 2 to 4.

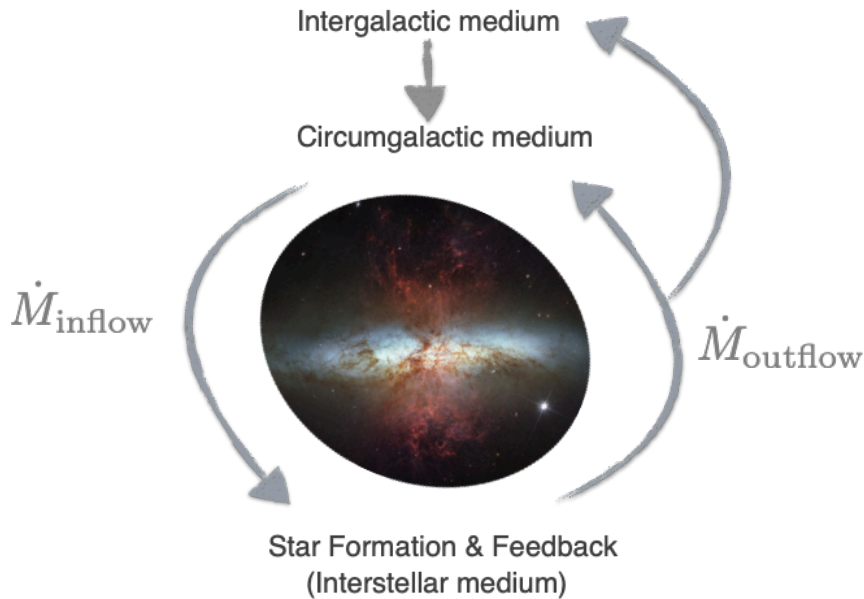


Figure 1.3: The baryon cycle of galaxies: Gas flows from the intergalactic medium (IGM) into the circumgalactic medium (CGM) surrounding the galaxy. From there, it cools and accretes onto the galactic plane where it proceeds to form stars. Stellar and AGN feedback drive outflows of gas back into the CGM, or if they are particularly energetic into the IGM. The image at the centre of this schematic depicts the starburst galaxy M82, showing the powerful outflows driven from the star-forming disc. Image credit for the M82 image: NASA/ESA/HubbleHeritage Team (AURA/STScI).

1.3 The Baryon Cycle of Galaxies

The term baryon cycle broadly describes the movement of gas as it cycles in and out of galaxies. Gas flows from the intergalactic medium (IGM) onto a galaxy halo and CGM gas accretes onto a disc in the galactic plane via cold streams and filaments or hot spherical accretion (e.g. Katz and White, 1993; Katz et al., 2003; Dekel et al., 2009). In the ISM, a fraction of that gas will form stars, regulated by stellar feedback (e.g. Hopkins et al., 2011; Agertz et al., 2013). SNe can drive outflows out of the galactic plane (e.g. Chevalier and Clegg, 1985; Heckman et al., 1990, 2000; Veilleux et al., 2005). Depending on the velocity of the outflow, gas might re-accrete onto the galaxy after some time as a galactic fountain (e.g. Shapiro and Field, 1976) or be energetic enough to leave the galactic potential (e.g. Heckman et al., 1990; Chisholm et al., 2015). AGN feedback is another driver of outflows (e.g. Veilleux et al., 2005; Fabian, 2012). Through this cycle, galaxies and the CGM become enriched in metals (e.g. Oppenheimer and Davé, 2008; Tumlinson et al., 2011; Péroux and Howk, 2020).

The above behaviour can be summarised succinctly in a few analytic rate equations. The

models of galaxy formation and evolution that take this approach are called ‘gas-regulator’, ‘bathtub’, or ‘equilibrium’ models (e.g. Finlator and Davé, 2008; Bouché et al., 2010; Davé et al., 2012; Dekel et al., 2013; Lilly et al., 2013; Dekel and Mandelker, 2014; Peng and Maiolino, 2014; Belfiore et al., 2019; Tacchella et al., 2020). They offer a simple framework for understanding the complex physics underpinning galaxy evolution, without the need for full hydrodynamical simulations or more involved semi-analytic models. Gas-regulator models assume that a star-forming galaxy is approximately in equilibrium between inflows and outflows, so while galaxies and their surrounding halos are not quite closed boxes, they can be approximated as such. Usually, a constant conversion of gas into stars is assumed, following the SK relation. In this case the SFR will be exclusively regulated by the inflow of gas. Since the driving of outflows carries a dependence on the SFR (with SNe feedback assumed to be doing the driving), even the outflow rate is determined by the inflow rate of gas. This implies that, to first order, galaxy evolution depends only the inflow rate of gas.

In general these models are particularly good at reproducing the mass-metallicity⁶ relationship of galaxies (see e.g. Finlator and Davé, 2008). Model estimates match the gas fraction of galaxies (e.g. Davé et al., 2012) and the SFMS (although, e.g. Dekel and Mandelker, 2014, note some tension for $z < 3$). Since approximately 90 per cent of the star formation in the Universe occurs in galaxies residing on the SFMS (e.g. Rodighiero et al., 2011, 2015), gas-regulator models offer a simple way to learn about the galaxy population at large. However, it is unclear how quenching should be treated in this framework. The only way for a galaxy to stop star formation would be to first shut off gas inflow completely, and then exhaust the residual ISM gas supply. Gas-regulator models are incapable of explaining suppressed SFRs like those observed in ETGs and PSBs (e.g. Davis et al., 2014, 2015; French et al., 2015; Rowlands et al., 2015; Suess et al., 2017; van de Voort et al., 2018). Peng and Maiolino (2014) suggested to use a variable SFE in the model, which would allow to take into account quenching. This is a more physical approach than assuming the SFE is constant, as evident from the observed variations in SFE between and within galaxies detailed in Section 1.2.1.1. Belfiore et al. (2019) also argue that an environmentally-dependent, variable SFE is required in gas-regulator models, to more accurately model gas-phase metallicity gradients in galaxies. Tacchella et al. (2020) similarly advocate for a variable, cloud-scale SFE in gas-regulator models, motivated by the breaks in the power spectral density of a galaxy’s SFR, one of which is associated with cloud-scale processes. This highlights that the star formation physics play a key role in shaping galaxy evolution and the baryon cycle. To fully understand what sets the SFE we need to study the ISM physics in more detail. These will be introduced in the following section.

1.4 The Interstellar Medium and Cloud-scale Star Formation

The term interstellar medium encompasses all gas and dust that exist within galaxies. It consists mainly of hydrogen (73.81 per cent by mass) and helium (24.85 per cent), with

⁶Metallicity refers to the abundance of metals, a term encompassing all elements heavier than Helium. The metallicity was negligible following the big bang and increased to solar abundance through nucleosynthesis processes in stars (e.g. Iliadis, 2007; Karakas and Lattanzio, 2014).

metals contributing 1.34 per cent at solar abundance (Asplund et al., 2009). The gaseous ISM components can be divided into multiple phases based on their densities, temperatures and ionization states (e.g. Field et al., 1969; McKee and Ostriker, 1977; Ferrière, 2001; Cox, 2005; Tielens, 2005; Draine, 2011).

By temperature, the ISM can be divided into a hot ($T \geq 10^{5.5}$ K, hydrogen is fully ionised), warm (5000 – 10000 K, where the hydrogen could be ionised or neutral) and cold ($T < 100$ K, hydrogen is neutral or molecular) phase. Most relevant for star formation is the cold gas phase, because gas will only be able to collapse into stars under its self-gravity if it can cool efficiently. The strong observational dependence of the SFR on Σ_{H_2} (e.g. Wong and Blitz, 2002, see also Section 1.2.1.1) suggests that molecular hydrogen is a pre-requisite for star formation. However, the tight molecular SK relation could also be a consequence of the fact that the ISM sites that are suitable for star formation also full-fill the conditions for H₂ formation (e.g. Krumholz et al., 2011). The ISM is very dynamic due to its turbulent state, thereby allowing a multi-phase medium to exist and mix. The nature and effects of turbulence will be discussed in more detail in the following section.

1.4.1 Turbulence in the Interstellar Medium

Big whirls have little whirls
That feed on their velocity,
And little whirls have lesser whirls
And so on to viscosity

L. F. Richardson, *Weather Prediction
by Numerical Process*

In a turbulent fluid, the velocity fluctuates randomly and unpredictably. Turbulence occurs when the ratio of inertial to viscous forces in the fluid is large. This is described by the Reynolds number,

$$Re = \frac{vL}{\nu}, \quad (1.4.1)$$

where v is the mean velocity of the flow, L the characteristic length scale and ν the viscosity of the fluid. The transition from laminar to turbulent flow occurs when the Reynolds number exceeds $Re = 1000 - 3000$. The ISM has a Reynolds number of $10^6 - 10^8$ (e.g. Tielens, 2005) and can thus be considered turbulent. Observed Mach numbers⁷ in the Milky Way range from 4 to 20 (e.g. Burkhart et al., 2010; Kainulainen and Tan, 2013; Kainulainen and Federrath, 2017), making the ISM turbulence supersonic.

Turbulence forms a so-called ‘turbulent cascade’ between the scale at which the energy is injected in the medium (driving scale) and the scale at which it dissipates. This leads to a dependence of the velocity dispersion on the current length scale of turbulence, $\sigma \propto l^c$ (e.g. Elmegreen and Scalo, 2004; McKee and Ostriker, 2007; Hennebelle and Falgarone, 2012). Incompressible turbulence has a dissipationless cascade, meaning that as eddies transfer energy from larger to smaller scales until viscosity dissipates the energy into heat. This

⁷ $\mathcal{M} = \sigma/c_s$, the ratio of velocity dispersion to the sound speed of the medium

was first described by Kolmogorov (1941). Incompressible turbulence leads to a velocity scaling of $\sigma \propto l^{\frac{1}{3}}$, $c = \frac{1}{3}$. The other extreme in types of turbulent forcing is compressive turbulence, discussed by Burgers (1939). Burgers (1939) turbulence dissipates through shocks, and produces a velocity scaling of $\sigma \propto l^{\frac{1}{2}}$, $c = \frac{1}{2}$.

Larson (1981) presented the first evidence for turbulence in the ISM by finding a linewidth – size relation in Milky Way molecular clouds. These obeyed a velocity scaling with $c = 0.38$, close to that of Kolmogorov turbulence (Larson, 1981). The relation between cloud size and velocity dispersion has since been observationally confirmed many times. However, subsequent studies found scalings of $c \approx 0.5$ (e.g. Solomon et al., 1987; Heyer and Brunt, 2004; Caldú-Primo et al., 2013), more indicative of compressible turbulence.

Simulations of pure magneto-hydrodynamical (MHD) and hydrodynamical (HD) turbulence predict that the probability distribution function (PDF) of the density has a log-normal form (e.g. Vazquez-Semadeni, 1994; Padoan et al., 1997; Scalo et al., 1998; Ostriker et al., 2001; Kritsuk et al., 2007; Federrath et al., 2008; Federrath et al., 2010; Molina et al., 2012). The density PDF becomes wider the more turbulent (i.e. higher \mathcal{M}) the ISM, as it will lead to more shocks. This density PDF can be described mathematically as:

$$P(s) = \frac{1}{\sqrt{2\pi\sigma_s^2}} \exp\left(-\frac{(s-s_0)^2}{2\sigma_s^2}\right), \quad (1.4.2)$$

where $s \equiv \ln(\rho/\rho_0)$, ρ_0 the mean gas density and $s_0 = -\frac{1}{2}\sigma_s^2$. The width of the PDF, σ_s^2 , depends on the turbulent forcing through the sonic Mach number, \mathcal{M} , and a dimensionless forcing parameter, b , (Federrath et al., 2008):

$$\sigma_s^2 = \ln [1 + b^2 \mathcal{M}^2]. \quad (1.4.3)$$

The turbulent forcing parameter is defined as

$$b = 1 + \left(\frac{1}{D} - 1\right) \zeta, \quad (1.4.4)$$

where D is the dimensionality of turbulence considered and $\zeta \in [0, 1]$ depends on the type of forcing. Purely solenoidal forcing yields $\zeta = 1$, while $\zeta = 0$ for purely compressive forcing. The log-normal form can also be understood as a consequence of the central limit theorem: The strength of shocks scales with \mathcal{M} , which also relates the pre- and post-shock densities (e.g. Landau and Lifshitz, 1987). If the turbulence in the ISM is at least partially compressible then energy will dissipate through shocks. This sets the density distribution of the gas, which becomes a normal distribution in log space, since the post-shock densities are additive.

If self-gravity is included in the turbulence simulations, the PDF develops a power-law tail at high densities (e.g. Klessen et al., 2000; Slyz et al., 2005; Hennebelle et al., 2008; Kritsuk et al., 2011). The slope of the tail and the density of the transition change over time as the collapse progresses. The slope varies from a steep slope of 3 and a transition at high density to 1-1.5 with a transition at a (significantly) lower density (e.g. Collins et al., 2012; Girichidis et al., 2014; Lee et al., 2015; Burkhardt et al., 2017). Over the last decades

this behaviour has been observed in Milky Way clouds (e.g. Kainulainen et al., 2009; André et al., 2011; Kainulainen et al., 2011; Lombardi et al., 2015; Alves et al., 2017).

A large number of other statistical methods have been applied to quantify the turbulence within the ISM, in an attempt to better understand its origins, as reviewed by Elmegreen and Scalo (2004). Among them are the delta-variance, fractal dimension, the structure function, the auto-correlation function, power spectrum and energy density spectrum. All of these can be applied to the velocity field, the density, or the combination $\rho^{\frac{1}{3}}v$. The slope of the power spectrum can be used to determine the type of turbulence, because Kolmogorov (1941) and Burgers (1939) turbulence scale differently. In one dimension, the power spectra will scale as $P(k) \propto k^{-5/3}$ and k^{-2} , respectively. The nature of the forcing (e.g. Federrath, 2013). It is more straightforward to interpret the slope of velocity spectra, because the density spectrum only contains information on the turbulent velocity field if the turbulence is incompressible.

Turbulence is expected to decay within a crossing time, $t_{\text{cr}} \approx L/\sigma$ (e.g. Mestel and Spitzer, 1956; Mac Low, 1999; Mac Low and Klessen, 2004; McKee and Ostriker, 2007). This is of order a few Myr for molecular clouds (e.g. Hennebelle and Falgarone, 2012; Chevance et al., 2020c) and not significantly affected or prolonged by MHD turbulent effects (e.g. Zweibel and Josafatsson, 1983; Mac Low et al., 1998; Stone et al., 1998; Cho and Lazarian, 2003). A decay time of a few Myr is somewhat shorter than the observed cloud lifetimes of 10 – 30 Myr (e.g. Engargiola et al., 2003; Kawamura et al., 2009; Meidt et al., 2015; Chevance et al., 2020b). Yet the ubiquity of velocity dispersions $\sigma \sim 10\text{--}20 \text{ km s}^{-1}$ in CO (e.g. Bigiel et al., 2008; Caldú-Primo et al., 2013) and HI (e.g. van Zee and Bryant, 1999; Tamburro et al., 2009; Ianjamasimanana et al., 2012) indicate that turbulence is omnipresent in the ISM. Even the value of $\sigma > 1 \text{ km s}^{-1}$ Sun et al. (2018, 2020b) find for cloud-sized regions in a sample of 70 LTGs is firmly in the regime of supersonic turbulence, since the sound speed of CO is $\sim 0.3 \text{ km s}^{-1}$. This implies that there must be some driving mechanism that regularly injects the energy required to sustain the turbulence in the ISM. It remains unclear what mechanism(s) drive the turbulence and on which scale(s) energy is injected into the ISM (e.g. Elmegreen and Scalo, 2004; Mac Low and Klessen, 2004; McKee and Ostriker, 2007; Hennebelle and Falgarone, 2012). Over time, many possible mechanisms have been proposed, which are listed below⁸:

- accretion of gas onto the galaxy (e.g. Field et al., 2008; Klessen and Hennebelle, 2010) and subsequent radial transport by gravity (e.g. Krumholz et al., 2018)
- stellar feedback (e.g. Norman and Ferrara, 1996; Matzner, 2002; Krumholz et al., 2018): specifically through photoionisation, SNe explosions and stellar winds
- ambient pressure (e.g. Schrubba et al., 2019)
- spiral arm shocks (e.g. Roberts, 1969; Wada, 2008)
- shear (e.g. Martig et al., 2009; Meidt et al., 2018)

⁸Mostly based on the discussion in Mac Low and Klessen (2004) and Hennebelle and Falgarone (2012).

- magneto-rotational instability (e.g. Balbus and Hawley, 1998)
- thermal instability (e.g. Vázquez-Semadeni et al., 2000; Kritsuk and Norman, 2002)
- proto-stellar jets and outflows (e.g. Nakamura and Li, 2007; Wang et al., 2010)

None of these possible energy-injection mechanisms can explain all turbulent ISM observations at once. For example, comparing simulations of turbulent molecular clouds with different types of forcing to observations, Brunt et al. (2009) conclude that the driving processes must act on scales comparable to the cloud size or larger. This rules out proto-stellar outflows as sole drivers of turbulence, even though it is an important contribution to the small-scale turbulence. Williams et al. (1994) find comparable velocity dispersions in star-forming and quiescent clouds, which implies that turbulence cannot solely be driven by stellar feedback processes. In some cases, e.g. magneto-rotational instability, thermal instability, stellar winds and stellar radiation, the amount of energy converted into turbulence is simply too low to sustain the observed velocity dispersions on its own.

Krumholz et al. (2018) developed an analytical model where the turbulent velocity dispersion is set by a combination of gas accretion and gravitational instabilities, and stellar feedback. This model manages to reproduce velocity dispersions of spiral and dwarf galaxies both in the local Universe and at high redshift. Conversely, shear is thought to be an important source of turbulence in ETGs (e.g. Martig et al., 2009).

Giant molecular clouds (GMCs) likely form at the centres of converging flows driven by the turbulent motions and shocks in the ISM, or through gravitational instabilities (e.g. Dobbs et al., 2014; Chevance et al., 2020c, and references therein). The fraction of molecular gas in the cloud is determined by the midplane gas pressure of its galaxy (e.g. Blitz and Rosolowsky, 2006). Due to their comparatively small sizes, molecular cloud populations have been studied most extensively in the Milky Way, and only a few other, nearby galaxies. The Physics at High Angular resolution in Nearby GalaxieS (PHANGS) project (Leroy et al., 2021b) is starting to revolutionise this, having observed 74 local late-type galaxies in ^{12}CO at spatial resolutions of ≤ 150 pc. In general, molecular cloud masses lie in the range $10^4 - 10^{6.5} M_{\odot}$ (e.g. Rosolowsky et al., 2003; Heyer et al., 2009; Freeman et al., 2017; Miville-Deschênes et al., 2017; Colombo et al., 2019), with sizes ranging from 1 – 100 pc.

Early observations of GMCs (Larson, 1981; Solomon et al., 1987) found them to have a constant surface density, which led to the belief that clouds are gravitationally bound entities in virial equilibrium. This is characterised by the virial parameter, α_{vir} , defined as the ratio of kinetic to gravitational potential energy:

$$\alpha_{\text{vir}} = \frac{2E_{\text{kin}}}{E_{\text{grav}}} = \frac{5\sigma^2 R}{GM} \propto \frac{\sigma^2}{\Sigma R}. \quad (1.4.5)$$

This definition follows Bertoldi and McKee (1992) for a spherical cloud with velocity dispersion σ , radius R , mass M , and surface density Σ . Clouds are gravitationally bound for $\alpha_{\text{vir}} < 2$ and in virial equilibrium if $\alpha_{\text{vir}} = 1$. An $\alpha_{\text{vir}} > 2$ would indicate that the structure is unbound, however external pressure can confine a structure even at large α_{vir}

(e.g. Schrupa et al., 2019). More recent observations of GMCs reveal that $\sigma/R^{0.5}$ scales with Σ (e.g. Heyer et al., 2009; Leroy et al., 2017; Sun et al., 2018; Colombo et al., 2019; Sun et al., 2020a), implying that clouds exist in various states of virialisation. Some molecular clouds are observed with $\alpha_{\text{vir}} \gg 10$, but the median of the LTG cloud population appears to be 2.7 (Sun et al., 2020b). The physical state of molecular clouds is a crucial aspect for star formation on the cloud-scale, which we discuss in the following Section.

1.4.2 Cloud-scale Star Formation

The Toomre length (introduced in Section 1.2.2) defines the largest scale on which a gas disc is susceptible to gravitational instability if perturbed. The smallest scale on which gravitational instability can occur is the Jeans (1902) length. On smaller scales the gas is pressure supported against collapse. The Jeans length is defined as:

$$\lambda_{\text{J}} = \left(\frac{\pi c_{\text{s}}^2}{G\rho} \right)^{\frac{1}{2}}, \quad (1.4.6)$$

where c_{s} is the sound speed of the cloud, and ρ its mean density. Gravitational instability occurs for $\lambda > \lambda_{\text{J}}$. This criterion can also be expressed in terms of the mass contained within the Jeans length:

$$M_{\text{J}} = \frac{4\pi}{3} \rho \left(\frac{\lambda_{\text{J}}}{2} \right)^3 \propto T^{\frac{3}{2}} \rho^{-\frac{1}{2}}, \quad (1.4.7)$$

where clouds with masses in excess of the Jeans mass, M_{J} , will be unstable and will start to collapse⁹. As a cloud collapses, the density increases and the Jeans mass decreases. This leads to fragmentation – within the larger collapsing cloud smaller regions become gravitationally unstable and start collapsing themselves. Low and Lynden-Bell (1976) find that fragmentation halts once $M < 0.004 M_{\odot}$. The above analysis neglects the presence of external pressure, which is unphysical for the conditions in the ISM. Bonnor (1956) and Ebert (1957) derived an analogous maximum mass for a cloud in hydrodynamic equilibrium with a surface pressure $\rho\sigma^2$.

However, GMCs themselves are not single homogeneous, spherical entities with uniform density. The intermittency of turbulence creates filamentary structures and gravitational fragmentation creates a hierarchy of overdense clumps and cores on various scales that are embedded in a more diffuse medium (e.g. Williams et al., 2000; McKee and Ostriker, 2007; Hennebelle and Falgarone, 2012; Chevance et al., 2020c). At scales below the sonic scale, turbulence within the gas becomes less important than self-gravity (e.g. Kritsuk et al., 2013). The formation of individual stars and binaries takes place in the dense cores at these small scales (e.g. McKee and Ostriker, 2007; Krumholz, 2014). In this thesis, we are interested in star formation at the scale of clouds and how it relates to the global SFR of galaxies. Therefore, this thesis will not review the formation process of individual stars and/or star clusters in more detail, but focus instead on what sets the overall star formation rate of GMCs.

⁹This is the definition used by e.g. Binney and Tremaine (2008) and McKee and Ostriker (2007), although they note that the Jeans mass is sometimes simply defined as $\rho\lambda_{\text{J}}^3$.

One important timescale in this context is the free-fall time, t_{ff} :

$$t_{\text{ff}} = \sqrt{\frac{3\pi}{32G\rho}}. \quad (1.4.8)$$

This is the time it would take a spherically symmetric cloud with average density ρ to collapse under its own gravity in the absence of forces opposing the collapse (e.g. Spitzer, 1978). The star formation efficiency (SFE) is the fraction of gas converted into stars on a certain timescale. The SFE per free-fall time is given by

$$\epsilon_{\text{ff}} = \frac{\dot{M}_*}{M_{\text{gas}}} t_{\text{ff}} = \frac{t_{\text{ff}}}{t_{\text{dep}}}, \quad (1.4.9)$$

which depends on the SFR, \dot{M}_* , and the mass of the cloud M_{gas} , in addition to the free-fall time¹⁰. The depletion time $t_{\text{dep}} \equiv M_{\text{gas}}/\dot{M}_*$ is defined as the time it will take to convert the entirety of the current gas reservoir into stars at the current SFR (assumed constant). If only gravity and thermal pressure were relevant in gas cloud collapse and the gas can cool efficiently, then $t_{\text{dep}} \rightarrow t_{\text{ff}}$ and the SFE should be 100 per cent.

Even if the free-fall time of GMCs is on the shorter side of astrophysical timescales with \sim few Myr, this nevertheless makes it impossible to observe the full collapse. Since observations only capture a snapshot of the star formation process within the clouds, observed SFEs are by necessity an instantaneous measure and do not completely reflect the theoretical ϵ_{ff} (Kim et al., 2021b). Often, if t_{ff} is unknown or too uncertain, observed SFEs will be quoted as $1/t_{\text{dep}}$, rather than calculated as per Equation 1.4.9. Instead of considering the efficiency of star formation over a free-fall time, which tends to be shorter than the lifetime of clouds, the SFE of a cloud can also be considered as an integrated quantity, ϵ_{int} . This is defined as

$$\epsilon_{\text{int}} = \frac{M_*(t \rightarrow \tau_{\text{life}})}{M_{\text{gas}}(t = 0)}, \quad (1.4.10)$$

i.e. the fraction of gas that is converted into stars across the lifetime of the cloud. The average integrated SFE for clouds across an entire galaxy can now be measured using a statistical method (Kruijssen and Longmore, 2014; Kruijssen et al., 2018).

1.4.2.1 Observations of the Cloud-scale Star Formation Efficiency

The average SFE per free-fall time for clouds in the Milky Way is 1 – 2 per cent (e.g. Myers et al., 1986; Evans and Lada, 1991; Evans et al., 2014; Lee et al., 2016; Vutisalchavakul et al., 2016), but with considerable variation. For example, Lee et al. (2016) find a scatter of 0.91 dex for their data and Vutisalchavakul et al. (2016) find efficiencies ranging from 0.03 – 10 per cent in the plane of the Milky Way. Murray (2011) finds similar variation in his sample of star forming complexes ($0.001 \leq \epsilon_{\text{ff}} \leq 0.592$) although an average ϵ_{ff} that exceeds that of other Milky Way studies with 15 per cent. The SFE within the CMZ varies

¹⁰The SFE can equally be defined with surface or volume densities of gas and SFR.

between 1 – 4 per cent (Barnes et al., 2017), which places it in between the Murray (2011) and the other results. Ochsendorf et al. (2017) find an average SFE of 0.12 or 0.25 in the LMC depending on whether they estimate the SFR by counting young stellar objects or $H\alpha$ and $24\mu\text{m}$ emission, respectively. This is more in line with the Murray (2011) values for the Milky Way. Krumholz et al. (2019) argues these systematically higher values than the $\epsilon_{\text{ff}} \sim 0.01$ average could be due to how the GMCs are selected.

Cloud-scale average estimates of the SFE per free-fall time in other galaxies exist for M 51 (Leroy et al., 2017, but see also Bigiel et al., 2016, Querejeta et al., 2019), 14 galaxies from the PHANGS sample (Utomo et al., 2018) and NGCs 3351, 3627, 4254 and 4321 (Gallagher et al., 2018). Gallagher et al. (2018) find an average SFE of 0.2 – 0.3 per cent both when tracing all molecular gas in CO and dense gas in HCN. This agrees well with Leroy et al. (2017) who finds an average of 0.36 per cent in M 51, again with significant variation between individual regions (0.04 – 2.5 per cent). The median for the PHANGS sample is ~ 0.7 per cent, with ~ 1 dex variation within and between the galaxies analysed (Utomo et al., 2018). The integrated SFE measurements are slightly larger, but show a similar picture: Kim et al. (2021a) finds integrated efficiencies ranging from 0.7 to 6.8 per cent for 6 galaxies, where the SFR is measured in $24\mu\text{m}$. Murray (2011) estimates an average 8 per cent for his sample of Milky Way clouds and Chevance et al. (2020b) find integrated SFEs in range 4 – 10 per cent in a subset of 9 PHANGS galaxies.

These results highlight two points: firstly, that the conversion of gas to stars on the cloud-scale is inefficient on average and secondly, that it varies greatly both within and between galaxies. Early hypothesis for the inefficiency of star formation were focussed on magnetic fields and their support against collapse (as proposed by Mouschovias and Spitzer, 1976, reviewed by Shu et al., 1987). Although the underlying physics are not fully understood to this day, the consensus is that the turbulence in the ISM, outlined in Section 1.4.1, plays a key role. Recent observations indicate that GMCs tend to be dispersed within $\lesssim 3$ Myr following the formation of massive stars, most likely due to photoionisation and stellar winds (Chevance et al., 2020a). This leads to a picture of clouds as transient entities, which only survive until stellar feedback processes destroy them following the formation of the first massive stars. It follows that cloud-scale star formation is inefficient, because only a small fraction of the gas within a cloud forms stars prior to its dispersal (see also e.g. Semenov et al., 2017, 2018; Chevance et al., 2020c, and references therein). Based on this understanding, a number of theoretical models for a variable cloud-scale star formation efficiency have been developed that depend on parameters associated with the turbulence.

1.4.2.2 Analytic Models of the Star Formation Efficiency

Building on the premise that the log-normal density PDF of the turbulent ISM determines the fraction of gas is converted into stars on a free-fall timescale, it is possible to analytically determine the ϵ_{ff} ¹¹ of clouds. In a generalised form (Federrath and Klessen, 2012)¹² the

¹¹In the literature this is often referred to as SFR_{ff} , however this is equivalent to the ϵ_{ff} defined in Equation 1.4.9 for $M_{\text{gas}} = M_{\text{cloud}}$ and the free-fall time of the average cloud density.

¹²The original Padoan and Nordlund (2011) model does not include the factor ϕ_t .

SFE is given by the integral over the density PDF defined in Equation 1.4.2:

$$\epsilon_{\text{ff}} = \frac{\epsilon_{\text{PSFB}}}{\phi_{\text{t}}} \int_{s_{\text{crit}}}^{\infty} \frac{t_{\text{ff}}(\rho_0)}{t_{\text{ff}}(\rho)} \frac{\rho}{\rho_0} P(s) ds. \quad (1.4.11)$$

The factor ϵ_{PSFB} accounts for the fact that proto-stellar feedback is expected to prevent some of the available gas from accreting onto a protostar during the star formation process. Estimates for its value range from $0.25 \geq \epsilon_{\text{PSFB}} \geq 0.7$ for individual star formation and $0.3 \geq \epsilon_{\text{PSFB}} \geq 0.5$ for clustered low-mass stars (e.g. Matzner and McKee, 2000). The ϕ_{t}^{-1} is a fudge factor of order unity that is determined via numerical simulations. This definition of the SFE explicitly includes a critical density, $s_{\text{crit}} = \ln(\rho_{\text{crit}}/\rho)$, that gas must exceed for star formation to proceed. The models in the literature differ in how they define the critical density, and their treatment of the free-fall time factor $t_{\text{ff}}(\rho_0)/t_{\text{ff}}(\rho)$. A brief summary of them is given below (see also Table 1.1, and Table 1 in Federrath and Klessen, 2012).

The first model is that of Krumholz and McKee (2005), who consider hydrodynamic turbulence only. They set the free-fall time factor to unity and argue that the critical overdensity for collapse, $\exp(s_{\text{crit}})$, is determined by $\lambda_{\text{S}} \geq \lambda_{\text{J}}$, where λ_{S} is the sonic scale. The physical motivation is that the sonic Mach number drops below 1 on scales smaller than the sonic scale (e.g. Vázquez-Semadeni et al., 2003; Federrath et al., 2010), which allows gravitational collapse to proceed (e.g. Mac Low and Klessen, 2004). This sets $s_{\text{crit}} = 2 \ln(\phi_{\text{x}} \lambda_{\text{J}}(\rho_0)/\lambda_{\text{S}}) = \ln[(\pi^2/5)\phi_{\text{x}}^2 \alpha_{\text{vir}} \mathcal{M}^2]$, where ϕ_{x} allows for some variations in the actual scale at which collapse sets in and is determined from numerical simulations. Based on the Vázquez-Semadeni et al. (2003) simulations, Krumholz and McKee (2005) set $\phi_{\text{x}} = 1.12$.

Full MHD turbulence is considered by Padoan and Nordlund (2011). The critical density is defined based on magnetic shock jump conditions and the critical mass for magnetic collapse, as $s_{\text{crit}} = \ln[0.067\theta^{-2} \alpha_{\text{vir}} \mathcal{M}^2 f(\beta)]$, where θ is the ratio between the cloud size and the largest turbulent scale, and a numerical factor ≤ 1 . The ratio of the thermal to magnetic pressure is $\beta = 2c_{\text{s}}^2/v_{\text{A}}^2$. Its inclusion in the critical density through $f(\beta) = (1 + 0.925\beta^{-1.5})^{2/3} (1 + \beta^{-1})^{-2}$ accounts for the effect of magnetic fields in hindering gravitational collapse. In this mode, the free-fall time factor is set to $t_{\text{ff}}(\rho_0)/t_{\text{ff}}(\rho_{\text{crit}})$, thus still allowing to evaluate it outside the integral in Equation 1.4.11.

The third model considered here is that of Hennebelle and Chabrier (2011). These authors were the first to argue that the free-fall time factor should be included in the integral when determining ϵ_{ff} , as the free-fall time changes with density. They re-evaluated the Krumholz and McKee (2005) and Padoan and Nordlund (2011) models in this so called multi-free-fall (multi-ff) approach and added a third approach for determining the critical density. Considering only hydrodynamical turbulence, the SFE is determined via the mass spectrum and the mass of the largest fluctuation which can become unstable within the cloud. This can be translated into a cut-off length y_{cut} defined as the ratio of the turbulent Jeans length (e.g. Bonazzola et al., 1987; Federrath and Klessen, 2012) to the cloud size. The critical overdensity is then $s_{\text{crit}} = \ln[\rho_{\text{crit,th}} + \rho_{\text{crit,turb}}] = \ln[(\pi^2/15)y_{\text{cut}}^{-1} \alpha_{\text{vir}} (3y_{\text{cut}}^{-1} \mathcal{M}^{-2} + 1)]$.

Model	t_{ff} time factor	Critical density	Transition density (s_t)	ϵ_{ff}
KM	1	$\frac{\pi^2}{5} \phi_{\text{X}}^2 \alpha_{\text{vir}} \mathcal{M}^2$	NA	$\frac{\epsilon_{\text{PSFB}}}{2\phi_{\text{t}}} \left[1 + \text{erf} \left(\frac{\sigma_s^2 - s_{\text{crit}}}{\sqrt{2\sigma_s^2}} \right) \right]$
PN	$t_{\text{ff}}(\rho_0)/t_{\text{ff}}(\rho_{\text{crit}})$	$(0.067)\theta^{-2} \alpha_{\text{vir}} \mathcal{M}^2 f(\beta)$	NA	$\frac{\epsilon_{\text{PSFB}}}{2\phi_{\text{t}}} \exp\left(\frac{1}{2}s_{\text{crit}}\right) \left[1 + \text{erf} \left(\frac{\sigma_s^2 - s_{\text{crit}}}{\sqrt{2\sigma_s^2}} \right) \right]$
HC	$t_{\text{ff}}(\rho_0)/t_{\text{ff}}(\rho)$	$\frac{\pi^2}{15} y_{\text{cut}}^{-1} \alpha_{\text{vir}} [3y_{\text{cut}}^{-1} \mathcal{M}^{-2} + 1]$	NA	$\frac{\epsilon_{\text{PSFB}}}{2\phi_{\text{t}}} \exp\left(\frac{3\sigma_s^2}{8}\right) \left[1 + \text{erf} \left(\frac{\sigma_s^2 - s_{\text{crit}}}{\sqrt{2\sigma_s^2}} \right) \right]$
B(KM)	1	$\frac{\pi^2}{5} \phi_{\text{X}}^2 \alpha_{\text{vir}} \mathcal{M}^2$	$\frac{1}{2}(2\eta - 1) \ln[1 + b^2 \mathcal{M}^2]$	$\frac{N\epsilon_{\text{PSFB}}}{2} \left[\text{erf} \left(\frac{\sigma_s^2 - 2s_{\text{crit}}}{\sqrt{8\sigma_s^2}} \right) - \text{erf} \left(\frac{\sigma_s^2 - 2s_t}{\sqrt{8\sigma_s^2}} \right) + 2C \frac{\exp(s_t(1-\eta))}{\eta-1} \right]$
B(PN)	$t_{\text{ff}}(\rho_0)/t_{\text{ff}}(\rho_{\text{crit}})$	$(0.067)\theta^{-2} \alpha_{\text{vir}} \mathcal{M}^2 f(\beta)$	$\frac{1}{2}(2\eta - 1) \ln[1 + b^2 \mathcal{M}^2]$	$\frac{N\epsilon_{\text{PSFB}}}{2} \exp\left(\frac{s_{\text{crit}}}{2}\right) \left[\text{erf} \left(\frac{\sigma_s^2 - 2s_{\text{crit}}}{\sqrt{8\sigma_s^2}} \right) - \text{erf} \left(\frac{\sigma_s^2 - 2s_t}{\sqrt{8\sigma_s^2}} \right) + 2C \frac{\exp(s_t(1-\eta))}{\eta-1} \right]$
multi-ff KM	$t_{\text{ff}}(\rho_0)/t_{\text{ff}}(\rho)$	$\frac{\pi^2}{5} \phi_{\text{X}}^2 \alpha_{\text{vir}} \mathcal{M}^2$	NA	$\frac{\epsilon_{\text{PSFB}}}{2\phi_{\text{t}}} \exp\left(\frac{3\sigma_s^2}{8}\right) \left[1 + \text{erf} \left(\frac{\sigma_s^2 - s_{\text{crit}}}{\sqrt{2\sigma_s^2}} \right) \right]$
multi-ff PN	$t_{\text{ff}}(\rho_0)/t_{\text{ff}}(\rho)$	$(0.067)\theta^{-2} \alpha_{\text{vir}} \mathcal{M}^2 f(\beta)$	NA	$\frac{\epsilon_{\text{PSFB}}}{2\phi_{\text{t}}} \exp\left(\frac{3\sigma_s^2}{8}\right) \left[1 + \text{erf} \left(\frac{\sigma_s^2 - s_{\text{crit}}}{\sqrt{2\sigma_s^2}} \right) \right]$
multi-ff HC	$t_{\text{ff}}(\rho_0)/t_{\text{ff}}(\rho)$	$\frac{\pi^2}{15} y_{\text{cut}}^{-1} \alpha_{\text{vir}} [3y_{\text{cut}}^{-1} \mathcal{M}^{-2} + 1]$	NA	$\frac{\epsilon_{\text{PSFB}}}{2\phi_{\text{t}}} \exp\left(\frac{3\sigma_s^2}{8}\right) \left[1 + \text{erf} \left(\frac{\sigma_s^2 - s_{\text{crit}}}{\sqrt{2\sigma_s^2}} \right) \right]$
multi-ff B	$t_{\text{ff}}(\rho_0)/t_{\text{ff}}(\rho)$	model-dependent	$\frac{1}{2}(2\eta - 1) \ln[1 + b^2 \mathcal{M}^2]$	$\frac{N\epsilon_{\text{PSFB}}}{2} \exp\left(\frac{3\sigma_s^2}{8}\right) \left[\text{erf} \left(\frac{\sigma_s^2 - s_{\text{crit}}}{\sqrt{2\sigma_s^2}} \right) - \text{erf} \left(\frac{\sigma_s^2 - s_t}{\sqrt{2\sigma_s^2}} \right) \right] + NC\epsilon_{\text{PSFB}} \left[\frac{\exp(s_t(1.5-\eta))}{\eta-1.5} \right]$

Table 1.1: Summary of the analytic star formation efficiency per free-fall time models. Adapted from Federrath and Klessen (2012), with the addition of the Burkhardt (2018) (B) model. KM stands for the model of Krumholz and McKee (2005), PN for Padoan and Nordlund (2011) and HC for Hennebelle and Chabrier (2011). As per Federrath and Klessen (2012), the KM and HC models can include the effect of magnetic fields on the collapse by multiplying the critical density by a factor $(1 + \beta^{-1})^{-1}$.

The general solution for the multi-ff SFE is given by:

$$\epsilon_{\text{ff}} = \frac{\epsilon_{\text{PSFB}}}{2\phi_{\text{t}}} \exp\left(\frac{3}{8}\sigma_s^2\right) \left[1 + \operatorname{erf}\left(\frac{\sigma_s^2 - s_{\text{crit}}}{\sqrt{2\sigma_s^2}}\right)\right], \quad (1.4.12)$$

into which the s_{crit} from the model of choice can be substituted. Federrath and Klessen (2012) extend the applicability of the Krumholz and McKee (2005) and Hennebelle and Chabrier (2011) models to MHD, by including the effects of magnetic fields in the critical density. Specifically, they do this by replacing the thermal pressure with the sum of the thermal and magnetic pressures, i.e. $P_{\text{th}} \rightarrow P_{\text{th}} + P_{\text{mag}}$. Using the definition of the plasma $\beta = P_{\text{th}}/P_{\text{mag}}$ and effective Mach number can be defined as $\mathcal{M}(1+\beta^{-1})^{-1/2}$, which replaces \mathcal{M} in the definition of s_{crit} .

Through predicting the dependence of the SFE on the physical conditions of clouds in the ISM, one can develop an intuition for the effect that the physical conditions have on the star formation process. All aforementioned models predict that ϵ_{ff} decreases with increasing α_{vir} and increases with increasing \mathcal{M} . This makes sense on the intuitive level, as more kinetic energy, compared to the self-gravity of the cloud, makes it harder to collapse. The more supersonically turbulent the gas, the stronger the shocks and compression, allowing for potentially faster collapse (which is how $\epsilon_{\text{ff}} > 1$ is possible in these models). Comparison with observations of Milky Way clouds (Heiderman et al., 2010; Lada et al., 2010) reveals a good agreement between the models and the data, although not all scatter in the data is captured by the models. Another bonus of an analytic theory for the physical processes determining the SFE is that Equation 1.4.12 can be used to improve the sub-grid modelling of star formation in numerical simulations (see e.g. Kimm et al., 2017; Trebitsch et al., 2017; Kretschmer and Teyssier, 2020; Nuñez-Castiñeyra et al., 2021).

Not captured by these models is the possibility that the SFE explicitly varies over time, i.e. even though the turbulent nature of the ISM does not change during the star formation process, the SFE does. Yet, observations of Milky Way GMCs indicate that this occurs in some star forming regions (e.g. Palla and Stahler, 2000; Lee et al., 2016; Caldwell and Chang, 2018). Burkhart (2018) argue that this can be accounted for by including the power law tail of the gas PDF, in addition to the log-normal part, in analytical models. The gas PDF can then be described as

$$P_{\text{LN+PL}}(s) = \begin{cases} \frac{N}{\sqrt{2\pi\sigma_s^2}} \exp\left(-\frac{(s-s_0)^2}{2\sigma_s^2}\right), & s < s_{\text{t}} \\ NC \exp(-\eta s), & s > s_{\text{t}}, \end{cases} \quad (1.4.13)$$

where $s_{\text{t}} = \ln(\rho_{\text{t}}/\rho_0)$ is the density contrast of the transition point from the log-normal to the power law form (e.g. Collins et al., 2012; Burkhart et al., 2017; Burkhart, 2018). The amplitude of the power law part is given by $C = \exp(1/2(\eta - 1)\eta\sigma_s^2)/(\sqrt{2\pi\sigma_s^2})$ and like the transition point $s_{\text{t}} = (\eta - 1/2)\sigma_s^2$ depends on the slope of the power law η . The normalisation N can be derived from requiring that the PDF is normalised to one. Subsequently, the PDF of Equation 1.4.13 can be integrated in the same manner and with the same choices for the critical density and the free-fall time factor as Equation 1.4.11. The multi-ff solution

becomes

$$\epsilon_{\text{ff}} = \frac{N\epsilon_{\text{PSFB}}}{2} \exp\left(\frac{3\sigma_s^2}{8}\right) \left[\text{erf}\left(\frac{\sigma_s^2 - s_{\text{crit}}}{\sqrt{2\sigma_s^2}}\right) - \text{erf}\left(\frac{\sigma_s^2 - s_t}{\sqrt{2\sigma_s^2}}\right) \right] + NC\epsilon_{\text{PSFB}} \left[\frac{\exp(s_t(1.5 - \eta))}{\eta - 1.5} \right], \quad (1.4.14)$$

and is limited to $\eta > 1.5$.

Through the dependence of s_t on η , the SFE as described in Equation 1.4.14 varies with time implicitly. Analytical and numerical analysis demonstrates that the slope of the power law varies from $\eta \approx 3$ at the beginning of collapse to $\eta \approx 1.5 - 1$ across a free-fall time (e.g. Girichidis et al., 2014; Burkhardt et al., 2017), although the exact timescale depends on the magnetic field strength (Burkhardt et al., 2015). As the power law tail becomes shallower at fixed \mathcal{M} and α_{vir} , the star formation accelerates and ϵ_{ff} increases. The SFE deviation from a constant value begins at steeper slopes for low Mach numbers. The Burkhardt (2018) SFE model predicts the variety in ϵ_{ff} of Milky Way clouds for moderate changes in the turbulent forcing parameter and within the range of \mathcal{M} observed for the Milky Way. It also explains the scatter between cloud mass and SFR of the Lada et al. (2012) relation as an evolutionary sequence with the SFR increasing with decreasing power-law slope at fixed cloud mass. The log-normal PDF-based models would need to invoke a variation of two orders of magnitude in Mach number to explain this scatter, far in excess of the Milky Way typical $\mathcal{M} = 4-20$ (e.g. Burkhardt et al., 2010; Kainulainen and Tan, 2013; Kainulainen and Federrath, 2017).

The power law slope becomes shallower over time because the fraction of dense gas increases the more collapse progresses (e.g. Burkhardt, 2018; Burkhardt and Mocz, 2019). Since ϵ_{ff} is related to η , this implies that the SFE should increase with increasing dense gas fraction. However, recent HCN observations of 30 nearby galaxies find that, statistically, the SFE is anti-correlated with stellar surface density, while the dense gas fraction correlates with it (e.g. Usero et al., 2015; Bigiel et al., 2016). This indicates that more than the competition of gravity and feedback determines the overall SFR (as predicted in e.g. Burkhardt, 2018; Krumholz et al., 2018). Instead it suggests that the galactic environment (and its influence on large scale turbulence), can also play an important role in governing the star formation process. This is consistent with a recent theoretical model that invokes galactic shear as the dominant process in setting the SFE (Meidt et al., 2018, 2020).

1.4.2.3 The Cloud-scale Star Formation Efficiency in Simulations

The highly compressive supersonic turbulence of the ISM cannot be fully described analytically. Simulations provide the opportunity to gain a better understanding of the properties and impact of (M)HD turbulence in the ISM (e.g. Elmegreen and Scalo, 2004; Mac Low and Klessen, 2004; Hennebelle and Falgarone, 2012). In case of the SFE specifically, simulations have been used to calibrate and validate the density PDF-based analytical models (e.g. Krumholz and McKee, 2005; Padoan and Nordlund, 2011; Federrath and Klessen, 2012; Mocz and Burkhardt, 2019). High-resolution simulations of turbulent boxes can also be used

to empirically derive the relation between the SFE and the properties of the turbulent ISM, if the star formation process is included.

Prominently, Padoan et al. (2012) used a suite of 45 MHD turbulent box simulations with solenoidal forcing, self-gravity and stringent criteria for sink particle star formation to determine ϵ_{ff} . Fitting the simulation results, Padoan et al. (2012) find that the SFE is well described by a negative exponential dependence on the ratio of free-fall to dynamical time $t_{\text{ff}}/t_{\text{dyn}} \propto \alpha_{\text{vir}}^{0.5}$, modulo a factor to account for the proto-stellar feedback:

$$\epsilon_{\text{ff}} \approx \epsilon_{\text{PSFB}} \exp(-1.6t_{\text{ff}}/t_{\text{dyn}}). \quad (1.4.15)$$

The simulations suggest that the virial parameter is the critical factor in setting the SFE. This implies that overdensities will only collapse (efficiently) if self-gravity dominates over the kinetic energy. This is somewhat different to the majority of the analytic models in which a high Mach number can also lead to a high SFE. Magnetic fields are found to have little impact, as for realistic ISM values the ϵ_{ff} varied by less than a factor of two (Padoan et al., 2012). Later on, Padoan et al. (2017) used simulations at significantly higher resolution that included SN feedback, making the turbulent forcing more realistic, and updated Equation 1.4.15 to $\epsilon_{\text{ff}} = 0.4 \exp(-1.6\alpha_{\text{vir}}^{0.5})$. Like the theoretical descriptions in Section 1.4.2.2, this parametrisation of the SFE can also be used in the sub-grid star formation model of simulations (e.g. Semenov et al., 2016).

The Padoan et al. (2012) model manages to reproduce the SFEs found in Milky Way GMC observations that had been published by 2012 (e.g. Krumholz and Tan, 2007; Evans et al., 2009; Murray, 2011). However, there is some tension with more recent results. The scatter in ϵ_{ff} it predicts is smaller than the observed scatter, implying that the Padoan et al. (2012) cannot fully explain the observations of Lee et al. (2016), even if it does better than the analytical models. Similarly, Vutisalchavakul et al. (2016) find large scatter in ϵ_{ff} , but no trend with the Padoan et al. (2012) model. Considering the cloud-scale regions in M51, Leroy et al. (2017) only find broad agreement with a lot of scatter around the Padoan et al. (2012) prediction, when considering the individual environments (arm, inter-arm, centre). The global average of the M51 regions appears completely uncorrelated (Leroy et al., 2017). A comparison of the virial parameters and SFEs in regions of the Milky Way and several nearby galaxies also demonstrates that turbulence-regulated SFE models (both analytic and numerical) only match the observed values of low pressure environments. All models significantly overpredict the SFE of clouds in high pressure environments (Schruba et al., 2019).

A recent numerical study implies that the discrepancy between models and observations is not caused by a failure of turbulent star formation theory. Kim et al. (2021b) use a suite of 55 radiative-transfer MHD simulations that follow the collapse of a molecular cloud and include star formation, SN and radiation feedback. The initial conditions vary both the virial parameter of the cloud and the strength of the magnetic field. The ϵ_{ff} values of the simulated clouds are in good agreement with Padoan et al. (2012) and qualitatively match the multi-ff Krumholz and McKee (2005) model. Interestingly, mock observations based on these simulations no longer follow the analytical and numerical trends, but instead show good agreement with cloud-scale SFE observations. Observational effects combined with

the evolution of the cloud properties over time completely obscures the prior, theoretical trend, suggesting that in truth there is less disparity between cloud-scale SFE observations and theory than recently thought (Kim et al., 2021b). This also implies that theoretical ϵ_{ff} parametrisations remain a good approximation of cloud-scale star formation and can continue being used in the star formation recipes of larger scale simulations.

1.5 This Thesis

This introduction has highlighted that on the galactic scale star formation is inefficient, that it depends on the galactic environment and is lower in stellar bulges. The mechanism by which massive galaxies are quenched remains unknown, but seems to be strongly related with morphology. Morphological quenching in particular appears to be a promising concept. Not only can it hypothetically explain why galaxies have global SFRs that fall below the standard star formation relations despite hosting molecular gas, but could conceivably be invoked to explain the locally suppressed SFRs in bulges compared to discs. However, morphological quenching has been a poorly explored, phenomenological concept. There remain many open questions, for example does a spheroid induce shear that is able to consistently drive turbulence in the gas? How much of the galactic gravitational potential must the spheroidal component dominate before it affects the star formation activity within the galaxy? Is there a specific gas fraction above which morphological quenching becomes ineffective, and if so, does it depend on any galaxy properties? With the parametrisations introduced in Section 1.4.2.2 and Section 1.4.2.3, it is now possible to model star formation in galaxy simulations in a more physically motivated way that also traces directly the turbulent state of the gas.

The aim of this thesis is to bridge the gap between cloud-scale and galaxy-scale star formation by using an empirically-motivated, cloud-scale sub-grid star formation model in galaxy simulations. In particular, this thesis is focussed on determining the impact of galaxy morphology on star formation and its quenching, using dedicated numerical simulations. In Chapter 2 a numerical framework to estimate cloud-scale quantities in galaxy and larger scale simulations is developed to accurately calculate an environmentally-dependent SFE. After validation against a constant SFE model, it is used in a suite of isolated galaxy simulations that include a bulge component of various different sizes and masses to explore how these changes in the gravitational potential affect the SFR of the galaxy. In Chapter 3 I use spatial power spectra to constrain the turbulence in the circumnuclear gas reservoir of the Chapter 2 simulations and a mix of 12 early- and late-type galaxies with visually matching ISM morphology. Chapter 4 extends the simulation suite introduced in Chapter 2 to study the effect of a varying gas fraction on the different potentials. Using the results, a prediction for the part of the galaxy stellar mass-redshift parameter space where the star formation physics regulate the baryon cycle of galaxies is made. Finally, I conclude in Chapter 5 with a discussion of the results obtained in this thesis and future research avenues.

Chapter 2

Heart of Darkness: the influence of galactic dynamics on quenching star formation in galaxy spheroids

Authors:

Jindra Gensior, J. M. Diederik Kruijssen, and Benjamin W. Keller

This chapter is has been published in similar form in *MNRAS*, 495, 199 (2020).

Jindra Gensior is the principal author of this article. Diederik Kruijssen proposed the original idea. Jindra Gensior developed the sub-grid model in discussion with Diederik Kruijssen and implemented it in `AREPO` with some support from Benjamin Keller. Jindra Gensior designed and generated the initial conditions, ran all simulations and performed the analysis and produced all figures. Jindra Gensior wrote the majority of the manuscript, with the exception of the method subsection on the feedback model, originally written by Benjamin Keller. All authors contributed through regular discussions and collaborated with corrections and suggestions to the manuscript, and Jindra Gensior performed the last improvements during the review process.

Abstract

Quenched galaxies are often observed to contain a strong bulge component. The key question is whether this reflects a causal connection – can star formation be quenched dynamically by bulges or the spheroids of early-type galaxies? We systematically investigate the impact of these morphological components on star formation, by performing a suite of hydrodynamical simulations of isolated galaxies containing a spheroid. We vary the bulge mass and scale radius, while the total initial stellar, halo and gas mass are kept constant, with a gas fraction of 5 per cent. In addition, we consider two different sub-grid star formation prescriptions. The first follows most simulations in the literature by assuming a constant star formation efficiency per free-fall time, whereas in the second model it depends on the gas virial parameter, following high-resolution simulations of turbulent fragmentation. Across all simulations, central spheroids increase the gas velocity dispersion towards the galactic centre. This increases the gravitational stability of the gas disc, suppresses fragmentation and star formation, and results in galaxies hosting extremely smooth and quiescent gas discs that fall below the galaxy main sequence. These effects amplify when using the more sophisticated, dynamics-dependent star formation model. Finally, we discover a pronounced relation between the central stellar surface density and star formation rate (SFR), such that the most bulge-dominated galaxies show the strongest deviation from the main sequence. We conclude that the SFR of galaxies is not only set by the balance between accretion and feedback, but carries a (sometimes dominant) dependence on the gravitational potential.

2.1 Introduction

It is a major open question how the physics of star formation on the scales of giant molecular clouds affect the macroscopic evolution of galaxies. Numerical simulations provide a controlled environment to test current hypotheses and identify the pertinent underlying physics. The main challenge for such experiments is that star formation takes place on length scales far below the resolution limit of modern high resolution galaxy and cosmological simulations e.g. Hopkins et al., 2018a. Therefore, it must be implemented as a sub-grid model, as pioneered by Cen and Ostriker, 1992; Katz, 1992. The star formation rate (SFR) volume density can be expressed as

$$\dot{\rho}_{\text{SFR}} = \epsilon_{\text{ff}} \frac{\rho}{t_{\text{ff}}}, \quad (2.1.1)$$

where ρ is the volume density of the star-forming gas and ϵ_{ff} the star formation efficiency (SFE) per free-fall time, i.e. the fraction of gas that is converted to stars over a time-scale

$$t_{\text{ff}} = \sqrt{\frac{3\pi}{32G\rho}}. \quad (2.1.2)$$

Because the free-fall time is proportional to $\rho^{-0.5}$, equation 2.1.1 effectively represents a volumetric star formation relation of the Schmidt (1959) and Kennicutt (1998b) form, $\dot{\rho}_{\text{SFR}} \propto \rho^{1.5}$.

While the empirical scaling relation between SFR and gas surface density ($\Sigma_{\text{SFR}} \propto \Sigma_{\text{g}}^n$, with $n \simeq 1.4$, see e.g. Kennicutt and Evans 2012) holds for late-type galaxies, which are traditionally considered to be star-forming (e.g. de los Reyes and Kennicutt, 2019), there is increasing evidence that this relation does not hold universally. Molecular gas has been detected in about 22 per cent of early-type galaxies (Young et al., 2011; Davis et al., 2019), with gas surface densities comparable to those found in late-types. However, galaxies with stellar spheroids¹ systematically exhibit longer gas depletion times (the time it takes for the gas within a galaxy to be converted to stars at the current SFR) than late-type galaxies, with gas fractions being either lower than or comparable to those of their massive spiral counterparts (Saintonge et al., 2012). Similarly, analysing the SFRs of galaxies in the ATLAS^{3D} survey, Davis et al., 2014 showed that early-type galaxies exhibit lower SFRs compared to their late-type counterparts. Davis et al. (2014) find that the early-type star formation relation lies a factor of ~ 3 below those of Kennicutt, 1998b and Bigiel et al., 2008.

The low SFR in spheroids is not restricted to early-type galaxies. The Central Molecular Zone (CMZ, i.e. the central few 100 pc of the Milky Way) exhibits similar behaviour. Despite a large abundance of dense gas, the observed SFR in the CMZ falls below predictions of aforementioned empirical scaling relations (Longmore et al., 2013; Kruijssen et al., 2014). The observation that star formation is suppressed across different (though all bulge-dominated) environments implies that physical processes beyond the simple density scaling of equation 2.1.1 must be considered to fully understand star formation in galaxies.

‘Morphological quenching’ (Martig et al., 2009) has been proposed as a phenomenological concept to explain the absence of star formation in the presence of molecular gas reservoirs. In this picture, galaxies with a dominant spheroidal component have a steeper gravitational potential well at the centre relative to disc-dominated galaxies. This means their angular velocity (Ω) increases towards the bulge-dominated centre, raising the degree of gravitational stability (expressed through the Q parameter of Toomre 1964). Martig et al. (2009) speculate that shear, caused by a larger and more peaked Ω profile, can induce and maintain a high turbulent velocity dispersion (σ) in the interstellar medium (ISM). This would then allow the gas to remain pressure-supported against collapse, thereby quenching star formation in the spheroid.

In the decade since being proposed, morphological quenching has been a mixed success. Observationally, Huang and Kauffmann, 2014 identify a strong correlation between gas depletion time and specific SFR (sSFR, the SFR normalised by the stellar mass). However, only a weak link between stellar density and star formation has been found, implying that while stellar bulges and low SFRs might correlate, they need not be causally related. While the green valley galaxies² studied in Belfiore et al., 2018 exhibit a strong suppression of sSFR in the galaxy centres, they also show an integrated (but smaller) suppression in sSFR compared to galaxies on the ‘main sequence’ of star-forming galaxies. This

¹Here used interchangeably with ‘bulges’ or ‘early-type galaxies’ to indicate the presence of a spheroidal stellar morphological component.

²In sSFR–stellar mass space, these fall in between the ‘main sequence’ of star-forming galaxies and the quenched galaxy population, and are therefore thought to be in the process of being quenched.

global suppression is restricted to galaxies with both a high central stellar density and a low-ionization emission line region. Some mass-matched galaxies with similarly high central densities exhibit ‘normal’ star formation activity, thus suggesting that morphological quenching can not be the sole driver of suppressed star formation (Belfiore et al., 2018). By contrast, Méndez-Abreu et al., 2019 find a clear difference in star formation relation for bulge and disc components, with bulges exhibiting systematically lower SFRs and longer gas depletion times. Similarly to the results of Belfiore et al., 2018, the sSFR profiles for their bulge components also exhibit a strong central and general suppression, suggesting that a dominant bulge can affect the star formation activity at all radii. As the gas content in bulge and disc components of their galaxies is similar, Méndez-Abreu et al., 2019 argue that the observed suppression in star formation is caused by a dynamical process that stabilises the gas, such as morphological quenching.

The numerical perspective paints a similarly ambiguous picture. In high-resolution simulations comparing an isolated spiral and elliptical galaxy, Martig et al., 2013 found that morphological quenching is effective, albeit only at gas fractions lower than a few per cent. Even for gas fractions as low as 4.5 per cent, these authors find that the star formation relation for the two galaxy types is offset by only ~ 30 per cent. Investigating a variety of quenching mechanisms in isolated galaxy simulations, Su et al., 2019 only find a slight decrease of the SFR in their bulge-dominated galaxies, concluding that other quenching mechanisms are required to significantly suppress the star formation in these objects. Recently, Kretschmer and Teyssier, 2020 have demonstrated that morphological quenching can be reproduced in a cosmological zoom-in simulation when modelling star formation with a dependence on the virial parameter and Mach number of the gas, but not when using a constant SFE per free-fall time (ϵ_{ff} in equation 2.1.1).

In this chapter, we use a suite of hydrodynamical simulations of isolated galaxies to systematically quantify the effect of a spheroidal stellar component on the structure and dynamics of the ISM and galactic star formation, paying particular attention to the extent to which star formation can be suppressed by the presence of this component. As recent studies have shown, a physically-motivated, environmentally-dependent star formation model (captured through the choice of ϵ_{ff}) may be crucial for reproducing the observed effect. We therefore consider two different sub-grid prescriptions for star formation in this work. Throughout, we adopt a gas fraction of 5 per cent, appropriate for Milky Way-mass galaxies at $z = 0$, as well as for galaxies in the transition region between the main sequence and the quenched galaxy population (e.g. Saintonge et al., 2017; Catinella et al., 2018). The chapter is structured as follows. Section 2.2 presents a discussion of our sub-grid star formation prescription, discussing how star formation is traditionally modelled, before introducing our new sub-grid model that accounts for the dynamical state of the gas. The simulation suite is then introduced in Section 2.3. To investigate the effect of the star formation model, Section 2.4 compares simulations using our dynamics-dependent model to those using a constant efficiency per free fall time ϵ_{ff} , while Section 2.5 focuses on the impact of the bulge component on the galaxy. Section 2.6 places our results in context of recent observations and theoretical studies in the literature. Finally, we summarise our findings and conclude in Section 2.7.

2.2 Modelling Star Formation in Galaxy Simulations

2.2.1 Star Formation in the Literature

Simply using equation 2.1.1 as sub-grid star formation model theoretically allows star formation everywhere, regardless of the physical or dynamical properties of the ISM (even if the rate of star formation depends on the gas density). As star formation is observed to proceed in cold, dense, molecular gas (e.g. Wong and Blitz, 2002; Bigiel et al., 2008), a variety of thresholds are used in combination with the sub-grid model to prevent arbitrary and spurious star formation in e.g. hot, diffuse gas. A volume density threshold is the most common restriction used (e.g. Navarro and White, 1993; Springel and Hernquist, 2003; Kim et al., 2016). Only gas denser than the threshold can form stars, which is often used as analogous to the overdensities that are Jeans unstable and will eventually collapse. In addition, some models ensure that stars only form under the appropriate physical conditions by imposing a temperature ceiling for star formation (e.g. Stinson et al., 2006; Nickerson et al., 2019) or incorporating an H_2 fraction into equation 2.1.1 (e.g. Robertson and Kravtsov, 2008; Christensen et al., 2012; Grisdale et al., 2017).

The other main free parameter in star formation models defined by equation 2.1.1 is the efficiency per free-fall time ϵ_{ff} . Both ϵ_{ff} and the thresholds mentioned above are generally chosen such that the star formation in the simulated galaxy matches the observed relationship between SFR and gas surface density (Kennicutt, 1998b; Bigiel et al., 2008; Leroy et al., 2013). However, recent work suggests that the SFR is set by the balance between inflow and feedback-driven outflow, such that these self-regulate and the star formation prescription itself only has a weak effect on the SFR (Hopkins et al., 2011; Agertz et al., 2013). This weakens the importance of the choice of thresholds and ϵ_{ff} . Strong and efficient feedback will shape the density structure and kinematics of the ISM, and thus inhibit star formation by preventing gas from simply collapsing into dense peaks through gravity (Hopkins et al., 2011). The SFE itself determines how many stars form and subsequently how much feedback is injected into the gas. Agertz et al., 2013 demonstrate that, when including efficient momentum input from stellar feedback, changing ϵ_{ff} by a factor of 10 between simulations leads to a star formation relation that varies by a factor of 2 at most. This results in an effective degeneracy that is reflected by a wide range across the literature of (density) thresholds (these are somewhat resolution-dependent, but range from 0.1 cm^{-3} in Pillepich et al. 2018 to 1000 cm^{-3} in Hopkins et al. 2018a) and efficiencies ($\epsilon_{\text{ff}} = 0.01$ in Kim et al. 2016 to $\epsilon_{\text{ff}} = 1$ for the FIRE2 simulations of Hopkins et al. 2018a, even if the latter include additional criteria depending on the state of the gas, including self-gravity).

The common underlying assumption in the aforementioned simulations is that it is accurate to convert gas to stars with a constant ϵ_{ff} once the criteria for star formation are satisfied. However, there is observational evidence (Utomo et al., 2018; Schrubba et al., 2019, and references therein) that the SFE varies up to an order of magnitude both within and between galaxies. Similarly, Chevance et al. (2020b) find that the galactic environment (and galactic dynamics in particular) often determine the lifetimes of molecular clouds and thus their integrated star formation efficiencies. Analytical studies (Krumholz and McKee,

2005; Hennebelle and Chabrier, 2011; Padoan and Nordlund, 2011; Federrath and Klessen, 2012; Burkhart, 2018) corroborate this further, all predicting an additional dependence of the SFR on the turbulent state of the ISM, rather than just gas self-gravity. All of these studies conclude that the SFE depends on the local environmental conditions. In view of our goal to assess how gas dynamics in stellar spheroids can impact (galactic-scale) star formation, it is crucial to include some form of environmental dependence in the star formation modelling of our simulations.

Most theoretical predictions for ϵ_{ff} are based on analysis of the gas density probability distribution function (PDF) and link it to the virial parameter α_{vir} , the sonic Mach number \mathcal{M} , the turbulent forcing parameter b and the ratio of thermal to magnetic pressure, β (Federrath and Klessen, 2012). When investigating these dependences in high resolution simulations of turbulent molecular clouds, Padoan et al. (2012, 2017) show that of these four parameters, the SFE per free-fall time primarily depends on the virial parameter. Recently, these findings have been used by Semenov et al., 2016 and Kretschmer and Teyssier (2020) as a sub-grid star formation model, in combination with a sub-grid model for gas turbulence, as well as by e.g. Kimm et al. (2017), Trebitsch et al. (2017) and Rosdahl et al. (2018) without including a sub-grid turbulence model. Similar to the work done by these groups, we have developed a sub-grid star formation model based on the gas dynamics for use in the moving mesh code `AREPO` (Springel, 2010), which we introduce next.

2.2.2 A Sub-Grid Star Formation Model based on Gas Dynamics

In order to account for the dependence of ϵ_{ff} on the virial parameter found in numerical simulations of turbulent fragmentation, we implement an environmentally-dependent ϵ_{ff} based on the parametrisation of Padoan et al., 2017. It directly expresses ϵ_{ff} in terms of the virial parameter of the gas, by writing

$$\epsilon_{\text{ff}} = 0.4 \exp(-1.6\alpha_{\text{vir}}^{0.5}). \quad (2.2.1)$$

The virial parameter is approximately the ratio of turbulent to gravitational potential energy of a (molecular) gas cloud and can also be expressed as ratio of free-fall to turbulent crossing time (t_{cr}) of the cloud (Bertoldi and McKee, 1992), i.e.

$$\alpha_{\text{vir}} = \frac{40}{3\pi^2} \left(\frac{t_{\text{ff}}}{t_{\text{cr}}} \right)^2, \quad (2.2.2)$$

with

$$t_{\text{cr}} = \frac{L}{2\sigma}, \quad (2.2.3)$$

where L is the length scale associated with turbulence, over which σ and α_{vir} are calculated. Substituting equations 2.1.2, 2.2.2 and 2.2.3 into equation 2.2.1 yields the final expression for the SFE per free-fall time for each gas cell:

$$\epsilon_{\text{ff}} \simeq 0.4 \exp\left(-\frac{2.018}{\sqrt{G}} \frac{\sigma}{L\rho^{0.5}}\right). \quad (2.2.4)$$

For any numerical implementation of this model, it is necessary to define the length scale L . Without a sub-grid model for turbulence such as in Semenov et al., 2016, which enables these authors to associate L with the size of a resolution element, we must decide on a suitable length scale that allows the model to work independently of resolution. As the virial parameter is a cloud-scale property, we need to evaluate it for local overdensities. To achieve this, we use a version of Sobolev’s approximation (Sobolev, 1960) to determine the size of a local overdensity around a gas cell. In analogy with Sobolev’s original approximation, which uses velocity gradients to determine the characteristic size scale for radiative transfer in stellar envelopes, we define L based on the characteristic length scale for changes in the density of the surrounding gas as set by the density gradient $|\nabla\rho| = |d\rho/dr|$, i.e.

$$L = \left| \frac{\rho}{\nabla\rho} \right|, \quad (2.2.5)$$

which we refer to as density gradient length scale.

This now shifts the focus onto how to calculate $\nabla\rho$. Because AREPO is an Eulerian-Lagrangian hybrid method, one could obtain the gradient either using the cell interfaces of the mesh, or using a smoothing kernel like a smooth particle hydrodynamics (SPH) code. Using only the neighbouring cell interfaces introduces a resolution dependence, which is undesirable. Additionally, the virial parameter calculation would not be self-consistent, as σ , ρ and $\nabla\rho$ would all be calculated on different length scales. Calculating the density gradient using a smoothing kernel (W) instead causes a dependence on the number of neighbouring cells (n_{ngb}) picked up by the kernel and in turn on the smoothing length h , as h is traditionally chosen such that n_{ngb} is a fixed, pre-determined number. As with using cell interfaces, this would make $\nabla\rho$ dependent on a fixed number of neighbours, and cause us to evaluate σ , $\nabla\rho$ and ρ on different scales. Instead, we therefore evaluate $\nabla\rho$ and ρ on a length scale which matches the density gradient length scale. To achieve this, we use the kernel approach of equation 2.2.6:

$$\nabla\rho(\mathbf{r}) = \sum_{j=1}^{n_{\text{ngb}}} m_j \nabla W(|\mathbf{r} - \mathbf{r}_j|, h). \quad (2.2.6)$$

However, following the above reasoning, we consider the number of neighbours an independent variable that is decoupled from the smoothing length. We keep h fixed and introduce a third length scale l_{tw} , which is the distance from the central gas cell on which we find neighbours. This allows us to vary l_{tw} in an iterative process aimed at matching the density gradient length scale L (calculated based on $\nabla\rho$ and ρ) and l_{tw} .

Figure 2.1 visualises how the code works and how the length scales are determined for an overdensity. Specifically, it progresses as follows:

1 Determine and fix h :

1.1 Perform a tree-walk to find 32 weighted neighbours (Figure 2.1, panel a)

1.2 Set h to $2\times$ the distance to the furthest neighbour (Figure 2.1, panel b), to not be too limited by the choice of n th neighbour and the distance to it

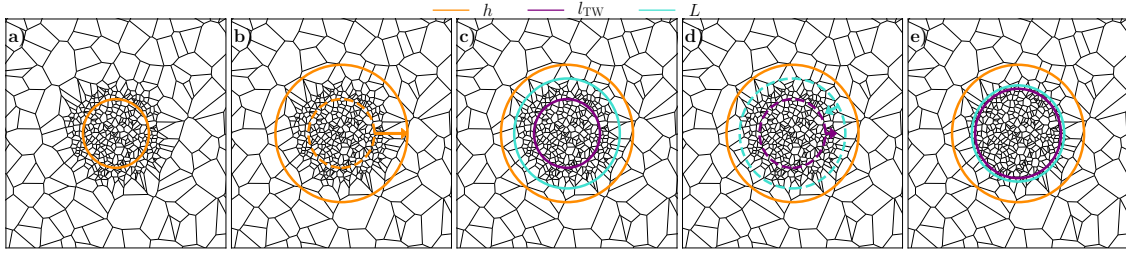


Figure 2.1: Idealised overdensity on a Voronoi mesh; coloured lines indicate the smoothing length of the kernel (h , orange), the tree-walk length scale (l_{tw} , purple) and the density gradient length scale (L , cyan). The five panels illustrate our algorithm for calculating the density gradient length scale (and subsequently the virial parameter). Panels a and b show how h is set by identifying a distance within which a certain number of neighbours can be found (panel a) and then extending it by a factor of 2. After that, we keep h constant, as seen in panels c–e. We then find cells within a distance l_{tw} and calculate L based on their density and density gradient (panel c). Panel d shows how l_{tw} is adjusted and iterated over, because l_{tw} and L do not match for the initial l_{tw} in panel c. The overdensity is successfully identified once l_{tw} and L converge (panel e).

2 Iterate over l_{tw} , at fixed h , until $|l_{\text{tw}} - L| \leq c_{\text{tw}}$ is fulfilled (Figure 2.1, panels c–e)

2.1 Our initial guess for l_{tw} is set as $l_{\text{tw}} = 0.5h$ (see panel c).

2.2 Adjust l_{tw} by multiplying/dividing by a small factor (depending on the change in density gradient, but capped at $\sqrt{2}$) to become closer to the current value of L , for $L > l_{\text{tw}}$ (panel d) and $L < l_{\text{tw}}$ respectively; repeat until convergence is reached.

Once the density gradient and tree-walk length scales match to within the convergence criteria, we evaluate the velocity dispersion over the gas cell neighbours within l_{tw} and include the thermal component from the sound speed c_s when calculating α_{vir} , i.e.

$$\sigma = \sqrt{\sigma_{\text{gas}}^2 + c_s^2}. \quad (2.2.7)$$

Now all quantities relevant for ϵ_{ff} are known and the star formation rate can be calculated. This self-consistent approach distinguishes our sub-grid star formation model from other models in the literature that also do not include a sub-grid prescription for turbulence, in which the velocity dispersion is calculated from the velocity gradient across the star forming cell using only the nearest neighbours (e.g. Kimm et al., 2017). We refer to Appendix A.1 for a quantitative demonstration of how the sub-grid model is only weakly affected by resolution.

2.3 Method

The simulations described in this chapter have been run with the moving-mesh code AREPO (Springel, 2010). The equations of hydrodynamics are solved on an unstructured

mesh, built from a Voronoi tessellation, using a second-order accurate, unsplit Godunov solver. The hydrodynamics solution is Galilean invariant, because the Voronoi generator points move with the gas fluid. Collisionless particles (i.e. stars and dark matter) are treated as Lagrangian, with gravity being solved using a tree-based scheme. To achieve optimal gravitational resolution, we use an adaptive gravitational softening length (Price and Monaghan, 2007).

2.3.1 Star Formation, Feedback and Cooling

2.3.1.1 Star Formation and Cooling

To model the thermal state of the ISM, we use the Grackle chemistry and cooling library³ (Smith et al., 2017), with the 6 species non-equilibrium chemistry network. This means we track atomic hydrogen, helium and their ions throughout the simulation. In combination with tabulated metal abundances these are then used to determine the cooling rate. Interstellar radiation is taken into account by including the Haardt and Madau, 2012 constant UV-background. As the galaxies in this study resemble evolved objects, we assume solar metallicity for each galaxy.

The SFR of a gas cell is calculated as described in section 2.2.2, using a cubic spline kernel (Monaghan, 1992).⁴ We require the length scales L and l_{tw} to agree to within 10 per cent of the smoothing length during the velocity dispersion and density gradient calculation, i.e. $c_{\text{tw}} = 0.1h$. Whether a gas cell is converted to, or spawns a star particle is then decided stochastically.

As discussed in section 2.2.1, further constraints on the properties of star-forming gas are required to prevent spurious star formation, especially in simulations with a constant ϵ_{ff} (see Section 2.3.2). Based on the values used in the literature and appropriate for our resolution, we use a minimum density threshold of 1 cm^{-3} , as well as a maximum temperature threshold of 10^3 K . To enable a fair comparison between the constant and dynamics-dependent SFE, we apply the same restrictions to gas in simulations run with the virial parameter-dependent ϵ_{ff} . The dynamics-dependent model does not depend on these thresholds as strongly as the model with a constant SFE, because ϵ_{ff} is regulated by the state of the gas. We refer to Appendix A.2 for a more detailed discussion of how the results obtained with the dynamics-dependent SFE are only weakly affected by the choice of thresholds.

2.3.1.2 Feedback Model

To study the effects of the star formation model on a gas disc, we must include a model for stellar feedback. In the controlled experiments presented here, we use a simple model for feedback from Type II supernovae (SNe), first introduced by Hopkins et al. (2014) and Kimm and Cen (2014). This ‘mechanical feedback’ has excellent numerical convergence

³<https://grackle.readthedocs.io/>

⁴To isolate the effect of the new sub-grid star formation model from any changes caused by the differences in gravitational potential, we repeat three of our simulations with a constant $\epsilon_{\text{ff}} = 1$ per cent (see Section 2.3.2).

properties, with the same amount of total momentum injected over 6 decades of mass resolution (Hopkins et al., 2018b). As was shown in Rosdahl et al. (2017), this model also produces similar self-regulating behaviour to the stochastic thermal model of Dalla Vecchia and Schaye (2012) and the kinetic model of Dubois and Teyssier (2008), both of which are widely used in both cosmological and isolated simulations of galaxy formation.

We follow an approach similar to Hopkins et al. (2014), where a kernel as in SPH is used to deposit feedback to the 32 nearest neighbours. These receive a share of feedback mass, metals, momentum, and thermal energy as a function of their M4 kernel weighting W_{ij} . For a given total SNe mass M_{ej} and energy $E_{51} = E_{\text{SN}}/10^{51} \text{erg s}^{-1}$, we calculate the terminal momentum of the blastwave at the end of the pressure-driven snowplough phase (and the beginning of the momentum-conserving snowplough phase) following Cioffi et al. (1988, equation 4.7), i.e.

$$p_{\text{term}} = 4.8 \times 10^5 \text{ M}_{\odot} \text{ km s}^{-1} \frac{(W_{ij} E_{51})^{13/14}}{\zeta_m^{3/14} n_0^{1/7}}, \quad (2.3.1)$$

with the metallicity parameter $\zeta_m = \text{MIN}(Z/Z_{\odot}, 0.01)$ and the gas density n_0 . For each resolution element receiving feedback, we calculate an energy conserving (Sedov-Taylor) momentum $p_{\text{ST}} = \sqrt{2W_{ij}m_i E_{\text{SN}}}$ (where m_i is the element mass after receiving ejecta) as well as the terminal snowplough momentum p_{term} . Each element then receives feedback momentum $p_{\text{fb}} = \text{MIN}(W_{ij}p_{\text{term}}, p_{\text{ST}})$ and thermal energy $E_{\text{SN}} = W_{ij}E_{\text{SN}} - 2(p - p_{\text{fb}})^2/m_i$ (i.e. what remains).

We assume a canonical $E_{51} = 1$ for the SNe energy, with one SNe occurring per 100 M_{\odot} of stellar mass formed (Chabrier, 2003; Leitherer et al., 2014) and a delay time of 4 Myr before SNe detonate. For simplicity, we detonate all SNe together 4 Myr after a star particle has formed, which Kimm et al. (2015) showed to have little change in the overall star formation history by $z \sim 3$ compared to having individual SNe detonate over a range of delay times sampled from STARBURST99 (Leitherer et al., 2014). In order to prevent the overcooling Kimm et al. (2015) found for long (10 Myr) SNe delays, we choose a smaller timescale, comparable to the feedback disruption times observed in Kruijssen et al., 2019a and Chevance et al., 2020b. Each SNe also ejects 10.5 M_{\odot} of mass (M_{ej}) and 2 M_{\odot} of metal ejecta, the same total amounts used in the FIRE-2 simulations (Hopkins et al., 2018a).

2.3.2 Initial Conditions

The initial conditions of our simulations have been created following the procedure outlined in Springel et al., 2005a. Each isolated galaxy consists of a stellar, dark matter, and gas component, with the stellar component possibly subdivided into a disc and a bulge component. All initial conditions are based on the standard AGORA disc (Kim et al., 2016). However, to assess how different gravitational potentials influence the SFR and whether bulges can suppress star formation, a set of initial conditions with a variety of bulge mass fractions and scale radii is needed. Thus, while otherwise similar to the initial conditions used in the AGORA disc, the bulge component can differ. Below, the components defining

Name	M_b [$10^{10}M_\odot$]	R_b [kpc]	Resolution [M_\odot]	SFE model	Remark
noB	0	0	1×10^4	$\epsilon_{\text{ff}} = f(\alpha_{\text{vir}})$	‘bulgeless’
B_M30_R1	1.41	1	1×10^4	$\epsilon_{\text{ff}} = f(\alpha_{\text{vir}})$	
B_M30_R2	1.41	2	1×10^4	$\epsilon_{\text{ff}} = f(\alpha_{\text{vir}})$	
B_M30_R3	1.41	3	1×10^4	$\epsilon_{\text{ff}} = f(\alpha_{\text{vir}})$	
B_M60_R1	2.83	1	1×10^4	$\epsilon_{\text{ff}} = f(\alpha_{\text{vir}})$	
B_M60_R2	2.83	2	1×10^4	$\epsilon_{\text{ff}} = f(\alpha_{\text{vir}})$	‘fiducial’
B_M60_R3	2.83	3	1×10^4	$\epsilon_{\text{ff}} = f(\alpha_{\text{vir}})$	
B_M90_R1	4.24	1	1×10^4	$\epsilon_{\text{ff}} = f(\alpha_{\text{vir}})$	‘compact bulge’
B_M90_R2	4.24	2	1×10^4	$\epsilon_{\text{ff}} = f(\alpha_{\text{vir}})$	
B_M90_R3	4.24	3	1×10^4	$\epsilon_{\text{ff}} = f(\alpha_{\text{vir}})$	
noB_cSFE	0	0	1×10^4	$\epsilon_{\text{ff}} = 1$ per cent	
B_M60_R2_cSFE	2.83	2	1×10^4	$\epsilon_{\text{ff}} = 1$ per cent	
B_M90_R1_cSFE	4.24	1	1×10^4	$\epsilon_{\text{ff}} = 1$ per cent	
B_M60_R2_hres	2.83	2	3×10^3	$\epsilon_{\text{ff}} = f(\alpha_{\text{vir}})$	‘high resolution’
B_M60_R2_lres	2.83	2	3×10^4	$\epsilon_{\text{ff}} = f(\alpha_{\text{vir}})$	‘low resolution’

Table 2.1: Initial conditions of the simulations. The naming convention of the simulations is to first list the presence of a bulge (‘B’ or ‘noB’), followed by the relative bulge mass (‘MX’ with X the percentage of the total mass constituted by the bulge) and then the bulge scale radius (‘RY’ with Y the radius in kpc). Runs with a constant ϵ_{ff} have ‘cSFE’ appended; similarly, the postfix ‘res’ indicates runs in which the resolution is varied. The final column lists the descriptive designations by which we refer to some of the simulations throughout this chapter.

our fiducial model are described in detail. Table 2.1 lists the full suite of simulations and the quantities that we vary across the suite.

The dark matter halo is modelled as a Hernquist, 1990 profile, with a concentration parameter of $c = 10$, a spin parameter of $\lambda = 0.04$, and a circular velocity $v_{\text{circ}} = 180 \text{ km s}^{-1}$, similar to those of the Milky Way (Bland-Hawthorn and Gerhard, 2016). A Hernquist, 1990 profile is also used to describe the bulge component. It is defined by the bulge mass M_{b} and its scale radius R_{b} . To explore the effect of varying the gravitational potential, we vary both of these parameters. In order to ensure that all changes are due to a change in the bulge component, all galaxies in the sample have the same initial total stellar mass, of $M_* \sim 4.71 \times 10^{10} M_{\odot}$. We split this mass into a bulge and disc component, i.e. $M_* = M_{\text{b}} + M_{\text{d}}$, and include a control run that only has a disc ($M_{\text{b}} = 0$). We consider bulge mass fractions of 30, 60, and 90 per cent of the initial stellar mass, and scale radii of 1, 2, and 3 kpc. Our fiducial model is chosen to have a bulge component with a mass and radius in the middle of the parameter space covered in this exploration, i.e. the scale radius is $R_{\text{b}} = 2 \text{ kpc}$ and the bulge contains 60 per cent of the initial stellar mass, yielding a $M_{\text{b}}/M_{\text{d}}$ ratio of 1.5. The stellar disc is described by an exponential radial profile with an initial scale length $R_{\text{d}} = 4.6 \text{ kpc}$, and a vertical sech^2 profile with scale height of $0.1 R_{\text{d}}$.

We express the initial amount of gas as ratio of gas to the total stellar mass, because the disc mass varies greatly between the initial conditions. For simplicity (to not include another dimension into the parameter space) we choose the same gas fraction for all galaxies in this study. To mimic the relative gas-poorness of early-type galaxies (Young et al., 2011) and in agreement with the findings of Saintonge et al., 2017 for galaxies of similar stellar mass, the initial total gas to stellar mass ratio is fixed to $M_{\text{gas}}/M_* = 0.05$.

With an average mass resolution of $\sim 1 \times 10^4 M_{\odot}$ and a density threshold for star formation of 1 cm^{-3} , we use a minimum gravitational softening length of 12 pc. With these choices, we ensure that gas cells are gravitationally resolved for densities up to two orders of magnitude higher than the density threshold. This is relevant in the context of our star formation model, because it ensures that the gas can condense into structures with densities higher than the threshold before becoming self-gravitating. The gravitational softening for the dark matter halo is coarser, with a softening length of 26 pc. The gravitational softening is modified for the resolution tests, with minimum softening lengths of 15 (35) and 6 (12) pc for baryons (dark matter) in the runs B_M60_R2_lres and B_M60_R2_hres, respectively.

We show a selection of initial conditions in Figure 2.2, to give the reader an idea of how the stellar component looks visually, as well as to quantify the impact of the different bulge radii and bulge/disc ratios on the shear experienced by the ISM in these galaxies. More massive and more compact (i.e. higher density) bulges increase the shear, most strongly so in the centre, but also throughout the galaxy. For the same reason, the galactocentric radius out to which the bulge dominates the galactic shear is larger for higher bulge densities.

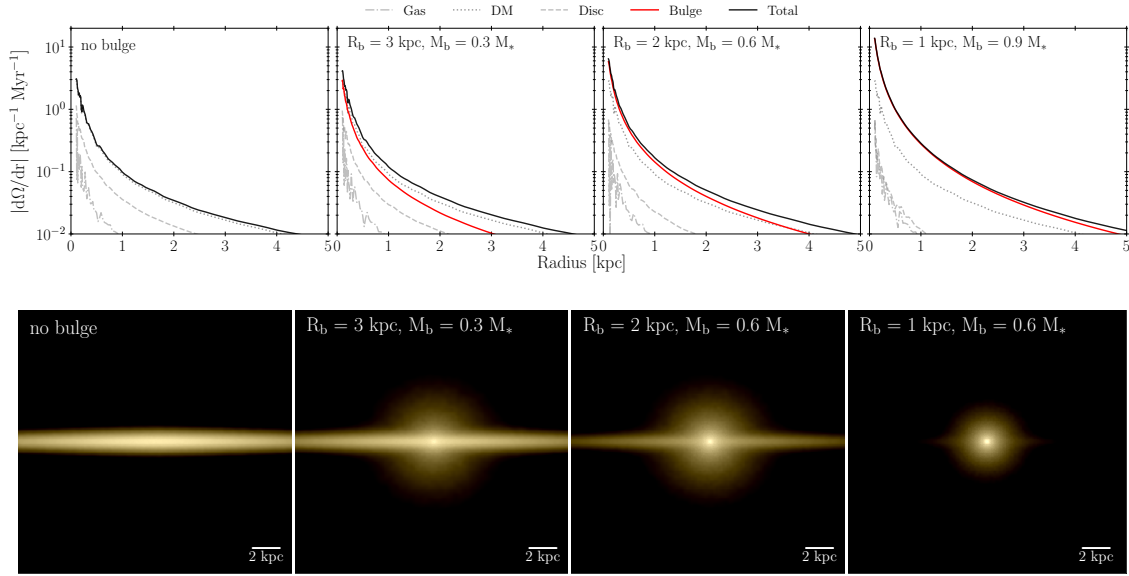


Figure 2.2: Gradient of the angular velocity $|d\Omega/dr|$ (a measure of shear) as a function of galactocentric radius (top) and mock colour images (using u, v, i filters) of the stars (bottom) for four initial conditions from our simulation suite. From left to right, these show the bulgeless model (noB), the weakest bulge model (B_M30_R3), the fiducial bulge model (B_M60_R2), and most dominant bulge model (B_M90_R1). For the first two of these models, the dark matter halo is the dominant source of shear. The total shear increases in the presence of a bulge; the more prominent the bulge component, the stronger the effect. The shear experienced by the fiducial run is dominated by the bulge component in the inner 3.5 kpc. For the most compact bulge, the shear induced by the bulge component dominates over the contribution from the dark matter out to 7 kpc.

2.4 Comparison of Star Formation Models with a Constant or Varying Star Formation Efficiency

2.4.1 Star Formation

To assess how the global SFR is affected by the dynamics-dependent and constant SFE models, as well as by different stellar potentials, we consider the radially-binned star formation relation of a subset of six simulations, shown in Figure 2.3. Following Kruijssen and Longmore, 2014, who show that the temporal and spatial variations of the star formation relation caused by cloud evolution introduce considerable scatter on sub-kpc scales, we calculate the SFR and gas surface density in radial annuli of 750 pc width. We exclude the central 300 pc from our analysis, because we omit feedback from active galactic nuclei and lack the resolution to accurately model the star formation activity in the very nucleus. Though mostly relevant for the spheroid-dominated galaxies, we apply this cut to

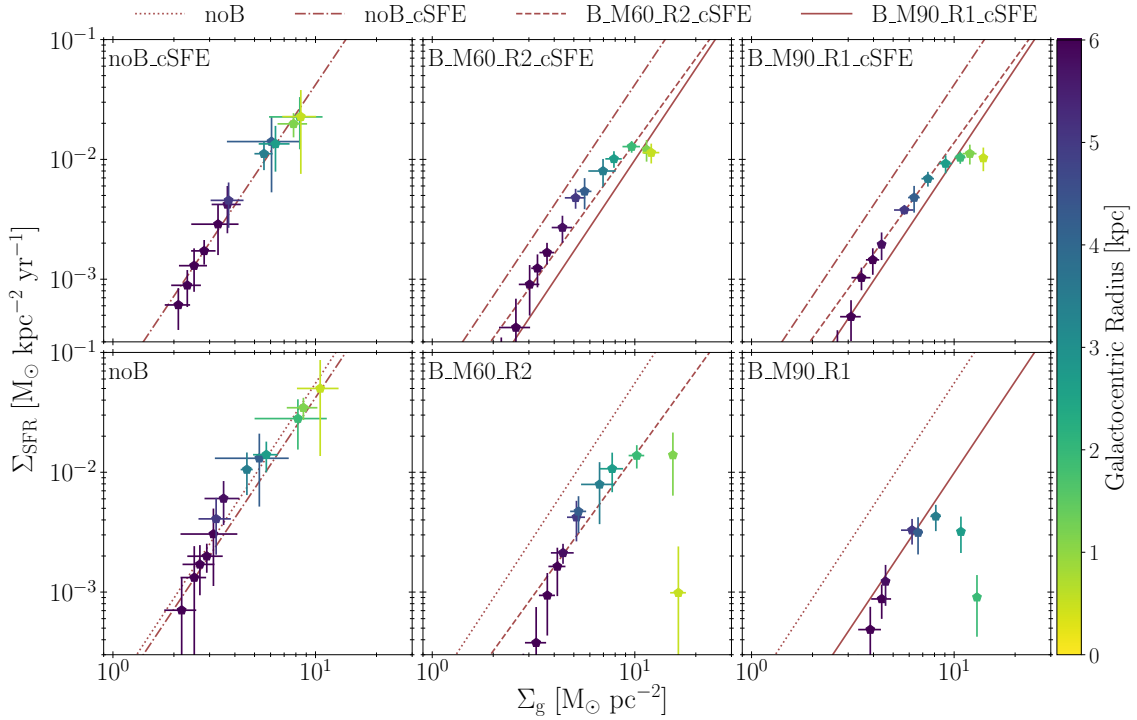


Figure 2.3: SFR surface density as a function of gas surface density for the bulgeless (left), fiducial (centre) and compact-bulge (right) simulations, contrasting the constant (top) and dynamics-dependent (bottom) SFE models. The colour coding indicates the galactocentric radius. Red lines show the best-fitting power law relations for the panels indicated in the legend. Each point represents a time average of snapshots separated by 100 Myr; the snapshot-to-snapshot variation is shown by the error bars. The central 300 pc are excluded from the analysis (see Section 2.4.1). This figure shows that the presence of a spheroid suppresses the SFR towards small galactocentric radii in all simulations, but most strongly so for the dynamics-dependent star formation model.

all galaxies in the sample. We refer to Section 2.5.2 and 2.6.3 for more details. In analogy to observations (e.g. Kennicutt and Evans, 2012; Leroy et al., 2013; Haydon et al., 2020), we only use the stars which formed in the past 10 Myr to calculate the mean SFR over this time interval. To obtain a measure of the variation in Σ_{SFR} and Σ_{g} we average over snapshots separated by 100 Myr; this variation is indicated by the error bars in Figure 2.3. We remind the reader that all simulated galaxies have a gas fraction of 5 per cent.

Both bulgeless runs follow a similar star formation relation and are largely insensitive to the sub-grid star formation model. The net SFR of the dynamics-dependent efficiency run is slightly higher, as indicated by the different normalisation. However, within the error bars arising from time variation, the SFRs of the simulations agree remarkably well with each other. A similar star formation relation is seen for the B_M60_R2_cSFE simulation,

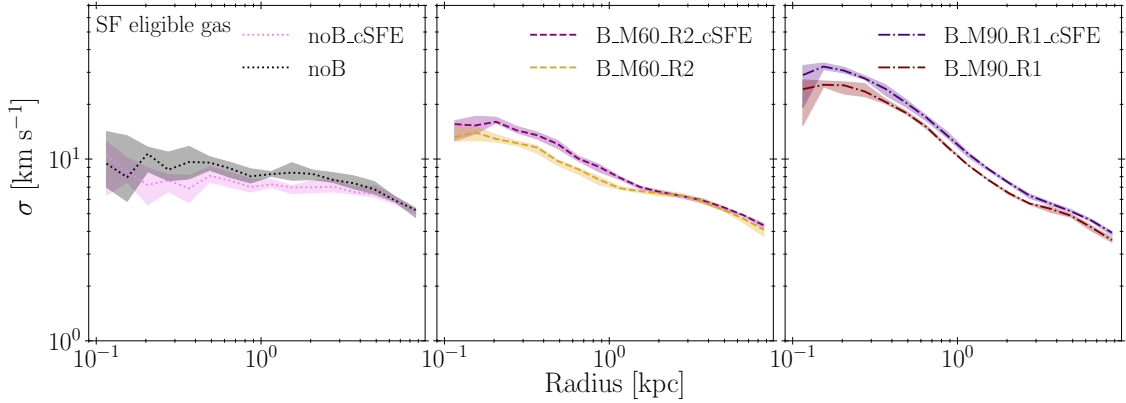


Figure 2.4: Comparing the effect of different sub-grid star formation models on the turbulent velocity dispersion of the gas, for the bulgeless (left), fiducial (middle) and compact bulge (right) galaxies. The panels show the result for gas that satisfies the density and temperature thresholds for star formation.

but its overall SFR is lower, indicated by the offset between the best fit lines in the upper middle panel of Figure 2.3. This reflects the stabilising effect of the bulge (see below). The dynamics-dependent ϵ_{ff} model in the bottom middle panel shows a similar relation down to the inner 1.5 kpc. At smaller radii, the B_M60_R2 run shows a pronounced drop in SFR, similar to those observed by Méndez-Abreu et al., 2019. Differences in SFR resulting from different sub-grid models are even starker for the B_M90_R1 and B_M90_R1_cSFE simulations. Run B_M90_R1_cSFE effectively follows the same star formation relation as run B_M60_R2_cSFE. However, the SFR of run B_M90_R1 peaks at a radius of ~ 3.5 kpc before decreasing again, despite increasing gas surface densities, showing a much stronger suppression of star formation than in the fiducial run or the compact bulge run with a constant SFE.

The above comparison highlights why models with a constant SFE have been so widely used. For a disc galaxy without a pronounced spheroid, the SFR is similar to that obtained with a dynamics-dependent star formation model, irrespective of the choice of ϵ_{ff} , density threshold, and temperature ceiling, as expected from the self-regulation of star formation and feedback (Agertz et al., 2013). However, in order to successfully reproduce the suppressed SFRs towards the centres of bulge-dominated galaxies (e.g. Longmore et al., 2013; Davis et al., 2014), a dynamics-dependent sub-grid model is required.

We expect that the implications of changing the sub-grid star formation model extend beyond the star formation relation, because the feedback resulting from star formation will impact the gas differently depending on where, when and at which rate the stars are formed. In turn, this will impact the ISM structure and kinematics, thereby influencing future star formation. Therefore, we now proceed with a detailed analysis of how the cloud-scale baryon cycle of ISM evolution, star formation, and feedback is affected by the star formation model and galactic morphology.

2.4.2 Effect on ISM properties

We now turn to an analysis of the impact of different star formation models on the state of the turbulent ISM. Specifically, we consider the gas velocity dispersion and the virial parameter, which directly enter into the dynamics-dependent star formation model. In addition, we consider the turbulent pressure, because it is a crucial component for balancing self-gravity and maintaining hydrostatic equilibrium. We also consider the ISM morphologies and gas surface density profiles of the modelled galaxies, because these set the SFR and are likely to be affected by changes in the star formation model.

To ensure a representative and reproducible analysis of these properties, we measure them in different snapshots and use the median and 16th-to-84th percentiles over these snapshots. This allows us to quantify the overall trends, as well as to quantify the stochastic variation in time introduced by the quantisation of star formation and feedback into individual events (e.g. Kruijssen et al., 2018). We use snapshots starting at 300 Myr, to allow the galaxies to settle into equilibrium, and subsequent ones separated by 100 Myr (roughly a galactic dynamical time), to make sure that snapshots are independent. We run the simulations for a Gyr, resulting in a total of eight snapshots combined this way. Unless explicitly stated otherwise, we will use this approach to calculate any quantities throughout the rest of the chapter.

2.4.2.1 Velocity Dispersion

We show the radial gas velocity dispersion profiles in Figure 2.4, where we compare simulations run with sub-grid models using a constant and dynamics-dependent efficiency, but with the same (stellar) gravitational potential. The velocity dispersion in galaxy discs is set by a combination of the gravitational potential and stellar feedback (Krumholz et al., 2018). Because we fix the potential, differences between models can only be the consequence of differences between the star formation models. While the star formation prescription itself cannot directly affect the velocity dispersion, differences in the resulting SFRs imply the injection of different amounts of total energy and momentum by stellar feedback. This means that the star formation model indirectly changes the gas velocity dispersion through stellar feedback.

Considering the bulgeless simulations first, the velocity dispersions remain approximately flat in the inner ~ 5 kpc of the galaxy. This is seen more strongly for the simulations with a constant SFE. The dynamics-dependent efficiency run has a higher absolute SFR, causing the gas in this galaxy to be more turbulent. However, these differences remain largely within the variation of the median σ over time. The variance of the median does increase towards the centre of the galaxy for both star formation models. This increase is driven by the greater degree of stochasticity towards the galactic centre, where the star formation is burstier.

Focussing on the differences between sub-grid star formation models in the presence of a bulge (middle and right panels of Figure 2.4), three points become apparent. Firstly, irrespectively of the sub-grid star formation model and the (subset of) gas considered, the velocity dispersion increases towards the centre of the galaxy, specifically within the inner

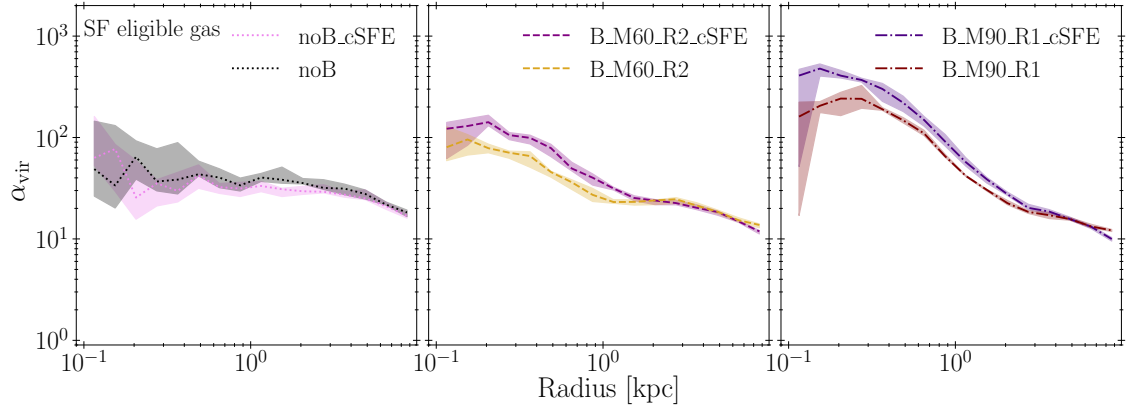


Figure 2.5: Comparing the effect of different sub-grid star formation models on the virial parameter of the gas, for the bulgeless (left), fiducial (middle) and compact bulge (right) galaxies. The panels show the result for gas that satisfies the density and temperature thresholds for star formation.

1–3 kpc. This is a result of the deeper central stellar potential in bulge-dominated galaxies. For a more elaborate exploration of how the underlying gravitational potential affects σ , we refer to Section 2.5.1. Secondly, there is a small but distinct difference in σ between the different sub-grid models, within the respective bulge-dominated regions. These are the inner 1–2 kpc for the fiducial models, and nearly all of the galaxy (but most prominently the inner 3–4 kpc) for the most dominant bulge. In the simulations with a constant SFE, the SFR is not (as) strongly suppressed in the central regions. The resulting, higher momentum and energy input from stellar feedback is responsible for the offset in velocity dispersions. It adds to the increase of the velocity dispersion caused by the presence of a bulge, and causes the central rise of the velocity dispersion to extend further out into the disc. Thirdly, the variance of the velocity dispersion is smaller in galaxies with a bulge than in the simulations without a bulge. This relates back to the star formation within the galaxy. Those galaxies with a high(er) SFR do so because they experience larger extremes, with more subsequent feedback events, leading to a larger variation in σ over time.

In conjunction with Figure 2.3, Figure 2.4 highlights the necessity of a dynamics-dependent star formation model. Despite very different gas velocity dispersions, the SFRs of runs B_M90_R1_cSFE and B_M60_R2_cSFE are nearly the same. Only B_M60_R2 and B_M90_R1 reproduce the trend obtained from cloud-scale simulations that highly turbulent, super-virial gas should form stars less efficiently (e.g. Federrath and Klessen, 2012; Padoan et al., 2012, 2017).

2.4.2.2 Virial Parameter

Next, we compare the effect of the sub-grid star formation model on the virial parameter. As $\alpha_{\text{vir}} \propto \sigma^2$, the virial parameter is expected to show similar trends with radius as the velocity dispersion. This is indeed seen in Figure 2.5.

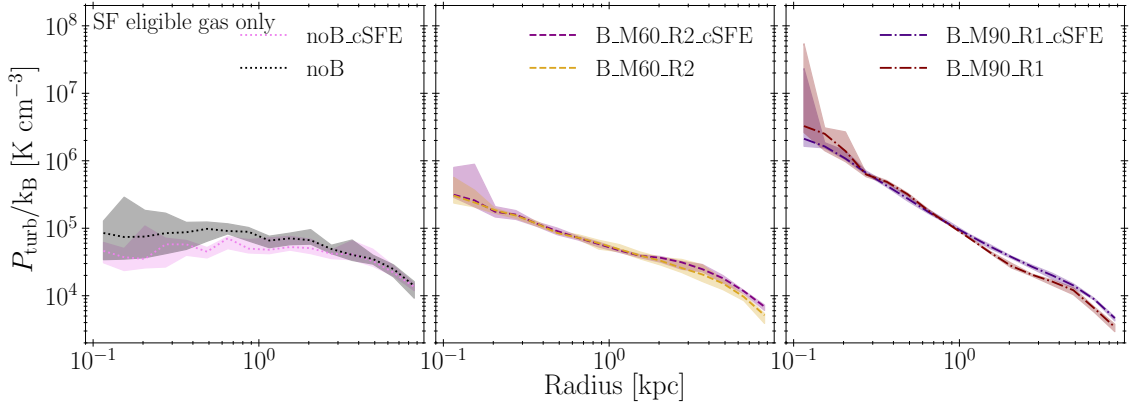


Figure 2.6: Comparing the effect of different sub-grid star formation models on the turbulent pressure of the gas, for the bulgeless (left), fiducial (middle) and compact bulge (right) galaxies. The panels show the result for gas that satisfies the density and temperature thresholds for star formation.

When considering the gas eligible for star formation, the gas virial parameters in the bulgeless galaxies increase a little from the disc to the centre. The simulations with a constant SFE show a more pronounced upturn in α_{vir} within the inner 200 pc, but these differences fall largely within the temporal variance of the models. The median virial parameters are slightly higher in the simulations with a dynamics-dependent ϵ_{ff} , which mirrors the slight elevation of the velocity dispersion caused by the higher SFR and the resulting stellar feedback.

For the simulations with the fiducial bulge, the difference between the virial parameters predicted by the two sub-grid star formation models near the galaxy centres is larger than that between the velocity dispersions in Figure 2.4, even after accounting for the fact that $\alpha_{\text{vir}} \propto \sigma^2$. This is related to an additional dependence of $\alpha_{\text{vir}} \propto L/M$, which means that a higher gas density lead to a lower virial parameter at fixed cloud size. While the gas in the centre of the galaxy is less turbulent for the dynamics-dependent model, it is also more dense, due to the prominent absence of star formation, and the fact that clouds near galaxy centres are more compact due to the elevated tidal field strength, shear, and geometric convergence (e.g. Kruijssen et al., 2019b). All of these factors result in the median virial parameter being lower in simulations run with a dynamics-dependent SFE.

The trends for the most bulge-dominated galaxies are similar to those of the fiducial runs. Together, all panels sketch a picture in which the presence of a bulge elevates the gas virial parameters towards the galactic centre. This increase is slightly less pronounced when using a dynamics-dependent SFE, due to the suppression of star formation and any subsequent feedback by the elevated virial parameter (see equation 2.2.1).

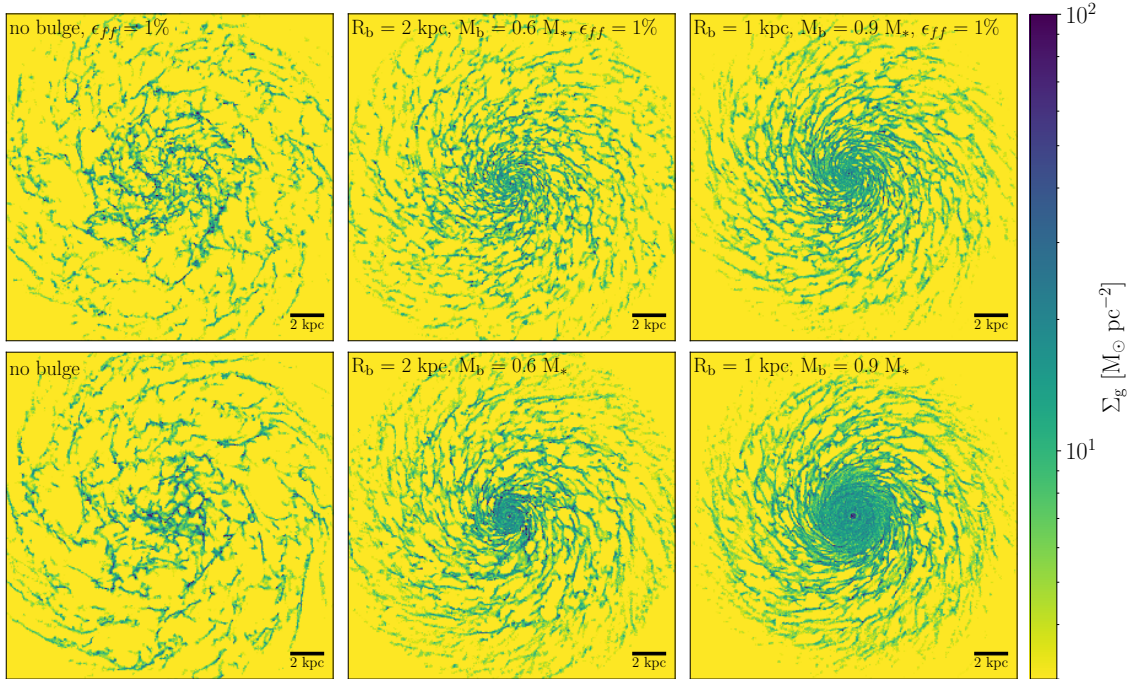


Figure 2.7: Surface density projection of the gas discs for the bulgeless (left), fiducial (middle) and compact bulge (right) galaxies. The top panels show the result for galaxies simulated with a constant SFE sub-grid star formation model, whereas the bottom panels show the dynamics-dependent analogue. The maps are shown at 600 Myr after the start of the simulations and measure 20 kpc on a side. The unsuppressed SFR and subsequent feedback in both bulgeless simulations leads to a flocculent ISM, with most of the gas along spiral arms, whereas the bulge-dominated galaxies host smooth, quiescent central gas discs.

2.4.2.3 Turbulent Pressure

In Figure 2.6, we show how the turbulent pressure, $P_{\text{turb}} = \rho\sigma^2$, of the gas changes between the different sub-grid models for star formation. In the bulgeless simulations, the turbulent pressure increases inwards throughout the disc, until it flattens within the inner 2 kpc. Due to the overall similar SFR (and as with σ and α_{vir}), the profiles of the different sub-grid star formation models agree within the variation of the median over time. The median P_{turb} of gas in the fiducial and compact bulge models keeps increasing towards the centre without such flattening. This is caused by the additional hydrostatic pressure generated by the bulge, which the turbulent pressure equilibrates to (e.g. Schruba et al., 2019).

2.4.2.4 ISM Morphology and Gas Surface Density Profile

We show the effect of the star formation model on the distribution of gas within the galaxy in Figure 2.7. The bulgeless galaxies look very similar in projection. The molecular ($\Sigma_g \gtrsim 10 M_{\odot} \text{pc}^{-2}$) gas is distributed along thin arm-like structures and the centre exhibits

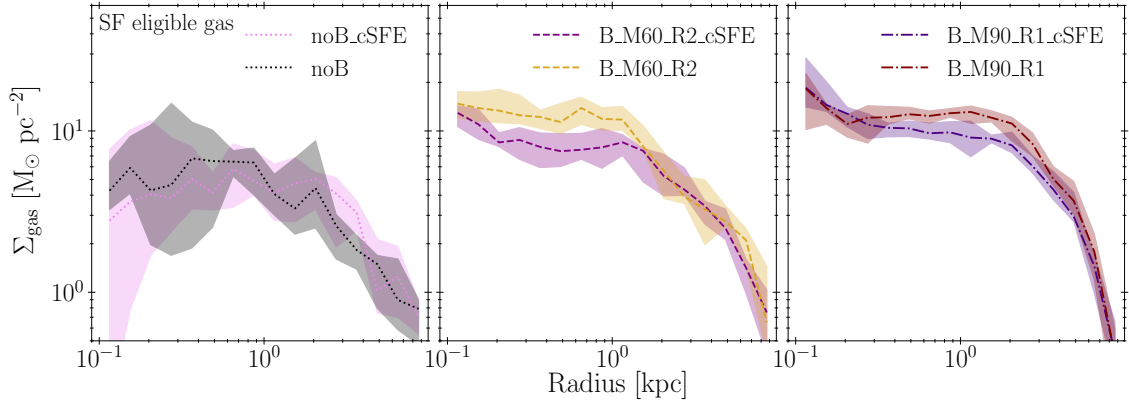


Figure 2.8: Comparing the effect of different sub-grid star formation models on the gas surface density profile, for the bulgeless (left), fiducial (middle) and compact bulge (right) galaxies. The panels show the result for gas that satisfies the density and temperature thresholds for star formation.

considerable sub-structure. Thus, while undergoing a lot of variation, the median surface density as a function of radius, shown in Figure 2.8, is similar at all radii.

Both fiducial bulge galaxies host a larger molecular gas reservoir in their centre. However, the central ~ 2 kpc of the constant ϵ_{ff} galaxy are more sub-structured than for the galaxy with the dynamics-dependent ϵ_{ff} . Because galaxy B_M60_R2_cSFE forms (more) stars than B_M60_R2 at all radii, including in the centre, stellar feedback is more effective at disrupting the gas. In the dynamics-dependent model, where feedback is weaker due to the low SFR, the gas is able to settle into a smooth, high-density disc at the centre. The compact bulge simulations behave very similarly. The gas disc in run B_M90_R1 is even larger and smoother than that of B_M60_R2. Run B_M90_R1_cSFE has a small disc at the very centre, but at a lower density and with more substructure than in B_M90_R1.

The behaviour seen in the gas surface density maps is reflected in the radial gas surface density profiles in Figure 2.8, where the median Σ_{g} of B_M60_R2 and B_M90_R1 is consistently offset to larger surface densities with respect to the analogous simulations with a constant SFE. Again, this difference results from the differing SFRs and corresponding feedback intensities introduced by taking galactic dynamics into account.

In principle, it could be argued that the specific value of ϵ_{ff} in the constant SFE model could be adjusted to yield SFRs and galaxy properties more similar to those found for a dynamics-dependent star formation model. Alternatively, the overall offsets may be considered to be too small given the numerical and observational uncertainties. However, taken at face value, the differences shown in this section highlight the importance of carefully choosing the sub-grid star formation model and associated parameters, as the consequences reach beyond global scalings of the SFR and instead affect the structural evolution of the galaxy and its ISM at large. We furthermore stress that significantly suppressed star formation in a bulge-dominated galaxy is only reproduced when explicitly accounting for

the effect of galactic dynamics in the sub-grid star formation model, which then in turn introduces further differences. Conversely, galaxies evolved with the constant SFE model do not reflect any of the changes in ISM kinematics that result from the presence of different types of bulge.

2.5 Effect of the Gravitational Potential on Interstellar Medium properties

We now proceed to only consider the dynamics-dependent star formation model and vary the gravitational potential across the comprehensive parameter space covered by our simulations. We then compare how the variety of ISM-related quantities from Section 2.4 differ between these simulations. This comparison is aimed at revealing the physical mechanisms that link galactic morphology to ISM properties, star formation, and quenching, with the eventual goal of quantifying how these effects may change the star formation relation in these galaxies. In Section 2.6, we will demonstrate how the dynamical suppression of star formation can drive entire galaxies off the main sequence of star-forming galaxies, into the red cloud of quenched systems.

2.5.1 Turbulent Velocity Dispersion

The velocity dispersion of the gas is one of the main gas properties setting the virial parameter (and thus the SFE). In Figure 2.9, we show the radial profiles of σ for all simulations with a dynamics-dependent SFE. The bulgeless simulation is included in every panel as a reference line. Because the bulgeless galaxy is a pure exponential disc, the median velocity dispersion is approximately flat as a function of radius, only declining slightly in the outskirts of the disc.

From the velocity dispersion profiles displayed in Figure 2.9 it is clear that both R_b and M_b have an influence on the dynamical state of the gas. All three mass fractions exhibit a similar behaviour, in that the velocity dispersion of the gas increases towards the centre of the galaxy in the presence of a bulge. The more centrally concentrated the bulge (i.e. the smaller R_b is), the stronger the effect. Bulges with smaller R_b induce more turbulence at a given M_b . Additionally, gas further away from the centre is affected by the potential. It is likely that the true dependence on bulge properties uses a combination of R_b and M_b , such as through a linear, surface, or volume mass density enclosed at each radius (reflecting the potential, force, and tidal field, respectively). In either of these cases, we expect a monotonic trend of ISM properties and SFR with M_b/R_b^n with $n = 1-3$. We demonstrate such a dependence of the SFR on the enclosed mass surface density ($n = 2$) in Section 2.6.1.

The set of galaxies with the lowest bulge fraction, $M_b = 0.3M_*$ shows the smallest differences in velocity dispersion. Only the $R_b = 1$ kpc bulge displays a strong σ increase in the inner few hundred pc, by $\lesssim 0.3$ dex. At this bulge mass, the two more extended bulges have very similar velocity dispersion profiles, largely resembling the bulgeless galaxy. Based on the discussion so far, this may seem surprising, because one would expect the B_M30_R2

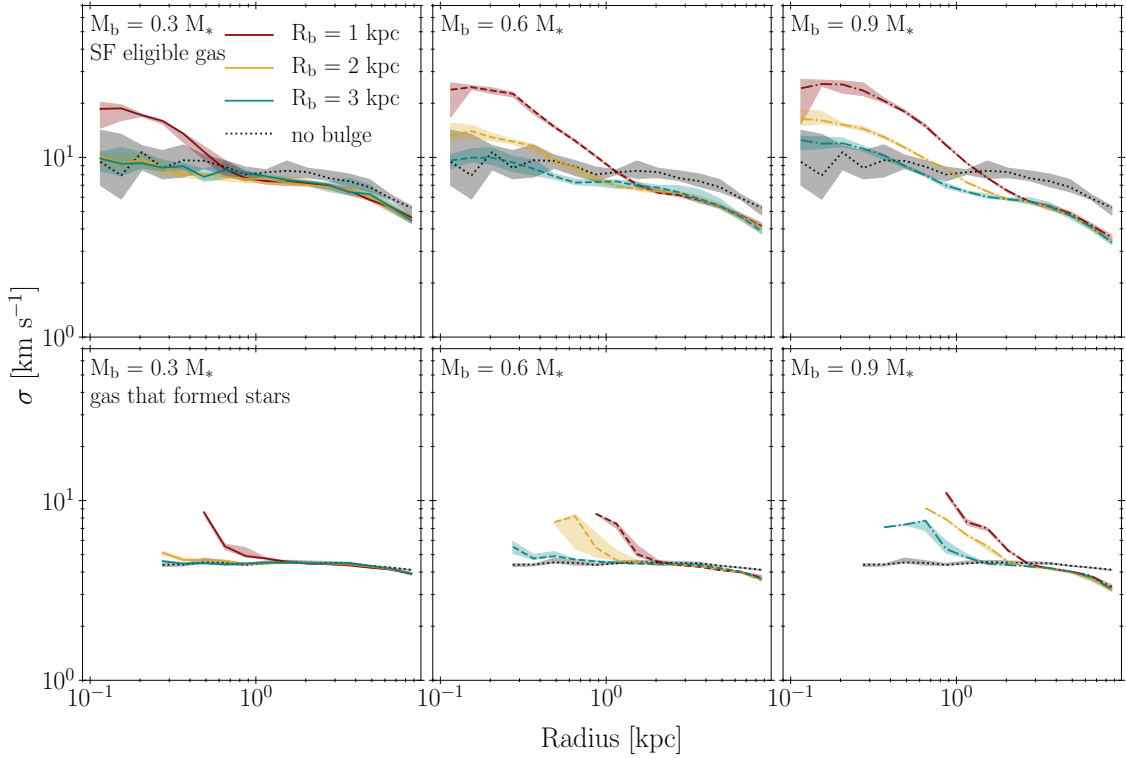


Figure 2.9: Radial profiles of the gas turbulent velocity dispersion for different gravitational potentials. Each panel compares the effect of different bulge scale radii at a constant bulge mass, with the columns showing simulations with bulges containing 30, 60 and 90 per cent of the initial stellar mass, from left to right. The top row shows the result for gas that satisfies the density and temperature thresholds for star formation, whereas the bottom row only includes gas from which stars formed. The central 300 pc are excluded from the analysis of the bottom panels (see Section 2.4.1). Each panel includes a dotted line showing the bulgeless simulation.

run to exhibit a larger velocity dispersion than the B_M30_R3 run. However, as can be seen in the rotation curves of Figure 2.2, the galaxy with the weakest bulge resembles the bulgeless run very closely. It has the second largest net SFR of all simulations with a dynamics-dependent ϵ_{ff} . The resultant feedback is sufficient to increase σ to same level as in run B_M30_R2. At bulge mass fractions of 60 and 90 per cent, the effect of the bulge scale radius becomes more discernible, because the bulge potential is no longer drowned out by the dark matter halo. Even run B_M60_R3 shows a higher velocity dispersion towards the centre than in its outskirts, although the total dynamic range of σ is again only of order ~ 0.3 dex. For the most dominant bulge (B_M90_R1), the effect of the potential on σ is noticeable out to 3 kpc, increasing the velocity dispersion by nearly an order of magnitude when going from the outer disc to the centre of the galaxy.

Qualitatively, the above trends hold irrespectively of whether we consider all gas eligible

for star formation, or only that from which stars have formed. Because we exclude the central 300 pc from the star formation analysis, we exclude them in the profiles of gas that formed stars, too. The only difference between both subsets of gas cells is that the median velocity dispersions of the star-forming gas are ~ 0.4 dex lower than those of all star formation eligible gas, since star formation preferentially proceeds in regions with lower velocity dispersions (e.g. Padoan et al., 2012). This means that, irrespectively of the gas tracer used, both the increase of the gas velocity dispersion towards small galactocentric radii and the overall larger values of σ for the most massive, centrally concentrated spheroids are strong, observationally testable predictions of our simulations. These trends are key empirical diagnostics signposting a strong interplay between galactic dynamics and ISM kinematics in galactic spheroids and early-type galaxies.

2.5.2 Virial Parameter

Figure 2.10 shows that the virial parameter follows the same trends as the velocity dispersion with respect to bulge mass and scale radius. Resulting from the increase in turbulent velocity dispersion towards the centres of the galaxies with a bulge, α_{vir} also increases towards the centres, and more strongly so for more compact and massive bulges. Quantitatively, the difference in α_{vir} between the centre and the outskirts of the disc in a bulge-dominated galaxy can reach around an order of magnitude for the most compact bulges. For the most compact bulge, the difference remains up to ~ 0.3 dex when contrasting the virial parameter at radii of 2.5–3 kpc to the outer disc. Again, the bulgeless galaxy has a much flatter profile, with a higher median α_{vir} in the outer disc.

The gas that formed stars (bottom row of Figure 2.10) has a lower median α_{vir} than all gas eligible for star formation, as well as a clearer segregation between the different bulges within the inner 2–4 kpc. The bulgeless and weakest bulge galaxies (noB, B_M30_R3 and B_M30_R2) form stars with virial parameters in range $\alpha_{\text{vir}} = 1\text{--}5$, as expected from star formation theory and in accordance with recent observations (e.g. Sun et al., 2018; Schrubba et al., 2019). The more bulge dominated galaxies exhibit larger median virial parameters, especially in the inner 1–2 kpc, reaching a maximum of $\alpha_{\text{vir}} = 50$ for run B_M90_R1. Although this might seem disconcertingly high, such high virial parameters have been observed for some clouds in the CMZ of the Milky Way (e.g. Kruijssen et al., 2014; Kauffmann et al., 2017). In addition, Figure 2.11 reveals that the vast majority of stars forms with much smaller virial parameters. Because α_{vir} is constituted by multiple physical quantities (cloud mass, radius, velocity dispersion) that are all affected by star formation and feedback over time, the median virial parameter exhibits a larger time variation between different snapshots than the quantities it is based on. This results in larger scatter than seen for the velocity dispersions in Figure 2.9.

For the most compact bulges, there is a pronounced increase of the time variability of the virial parameter of gas eligible for star formation at the very centre of the galaxy, with large downward excursions. Over the course of the simulation, gas flows towards the centre of the galaxy. Due to the amount of turbulence induced by the compact bulges, star formation is strongly suppressed and gas continues to build up. Eventually, the gas becomes so dense that it is no longer gravitationally fully resolved, i.e. overdensities identified by

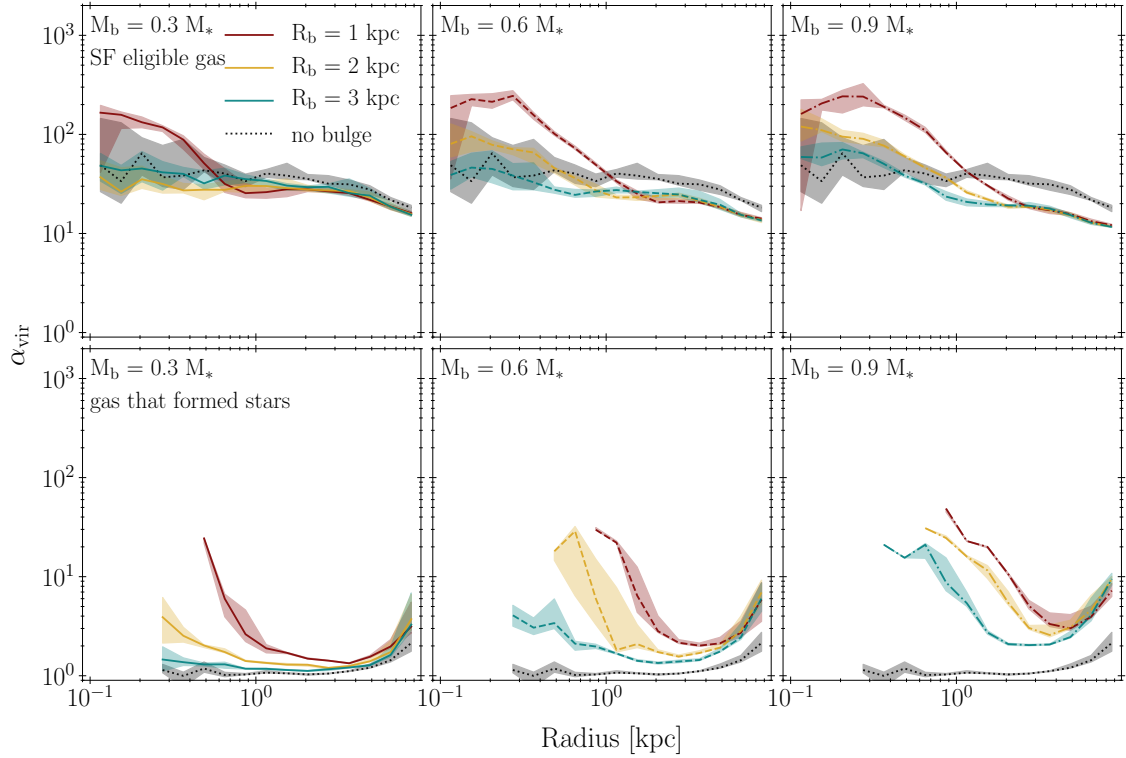


Figure 2.10: Radial profiles of the gas virial parameter for different gravitational potentials. Each panel compares the effect of different bulge scale radii at a constant bulge mass, with the columns showing simulations with bulges containing 30, 60 and 90 per cent of the initial stellar mass, from left to right. As before, the top row shows the result for gas that satisfies the density and temperature thresholds for star formation, whereas the bottom row only includes gas from which stars formed. The central 300 pc are excluded from the analysis of the bottom panels (see Section 2.4.1). Each panel includes a dotted line showing the bulgeless simulation.

our model are smaller than the gravitational softening length, despite consisting of tens of gas cells. Despite its high velocity dispersions, the virial parameter then decreases again, resulting in star formation. As discussed in more detail in Section 2.6.3, this downward spike of the virial parameter is at least partially a numerical artefact stemming from our resolution, which motivates the exclusion of the central 300 pc from the star formation related analysis (see Section 2.4.1).

We show the cumulative distribution of virial parameters for all gas cells that formed stars in Figure 2.11. Stars in the bulgeless simulation form from gas with a median virial parameter of $\alpha_{\text{vir}} = 1.1$. The median virial parameters are higher for the galaxies with bulges, more so for galaxies with more massive and compact bulges, up to a maximum of ~ 3.5 for the most bulge-dominated galaxy. This is a reflection of the elevated virial parameters in (the central parts of) these galaxies compared to the bulgeless run, as seen

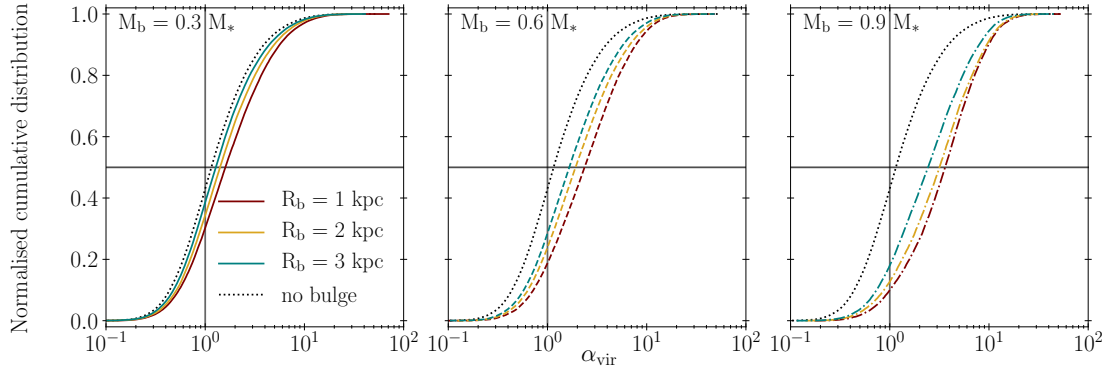


Figure 2.11: Normalised cumulative distribution of the virial parameter with which stars have formed at 1 Gyr. Each panel compares the effect of different bulge scale radii at a constant bulge mass, with the columns showing simulations with bulges containing 30, 60 and 90 per cent of the initial stellar mass, from left to right. Each panel includes a dotted line showing the bulgeless simulation, a black horizontal line indicating the median of the distribution, and a black vertical line indicating virial equilibrium, i.e. $\alpha_{\text{vir}} = 1$.

in the bottom row of Figure 2.10. Between 2–8 per cent of stars are formed with $\alpha_{\text{vir}} \geq 10$ across all simulations, and only a handful of stars with $\alpha_{\text{vir}} \geq 20$.

2.5.3 Turbulent Pressure

Figure 2.12 shows the radial profiles of the turbulent gas pressure for different gravitational potentials. The clear differences between the different simulations suggests that turbulent pressure is the most unambiguous tracer of the underlying gravitational potential. The bulgeless galaxy has a roughly constant median P_{turb} out to ~ 5 kpc, before it starts declining, as both the gas density and the velocity dispersion decrease. All of the galaxies with bulges have steeper profiles. They have higher turbulent pressures in their centres, with a faster decline towards the outskirts. Even for the $0.3 M_*$ bulges, where the central values fall within the uncertainty implied by the time variation of the bulgeless galaxy, we find a distinctly different shape of the pressure profile compared to the bulgeless model. The increase of the median P_{turb} within the inner kpc is achieved at lower bulge densities than for σ and α_{vir} , with the B_M30_R2 already showing a statistically significant central enhancement of P_{turb} . This results from the fact that increased gas densities and velocity dispersions both contribute to boosting the pressure, such that P_{turb} is the cleanest tracer of the effect of the bulge on the ISM properties.

Broadly speaking, the trends of P_{turb} with R_b and M_b are similar to the behaviour of α_{vir} and σ with radius. The most compact galaxies have median central pressures that are 1-2 orders of magnitude larger than that of the bulgeless galaxy. This links back to the star formation activity within these galaxies, which we will quantify further in Section 2.5.5. A dearth of star formation in the central region allows the high density gas to dominate, such

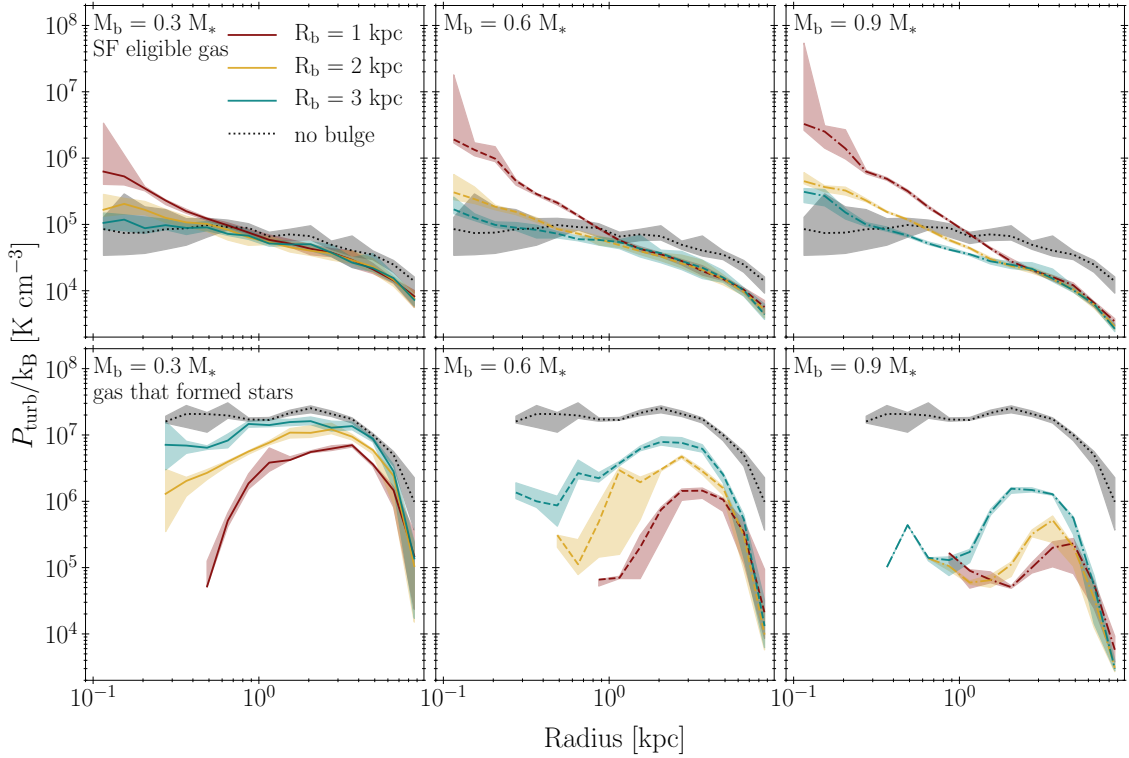


Figure 2.12: Radial profiles of the turbulent gas pressure for different gravitational potentials. Each panel compares the effect of different bulge scale radii at a constant bulge mass, with the columns showing simulations with bulges containing 30, 60 and 90 per cent of the initial stellar mass, from left to right. As before, the top row shows the result for gas that satisfies the density and temperature thresholds for star formation, whereas the bottom row only includes gas from which stars formed. The central 300 pc are excluded from the analysis of the bottom panels (see Section 2.4.1). Each panel includes a dotted line showing the bulgeless simulation.

that nearly all gas is eligible for star formation. In combination with the higher velocity dispersions, this leads to a consistently high P_{turb} .

As for the velocity dispersion, the strong increase in turbulent pressure towards the centre of the galaxy traces the gravitational potential generated by the bulge. The corresponding increase of the turbulent pressure for larger bulge mass fractions and smaller scale radii is an observationally testable prediction of our simulations.

Contrary to what we find for the radial profiles of the velocity dispersion and virial parameter, the turbulent gas pressure profiles of the gas that formed stars do not closely mirror those of the star formation eligible gas. The shape of the bulgeless galaxy’s profile is similar to that of the eligible gas, but median pressures are two orders of magnitude higher. For galaxies with bulges, the trend seen in the top panels is inverted: the more bulge-dominated a galaxy, the lower the median P_{turb} of the gas that formed stars. This

happens because the bulge suppresses the formation of density contrasts in the ISM (see Section 2.5.4). While the bulgeless galaxy achieves considerable fragmentation and thus major density (and therefore pressure) contrast between the diffuse ISM and its condensations, the suppression of fragmentation by the bulges in the other simulations means that the pressure contrasts are smaller.

2.5.4 ISM Morphology

Lastly, we focus on how the gravitational potential affects the spatial distribution and structure of the ISM within the galaxies. Figure 2.13 shows the projected gas surface density maps of all galaxies evolved with a dynamics-dependent SFE at 600Myr after the start of the simulation. Each galaxy starts out with the same, smooth exponential gas disc. Therefore any difference in disc structure is due to the combined effects of star formation, stellar feedback, and the dynamical evolution in the underlying gravitational potential, which differs between the simulations depending on the bulge properties.

The outskirts of all galaxies look similar, with dense gas arrayed along tightly wound spiral arms. However, the centres clearly differ between the ten simulations shown here. In the most massive and compact bulges, the gas settles into a smooth, dense disc. The spatial extent of these discs range from being several hundred pc in radius for the intermediate bulges (B_M30_R1, B_M60_R2, and B_M90_R3) to extending a size of 2 kpc for the compact bulge simulation (B_M90_R1). By contrast, the bulgeless galaxy and the simulation with the weakest bulge (B_M30_R3) host a central gas reservoir with considerable substructure, even though they also contain a large amount of dense gas in their central region. These central regions do not resemble discs, but fragment into star-forming units and are subsequently disturbed further by stellar feedback.

The gas surface density maps of Figure 2.13 show a stellar bulge stabilises the ISM of its host galaxy. Thanks to the increased shear velocities, the gas velocity dispersions are elevated, which together prevents the gravitational instability of the gas reservoir and suppresses star formation, in the process preventing the disruption of the ISM by stellar feedback. This is a powerful illustration of the interplay between galactic dynamics, ISM structure, and star formation, which predicts clear, monotonic trends with the morphology of the host galaxy.

2.5.5 Star Formation

We conclude our parameter survey of the impact of the gravitational potential on the ISM and star formation by focusing on the SFR of the simulated galaxies. Based on the results presented in Sections 2.5.1-2.5.3, with the gas velocity dispersion, virial parameter, and turbulent pressure all increasing towards the galactic centres, and most strongly so for the most massive and compact bulges, we expect the SFR in these galaxies to follow suit. Figure 2.14 shows the star formation relation, between the SFR surface density and the gas surface density, for all galaxies in the sample. The data points and colours indicate different galactocentric radii, showing how the star formation relation depends on radius. As elsewhere in this section, we only consider the simulations run with a dynamics-dependent

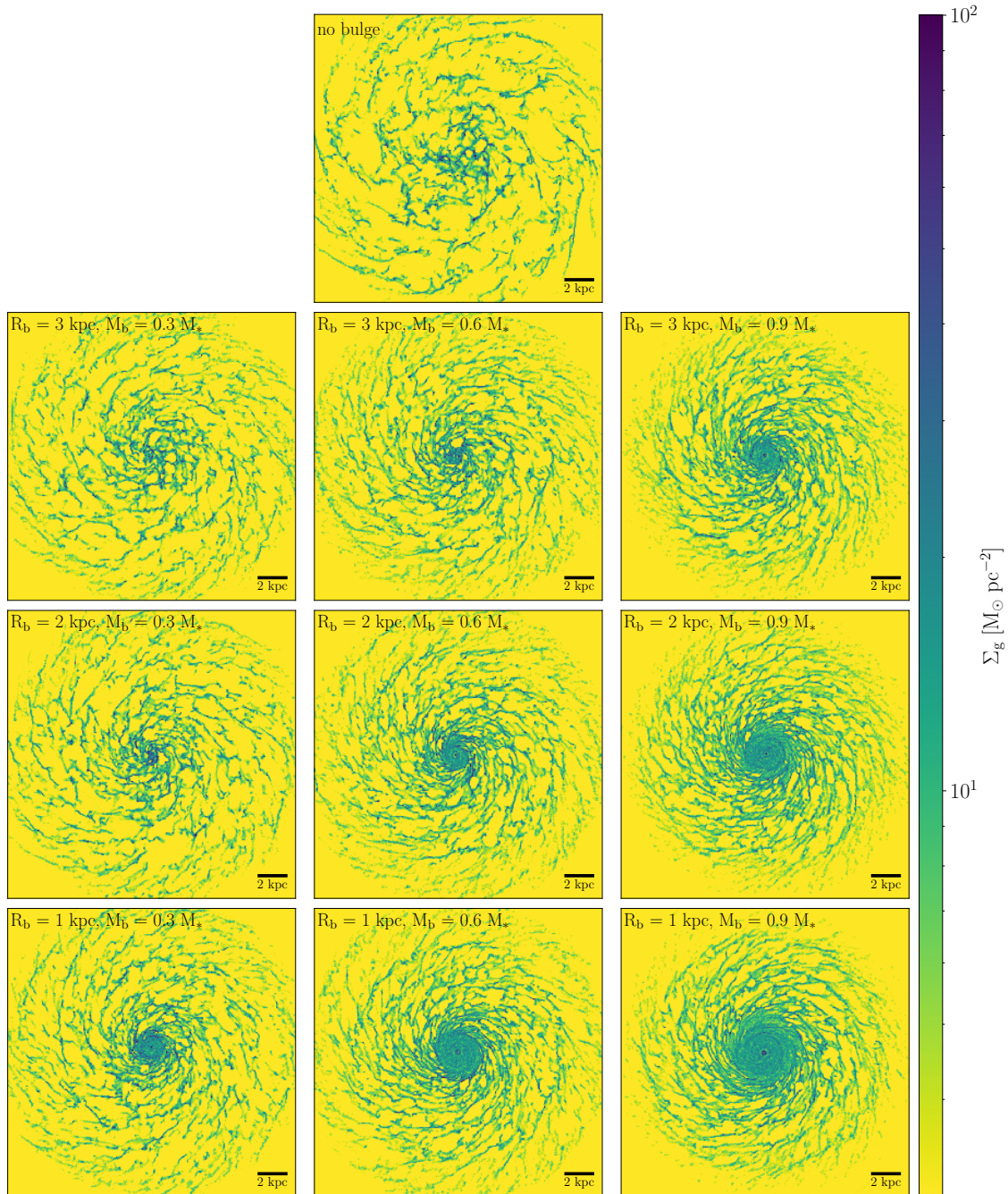


Figure 2.13: Surface density projection of the gas discs evolved with a dynamics-dependent star formation model. The top panel shows the bulgeless simulation. In the other panels, the bulge mass fraction increases towards the right and the bulge scale radius increases upwards, as indicated by the annotations, such that the bulge density increases towards the bottom right. The maps are shown at 600 Myr after the start of the each simulation and measure 20 kpc on a side. The suppressed SFR in bulge-dominated galaxies enables the build-up of a quiescent, undisturbed, and therefore smooth nuclear gas disc. The spatial extent of this disc increases with the density of the bulge. Only galaxies with a negligible bulge component show signs of substructure driven by gravitational instability and stellar feedback.

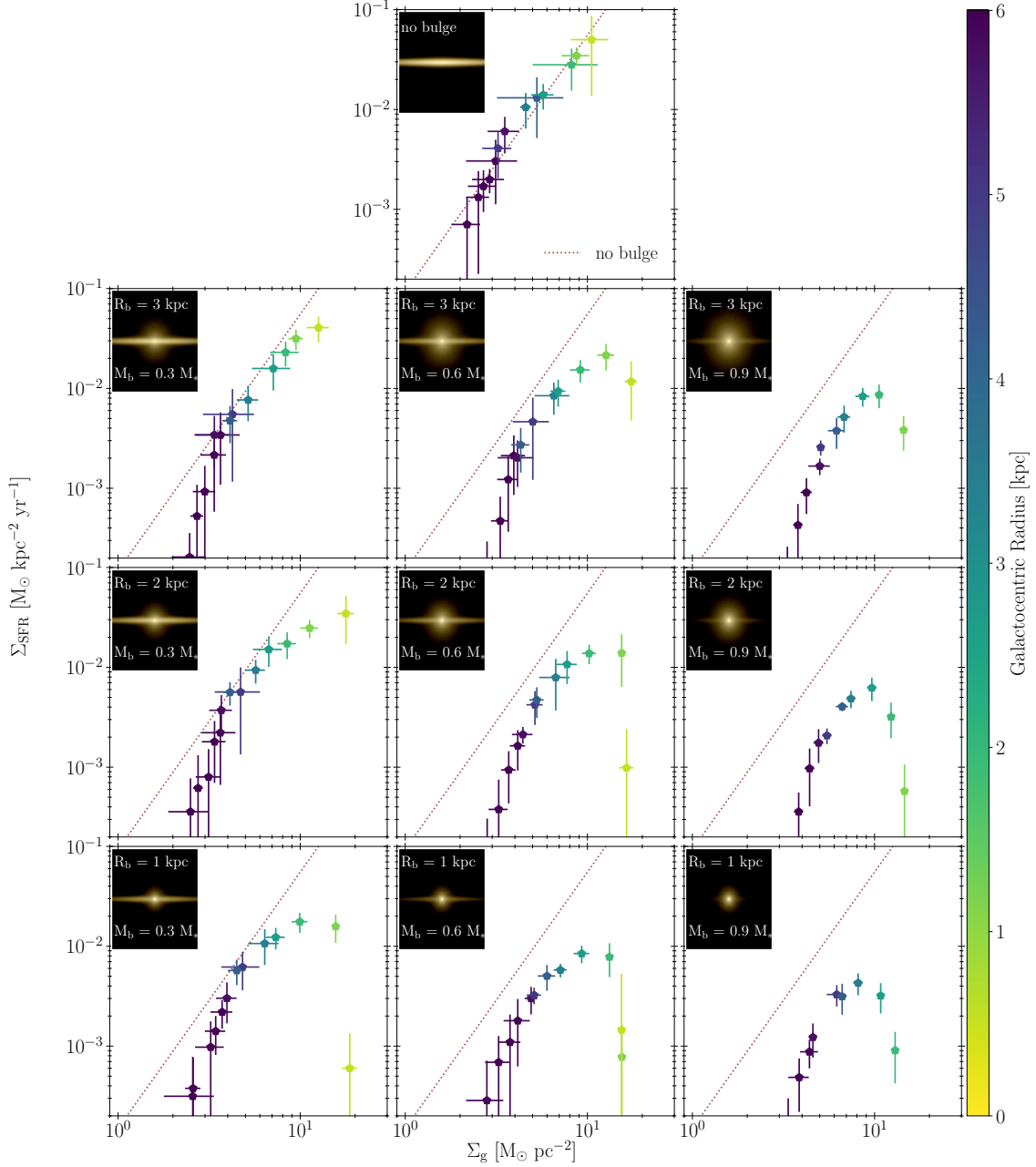


Figure 2.14: SFR surface density as a function of gas surface density for all galaxies evolved using a dynamics-dependent ϵ_{ff} . The colour coding indicates the galactocentric radius. For reference, the top-left corner of each panel shows a fake colour image of the stellar content of each galaxy. The dotted red line indicates the best-fitting power law to the star formation relation of the bulgeless galaxy, and is included to guide the eye and highlight how the star formation relation changes due to differences in the gravitational potential. The SFRs are calculated from stars that formed within the past 10 Myr of any snapshot. Each point represents a time average of snapshots separated by 100 Myr; the snapshot-to-snapshot variation is shown by the error bars. The central 300 pc are excluded from the analysis (see Section 2.4.1). This figure shows that the presence of a spheroid suppresses the SFR towards small galactocentric radii in all simulations, and that this suppression intensifies for higher-density bulges, which are located towards the bottom right.

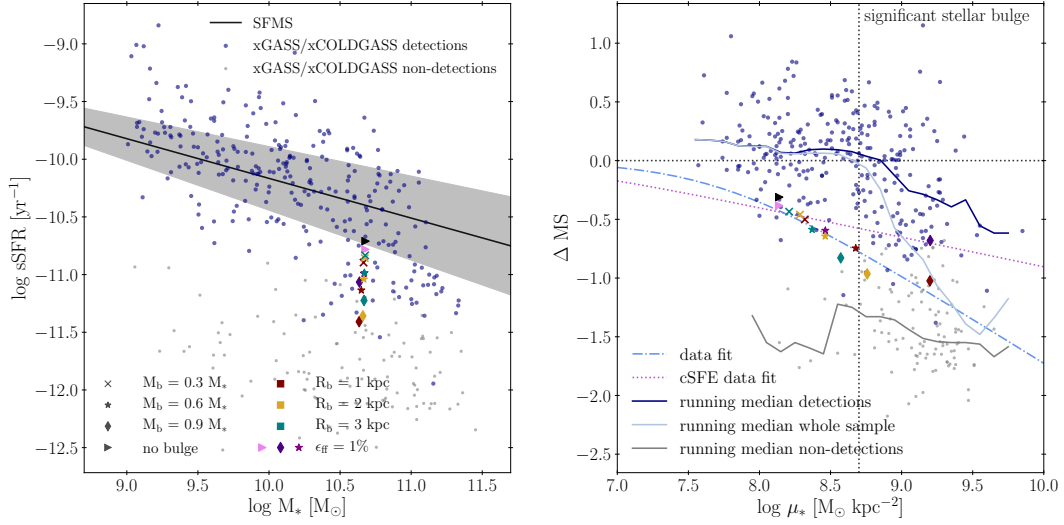


Figure 2.15: Simulation data overlaid on the data from the xCOLDGASS (Saintonge et al., 2017) and the xGASS (Catinella et al., 2018) surveys. The left panel shows the sSFR–stellar mass plane and the right panel shows the offset from the main sequence as a function of stellar surface density (μ_*). The definition of the star formation main sequence is taken from Catinella et al. (2018). All simulated galaxies with dynamics-dependent star formation exhibit a strong trend: the global SFR falls further below the main sequence, the more bulge dominated the galaxy. This trend is shown by the dot-dashed blue line in the right panel; solid lines show the running median of the detected (navy), non-detected (grey) and entire sample (steel blue) of xGASS/xCOLDGASS galaxies. Constant efficiency galaxies follow a much shallower trend with μ_* , as indicated by the dotted purple line. As for the Schmidt-Kennicutt diagrams the central 300 pc of the simulated galaxies are excluded from the analysis.

star formation model. As before, we exclude the central 300 pc from our analysis, to ensure that our conclusions are not influenced by unresolved star formation at the centre. This is discussed further in Section 2.6.3.

The star formation relation follows a simple, monotonic, power law form for the bulgeless galaxy (see the red dotted lines in Figure 2.14). However, this changes as the bulge mass fraction and compactness increases, particularly towards the centres of the galaxies. Out of all galaxies, only the weakest bulge simulation (B_M30_R3) is marginally consistent with the bulgeless galaxy to within the time variability between different snapshots, as encapsulated by the error bars. All other galaxies exhibit a pronounced flattening or turnover of the star formation relation towards the galactic centre. The degree of the flattening and the overall suppression of the SFR within the galaxy increase for more massive and compact bulges. For the galaxy with the most compact bulge (B_M90_R1), this yields a total, galaxy-wide SFR that is a factor of ~ 5 lower than that of the bulgeless galaxy.

All galaxies exhibit a clear central suppression of the SFR, by up to two orders of

magnitude (which is similar to the suppression of the SFR observed in the CMZ of the Milky Way, Longmore et al. 2013). However, the uncertainty introduced by the time variability of the SFR also seems to increase as the suppression becomes more pronounced, towards more dominant bulges. This is a statistical effect. We use radial bins with a constant radial thickness, implying that the area over which the SFR is integrated for each bin increases towards the outskirts of the galaxy, driving down the uncertainties. However, outside radii of ~ 3 kpc, the scatter increases again. This results from the outward decrease of the gas surface density and the SFR, implying fewer star formation events at large radii and increased stochasticity. The time variability is the smallest at radii of a few kpc.

In conclusion, Figure 2.14 shows that the gravitational potential generated by a stellar spheroid strongly influences the star formation relation of galaxies. The galaxies with the most massive and compact bulges are affected the most, showing a flattening or turnover of the star formation relation, as well as the lowest total SFR with suppressions by up to a factor of ~ 5 .

2.6 Discussion

2.6.1 Comparison with Observations

The discussion of Sections 2.5.4 and 2.5.5 shows that the presence of a bulge leads to decreased ISM fragmentation and suppressed SFRs towards galactic centres. Here, we place these results in the context of the observed galaxy population.

2.6.1.1 Main Sequence of Star-forming Galaxies

It was shown in Section 2.5.5 that the integrated SFRs of the simulated galaxies can be suppressed by up to a factor of ~ 5 due to the dynamical effects induced by a stellar spheroid. In Figure 2.15, we place the implications of this result in the context of the galaxy population. We show the global sSFR as a function of stellar mass (spanning the ‘main sequence of star-forming galaxies’, e.g. Noeske et al. 2007b; Peng et al. 2010), as well as the offset of the main sequence as a function of stellar surface density (μ_*), both for our suite of simulations and for the galaxy population observed as part of the xCOLDGASS (Saintonge et al., 2017) and xGASS (Catinella et al., 2018) surveys. Before proceeding, we note that all of our galaxies have the same initial M_* and low gas fraction of 5 per cent. Being isolated simulations, they do not include gas accretion or any other influences of the large-scale cosmic environment and are chosen to resemble $z = 0$ galaxies.

The left-hand panel of Figure 2.15 shows that the global sSFR of our sample ranges from the star formation main sequence (for the bulgeless galaxy), to the lowest sSFR at which gas is detected within the surveyed galaxies, approximately 1 dex below the main sequence, where star formation in galaxies has been ‘quenched’. The simulated galaxies thus span a range consistent with the observed, vertical scatter below the star formation main sequence. This means that, even without including any feedback from active galactic nuclei, our simulations bridge the transition region (the ‘green valley’) towards the quenched galaxy

population (the ‘red cloud’), purely relying on the interplay between galactic morphology, (hydro)dynamics, the properties of the ISM, and star formation.

It is reasonable to expect that the offset from the main sequence depends on the density of the stellar spheroid or bulge. The right-hand panel of Figure 2.15 shows the offset from the main sequence as a function of the stellar mass surface density (μ_*), together with the observed galaxies from xCOLDGASS and xGASS. Our simulations with a dynamics-dependent star formation model follow a clear trend of increased quenching of star formation towards increasing μ_* . This highlights that the stellar surface density (i.e. a combination of the bulge mass and scale radius) is the physical quantity driving the suppression of star formation. Compared to the running medians of detections and non-detections and the full sample, the fit to our sample does not quantitatively match any of the individual trends and also exhibits considerably less scatter than the observed galaxies. This is not necessarily surprising. Firstly, we did not fine-tune our simulations to match the xGASS and xCOLDGASS galaxies. Secondly, we only vary the bulge properties in this experiment, but it is likely that other quantities (e.g. gas fraction) affect the offset from the main sequence. We will explore this further in a follow-up study (Gensior et al. in prep.).

Most importantly, our simulations reproduce the overall trend that star formation is suppressed or quenched as the stellar surface density of the central bulge or spheroid increases. By contrast, the simulations with a constant SFE show a very different trend. Their offset from the main sequence is considerably smaller, with a much shallower dependence on μ_* . The total dynamic range in sSFR is a factor of ~ 2 , much smaller than for the dynamics-dependent SFE. Finally, Figure 2.14 illustrates that the bulge-dominated galaxies in our sample also qualitatively reproduce the trends observed by Méndez-Abreu et al., 2019. The more bulge-dominated they are, the more significant the drop of SFR towards the centre.

2.6.1.2 ISM Properties

A clear prediction of our models is that the velocity dispersion, virial parameter, and ISM pressure increase towards galactic centres. For velocity dispersions and ISM pressures, this is a well-established observational result (e.g. Kruijssen and Longmore, 2013; Leroy et al., 2016; Sun et al., 2018; Schruba et al., 2019; Sun et al., 2020a). Indeed, the velocity dispersions spanned by our simulations are consistent with the range found in the above studies. The turbulent pressures are also consistent with observations of star-forming galaxies in the local Universe (e.g. Faesi et al., 2018). There is tentative observational evidence that the gas virial parameter also increases towards galactic centres, especially in the presence of strong dynamical features (Sun et al., 2018). The radial median values of the virial parameter found in our simulations are 10–100, which might seem higher than expected, but falls within the range that Sun et al., 2018 find for M33 and M31.

A number of early-type galaxies are observed to host molecular gas in an almost featureless, smooth disc of molecular gas around the galactic centre (e.g. North et al., 2019). Similar, smooth gas discs form naturally in our simulations with a dynamics-dependent SFE, with a spatial extent that increases with the stellar (surface) density of the bulge or spheroid. These smooth gas discs do not form when a constant SFE is used, in which

case considerable substructure remains. This shows that the discovery of smooth gas discs in galaxy spheroids supports the idea that the SFE depends on the dynamical state of the ISM. At first sight, the gas in our galaxies extends further than the inner 1 – 2kpc (see e.g. Figure 2.13), as found in the observations of North et al. (2019). However, we remind the reader that we model all gas within the galaxies, without applying any density threshold or carrying out synthetic observations. Given the gas surface density profiles of our simulations (see Figure 2.8), it is likely that the molecular gas traced by CO drops off beyond radii of ~ 2 kpc.

In summary, the ISM properties of our simulations are qualitatively consistent with those found in observations, and provide an interesting physical perspective on the existence of quiescent, smooth gas reservoirs in early-type galaxies. We expect that quantitative comparisons between these simulations and the observations can help shed more light on the detailed interplay between dynamics, ISM structure, and star formation.

2.6.2 Comparison with Other Simulations

In Section 2.1, we summarised a variety of simulations in the literature focusing on the impact of galaxy morphology on star formation. To date, the main missing step in the ‘morphological quenching’ framework had been how galactic morphology translates into a cloud-scale suppression of star formation. In our simulations, we capture this process by resolving the cold ISM and including a dynamics-dependent sub-grid model for star formation, in which star formation is gradually suppressed towards high virial parameters. We show that the inclusion of such a model unlocks a variety of interesting predictions that may explain the observed correlations between galactic morphology, star formation, and quenching. Our suite of simulations systematically surveys the parameter space spanned by the properties of the stellar spheroids. However, our results must be regarded as a single, homogeneous set of experiments, using a single numerical method and basing itself on a number of necessary numerical choices. Here we discuss our results in the context of other numerical studies.

In a recent study, Su et al., 2019 find that morphological quenching is not capable of shutting down star formation completely, even if the SFR is lower in the presence of a bulge. As Figures 2.14 and 2.15 show, we find a similar trend for the galaxies in our suite, in which the SFR of the most bulge-dominated galaxy (B_M90_R1) is the lowest. However, the difference in SFR between our bulgeless and most bulge-dominated galaxy is ~ 3 times larger than found by Su et al. (2019). However, there are a number of differences in the numerical setup and the initial condition that could be responsible for this offset. Su et al. (2019) use the star formation model from FIRE2 (Hopkins et al., 2018a), in which star formation can only proceed in self-gravitating regions, with a constant $\epsilon_{\text{ff}} = 1$, whereas our simulations use a gradual suppression of the SFR as a smooth function of the virial parameter. Furthermore, the isolated galaxy simulations of Su et al. (2019) include a halo of hot gas, which by cooling feeds the supply of star-forming gas, boosting gas fraction and star formation. This likely contributes to the larger SFRs relative to the ones in our galaxy sample.

Our simulations with a constant SFE are similar to the spiral and elliptical galaxy

simulations with a gas fraction of 4.5 per cent from Martig et al. (2013). We find a smaller difference in global SFR between noB_cSFE and B_M60_R2_cSFE/B_M90_R1_cSFE compared to their simulations, and a slightly larger normalisation than their star formation relation. However, the agreement is satisfactory overall. Our simulations show that the dependence of the sub-grid star formation model on galactic dynamics is required to reproduce a more pronounced suppression of star formation and change the star formation relation. Our findings are also in good agreement with the early-type galaxy simulation of Kretschmer and Teyssier, 2020, which shows that a bulge-dominated spheroid can suppress star formation in the centre of a galaxy. Their study also further supports the argument that a more physically-motivated, dynamics-dependent star formation model is necessary to accurately model star formation in such systems.

Even if they do not use it to investigate morphological quenching, Semenov et al., 2016, 2017, 2018 make use of the Padoan et al. (2012) parametrisation of the virial parameter to calculate the SFE in their simulations. Apart from using a different method for calculating α_{vir} , their sub-grid star formation model is the most similar in the literature compared to the prescription we are using. Despite the fact that their isolated galaxy contains a bulge, Semenov et al., 2016 do not see any central suppression of star formation. However, their simulation differs in two important ways from the galaxies in our suite. Firstly, their bulge component only holds ~ 9 per cent of the initial stellar mass of the galaxy confined to the centre, thus being most similar to our bulgeless galaxy, which does not significantly deviate from the observed star formation relation (Kennicutt and Evans, 2012). Secondly, the gas content of their simulation is a factor of 4 larger, at 20 per cent of the initial stellar mass, compared to the 5 per cent that we use to mimic gas-poor, early-type galaxies.

Previous work has suggested that there may exist a critical gas fraction below which ‘morphological quenching’ (or, in the context of our results, rather the ‘dynamical suppression of star formation’) may proceed. Martig et al., 2013 perform simulations of idealised galaxy models and find a considerably stronger suppression of star formation at a gas fraction of 1.3 per cent than at 4.5 per cent. In the context of our work, we remind the reader that Martig et al., 2013 use a constant star formation efficiency, which implies that the dynamical suppression of star formation is less pronounced than when using a dynamics-dependent model. As a result, this suppression may not be able to manifest itself at gas fractions as high as in our simulations. None the less, the important insight is that the suppression weakens towards larger gas fractions. The high-redshift ($z > 5.7$) simulations of highly gas-rich (~ 50 per cent) galaxies by Trebitsch et al. (2017) further highlight that gas fraction is an important quantity to consider, because bursty star formation continues to proceed at a roughly constant time-averaged rate in their most massive halo, even after the build-up of a small central bulge. Similarly, Kretschmer and Teyssier, 2020 only see a suppression of star formation in their cosmological zoom-in simulation of an early-type galaxy after a drop in gas fraction following a merger-induced starburst, once again indicating that gas fraction plays a key role in the suppression of star formation by a dominant bulge component. Exploring how the gas fraction of our galaxies affects their SFRs is beyond the scope of this chapter. We refer to Chapter 4 for a study of effect the gas fraction has on dynamical suppression.

2.6.3 Numerical Caveats

2.6.3.1 Gravitational Softening and the Implications for our Sub-Grid Model

Current numerical simulations of galaxies use particles with masses much larger than those of the individual stars that they are constituted by. To prevent spurious heating from close encounters by these massive particles, gravitational forces must be softened. While adaptive gravitational softening minimises the error in the force calculation (Price and Monaghan, 2007), one still has to choose a (minimum) length scale below which the gravitational force is softened.

Our sub-grid star formation model is aimed at self-consistently identifying an overdense region around a gas cell, for which the gas density and velocity dispersion can then be calculated. Since the gravitational softening length is larger than the cell radius by definition, it is conceivable that in a very dense, clumpy medium the overdensity identified is smaller or comparable in radius to the softening length. We have quantified this directly in our simulations and find that this occurs for ≤ 1 per cent of gas cells in our simulation at any given timestep, where the exact fraction depends on the prior amount of star formation and feedback experienced by the gas. The virial parameters corresponding to these regions are all $\alpha_{\text{vir}} < 2$, with the majority having $\alpha_{\text{vir}} < 1$.

There are two possible ways in which these edge cases can be handled. Firstly, one can define a hard threshold for l_{tw} , requiring it to be at least equal to the softening length of the cell. Secondly, one can simply accept that some overdensities fall within the gravitationally softened volume. The former option goes against the principle of self-consistently determining an overdensity based on which all other quantities are calculated. Choosing the latter option implies that a disproportionately large fraction of stars will form from overdensities in gravitationally softened regions, as $\epsilon_{\text{ff}} \propto \exp(-\alpha_{\text{vir}}^{0.5})$.

The purpose of gravitational softening is to prevent numerical noise from artificial hard scatterings. Hence, it can be argued that gas that becomes dense enough to fall within the smallest softening considered should, in the context of this simulation, count as self-gravitating and form stars. This is the standard assumption made when using simple sub-grid star formation models with a constant ϵ_{ff} . In that case, a fraction of gas above the star formation threshold (usually some factor less than the maximum gravitationally resolved density) is converted to stars every timestep. However, the main advantage of our model is that the SFE is now determined by gas dynamics, rather than just converting the most gravitationally unresolved gas into stars as models with a constant SFE do. This enables star formation in self-gravitating clumps that might be less dense (i.e. that would otherwise have a much lower probability of star formation) and, most importantly, prevents star formation in dense gas that is highly unbound due to external forces acting on the ISM. Both of these features of the dynamical SFE model cannot be achieved by a model with a constant SFE. In the end, only a small subset of gas cells in our model are gravitationally unresolved. We therefore accept this as a minor drawback – treating this subset as self-gravitating and (potentially) star-forming clouds is equivalent to how they would be treated in a constant SFE model. In light of the fact that we use a more physically-motivated sub-grid star formation model, and to conserve the full self-consistency of the calculation,

we choose to not enforce a hard limit for the tree-walk length.

The above problem is intricately linked to our choice of excluding the central 300 pc from our SFR analysis. Since we do not include any form of feedback other than type II SNe, gas is able to accumulate at the centres of galaxies, especially in those with high central stellar surface densities. There, the gas is turbulent enough to suppress star formation, resulting in increasing gas densities in the centre, eventually allowing some individual clumps to become smaller than the gravitational softening length. Given that we do not resolve the dynamical mechanisms relevant near galactic centres, which require sub-pc resolution (e.g. Kruijssen et al., 2019b), and also omit feedback from active galactic nuclei, which may also affect the SFE of the most central gas reservoir, we choose to omit the central regions within a 300 pc radius when analysing the SFR. With this radial cut, the majority of stars from gas cells with l_{tw} smaller than the gravitational softening length are excluded during the analysis.

2.6.3.2 A Note on Numerical Chaos

As recently demonstrated by Keller et al., 2019 and Genel et al., 2019, numerical simulations of galaxy formation and evolution are sensitive to (chaotic) stochasticity. As a means of assessing whether differences between models reflect the underlying differences in physical models or initial conditions, Keller et al., 2019 advise to run a large number of identical simulations with different random seeds. While it is not feasible to simulate every galaxy in our suite a large number of times, all quantities analysed in this chapter are represented as averages over time, with an indication of the variance given by error bars. Because we model idealised galaxies, these temporal variations are expected to be analogous to the stochasticity investigated by Keller et al., 2019 and Genel et al., 2019. Using the temporal variation to quantify the uncertainties on the quantities considered thus ensures that our conclusions remain robust and appropriately reflect how the results depend on the underlying physics.

To further test the effect of numerical effects, we simulated a subset of the galaxies in our suite with different random number seeds (which influence the stochasticity of star formation and the subsequent evolution of the galaxy), finding that any differences caused by these numerical effects are smaller than the variation quantities exhibit over time.

2.7 Summary and Conclusions

In this work, we present hydrodynamical simulations of a suite of isolated galaxies with gas-fractions appropriate for $z = 0$ galaxies, to systematically explore whether stellar bulges or spheroids can dynamically suppress star formation. We systematically vary the bulge mass fraction and scale radius to cover a total of ten different galactic morphologies. We also introduce a new, physically-motivated sub-grid model for star formation that includes a dependence of the SFE per free-fall time (ϵ_{ff}) on galactic dynamics via the virial parameter, motivated by the simulations of turbulent fragmentation by Padoan et al. (2012). Contrary to many previous sub-grid star formation models of this nature, we do not use a sub-grid turbulence model. Instead, the physical quantities entering the virial

parameter are calculated by iterating over neighbouring gas cells until an overdensity is identified self-consistently. This approach is analogous to on-the-fly cloud identification and thus establishes the virial parameter for spatially-resolved, physically meaningful units. To enable a comparison to traditional sub-grid star formation models, we also consider simulations with a constant $\epsilon_{\text{ff}} = 1$ per cent for a subset of the galaxies. These include a bulgeless galaxy and two models with a bulge.

Concerning the two different sub-grid star formation models, we draw the following conclusions:

1. The global SFR exhibits little difference between using a constant or dynamics-dependent SFE, as long as no dominant stellar spheroid is present. However, in the presence of a spheroid, the SFRs of simulations with a dynamics-dependent SFE fall below those with a constant SFE. The more bulge-dominated the galaxy, the larger the difference in SFR.
2. The observed suppression of star formation at the centres of spheroid-dominated galaxies can only be reproduced with the dynamics-dependent sub-grid model.
3. The gas reservoirs hosted in the centres of galaxies modelled with a dynamics-dependent ϵ_{ff} self-consistently settle into smooth disc of molecular gas. The central ISM of galaxies modelled with a constant SFE remains much substructured and porous. This means that the observed existence of smooth gas discs in early-type galaxies can only be understood if the SFE depends on the dynamical state of the gas.
4. When no bulge is present, there are small differences in gas distribution and ISM kinematics between the sub-grid star formation models, but the galaxies evolve very similarly.
5. The gas velocity dispersion, virial parameter, and turbulent pressure differ between both sub-grid star formation models, but mostly within the bulge-dominated region. They show no major differences at larger radii.

We proceed to investigate the impact of a stellar spheroid on the SFR and ISM properties of the simulated galaxies. To do so, we adopt the dynamics-dependent star formation model and simulate a suite of ten isolated galaxies that systematically surveys a two-dimensional parameter space of bulge properties. This space spans a factor of three in bulge mass (from 30–90 per cent of the initial stellar mass in the bulge component) and also in bulge scale radius (from 1–3 kpc). We also include a bulgeless galaxy, so that the final suite ranges from disc-dominated to spheroid-dominated galaxies. All galaxies have a gas fraction of 5 per cent, appropriate for Milky Way-mass galaxies at $z = 0$ (e.g. Saintonge et al., 2017; Catinella et al., 2018). Our results can be summarised as follows.

1. Spheroids drive turbulence and increase the gas velocity dispersion, virial parameter, and turbulent pressure towards the galactic centre. The strengths of these effects depends on the bulge mass and radius. More compact (smaller R_{b}) and more massive (larger M_{b}) bulges tend to drive more turbulence. The radial range across which the ISM properties change is the largest in galaxies with the most massive bulges.

2. As a result of the above changes to the ISM, a stellar spheroid stabilises the ISM of its host galaxy. Thanks to the increased shear velocities, the gas velocity dispersions are elevated, which together prevents the gravitational instability of the gas reservoir and suppresses fragmentation, thereby also preventing the disruption of the ISM by stellar feedback. This leads to the build-up of a smooth disc of molecular gas around the centre of the galaxy. The smoothness and spatial extent of this disc increases for more bulge-dominated galaxies.
3. As a result of the high virial state and the suppression of fragmentation, star formation is dynamically suppressed in the centres of the simulated galaxies hosting a bulge component. This leads to a flattening of the spatially-resolved star formation relations in these systems, because the gas surface density typically increases inwards.
4. In bulge-dominated systems, the dynamical suppression star formation in the centres leads to a measurable galaxy-integrated decrease of the SFR. In our simulations, the factor by which the global SFR is suppressed is up to a factor of ~ 5 . This drives an offset from the main sequence of star forming galaxies. As a result, galaxies with dominant spheroids populate the green valley and reach into the red cloud of quenched galaxies. This offset from the main sequence increases towards larger stellar surface densities of the bulge, clearly highlighting the impact of the gravitational potential.
5. We argue that the ‘dynamical suppression’ of the SFR in galaxy spheroids⁵ is capable of significantly affecting the global SFR and the subsequent evolution of galaxies, presumably most strongly for those with low ($\lesssim 5$ per cent) gas fractions. This form of ‘quenching’ proceeds without expelling the gas by feedback from massive stars or active galactic nuclei, but by dynamically stabilising the gas reservoir and rendering it quiescent.
6. Following from these results, the SFR of galaxies is not exclusively set by the balance between accretion and feedback, but carries an important dependence on the gravitational potential. This dependence can dominate at the low gas fractions that characterise early-type galaxies and the bulges of late-type galaxies.

We demonstrate that the gravitational potential plays an important role in regulating star formation in spheroid-dominated galaxies, and is capable of dynamically quenching star formation in these systems. Including a dependence on gas dynamics in the sub-grid star formation model is crucial to fully model this effect in simulations of galaxy formation and evolution. However, as the comparison of our simulations to observations shows, even in spheroid-dominated systems there exists considerable scatter around the relation between decreasing SFR with the stellar surface density of the spheroid. This implies that additional physical quantities, such as the gas fraction, are similarly relevant in setting the galactic SFR. This leaves important avenues for extending our analysis and improving the predictive power of these simulations.

⁵This terminology is preferred over ‘morphological quenching’, which skips the dynamical step that we find to be crucial.

Chapter 3

The WISDOM of Power Spectra: quantifying how the galactic gravitational potential impacts the central gas reservoirs of galaxies

Authors:

Jindra Gensior, Timothy A. Davis, Martin Bureau and
J. M. Diederik Kruijssen

This chapter is based on a manuscript in preparation that will be submitted to an international astrophysics journal following the submission of this thesis.

Jindra Gensior is the principal author of this article. The original idea of comparing the gas reservoirs in simulations and observations comes from a discussion between Jindra Gensior and Timothy Davis. Diederik Kruijssen suggested using power spectra. Jindra Gensior performed the analysis on the simulations and observations. The zeroth moment maps of the WISDOM galaxies were provided by Timothy Davis. All authors contributed through several discussions, and Jindra Gensior produced all figures and wrote the manuscript. All authors actively collaborated on corrections and suggestions for the manuscript.

Abstract

Recent simulations predict that the dynamical suppression of star formation in a spheroid-dominated galaxy is preceded by the suppression of fragmentation in its interstellar medium. The density power spectrum is a powerful tool to constrain the degree of fragmentation within a gas reservoir. Specifically, it can answer the question whether the shear induced by a dominant spheroidal potential can induce enough turbulence to suppress fragmentation alongside the star formation, or if there is a different source of turbulence responsible for the smooth central gas discs observed. In this chapter we compute surface density power spectra for the nuclear gas reservoir of ten isolated galaxy simulations and twelve galaxies observed as part of the mm-Wave Interferometric Survey of Dark Object Masses (WISDOM) project. Both simulated and observed galaxies range from disc-dominated galaxies to spheroids, varying more than an order of magnitude in central stellar surface density, which is a tracer of bulge dominance. We find that for the simulations, the power spectra steepen with increasing central stellar surface density, thereby clearly linking the suppression of fragmentation to the shear-driven turbulence induced by the spheroid. By contrast, the WISDOM observations show a different (but potentially consistent) picture: no clear trend is visible between power spectrum slope and central stellar surface density, but the WISDOM power spectrum slopes correlate with the central gas surface density. This implies that the potential of the gas rather than the stars might control the driving of turbulence in the real-Universe spheroids.

3.1 Introduction

It remains an open question how galaxies become quiescent and cease their star formation activity while retaining a molecular gas reservoir. Empirically, the global star formation rate (SFR) of galaxies is proportional to the surface density of their gas reservoir (e.g. Kennicutt, 1998b; Bigiel et al., 2008; de los Reyes and Kennicutt, 2019). However, these relations are based on late-type, star-forming galaxies. By contrast, the ~ 25 per cent of early-type galaxies (ETGs) which host molecular gas (e.g. Young et al., 2011; Davis et al., 2019) exhibit a suppressed SFR despite hosting similar gas reservoirs (Davis et al., 2014). A similar behaviour is seen in the central, bulge-dominated region of the Milky Way (Longmore et al., 2013; Kruijssen et al., 2014). Additionally, there is some evidence for intermediate redshift early-type galaxies that are quiescent despite hosting molecular gas reservoirs (Suess et al., 2017; Williams et al., 2021).

In recent years, the ‘dynamical suppression’ of star formation (also known as ‘morphological quenching’;¹ Martig et al., 2009) has emerged as a viable pathway to quiescence in bulge-dominated galaxies (e.g. Martig et al., 2009, 2013; Gensior et al., 2020; Kretschmer and Teyssier, 2020; Gensior and Kruijssen, 2021). Dynamical suppression describes the process where shear, induced by the spheroidal component of the gravitational potential,

¹For the remainder of this chapter we will exclusively use the term *dynamical suppression*, since the galactic dynamics play a crucial role in the suppression and quenching, whereas to morphological quenching places all emphasis on the presence of a bulge.

drives turbulence in the gas, thereby stabilising it and suppressing star formation. Although dynamical suppression requires low gas fractions to be effective (Martig et al., 2013; Gensior and Kruijssen, 2021), it offers a compelling explanation for the suppressed star formation activity observed in ETGs with gas reservoirs.

A key step within the dynamical suppression of star formation is the (dynamical) suppression of fragmentation. Gensior et al. (2020) simulated ten isolated galaxies with identical stellar mass, but morphologically ranging from disc galaxy to spheroid. The galaxies with dominant bulges formed a smooth, dense circumnuclear gas reservoir that increased in size with increasing central stellar surface density (μ_* , a tracer for the dominance of the spheroidal component). These look remarkably similar to the molecular gas reservoir observed in the lenticular galaxy NGC 0383 (North et al., 2019). By comparison, the interstellar medium (ISM) of the low μ_* galaxies in the Gensior et al. (2020) sample is porous, sub-structured and clumpy throughout the entire galaxy. This is more comparable to spiral galaxies, such as e.g. M33 (Koch et al., 2020) or those within the PHANGS sample (e.g. Leroy et al., 2021a,b). Gensior et al. (2020) attribute the visual suppression of fragmentation to the shear-driven turbulence, but do not investigate it further. In this chapter we wish to quantify the effect the gravitational potential and galactic dynamics have on the gas reservoir of a galaxy and its turbulent state. To do so, we turn to an ISM statistic that has been used numerous times to analyse turbulence in galaxies: the spatial power spectrum of the ISM.

The power spectrum encodes information on the nature of the turbulence (e.g. Elmegreen and Scalo, 2004). For example, the slopes of the density and velocity power spectra can be used to distinguish whether the turbulence is incompressible (Kolmogorov, 1941), or compressible (e.g. Burgers, 1939; Fleck, 1996) and whether the turbulent forcing is solenoidal or compressive (e.g. Federrath, 2013; Nandakumar and Dutta, 2020, for an application to a spiral galaxy). Power spectra have been extensively studied for regions within the Milky Way (e.g. Crovisier and Dickey, 1983; Green, 1993; Stutzki et al., 1998; Lazarian and Pogosyan, 2000; Miville-Deschênes et al., 2003; Swift and Welch, 2008; Miville-Deschênes et al., 2010; Martin et al., 2015; Pingel et al., 2018). Over the last two decades this has been extended to external galaxies such as the Magellanic Clouds (e.g. Stanimirovic et al. (1999) for the Small Magellanic Cloud and Elmegreen et al. (2001) and Block et al. (2010) for the Large Magellanic Cloud, see also Koch et al. 2020) and nearby spirals (e.g. Dutta et al., 2013) and dwarfs (e.g. Dutta et al., 2009a; Zhang et al., 2012).

Crucially for our purpose, the density power spectrum is very sensitive to the morphology of the tracer (Koch et al., 2020). Specifically, the absence of fragmentation shifts power from the smaller to the larger spatial scales (Renaud et al., 2013; Grisdale et al., 2017). Therefore, a suppression of fragmentation in the data will be visible as a steep power spectrum. However, there is some debate surrounding the shape (and slope) of extragalactic power spectra. Some studies find that their data is better represented by a broken power law (e.g. Dutta et al., 2009a; Block et al., 2010; Combes et al., 2012) where the small scale power law has a steeper slope than the large scale one. This break in the power spectrum is hypothesised to indicate the transition from three dimensional turbulence on small scales to two dimensional turbulence on the large scales, the location of the break

coinciding with the scale height of the galaxy (e.g. Dutta et al., 2009a). Yet, a break in the power spectrum is far from ubiquitous (e.g. Stanimirovic et al., 1999; Dutta et al., 2009b; Zhang et al., 2012; Dutta et al., 2013; Koch et al., 2020). Recently, Koch et al. (2020) found evidence that the break could be an artefact from not accounting for the shape of the point spread function of the data and can otherwise result from a bright, dominant source (see also Willett et al., 2005). Similarly, different methods of calculating the power spectrum (in particular, whether the uv -plane visibility (e.g. Begum et al., 2006) or the zeroth moment, surface density map is used in the computation²) and different tracers (e.g. Combes et al., 2012; Koch et al., 2020, and references therein) can yield very different results for the power spectrum slope(s). The above might imply that the density power spectrum is a poorly constrained probe for ISM turbulence, at least when considering whole galaxies. However, given its sensitivity to the morphology of the gas and especially when taking care to systematically apply the same procedure to the simulations, the density power spectrum should be a good tool to quantify the impact of the gravitational potential on the turbulence within the galaxy. If the visually smooth, circumnuclear gas reservoirs of the bulge-dominated galaxies are the result of shear-driven turbulence, we expect to see a continuous steepening of the power spectrum slope going from the disc-dominated galaxies with a porous and sub-structured ISM to the bulge-dominated ones.

Given the close visual agreement between the Gensior et al. (2020) smooth circumnuclear gas reservoirs and those of ETGs like NGC 0383, we wish to compare the power spectrum findings from the simulations to observations. To do so, we turn to the mm-Wave Interferometric Survey for Dark Object Masses (WISDOM; e.g. Onishi et al., 2017) project. The primary aim of WISDOM is to accurately measure the mass of each galaxy’s central super-massive black hole (SMBH) using the gas dynamics. As a result we have exquisite, high-resolution CO maps of the circumnuclear gas reservoir in a variety of different galaxies, ranging from late- to early-types. This makes WISDOM the ideal comparison sample for our purposes.

This chapter is structured as follows: In Section 3.2 we give an overview of the Gensior et al. (2020) simulations and WISDOM observations used, as well as our method of obtaining the density power spectrum. The power spectra of simulations and observations are presented in Section 3.3 and their trends are discussed in Section 3.4. Finally, we summarise our findings and conclude in Section 3.5.

3.2 Methods

3.2.1 Simulations

3.2.1.1 Simulation Set-up

We analyse the ISM morphologies of the isolated galaxies presented in Chapter 2 (Gensior et al., 2020) that were simulated with a dynamics-dependent star formation efficiency

²For example, the measured slope for NGC 628 ranges from 1.6 (Dutta et al., 2008, visibility method), to 2.2 (Walker et al., 2014), to 2.6 (Grisdale et al., 2017), the latter both obtained from surface density maps. See also the discussion for DDO 210 in Zhang et al. 2012.

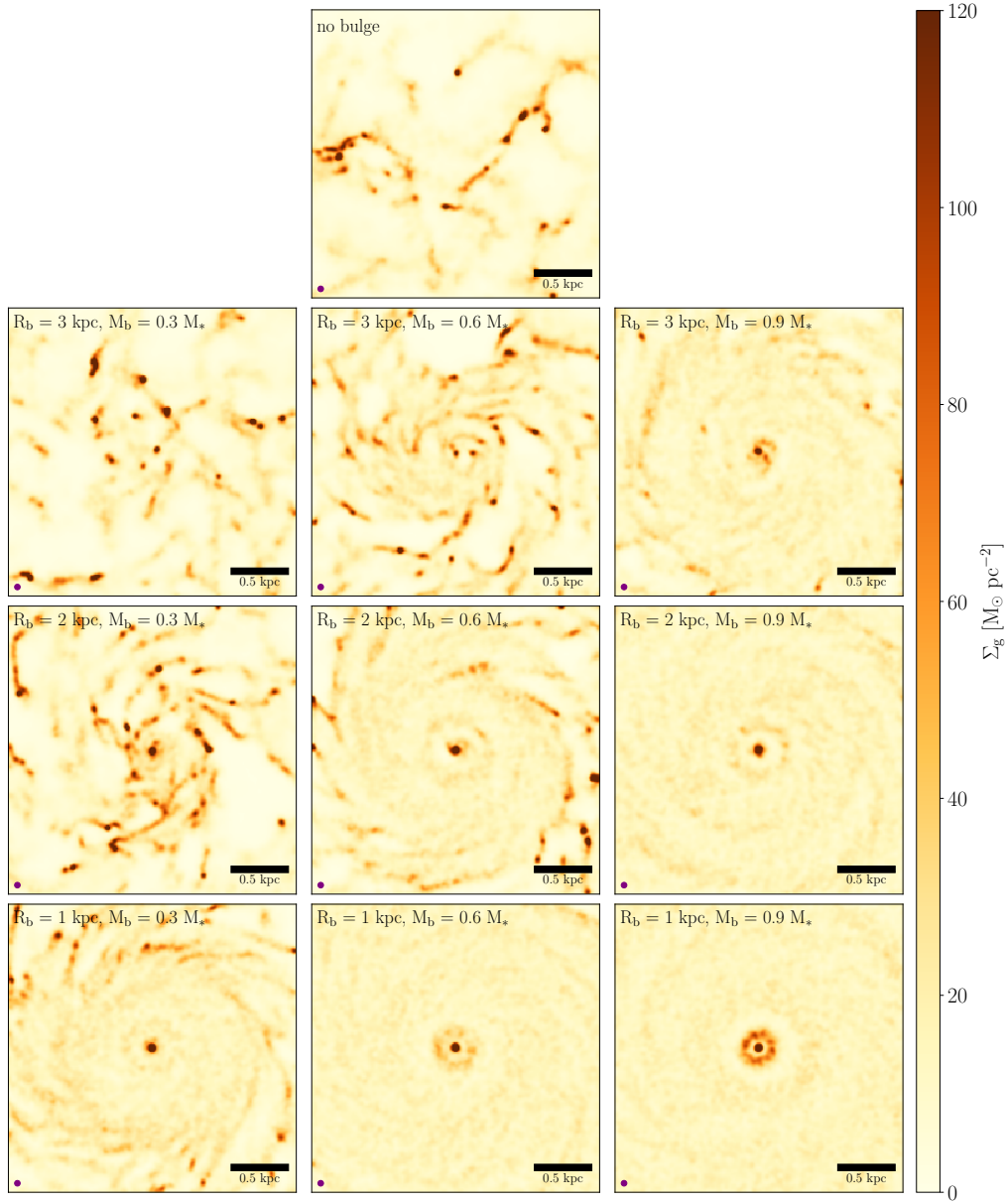


Figure 3.1: Gaussian-smoothed and regridded surface density projection for the central gas reservoir of each simulation considered in this chapter, 600 Myr after the start of the simulation. The bulge mass of the simulations in the columns increases from 30 per cent on the left to 90 per cent on the right, while the bulge scale radius decreases from top to bottom. Each map has an extent of 2.25 kpc a side and the purple circle in the bottom left corner indicates the size of the Gaussian beam. The central regions of the bulge-dominated galaxies (bottom right) are much smoother and devoid of sub-structure, compared to the clumpy ISM found in the central regions of the disc-dominated simulations (top left).

(SFE). We briefly describe the initial conditions and simulation physics below, but refer the reader to Section 2.3 for a more complete description.

The suite comprises of ten simulations, where each isolated galaxy consists of a gaseous and stellar component within a Hernquist (1990) dark matter halo. In all cases excepting one (run no_B), the stellar contribution is split into an exponential disc and Hernquist (1990) bulge component. The total initial stellar mass is fixed at $M_* \sim 4.71 \times 10^{10} M_\odot$, but we vary the mass fraction of the bulge component from 30 – 90 per cent and its scale radius from 1 – 3 kpc between the simulations to create a range of different gravitational potentials. All galaxies are initiated with a gas-to-stellar mass ratio $M_{\text{gas}}/M_* = 0.05$, in good agreement with the gas fraction of massive galaxies in the local Universe (e.g. Saintonge et al., 2017) and within the upper range of early-type galaxies (Young et al., 2011).

The simulations are performed with the moving-mesh code AREPO (Springel, 2010; Weinberger et al., 2020), which treats stars and dark matter as Lagrangian particles, while the hydrodynamics are solved on an unstructured mesh in form of a Voronoi tessellation. Gravity is solved in a tree-based scheme and we use an adaptive gravitational softening approach (Price and Monaghan, 2007) for optimal gravitational resolution. With a mass resolution of $\sim 1 \times 10^4 M_\odot$ for gas and stars, and a resolution of $\sim 1 \times 10^5 M_\odot$ for the dark matter, we fix the minimum softening length at 12 pc for gas and stars and 26 pc for dark matter, respectively. This ensures that the gas is well resolved at our star formation density threshold $n_{\text{thresh}} = 1 \text{ cm}^{-3}$ and beyond.

Star formation is modelled using the Katz (1992) parametrisation for the star formation rate $\dot{\rho}_{\text{SFR}} = \epsilon_{\text{ff}} \rho t_{\text{ff}}^{-1}$, where ϵ_{ff} is the star formation efficiency per free-fall time, ρ the density and $t_{\text{ff}} = \sqrt{3\pi/32G\rho}$ the free-fall time of the gas. We introduce a dependence on the gas dynamics using the virial parameter, α_{vir} , dependent star formation efficiency of Padoan et al. (2012, 2017):

$$\epsilon_{\text{ff}} = 0.4 \exp(-1.6\alpha_{\text{vir}}^{0.5}). \quad (3.2.1)$$

This dynamics-dependent star formation efficiency reproduces the observed suppressed star formation rates in early-type galaxies (Gensior et al., 2020; Kretschmer and Teyssier, 2020), but converges to the Kennicutt (1998b) relation for late-type or gas-rich galaxies (e.g. Semenov et al., 2016; Gensior and Kruijssen, 2021).

The virial parameter is calculated from a cloud-like overdensity around each star-forming gas cell using the algorithm presented in Gensior et al. (2020). Apart from a minimum density threshold of $n_{\text{thresh}} = 1 \text{ cm}^{-3}$, the gas must also be cooler than $1 \times 10^3 \text{ K}$ to be eligible for star formation. We model the thermal state of the gas using the Grackle chemistry and cooling library³ (Smith et al., 2017) with the six species chemistry network enabled. Tabulated atomic metal line cooling at solar metallicity and heating from the interstellar radiation field using the Haardt and Madau (2012) UV-background are included as well.

We consider feedback from massive stars in the form of type II supernovae (SNe). These are modelled using the mechanical feedback formulation (Hopkins et al., 2014; Kimm and

³<https://grackle.readthedocs.io/>

Cen, 2014): Numerically the energy, mass and metals injected by each SN are distributed to the 32 nearest neighbours using an SPH kernel. We assume one SN per $100 M_{\odot}$ of stellar mass formed (Chabrier, 2003; Leitherer et al., 2014), where each SN injects $1 \times 10^{51} \text{erg s}^{-1}$ of energy and ejects $10.5 M_{\odot}$ of mass and $2 M_{\odot}$ of metals into the surrounding medium. The SN are detonated with a delay time of 4 Myr, towards the upper end of the range recent observations of feedback disruption timescales show (Kruijssen et al., 2019a; Chevance et al., 2020a,b).

3.2.1.2 Obtaining Gas Surface Density Maps

Gas surface density maps for each simulation snapshot are created using the ray-tracing functionality within AREPO. The primary focus of this work is to analyse the circumnuclear gas disc in galaxies, therefore we create maps that focus on the central 2.25 kpc of each simulated galaxy. This is comparable in extent to the larger WISDOM maps, e.g. that of NGC 0383. Each gas surface density map is computed by integrating the densities of gas cells that fall within each pixel from 1 kpc below to 1 kpc above the galactic mid-plane. The pixel size of our original map is 1.2 pc per pixel, comparable to the size of the densest Voronoi cells. It is chosen to ensure that all structure is sufficiently resolved. In order to make this more comparable to the observations, we smooth each map with a Gaussian kernel that has a full width at half maximum (FWHM) of 43 pc, comparable to the geometric average of the NGC 0383 beam. Following the smoothing, each map is regridded to a coarser resolution of 10.8 pc/pix while conserving the surface density.

Although we use NGC 0383 as a point of reference, we have tested the resolution dependence of our results using different beam sizes and find that it does not qualitatively affect our conclusions. Additionally, we have created mock radio interferometer observations of the simulations using the KINematic Molecular Simulation (KinMS)⁴ tool (Davis et al., 2013a, 2020a). Similarly to the resolution test, we did not find a qualitative difference in the results between the projections and the KinMS maps. Therefore, we use the surface density projections as described above and refer the interested reader to Appendices B.1 and B.2 for a more quantitative discussion of these tests.

To ensure that we average over fluctuations due to cloud-scale rapid cycling (e.g. Kruijssen et al., 2019a; Chevance et al., 2020b), we generate 8 surface density maps per simulation, starting from the 300 Myr snapshot, when the gas disc has settled into equilibrium. Subsequently a map is generated for snapshots separated by 100 Myr, approximately a galactic dynamical time, until the end of the simulation at 1 Gyr. Figure 3.1 shows the central region of each simulated galaxy, 600 Myr after the beginning of the simulation. One can clearly see the aforementioned differences in ISM structure: the surface density maps of the disc-dominated galaxies (top left panels) are dominated by dense clumps and filamentary structure, whereas the surface density distribution in the bulge-dominated galaxies (bottom right panels) appears very smooth, apart from the very bright central spot.

⁴<https://github.com/TimothyADavis/KinMSpy>

Name	Type	Distance [Mpc]	$\log(M_{\text{H}_2}/M_{\odot})$	$\log(M_{*}/M_{\odot})$	$R_{e,K}$ ["]	$\log(\mu_{*}/M_{\odot}\text{kpc}^{-2})$	$\log(\text{SFR}/M_{\odot}\text{yr}^{-1})$	WISDOM
FRL 0049	-3.0 (Spiral) ⁵	86.7 [1]	9.6 [9]	10.3 [1]	3 [1]	9.31	1.21 [1]	1
NGC 0383	-2.9 (ETG)	66.6 [2]	9.1 [9]	11.6 [10]	16.23 [13]	9.40		16
NGC 0404	-2.8 (ETG)	3.06 [3]	6.7 [9]	9.1 [11]	64 [14]	8.36	-2.60 [15]	17
NGC 0524	-1.2 (ETG)	23.3 [4]	7.9 [9]	11.0 [12]	23.66 [13]	9.33	-0.56 [12]	18
NGC 1387	-2.8 (ETG)	19.9 [5]	8.5 [9]	10.7 [12]	15.72 [13]	9.51	-0.68 [12]	19
NGC 1574	-2.9 (ETG)	19.3 [6]	7.1 [9]	10.8 [12]	21.01 [13]	9.41	-0.91 [12]	20
NGC 4429	-0.8 (ETG)	16.5 [4]	7.5 [9]	10.8 [12]	48.84 [13]	8.81	-0.84 [12]	21
NGC 4501	3.3 (Spiral)	15.3 [4]	7.5 [9]	11.0 [12]	57.66 [13]	9.02	0.43 [12]	
NGC 4826	2.2 (Spiral)	7.36 [4]	7.5 [9]	10.2 [12]	69.27 [13]	8.62	-0.71 [12]	
NGC 5806	3.2 (Spiral)	21.4 [4]	8.5 [9]	10.6 [12]	29.69 [13]	8.77	-0.03 [12]	
NGC 6753	3.0 (Spiral)	43.7 [7]	9.9 [9]	10.8 [12]	19.62 [13]	8.78	0.32 [12]	
NGC 6958	-3.7 (ETG)	35.4 [8]	8.2 [9]	10.76 [12]	11.8 [13]	9.48	-0.58 [12]	22

Table 3.1: WISDOM galaxies considered in this paper and their galaxy properties, the references for which are given in the square brackets. Column 1 lists their names, column 2 their morphological type according to the HyperLEDA database. The distance to each galaxy is listed in column 3, obtained from the Atlas^{3D} survey (Cappellari et al., 2011a) where possible. Molecular gas masses in column 4 are estimated from the moment zero maps as described in the text. The stellar mass is listed in column 5, and like the star formation rates in column 8 taken from the z0MGS survey (Leroy et al., 2019) wherever possible. The effective radius in the K-band is given in column 6 using the 2MASS (Skrutskie et al., 2006) estimate where available. Column 7 lists the central stellar surface density (μ_{*}) of each galaxy, calculated from the stellar mass and effective radius listed here. Finally, column 9 lists the WISDOM papers associated with each galaxy. *References*: (1) Lelli et al. (in preparation) (2) Freedman et al. (2001), (3) Karachentsev et al. (2002), (4) Cappellari et al. (2011a), (5) Liu et al. (2002), (6) Tonry et al. (2001), (7) Bogdán et al. (2017), (8) Marino et al. (2011), (9) this work, (10) Ma et al. (2014), (11) Seth et al. (2010), (12) Leroy et al. (2019), (13) Skrutskie et al. (2006), (14) Baggett et al. (1998), (15) Thilker et al. (2010), (16) North et al. (2019), (17) Davis et al. (2020b), (18) Smith et al. (2019), (19) Boyce et al. (in preparation), (20) Ruffa et al. (in preparation), (21) Davis et al. (2018), (22) Thater et al. (in preparation).

⁵Hubble Space Telescope imaging of FRL 0049 reveals a disc and spiral arms, which in combination with a high gas fraction and SFR makes it more likely that this is a late-type galaxy (Lelli et al. in preparation, see also Malkan et al., 1998; Muñoz Marín et al., 2007), despite the HyperLEDA classification as ETG.

3.2.2 Observational Data

The surface density (zeroth moment) maps of twelve galaxies from the WISDOM programme form the observational side of our comparison. This sample comprises five late-type and six early-type galaxies as well as one dwarf spheroidal, with a range of central stellar surface densities. Table 3.1 lists the selected galaxies and their associated properties. We calculate the central stellar surface density as:

$$\mu_* = \frac{M_*}{2\pi R_e^2}, \quad (3.2.2)$$

where M_* and R_e are the galaxy’s stellar mass and effective radius respectively. To keep this calculation as self-consistent as possible we use stellar masses from the $z = 0$ Multiwavelength Galaxy Synthesis (z0MGS; Leroy et al., 2019) and K-band effective radii from the Two Micron All Sky Survey (2MASS; Skrutskie et al., 2006) survey whenever possible.

All WISDOM galaxies were observed with the Atacama Large Millimetre/submillimetre Array (ALMA) in both a compact and extended set-up, such that the data in all cases are sensitive to emission on scales up to ~ 11 arcsec. In ten galaxies of the sample the $J = 2$ to $J = 1$ transition of ^{12}CO was observed. For NGC 4429 and NGC 4826 the $^{12}\text{CO}(3-2)$ line has been observed instead. The raw ALMA data were calibrated using the standard ALMA pipeline, as provided by the ALMA regional centre staff. Then the Common Astronomy Software Applications (CASA; McMullin et al., 2007) package was used to create the final data cube, from which the zeroth moment map has been generated using a masked moment technique. A more detailed description of the data reduction and calibration can be found in the WISDOM project associated papers (Davis et al., 2017, 2018; North et al., 2019; Smith et al., 2019; Davis et al., 2020b; North et al., 2021; Smith et al., 2021). We use this zeroth moment map to estimate the gas mass as listed in Table 3.1. To convert from temperature brightness units to surface densities, we assume a CO-to- H_2 conversion factor of $\alpha_{\text{CO}} = 4.8 \text{ M}_\odot (\text{K km s}^{-1})^{-1} \text{ pc}^{-2}$, a CO(2-1)/CO(1-0) intensity ratio of 0.8 as per Bigiel et al. (2008)⁶ and a CO(3-2)/CO(1-0) intensity ratio of 1.06 (Davis et al., 2018). Table 3.2 details the properties such as the synthesised beam and pixel sizes for all galaxies in the sample.

We show the moment zero maps of all galaxies we consider here in Figure 3.2. Given that the primary aim of the WISDOM project is to dynamically measure SMBH masses in nearby galaxies, the resultant set of observed circumnuclear gas reservoirs is quite heterogeneous. The sensitivity limit of the observations ranges from approximately 3 to $70 \text{ M}_\odot \text{ pc}^{-2}$, while the resolution is similarly varied. Extent and morphology of the circumnuclear gas reservoir also differ significantly between the twelve galaxies. FRL 0049, NGC 1387, NGC 1574 and NGC 6958 appear to have a smooth distribution of gas, with the density declining towards the outskirts of the gas disc. NGC 0383 and NGC 0524 appear marginally more sub-structured than the aforementioned galaxies with faint rings in their

⁶Previously analysed WISDOM galaxies are in better agreement with a line ratio of 0.8 (e.g. North et al., 2019), rather than the more recent 0.64 (den Brok et al., 2021). Hence, we assume a ratio of 0.8 for the entire sample.

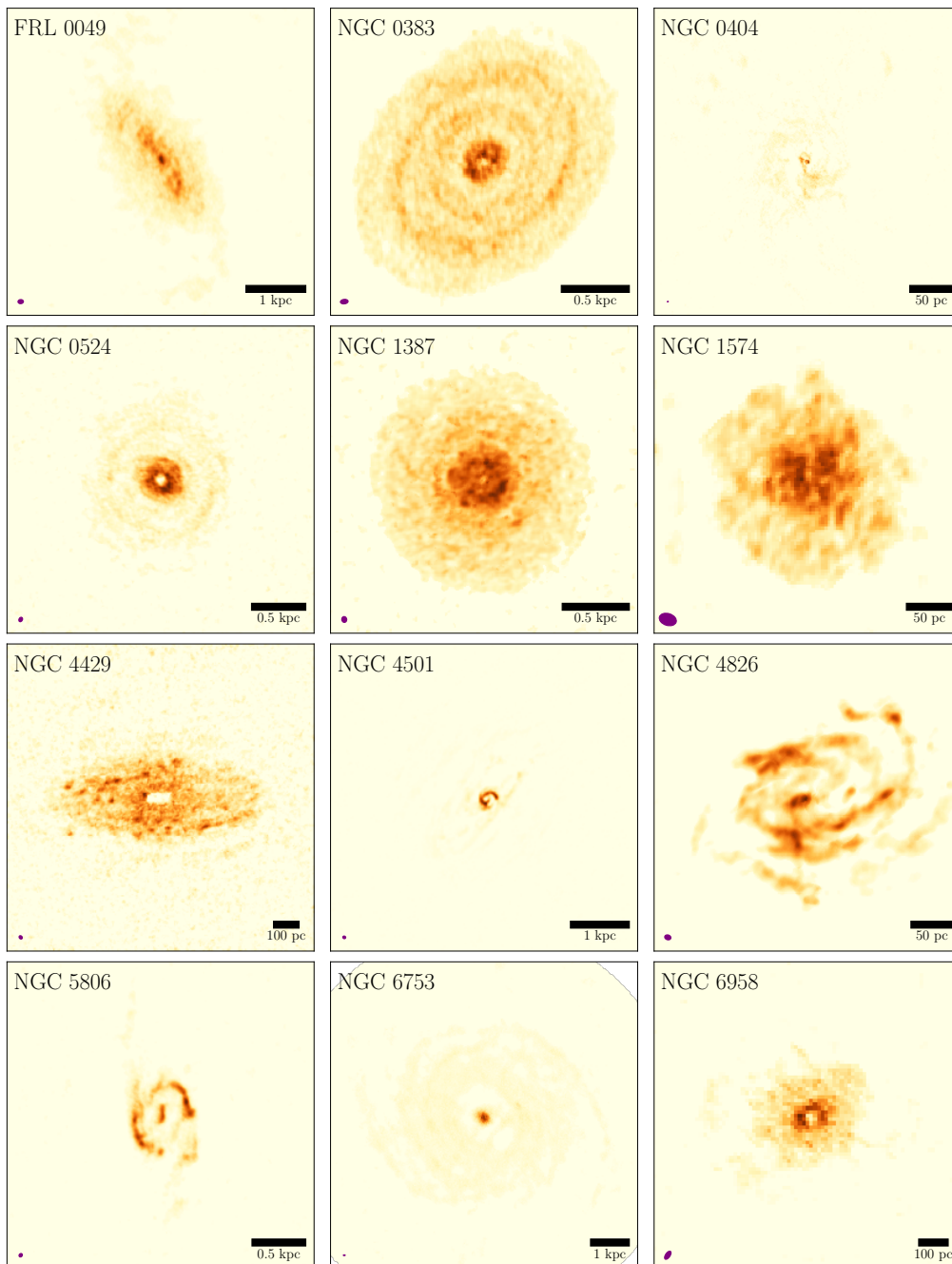


Figure 3.2: Moment zero maps of all WISDOM galaxies considered in this paper. The scale bar in the bottom right gives an indication to the size of the visible circumnuclear gas disc. A purple ellipse in the bottom left corner of each image shows the size of the beam.

overall fairly smooth gas distribution. NGC 4429, NGC 4826 and NGC 5806 appear to have multiple dense clumps in their circumnuclear discs, but the gas reservoir of the ETG NGC 4429 is noticeably more smooth compared to the spiral or ring patterns visible in the two LTGs. NGC 0524, 4429 and 6958 have holes in the centre of their gas distribution. The origin of these holes is still unclear, although they might be caused by shear induced by the central SMBH (Onishi et al., 2017; Davis et al., 2018; Smith et al., 2019).

Visually, the circumnuclear gas discs shown in Figure 3.2 seem to largely follow the prediction of Gensior et al. (2020) that a bulge-dominated galaxy with high central stellar surface density will have a smooth inner gas reservoir. To quantify this, and to better compare simulations and observations, we turn to computing surface density power spectra for the entire sample.

3.2.3 Obtaining Power Spectra

The power spectra are computed using the python package `TurbuStat`⁷ (Koch et al., 2019). The two-dimensional power spectrum is obtained by multiplying the Fourier transform of the surface density map by its complex conjugate. In this work, we focus on the one-dimensional power spectrum, which is generated by azimuthally averaging the two-dimensional power spectrum of each map. To simplify the comparison between simulations and observations, we only fit a single power law to each power spectrum:

$$P(k) = Ak^{-\beta}, \quad (3.2.3)$$

where A is the amplitude of the power law and β the power spectrum slope. As discussed in Section 3.1 sometimes a broken power law provides a better fit to the data (e.g. Dutta et al., 2009b; Grisdale et al., 2017) and we will discuss individual deviations from a single power law in more detail in the Section 3.3.2.

Individual bright emission regions are capable of dominating the power spectrum on small scales to the extent that it induces a bump and break in the power spectrum (e.g. Willett et al., 2005; Koch et al., 2020). In our *simulated* sample, we observe the same behaviour for all bulge-dominated galaxies. This effect is caused by the extremely dense region at the centre of these galaxies. There, gas accumulates continuously because star formation is suppressed and the simulations do not include AGN feedback, which could remove (some of) the innermost gas reservoir (Gensior et al., 2020). Therefore, we mask the centre of all simulated galaxies using a cosine bell window function⁸. To keep the analysis as consistent as possible, we similarly mask the centre of the WISDOM observations. The central region masked for each WISDOM galaxy depends on the beam-size, i.e. the fraction of the values tapered is a multiple of the relative beam size. To avoid contamination in the power spectrum from Gibbs ringing, we additionally use a Tukey function with $\alpha = 0.1$ to taper the edges of all gas maps.

The fit to the power spectrum is limited by the beam size on the small spatial scales, and by the spatial scale to which all flux has been recovered on the larger scales. Specifically, we

⁷<https://turbustat.readthedocs.io/en/latest/index.html>

⁸For more details on the centre masking we refer to Appendix B.2.4

Name	Position Angle [°]	Inclination [°]	beam size ["] [2]]	beam size [pc [2]]	pixel size ["]	pixel size[pc]	Sensitivity limit [$M_{\odot}\text{pc}^{-2}$]
FRL 0049	30	55.9	0.216×0.160	90.72×67.37	0.020	8.41	43.92
NGC 0383	142	37.6	0.175×0.101	56.58×32.60	0.035	11.30	23.33
NGC 0404	37	20.0	0.078×0.037	1.16×0.56	0.020	0.30	55.33
NGC 0524	40	20.6	0.377×0.280	42.62×31.62	0.100	11.30	3.09
NGC 1387	64	35.0	0.455×0.384	43.21×36.52	0.100	9.50	8.95
NGC 1574	340	25.0	0.201×0.136	18.79×12.70	0.035	3.27	24.00
NGC 4429	93	66.8	0.178×0.141	14.23×11.27	0.050	4.00	32.05
NGC 4501	135	58.7	0.669×0.592	49.60×43.90	0.110	8.16	9.85
NGC 4826	100	59.5	0.211×0.160	7.52×5.71	0.040	1.43	44.37
NGC 5806	170	60.0	0.328×0.273	34.07×28.33	0.050	5.19	16.22
NGC 6753	30	31.0	0.222×0.088	46.82×18.63	0.030	6.34	59.53
NGC 6958	115	70.0	0.184×0.089	31.57×15.30	0.075	12.87	69.40

Table 3.2: Zeroth moment map related quantities for all WISDOM galaxies considered in this paper (name in column 1): position angle, inclination, beam and pixel size (the latter both in arcsec and converted to physical sizes using the distances in Table 3.1) as well as the minimum surface density to which the observations were sensitive.

limit the fit to spatial scales larger than $3 \times \text{FWHM}_{\text{Gauss}}/\sqrt{8 \log 2}$, where the $\text{FWHM}_{\text{Gauss}}$ is the FWHM of the Gaussian smoothing kernel used on the simulations, or the geometric beam average for the WISDOM observations. This means we avoid the contamination of the power spectrum from beam effects and noise from pixelation (Koch et al., 2020).

3.3 Power Spectra

3.3.1 Simulations

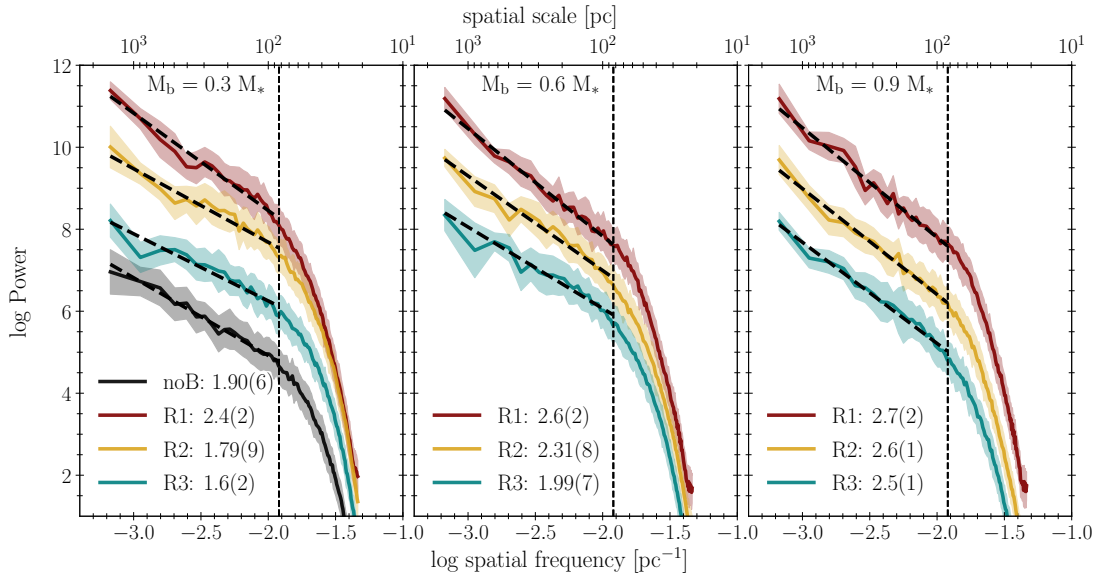


Figure 3.3: Surface density power spectra, computed on the snapshot 600 Myr after starting the simulations. Each panel compares the effect of changing bulge radii (1–3 kpc) at constant bulge mass, with the panels showing simulations with bulges containing 30, 60 and 90 per cent of the central stellar mass from left to right. The bulge-less galaxy is shown with the 30 per cent mass bulges. In each panel a vertical, black, dashed line indicates the smallest spatial scale considered for the fit, and the legend indicates the power law slope of each fit. All galaxies have a similar amount of power, but individual spectra are vertically offset from each other for visibility.

We first show example power spectra with the power law fit of Equation 3.2.3 for the suite of simulations at 600 Myr in Figure 3.3. Power spectra are depicted as solid lines, with the power law fit as a black, dashed line on-top. The shaded area around each line indicates the standard deviation of the azimuthal power in the two-dimensional power spectrum at any given spatial scale. This is assumed to be larger than the inherent uncertainty of the maps (Koch et al., 2020). The vertical dashed line indicates the smallest spatial scale considered for the fit. As detailed in Section 3.2.3 smaller scales are too affected by the beam to include them when fitting the power law.

Name	$\langle\beta\rangle$	time variation	$\langle\text{fit error}\rangle$	fit range [pc]
noB	1.84	0.09	0.11	83 – 1500
B_M30_R1	2.35	0.16	0.17	83 – 1500
B_M30_R2	1.78	0.09	0.16	83 – 1500
B_M30_R3	1.77	0.10	0.11	83 – 1500
B_M60_R1	2.69	0.06	0.14	83 – 1500
B_M60_R2	2.33	0.21	0.13	83 – 1500
B_M60_R3	1.89	0.10	0.11	83 – 1500
B_M90_R1	2.59	0.08	0.20	83 – 1500
B_M90_R2	2.58	0.04	0.14	83 – 1500
B_M90_R3	2.47	0.12	0.14	83 – 1500

Table 3.3: Results of the power law fit to the one dimensional power spectrum for all simulations. Column 2 lists the time-averaged best-fit slope. The standard deviation on the average over time is given in column 3, while column 4 shows the average uncertainty on the power spectrum fit.

The panels in Figure 3.3 represent the different bulge mass fractions of 30 (left), 60 (centre) and 90 (right) per cent. All simulated galaxies are well fitted by a single power law within the uncertainties of the azimuthal average. In each panel, the power spectrum slopes increase from the more extended ($R_b = 3$ kpc) to the more compact ($R_b = 1$ kpc) bulges. The slopes also increase from left to right, demonstrating that a more massive bulge with the same scale radius will result in a steeper power spectrum. This steepening of the power law is expected from an increasing lack of fragmentation (Grisdale et al., 2017). The trend shown in Figure 3.3 quantitatively confirms the qualitative observation that can be made from Figure 3.1: Namely, that galaxies with more compact and massive bulges, with higher central stellar surface density μ_* , host smooth central gas reservoirs in which fragmentation is suppressed, compared to the disc-dominated galaxies that have a clumpy and sub-structured ISM.

The power spectrum of the bulge-less galaxy is a mild outlier from the aforementioned trend, in that it has a slope that is steeper than that of one low μ_* , bulge-containing galaxy even accounting for the uncertainty of the fit. However, it is also the galaxy with the highest SFR of the sample (Gensior et al., 2020) and therefore receives the most SN feedback. The feedback contributes to the turbulence experienced by the gas (e.g. Krumholz et al., 2018) and will lead to a steeper slope in the bulgeless galaxy (see also e.g. Walker et al., 2014).

Table 3.3 summarises the time-averaged results of the power spectrum fit for all simulated galaxies. The trend seen in Figure 3.3 that galaxies with higher μ_* have steeper power spectra, holds true when averaged across 700 Myr, too. Next to the average slope, we quote both the standard deviation on the slope average as well as the average error on the slope fit for all simulations. For most of the sample, the variation in power spectrum slope over time is comparable to the average error on the power law fit. Only the most bulge-dominated galaxies have a noticeably smaller variation in slope over time. The larger time-variability of the power spectrum slope for the galaxies with low μ_* and a clumpy ISM indicates

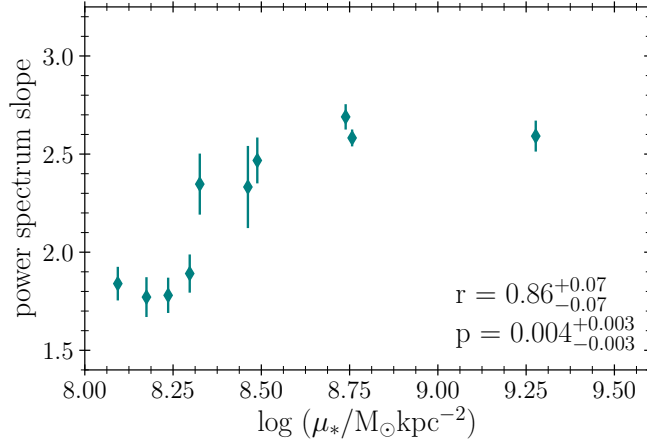


Figure 3.4: Time-averaged slope of the power law fits to the simulations (β) as a function of the galaxies central stellar surface density (μ_*). Error bars indicate the standard deviation of the best-fit power law slope over time. As indicated by the Spearman rank coefficient in the bottom right corner of the plot, there is a correlation between the slope of the power spectrum and the central stellar surface density of a galaxy.

that these clumps are transient structures, whose number and distribution changes over time leading to the variation in power spectrum slope. By contrast, the variation of the best-fit slope over time is smaller in high μ_* galaxies which have a very smooth ISM. A small variation in power spectrum slope over time is consistent with previous simulations (Bournaud et al., 2010; Grisdale et al., 2017). Table 3.3 also confirms that the average power spectrum slope of the noB run agrees with that of the runs B_M30_R3, B_M30_R2 and B_M60_R3 within the variation over time or the error on the fit.

To be more quantitative in linking the galactic gravitational potential and the power spectrum, we plot the power spectrum slopes as a function of central stellar surface density for all simulated galaxies in Figure 3.4. There is a clear trend of increasing power spectrum slope with increasing μ_* ⁹. We use the Spearman rank coefficient to assess the strength and statistical significance of this correlation. To take into account the uncertainty on the slopes (standard deviation over time), we perform 1000 Monte Carlo simulations assuming that each point is well described by a Gaussian distribution. This allows us to quote both rank coefficient and p-value with an uncertainty, as given by the average and 16th-to-84th

⁹Focussing on the three points with the highest central stellar surface densities, it appears as if the power spectrum slopes might flatten at $\log(\mu_*/M_\odot \text{kpc}^{-2}) \geq 8.75$. As described in more detail in Appendix B.3, we have performed additional simulations of isolated galaxies which populate the $8.75 < \log(\mu_*/M_\odot \text{kpc}^{-2}) < 9.3$ space and add an additional point at $\log(\mu_*/M_\odot \text{kpc}^{-2}) \approx 9.45$, to test this. Indeed, the additional power spectrum slopes are consistent with a much shallower trend, if not a complete flattening, at high central stellar surface densities. However, it is unclear whether this behaviour is physical in origin, or due to the inherent resolution limit of the simulations, as well as other parameter choices. Interestingly this flattening occurs at a slope of 2.6–2.7, which is close to the 2.66 expected of two dimensional Kolmogorov (1941) turbulence. If physical, this could indicate that there is a limit to how much fragmentation can be suppressed by shear before one reaches incompressible turbulence.

percentile of the Monte Carlo simulation. A Spearman coefficient of $r = 0.86_{-0.07}^{+0.07}$ with $p = 0.004_{-0.003}^{+0.003}$ confirms that the correlation between β and central stellar surface density is strong and statistically significant. This directly links the galactic gravitational potential to the suppression of fragmentation via the power spectrum slope. It confirms that the shear from a high μ_* potential does not only drive turbulence that suppresses star formation, but also tears apart clouds, and suppresses fragmentation. This is a strong prediction from the simulations to which we can compare the WISDOM observations.

3.3.2 Power Spectra of the Observations

Name	β	fit range [pc]
FRL 0049	3.02 ± 0.09	148 – 3387
NGC 0383	2.70 ± 0.46	83 – 1518
NGC 0404	2.33 ± 0.04	2 – 163
NGC 0524	2.05 ± 0.18	71 – 1243
NGC 1387	2.12 ± 0.10	70 – 944
NGC 1574	2.83 ± 0.11	26 – 192
NGC 4429	2.33 ± 0.22	24 – 809
NGC 4501	2.29 ± 0.11	90 – 816
NGC 4826	2.78 ± 0.22	9 – 177
NGC 5806	2.69 ± 0.29	60 – 1141
NGC 6753	2.81 ± 0.13	57 – 2325
NGC 6958	2.75 ± 0.44	42 – 692

Table 3.4: Power spectrum slope and fit error for all WISDOM galaxies, as well as the spatial range across which the power spectrum was fitted with the simple power law.

Figure 3.5 shows the individual power spectra of all the WISDOM galaxies considered in this paper. All spectra are plotted on the same spatial scale, both to make comparison easier and highlight the different spatial scales under consideration. Each panel contains an inset image of the centre-masked zeroth moment map on which the individual power spectrum was computed. The black, vertical, dashed line indicates the smallest spatial scale which was considered for the fit, and the navy, dashed line shows the power law fit to the power spectrum. We summarise the results of the 1D power spectra fits for the WISDOM galaxies in Table 3.4.

It is immediately apparent that only half of the galaxies (FRL 0049, NGC 0404, NGC 1387, NGC 1574, NGC 4429 and NGC 4826) are well described by a single power law. The other spectra show very pronounced bumps and breaks. In NGC 0383, NGC 0524 and NGC 5806 this is likely caused by the ring structures visible in the moment zero maps. NGC 4501 remains dominated by its bright centre, which is the likely cause for the bump in the spectrum at length scales of ~ 250 pc. Similarly, NGC 6753 possesses a very bright central region sitting in a very low density region which is itself surrounded by a low density gas disc with weak spiral arms. This likely gives rise to the complicated shape of the power

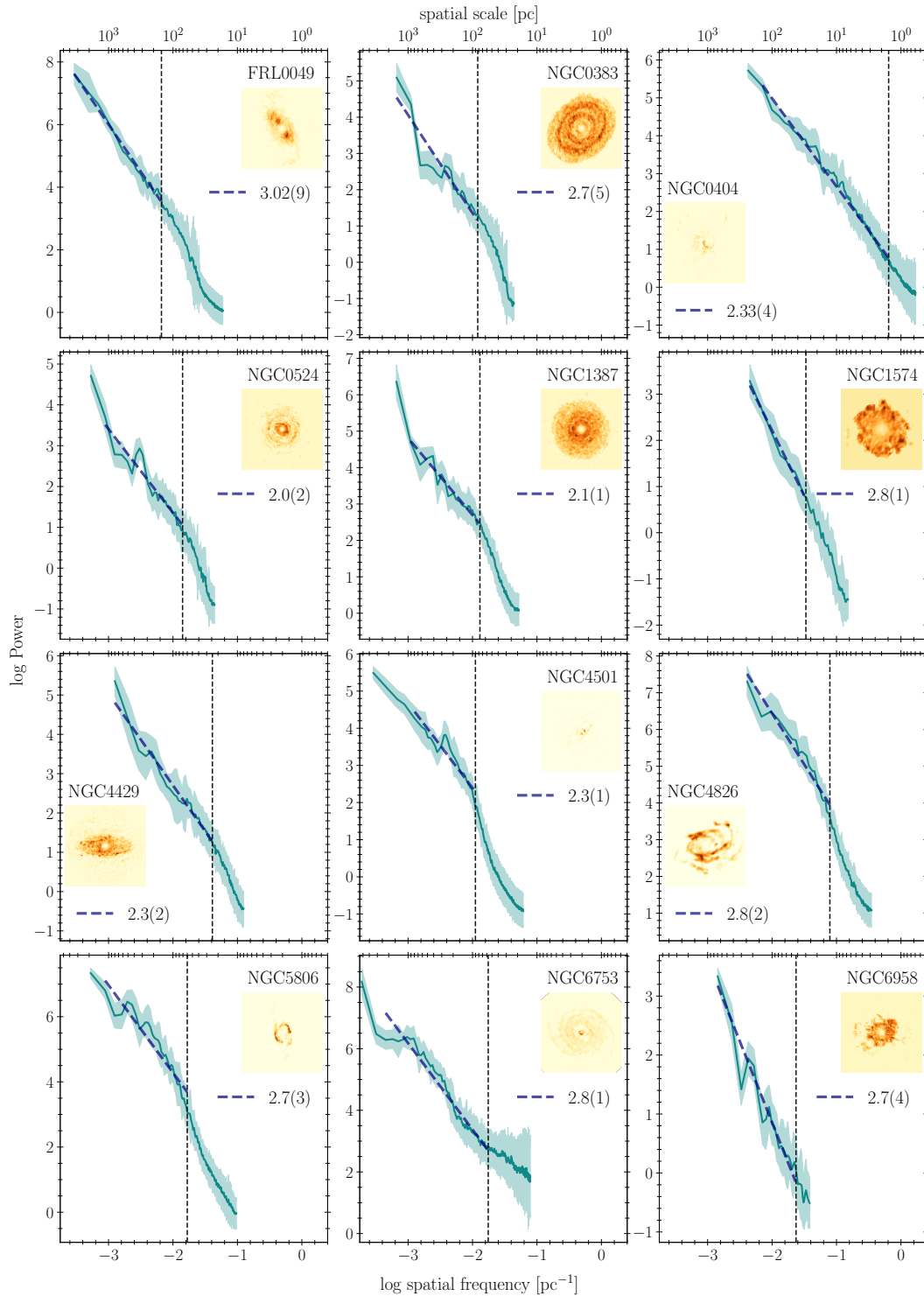


Figure 3.5: Power spectra of the WISDOM galaxies, plotted the same spatial scales for better comparison. The navy, dashed line shows the power law fit to each power spectrum, with the legend in the individual panels quoting the slope of the fit. The dashed black line in each panel indicates the smallest spatial scale which was considered for the fit. An inset image shows the centre-masked moment zero map of each galaxy, on which the power spectrum was computed.

spectrum which shows multiple break points.

We recompute the power spectra of the observations, allowing for a break. Comparing the Bayesian information criterion of the fits with and without a break yields only two galaxies, NGC 4826 and NGC 5806, that are better fit by a broken power law. A break in the density power spectrum is thought to indicate the scale height of the gas disc, as turbulence transitions from three-dimensional turbulence on small scales to two-dimensional turbulence on large scales (e.g. Dutta et al., 2009a). The break scale for NGC 4826 is at 27 pc, which would imply that it is an extremely thin gas disc. Scale heights of 31 ± 8 and 33 ± 8 pc have been measured for NGC 5907 and NGC 4565 respectively (Yim et al., 2014), but CO scale heights of ~ 100 – 200 pc are more common (Wilson et al., 2019). However, 27 pc approximately matches the size of the dense clumps visible in the zeroth moment map, which can plausibly cause the break. The break in NGC 5806 occurs at 190 pc and could be linked to the scale height. Alternatively, the fit might still be affected by the prominent ring structure.

In Figure 3.6 we show the WISDOM galaxies power spectrum slopes as a function of their central stellar surface density. Contrary to the clear trend seen in for the simulations in Figure 3.4, the slopes of the observed galaxies are much more scattered with respect to μ_* . For example, FRL 0049 has the steepest power spectrum with a slope of 3.02, while NGC 0524 has the shallowest with a slope of 2.05, but both galaxies have a central stellar surface density of $\log(\mu_*/M_\odot\text{kpc}^{-2}) \sim 9.3$. Discrepancies between the slopes of other galaxies with similar central stellar surface densities are somewhat smaller, like 0.45 between NGC 4429 and NGC 5806 or 0.63 for NGC 1387 and NGC 6958, but nonetheless a clear deviation from the prediction of the simulations. There is a very shallow decreasing trend of power spectrum slope with the central stellar surface density for these WISDOM observations, but it is not statistically significant. Neither for the whole data set ($r = -0.10^{+0.18}_{-0.18}$,

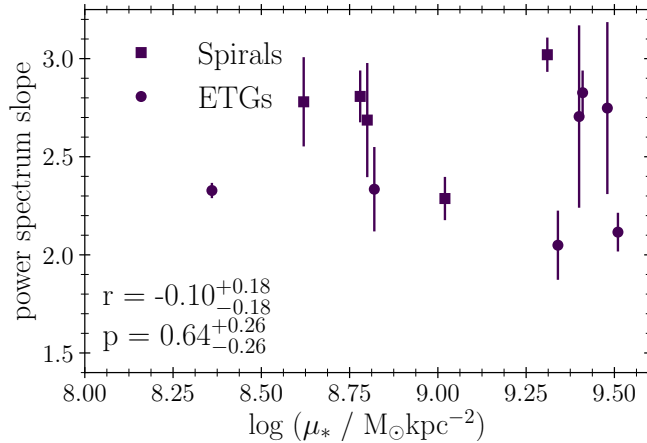


Figure 3.6: Slope of the power law fits to power spectra of the WISDOM galaxies as a function of central stellar surface density (μ_*). The error bars indicate the error on the power spectrum fit. There is no correlation between the slope of the power spectra and the central stellar surface density of the galaxies.

$p = 0.64_{-0.26}^{+0.26}$), nor for the sub-set of spiral galaxies ($r = 0.07_{-0.40}^{+0.20}$, $p = 0.72_{-0.24}^{+0.13}$) or ETGs ($r = 0.10_{-0.21}^{+0.11}$ with $p = 0.71_{-0.23}^{+0.18}$). This could in part stem from the unsuitability of some observations to fitting a single power law to their power spectrum. Alternatively, it could imply that the flattening seen for the simulations at high μ_* is physical, with the observations scattering around the part of parameter space in which it occurs. We will discuss this behaviour in more depth in Section 3.4.2. However, before doing so we wish to investigate whether the power spectrum slopes of the WISDOM galaxies are correlated with other physical quantities.

3.4 Discussion

3.4.1 Correlations with the Slopes of WISDOM Power Spectra?

In an attempt to find the underlying driver of turbulence in the observations, we have tested the correlation between the power spectrum slope and a large number of properties. Some are observational (the beam size, the extent of the fit, the lower limit of the fit, the sensitivity of observations), while others are properties of the galaxy (gas mass, extent of the gas reservoir, central gas surface density, stellar mass, gas fraction, ratio of gas-to-stellar extent, ratio of central gas-to-stellar surface density, SFR, specific SFR). The table listing all Spearman rank coefficients and the corresponding p-values can be found in Appendix B.4. If we define $p \leq 0.1$ as statistically significant, we find a single correlation (with central gas surface density) for the observations. This, as well as some other properties of interest will be discussed in more detail in the following subsections.

3.4.1.1 Sensitivity of the Observations

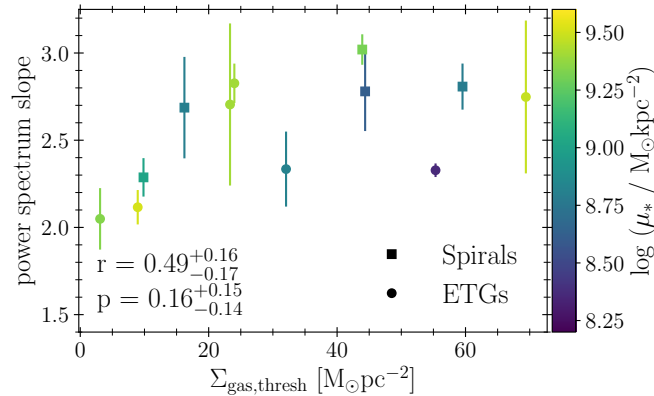


Figure 3.7: Slope of the power law fits to the power spectra of the WISDOM galaxies as a function of the sensitivity limit of the observations. The points are colour-coded by their central stellar surface density, μ_* , and the error bars show the uncertainty on the power law fit. There is a trend between power spectrum slope and the sensitivity limit of the observations, but it is not statistically significant.

Firstly, we investigate what effect the sensitivity of the observations has on the slope of the power spectra. Koch et al. (2020) highlight that observational effects can influence the power spectrum, even on scales larger than the beam. With sensitivity limits that differ by nearly two orders of magnitude, ranging from 3 (NGC 0524) to $70 \text{ M}_{\odot} \text{pc}^{-2}$ (NGC 6958), it is worth examining whether this affects the power spectrum. Indeed, Figure 3.7 shows a trend between the minimum surface density of gas that the observations are sensitive to and the slope of the resultant power spectrum. The power spectrum steepens the lower the sensitivity. Furthermore, considering both spirals and particularly ETGs individually, the galaxies with lower sensitivity but shallower power spectra are those of the sample which have a lower central stellar surface density. This admits the possibility that the relation between β and $\Sigma_{\text{gas,thresh}}$ might be masking an underlying trend between the power spectrum slopes and μ_* . This correlation has a Spearman rank coefficient of $r = 0.49^{+0.16}_{-0.17}$ and a $p = 0.16^{+0.15}_{-0.14}$, making it statistically not significant. To test if our results were affected, we have performed the observational analysis with all zeroth moment maps clipped to a surface density limit of $70 \text{ M}_{\odot} \text{pc}^{-2}$, to mimic uniform sensitivity. This crude approximation had a negligible effect on the relation between power law slopes and central stellar surface density shown in Figure 3.6. Despite that, we advise to be mindful of this when comparing power spectra of a heterogeneous set of observations.

3.4.1.2 Gas Fraction

Dynamical suppression has a strong dependence on the gas fraction of galaxies (Martig et al., 2013; Gensior and Kruijssen, 2021). Additionally, Gensior and Kruijssen (2021) demonstrate that the morphology of the circumnuclear gas reservoir can be strongly affected by the gas-to-stellar mass ratio of the galaxies. At fixed (high) central stellar surface density, the smooth circumnuclear gas disc decreased in extent until finally becoming porous and

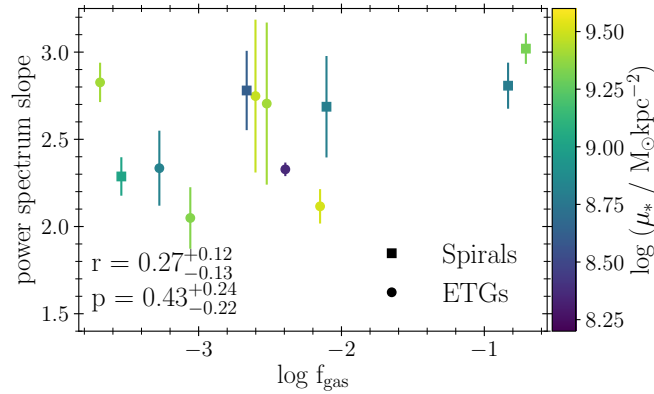


Figure 3.8: Slope of the power law fits to the power spectra of the WISDOM galaxies as a function of the molecular gas-to-stellar mass ratio, f_{gas} . The points are colour-coded by their central stellar surface density, μ_* , and the error bars show the uncertainty on the power law fit.

sub-structured like the rest of the ISM for gas-to-stellar mass ratios ranging from 1 to 20 per cent. For simplicity we have restricted ourselves in this study to the analysis of the Gensior et al. (2020) simulations with a constant gas-to-stellar mass ratio, but the observed galaxies have a range of gas fractions. Therefore, we investigate the molecular gas-to-stellar mass ratio of the WISDOM galaxies in relation to their power spectrum slopes in Figure 3.8, with the points colour-coded by their μ_* . However, as evidenced by the Spearman rank coefficient of $r = 0.27_{-0.13}^{+0.12}$ with a $p = 0.43_{-0.22}^{+0.24}$ we do not find a trend of statistical significance. There is also no uniform secondary trend in which the steeper slopes correspond to galaxies with higher μ_* , in contrast to the prediction from the simulations.

3.4.1.3 Specific Star Formation Rate

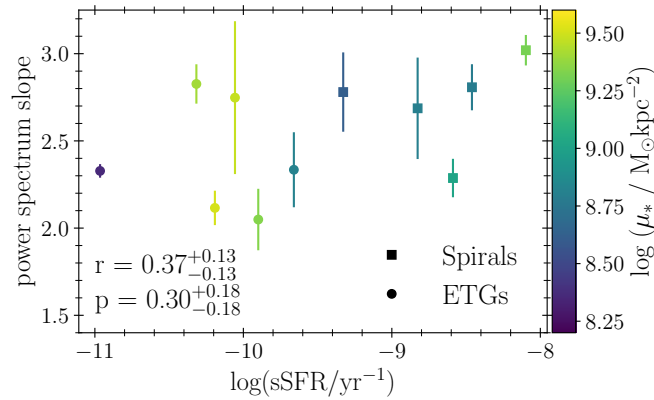


Figure 3.9: Slope of the power law fits to the power spectra of the WISDOM galaxies as a function of the specific star formation rate (sSFR). The points are colour-coded by their central stellar surface density, μ_* , and the error bars show the uncertainty on the power law fit.

The SFR is another quantity of interest as one of the primary drivers of feedback and thus turbulence. Here we examine whether there is a correlation between the power spectrum slope and the specific SFR (sSFR, the SFR normalised by the stellar mass of a galaxy) of the eleven WISDOM galaxies for which SFRs have been measured. Figure 3.9 shows that there is no trend between the power spectrum slope and the sSFR of a galaxy. This is affirmed by a Spearman coefficient of $r = 0.37_{-0.13}^{+0.13}$ with $p = 0.30_{-0.18}^{+0.18}$.

3.4.1.4 Central Gas Surface Density

We now examine the central gas surface density, μ_{gas} , which we calculate like μ_* in Equation 3.2.2. We use the molecular gas mass from Table 3.1 and estimate the half-light radius of the gas as the radius of a circle placed on the centre of the zeroth moment map that includes half of the total measured emission. Figure 3.10 shows the power spectrum slope as a function of μ_{gas} , as in previous plots colour-coded by μ_* . The observations show a trend

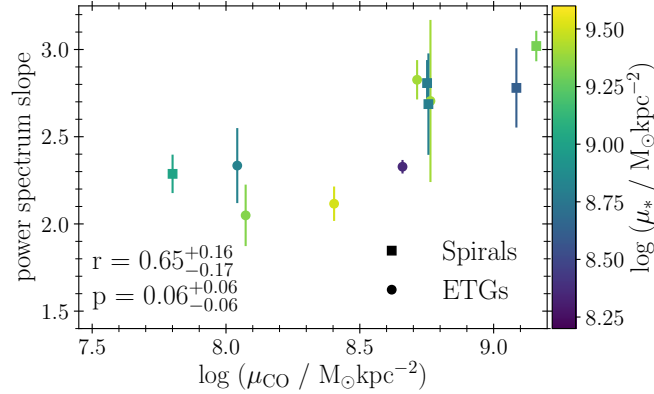


Figure 3.10: Slope of the power law fits to the power spectra of the WISDOM galaxies as a function of the central molecular gas surface density, μ_{gas} . The points are colour-coded by their central stellar surface density, μ_* , and the error bars show the uncertainty on the power law fit. There is a trend that might be statistically significant between power spectrum slope and central gas surface density.

of steeper power spectra with increasing central gas surface density. This correlation has a rank coefficient of $r = 0.65^{+0.16}_{-0.17}$ with $p = 0.06^{+0.06}_{-0.06}$, making it (marginally) statistically significant. This correlation implies that the central concentration of gas is more important in setting the ISM physics than its relative abundance with respect to the stars or the stellar potential. However, the differences in the sensitivity of the observations (see Table 3.2 and Section 3.4.1.1), affect the trend found here¹⁰. Therefore, a large(r), more homogeneous sample of observations is required to see whether this correlation between power spectrum slope and central gas surface density holds. The simulations do not show any trend with μ_{gas} due to the small dynamic range of central gas surface densities, caused by the great similarity of the flat surface density profiles in the inner kpc (see Figure 2.8 in Chapter 2).

3.4.1.5 Ratio of Central Gas-to-Stellar Surface Density

Finally, we consider the dependence of the power spectrum slope on the ratio of central gas-to-stellar surface density in Figure 3.11. There is a trend of steeper power spectrum slopes with increasing central gas-to-stellar surface density. However, it is weaker than the correlation with μ_{gas} and not statistically significant (Spearman $r = 0.51^{+0.12}_{-0.11}$, $p = 0.11^{+0.08}_{-0.08}$). Given the weak anti-correlation found between power spectrum slope and central stellar surface density in Figure 3.6, it likely may partially wash out the trend β and μ_{gas} . This implies that for the WISDOM galaxies the potential of the gas determines the slope of the power spectrum (and by extension the ISM turbulence). Conversely, the depth of the stellar potential (and shear induced turbulence) seem to have a smaller effect on these galaxies. This is highlighted by the fact that for every possible correlation discussed in this

¹⁰ Σ -clipping the observations weakens the trend and makes it statistically insignificant ($r = 0.45^{+0.13}_{-0.16}$, $p = 0.19^{+0.21}_{-0.09}$).

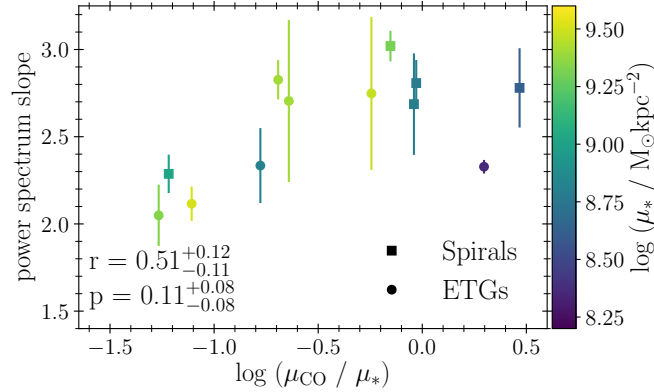


Figure 3.11: Slope of the power law fits to the power spectra of the WISDOM galaxies as a function of the ratio between central molecular gas-to-stellar surface density, μ_{gas}/μ_* . The points are colour-coded by their μ_* and the error bars show the uncertainty on the power law fit.

Section (3.4.1) there are no uniform secondary trends with μ_* for galaxies with different power spectrum slopes. Studying the velocity spectra of these galaxies could provide more insight into the discrepancies of in density power spectrum slopes for galaxies with visually similar discs and similar galactic properties, which we plan to do in a future study (Davis et al. in preparation).

3.4.2 Differences between Observations and Simulations

Figure 3.12 combines Figure 3.4 and Figure 3.6, showing the power spectrum slopes of simulations and observations as function of central stellar surface density. Shear induced by a deep gravitational potential is the main driver of turbulence in the simulations, as indicated by the trend of steeper power spectra as a function of μ_* . The observations with central stellar surface densities in range $8.3 \geq \log(\mu_*/M_*\text{kpc}^{-2}) \leq 8.8$ largely follow the simulated data. However, as pointed out in Section 3.3.2, instead of even steeper power spectra or a flattening of the trend for WISDOM observations with larger central stellar surface densities, the other eight galaxies are scattered in $\beta - \mu_*$ space with a shallow decreasing trend. Nonetheless, they remain broadly consistent with the simulations. In the remainder of this subsection, we wish to further discuss differences between the simulations and the observations that could contribute to the more nuanced picture with larger scatter of the observations.

It should be kept in mind that what we simulate are idealised galaxies in isolated boxes, where the only difference between them is the distribution of the stellar matter. Thus their only sources of turbulence are shear, (self-)gravity and SN feedback. The simulated galaxies have not evolved over a Hubble time in a cosmological setting, i.e. never accreted gas from the cosmic web, undergone mergers or interactions with other galaxies, and by construction do not contain black holes. In contrast to that, all of the WISDOM galaxies host an SMBH, which is active in some of them (e.g. FRL 0049, NGC 0383, NGC 6753). Although the

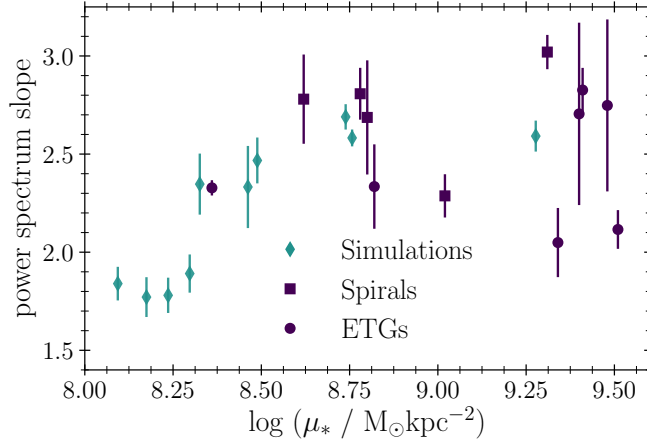


Figure 3.12: Power spectrum slopes of the simulations (teal) and the WISDOM observations (purple) as a function of central stellar surface density μ_* . Error bars signify the variation over time (simulations) or the error on the fit (observations).

radio-jet of NGC 0383 does not appear to have an impact on the gas disc or velocity field visually (North et al., 2019), it is unclear whether it would affect the power spectrum. To our knowledge, the impact of an active galactic nucleus on the power spectrum of a galaxy has not yet been investigated. The SMBHs radius of influence tends to be comparable to the lower spatial limit of the power spectrum fit, so its influence on the potential should therefore have little bearing on our results. However, it remains difficult to estimate the effect of the active SMBH on the power spectrum from the observations.

Cluster membership and related effects on galaxies can affect their power spectra: Investigating the power spectrum of Virgo cluster galaxy NGC 4254, Dutta et al. (2010) found that the power spectrum slope varies between different regions (inner vs. outer) of the galaxy, which also affected the velocity integrated power spectrum. Dutta et al. (2010) attribute this difference to galaxy harassment. As most of the WISDOM galaxies presented here are members of a galaxy group or cluster, this could contribute to the scatter in their power spectrum slopes and in the poor quality of the fit for some. It is also important to capture the effect of galaxy interactions and cosmological evolution in simulations, as evidenced by the density power spectrum slope comparison between observations and simulations of the SMC. With a (large scale) slope of 1.7, Grisdale et al. (2017) find a much shallower power law for their simulated SMC than Stanimirovic et al. (1999), who obtain a slope of 3.04 from HI observations. Grisdale et al. (2017) argue that this discrepancy is the result of running an isolated galaxy simulation which lacks tidal effects from galaxy interactions.

In short, while there is broad agreement between the simulations and the WISDOM observations, the discrepancies are likely the result of several factors. The observational heterogeneity (e.g. sensitivity, see Section 3.4.1) could dilute the effect of the stellar potential on the power spectrum slope, in combination with additional effects not captured by the simulations. A larger, more homogeneous sample of observations might be able to

address some of these issues. Similarly, high resolution cosmological zoom-in simulations might be able to produce a more realistic comparison.

3.4.3 Comparison with the Literature

3.4.3.1 Simulations

Over the past decade, power spectra have been used to assess the necessity for and quality of feedback models in simulations. Most of these show a break in the power spectrum on scales of several tens of pc to 1 kpc (e.g. Bournaud et al., 2010; Combes et al., 2012; Renaud et al., 2013; Walker et al., 2014; Grisdale et al., 2017 although the power spectrum break in Renaud et al., 2013 is on a much smaller scale of around 1 pc). Unlike these, the power spectra of our simulations are well described by a single power law, better comparable to the two runs with less intense feedback of Walker et al. (2014). The (large-scale, in case of broken power law fits) slopes range from 0.67 (Renaud et al., 2013) to 4.5 (Pilkington et al., 2011), although they mostly range from 1.3 to 2.6 (Bournaud et al., 2010; Combes et al., 2012; Walker et al., 2014; Grisdale et al., 2017) for runs with stellar feedback. This is in good agreement with the slopes we find for the simulated power spectra here (1.8–2.7). A trend in all aforementioned simulations in the literature is the steepening of the power spectra in simulations with (more) feedback. This might seem counter-intuitive compared to our result of steeper power spectra with increasing suppression of fragmentation and therefore suppression of star formation and the subsequent feedback. However, there is a simple explanation for this: Both strong feedback and the shear from the gravitational potential have the same effect. The shear-driven turbulence shifts the power in the gas from smaller to larger scales by suppressing fragmentation and the formation of GMCs. Similarly, strong feedback destroys clouds more effectively thereby also shifting the power from smaller to larger scales, steepening the power spectrum (e.g. Pilkington et al., 2011; Walker et al., 2014). We also find some indication to the effect of feedback in our simulated galaxies. Figure 3.4 shows that the bulge-less galaxy has a steeper power spectrum than a couple of other low μ_* galaxies. This is a direct consequence of its higher SFR (cf. Figures 2.14 and 2.15).

3.4.3.2 Observations

A variety of tracers have been used in the study of extragalactic power spectra. However, only M 31 (Koch et al., 2020) and M 33 (Combes et al., 2012; Koch et al., 2020), have been previously analysed in CO. With slopes of 1.59 for M31 and 1.5 Combes et al. (2012) or 0.91 Koch et al. (2020) for M 33, these are much shallower than those we find for the WISDOM galaxies presented here. If the ISM turbulence is truly scale-free, then it should not matter that the length scales considered are vastly different. The M 31 and M 33 data ranges from hundreds of pc to several tens of kpc, whereas the circumnuclear gas reservoir in some of our galaxies only spans a few hundred parsecs, and even in the most extreme case the largest length scale considered is 3.4 kpc. However, like Koch et al. (2020), we find that the morphology of the gas disc is important in determining the power spectrum slope

and shape. With often only a small disc detected, it is therefore difficult to compare¹¹. Encouragingly Miville-Deschênes et al. (2010) and Pingel et al. (2018) find power spectrum slopes of 2.7 when using dust and CO emission to study regions within the Milky Way, which is in better agreement with the slopes of the WISDOM galaxies than Combes et al. (2012) and Koch et al. (2020).

The power spectrum slopes of our galaxies are more comparable to those often observed in HI, which tend to lie in the range of 1.5 to 3.0 (e.g. Dutta et al., 2009b; Zhang et al., 2012; Dutta et al., 2013; Walker et al., 2014; Grisdale et al., 2017; Koch et al., 2020, and references therein). This raises an interesting question, namely whether HI power spectra of the WISDOM galaxies would be steeper or shallower than their CO counterparts. Turbulent theory predicts that the molecular gas should have a steeper slope than the atomic counterpart (Romeo et al., 2010), but Koch et al. (2020) find that for M31 and M33 the HI spectra are steeper. With the extremes of the HI power spectrum slopes at 0.3 Dutta et al. (2013) and 4.3 Zhang et al. (2012), both steeper and shallower HI power spectra for the WISDOM galaxies would not be without precedence¹².

We do not see an indication for a ubiquitous break in the power spectrum that would indicate a transition from turbulence in the plane of the galaxy to three-dimensional turbulence at the scale height of the galaxy (e.g. Dutta et al., 2009a). Instead the morphological features specific to the galaxies (such as rings) show up as bumps or wiggles in the power spectrum. Only two galaxies would be better described by a broken power law. For NGC 4826 the break scale appears around the size of the bright clumps within the gas disc, making it more likely that the break in the power spectrum indicates a transition from turbulence in the large-scale ISM to the largest fragments. The break in NGC 5806 could be around the disc scale height, but it might also be caused by the effect of the dominant ring on the power spectrum. In general we find that the morphology of the gas is important in determining the power spectrum shape, in good agreement with Koch et al. (2020).

The lack of a correlation between the power spectrum slopes of the WISDOM galaxies and their sSFR matches the current picture in the literature. Zhang et al. (2012) find a tentative anti-correlation between SFR and power spectrum slope for their dwarfs with a B-band magnitude lower than -14.5, but none for the entire sample. Similarly, Dutta et al. (2009b) see tentative evidence for a tentative correlation with the SFR in five dwarf galaxies, but find only scatter for a larger sample of 18 late-type galaxies (Dutta et al., 2013). The trend of steeper power spectrum slopes with increasing central gas surface density we find for the WISDOM galaxies seems somewhat more controversial. On the one hand, Koch et al. (2020) argue that the shallow power spectrum they find for M 33 is caused by the central concentration of CO within the inner 2 kpc. On the other hand, the behaviour of the WISDOM galaxies matches what Walker et al. (2014) find for their simulations. There, both of the galaxies with an exponential HI surface density profile have a steeper power spectrum than the galaxy that evolved to have a flat HI surface density profile from the

¹¹We see evidence from the simulations that including a larger region in the power spectrum fit leads to a flattening of the power spectra, as more of the clumpy, sub-structured ISM is included.

¹²However, only 10 per cent of the ETGs in clustered environments show signatures of HI (e.g. Serra et al., 2012), so HI power spectra are likely only possible for field ETGs.

same initial conditions (Walker et al., 2014).

Lastly, as previously highlighted by Koch et al. (2020), we find that the observational factors are important. The power spectrum slopes show a trend with the sensitivity of our observations, which also affects the correlation with the central gas density we find (through its impact on the measured gas masses). Even though beam size (map resolution), inclination and surface density thresholds do not qualitatively affect the trend with central stellar surface density displayed by the power spectra of the simulations¹³, they make a small quantitative difference. Similarly the discrepancy in spectral index between smoothing the simulated map with a Gaussian beam or a mock interferometric beam¹⁴ highlights how sensitive the absolute value of the power spectrum slope is to how the data was taken and the method of analysis. This makes it doubly difficult to compare results with(in) the literature, and draw sound conclusions, as some discrepancies might be purely methodology dependent (see also Zhang et al., 2012).

3.5 Summary and Conclusions

In this paper, we have analysed the density power spectra of the circumnuclear gas reservoir in 10 isolated, simulated galaxies from Gensior et al. (2020) and 12 galaxies from the WISDOM project (e.g. Onishi et al., 2017), making it the largest sample of CO extragalactic power spectra studied to date. The simulated galaxies range from disc galaxy to spheroid, at a fixed gas to stellar mass ratio of 5 per cent. Their circumnuclear gas reservoir becomes increasingly smooth with increasing μ_* , as the bulge-dominance increases. The WISDOM galaxies comprise a mix of late- and early-type galaxies, some of which have very sub-structured, others very smooth gas reservoirs. We compute the azimuthally-averaged, one dimensional power spectrum of the surface density, which is sensitive to the turbulent forcing in the gas. Our findings are summarised below:

1. There is a strong correlation between the power spectrum slope (β) and the central stellar surface density (μ_*) of the simulations. The power spectra are steeper in galaxies with higher μ_* and smoother central gas reservoirs. This confirms that the shear induced by the gravitational potential results in the dynamical suppression of fragmentation.
2. The flattening of the power spectrum slopes at $\log(\mu_*/M_\odot\text{kpc}^{-2}) \geq 8.75$ to a constant value of 2.6–2.7 could be physical or an artefact caused by the inherent resolution of the simulation and other parameter choices. If the flattening is physical, the close correspondence with the slope of two-dimensional Kolmogorov (1941) turbulence (2.66) could indicate that high shear eventually drives incompressible turbulence.
3. Contrary to the simulations, the observations do not show a trend between power spectrum slope and central stellar surface density as a whole, nor divided into sub-samples of early- and late-type galaxies. However, the majority of the WISDOM galaxies have $\log(\mu_*/M_\odot\text{kpc}^{-2}) \geq 8.75$, power spectrum slopes scattering around the simulations

¹³For more details on these tests, please refer to Appendix B.2.

¹⁴Please refer to Appendix B.1 for more detail.

where they show a flattening of β with μ_* . This could indicate that the flattening is physical in origin. The large scatter in the observational slopes likely results from a combination of physical effects not captured in the simulations which the power spectrum, observational heterogeneity and different gas morphologies (e.g. rings and spiral arm structure) affecting the quality of the power spectrum fit.

4. Out of all the properties we test for, we only find a (marginally) statistically significant correlation between the power spectrum slope and the central gas surface density of the WISDOM observations. Although this depends on the sensitivity of the observations, this suggests that the potential of the gas, rather than the stellar gravitational potential may shape the ISM and be the dominant driver of turbulence.

We demonstrate using isolated galaxy simulations that the shear and turbulence induced by a spheroidal component that dominates the gravitational potential can suppress fragmentation, resulting in a steep density power spectrum. The observations of 12 WISDOM galaxies show a more nuanced picture, and their power spectrum slopes depend most strongly on the central gas concentration. However, the heterogeneity of the observations and the sometimes poor description of a galaxy's power spectrum by a power law make it difficult to make any strong statements. Velocity power spectra of the WISDOM galaxies could further elucidate the turbulent mechanisms and possible discrepancies between galaxies with similar properties and different density power spectrum slopes. Power spectra of a larger, more homogeneous sample of observations are required to firmly determine if the tentative correlation we found in the WISDOM sample holds true (Gensior et al. in preparation, for a similar study of the PHANGS sample of galaxies). In addition, high resolution cosmological (zoom) simulations that resolve the cold ISM in sufficient detail could shed more light on density power spectra from the theoretical side.

Chapter 4

The Elephant in the Bathtub: when the physics of star formation regulate the baryon cycle of galaxies

Authors:

Jindra Gensior and J. M. Diederik Kruijssen

This chapter has been published in similar form in *MNRAS*, 500, 2000 (2021).

Jindra Gensior is the principal author of this article. The original idea stems from a discussion between the authors. Jindra Gensior designed and generated the initial conditions for and ran the simulations, performed all analysis, produced all figures and wrote the manuscript. Both authors collaborated with corrections and suggestions to the manuscript, and Jindra Gensior performed the last improvements during the review process.

Abstract

In simple models of galaxy formation and evolution, star formation is solely regulated by the amount of gas present in the galaxy. However, it has recently been shown that star formation can be suppressed by galactic dynamics in galaxies that contain a dominant spheroidal component and a low gas fraction. This ‘dynamical suppression’ is hypothesised to also contribute to quenching gas-rich galaxies at high redshift, but its impact on the galaxy population at large remains unclear. In this chapter, we assess the importance of dynamical suppression in the context of gas regulator models of galaxy evolution through hydrodynamic simulations of isolated galaxies, with gas-to-stellar mass ratios of 0.01–0.20 and a range of galactic gravitational potentials from disc-dominated to spheroidal. Star formation is modelled using a dynamics-dependent efficiency per free-fall time, which depends on the virial parameter of the gas. We find that dynamical suppression becomes more effective at lower gas fractions and quantify its impact on the star formation rate as a function of gas fraction and stellar spheroid mass surface density. We combine the results of our simulations with observed scaling relations that describe the change of galaxy properties across cosmic time, and determine the galaxy mass and redshift range where dynamical suppression may affect the baryon cycle. We predict that the physics of star formation can limit and regulate the baryon cycle at low redshifts ($z \lesssim 1.4$) and high galaxy masses ($M_* \gtrsim 3 \times 10^{10} M_\odot$), where dynamical suppression can drive galaxies off the star formation main sequence.

4.1 Introduction

The past 10-15 years have brought major progress in understanding the scaling relations describing the galaxy population. Star-forming galaxies are organised along the star formation main sequence (SFMS; see e.g. Noeske et al. 2007b; Peng et al. 2010), which is a tight relation between galaxy mass and star formation rate (SFR). The main source of progress has been the development of simple models describing the baryon cycle of galaxies as they evolve over cosmic time. These models relate the galactic-scale processes of star formation and stellar feedback to gas accretion onto dark matter haloes. A family of galaxy evolution models referred to as ‘bathtub’ or ‘gas-regulator’ models (e.g. Finlator and Davé, 2008; Bouché et al., 2010; Dekel et al., 2013; Lilly et al., 2013) do this by parametrising these complex physical processes in simple, analytically-solvable equations. In these models, the gas inflow onto a galaxy determines its properties and evolution. Star formation is solely dependent on the presence of cold gas that is converted into stars with a constant efficiency, as observed in most star-forming galaxies (e.g. Kennicutt, 1998b; Leroy et al., 2013). The star formation rate is thus regulated by the balance between gas inflow and the stellar feedback-driven outflow (Hopkins et al., 2011; Agertz et al., 2013).

Gas-regulator models are particularly compelling, because they allow one to interpret observational results and make predictions for the evolution of the galaxy population without requiring sophisticated semi-analytic models or full hydrodynamic simulations. For instance, they have been highly successful in reproducing and explaining scaling relations

relating to the chemical enrichment of galaxies, like the mass-metallicity relation (Lequeux et al., 1979; Tremonti et al., 2004) or the mass-metallicity-SFR relation (Mannucci et al., 2010). By contrast, the specific SFR (sSFR, the SFR normalised by the stellar mass of the galaxy) is reproduced well by regulator models at redshift $z \geq 3$, but discrepancies arise at lower redshifts (Dekel and Mandelker, 2014). Furthermore, gas-regulator models are focused on the star-forming population of galaxies, and it is not clear how they extend to the quiescent population of galaxies that are (in the process of being) quenched. Peng and Maiolino (2014) suggest that this population could be accounted for by simply lowering the value of the star formation efficiency, which is otherwise assumed to be constant.

In the gas-regulator framework, the quenching of galaxies is a direct result of no longer hosting a reservoir of cold, molecular gas. This can be achieved through heating by active galactic nuclei (AGN) or by expelling the available gas (see e.g. Bower et al., 2006; Croton et al., 2006; Fabian, 2012; Lacerda et al., 2020). Gas supplies can also be depleted through strangulation (Larson et al., 1980) or halo quenching (Dekel and Birnboim, 2006). In galaxy clusters or groups, galaxies can be quenched by external effects removing the gas, such as ram pressure stripping (Gunn and Gott, 1972) or harassment (Moore et al., 1996). However, it remains a major open question how galaxies quench and remain quiescent while retaining (a substantial amount of) molecular gas (e.g. Davis et al., 2014), especially in isolated galaxies that do not experience strong AGN feedback. This cannot be accomplished through halo quenching on its own, because in that case galaxies should remain star-forming until all their molecular gas is depleted, contrary to the observations. Martig et al. (2009) proposed that a galaxy’s gaseous component may be stabilised against gravitational collapse and star formation by the presence of a dominant spheroidal component. This process was originally dubbed ‘morphological quenching’ and has been put forward as a possible quenching mechanism in spheroid-dominated galaxies. In this picture, the spheroid’s gravitational potential increases the shear experienced by the gas, which in turn enhances its velocity dispersion and its Toomre (1964) Q parameter. This prevents the fragmentation of the gas into dense clouds and subsequently suppresses star formation.

Isolated, early-type galaxies in the local Universe exhibit SFRs per unit molecular gas mass that are suppressed compared to late-type galaxies (compare Bigiel et al., 2008; Davis et al., 2014). It has been proposed that morphological quenching is responsible for the inefficient star formation in early-type galaxies (Martig et al., 2013; Davis et al., 2014). Morphological quenching has also been invoked as a quenching mechanism at intermediate redshifts of $0.6 \lesssim z \lesssim 1.2$ for galaxies with compact central bulges (Kim et al., 2018), and to explain the existence of two gas rich post-starburst galaxies at $z \sim 0.7$ (Suess et al., 2017). Genzel et al. (2014) showed that the Toomre Q parameter increases towards the centres of galaxies at $z \sim 2$ and interpreted this as an early sign of morphological quenching. Similarly, a number of studies have related the SFRs of galaxies at $z \sim 2-3$ to their morphologies and hypothesise that morphological quenching is at least partially responsible for the quiescent galaxy population (e.g. Wuyts et al., 2011; Barro et al., 2013; Huertas-Company et al., 2015; Barro et al., 2017).

In Genzior et al. (2020), we set out to rigorously explore the phenomenological concept

of morphological quenching¹ by running a suite of isolated galaxy simulations with a sub-grid star formation model that relates the star formation efficiency to galactic dynamics via a dependence on the virial parameter of the gas. The parameter space spanned by these simulations ranges from disc galaxies to spheroids and was designed to assess whether a dominant bulge component would be able to induce turbulence and suppress star formation in the galaxy, for Milky Way-mass galaxies with a gas to stellar mass ratio of $M_{\text{gas}}/M_{\star} = 0.05$. In particular, we showed that the shear induced by the deep potential well of the bulge can drive up the gas velocity dispersion sufficiently to render the gas supervirial, thereby suppressing star formation in the central region. This tested and confirmed the hypothesis of Martig et al. (2009) that the median velocity dispersion of the gas increases towards the galactic centre in the presence of a bulge (Gensior et al., 2020). Both the increase in velocity dispersion and the subsequent suppression of star formation are enhanced at higher stellar surface densities (μ_{\star}), which is a proxy for the dominance of the bulge in the galactic potential. This is consistent with the dearth of star formation observed in a post-starburst galaxy with a gas fraction of 5 per cent by Suess et al. (2017) and also agrees with the result of Kretschmer and Teyssier (2020), who found that dynamical suppression is sufficient to quench a galaxy in a cosmological zoom-in simulation following a merger-driven starburst and subsequent gas expulsion.

In the context of the aforementioned gas-regulator models, these results raise a critical question: is there any part of the galaxy population for which the physics of star formation can dominate the baryon cycle through dynamical suppression? If the answer is affirmative, this would necessitate the extension of gas-regulator models with an environmentally-dependent star formation efficiency, such that the SFRs of galaxies are not exclusively set by their gas accretion rates.

There are suggestions in the literature that dynamical suppression is sensitive to the gas fraction of the galaxy and ineffective if the galaxy has a large, or continuously replenishing gas reservoir. For instance, Martig et al. (2013) only report a suppression of star formation for their galaxy simulated with a gas fraction of 1.3 per cent, but not for their galaxy with a gas fraction of 4.5 per cent. However, their simulations use a constant star formation efficiency, which leads to galaxies with approximately the same SFR even if μ_{\star} differs by ~ 0.7 dex. With this insensitivity to the galactic potential, simulations with a constant star formation efficiency consequently do not accurately reproduce the observed star formation suppression of spheroid-dominated galaxies (Gensior et al., 2020). None the less, it is plausible that the dynamical suppression of star formation is only triggered below some threshold gas fraction, where the gas no longer dominates the local gravitational potential. Indeed, simulations with more sophisticated sub-grid star formation models yield similar behaviour. Simulations of reionization with dynamics-dependent star formation indicate that at extremely high redshift ($z > 5.7$), with gas fractions exceeding 50 per cent, the time-averaged star formation rate remains unaffected by the build-up of a bulge component (Trebitsch et al., 2017). Likewise, Su et al. (2019) performed simulations of isolated

¹We will exclusively use the term dynamical suppression from here onward, as the galactic dynamics are a crucial component for the suppression and quenching, while morphological quenching places all emphasis on the presence of a bulge.

galaxies and found that continued accretion and cooling of gas from the hot circumgalactic medium prevents the galaxies from quenching, even if the presence of a bulge causes a mild suppression of star formation.

In this chapter, we investigate the impact of dynamical suppression on the galaxy population across cosmic time. We wish to establish whether there exist any conditions under which the physics of star formation represent the rate-limiting step in (and therefore regulate) the baryon cycle and, if so, determine the galaxy mass and redshift range for which this is predicted to occur. Therefore, we extend the parameter space covered in Gensior et al. (2020) by repeating our simulations of galaxies with different gravitational potentials for a wide variety of different gas fractions. In Section 4.2, we outline the numerical methods used and introduce the simulations. The results are presented in Section 4.3. In Section 4.4, we assess the impact of our results on the galaxy population by predicting at which galaxy masses and redshifts dynamical suppression should affect the SFR in galaxies. Finally, we summarise and discuss these results in Section 4.5.

4.2 Simulations

All simulations analysed in this work were performed with the moving-mesh code `AREPO` (Springel, 2010). In `AREPO`, stars and dark matter are treated as Lagrangian particles, while the equations of hydrodynamics are solved on an unstructured mesh, created from a Voronoi tessellation, with a second-order, unsplit Godunov solver. Gravitational interactions are calculated using a tree-based scheme.

Treatment of star formation, cooling and feedback is the same as in Gensior et al. (2020), which we briefly summarise here. The sub-grid model for star formation uses a virial parameter (α_{vir}) based star formation efficiency per free-fall time (ϵ_{ff}) as in Padoan et al. (2012, 2017):

$$\epsilon_{\text{ff}} = 0.4 \exp(-1.6\alpha_{\text{vir}}^{0.5}), \quad (4.2.1)$$

which we use to calculate the star formation rate density $\dot{\rho}_{\text{SFR}}$ of a gas cell as

$$\dot{\rho}_{\text{SFR}} = \epsilon_{\text{ff}} \frac{\rho}{t_{\text{ff}}}. \quad (4.2.2)$$

Equation 4.2.1 introduces a dependence on the gas dynamics into the Katz (1992) star formation prescription of equation 4.2.2, which otherwise just depends on the gas density ρ , both explicitly and through the free-fall time $t_{\text{ff}} = \sqrt{3\pi/32G\rho}$. The virial parameter is calculated self-consistently using the density gradient based approach introduced by Gensior et al. (2020), where

$$\alpha_{\text{vir}}^{1/2} \propto \left| \frac{\nabla\rho}{\rho} \right| \frac{\sigma}{\rho^{1/2}}, \quad (4.2.3)$$

which is calculated exclusively using the gas properties. This approach effectively performs an on-the-fly cloud identification by iterating over neighbouring gas cells until an overdensity is identified, from which the velocity dispersion σ and subsequently the virial parameter are calculated. For consistency with the simulations described in Gensior et al. (2020), we

Name	M_b [$10^{10}M_\odot$]	R_b [kpc]	f_{gas}
B_M90_R1_fg1	4.24	1	0.01
B_M90_R1_fg3	4.24	1	0.03
B_M90_R1_fg5	4.24	1	0.05
B_M90_R1_fg10	4.24	1	0.10
B_M90_R1_fg20	4.24	1	0.20
B_M60_R2_fg1	2.83	2	0.01
B_M60_R2_fg3	2.83	2	0.03
B_M60_R2_fg5	2.83	2	0.05
B_M60_R2_fg10	2.83	2	0.10
B_M60_R2_fg20	2.83	2	0.20
B_M30_R3_fg1	1.41	3	0.01
B_M30_R3_fg3	1.41	3	0.03
B_M30_R3_fg5	1.41	3	0.05
B_M30_R3_fg10	1.41	3	0.10
B_M30_R3_fg20	1.41	3	0.20

Table 4.1: Initial conditions of the simulations. Simulations are named by their bulge component and gas fraction, i.e. prefix ‘B’, followed by the relative bulge mass (‘MX’ with X the percentage of the total mass constituted by the bulge), the bulge scale radius (‘RY’ with Y the radius in kpc) and lastly the ratio of gas to stellar mass (‘fgZ’ with Z the ratio multiplied by 100).

impose a minimum density threshold of 1 cm^{-3} and a maximum temperature threshold of $1 \times 10^3 \text{ K}$ to define gas that is eligible for star formation. To model the thermal state of the gas, we use the Grackle chemistry and cooling library² (Smith et al., 2017), with the six species chemistry network and tabulated atomic fine structure cooling at solar metallicity. A constant Haardt and Madau (2012) UV-background is used to model heating due to the interstellar radiation field. Feedback from star formation is included as mechanical feedback from Type II supernovae (SNe) (Hopkins et al., 2014; Kimm and Cen, 2014). Each SN injects $1 \times 10^{51} \text{ erg s}^{-1}$ of energy and ejects $10.5 M_\odot$ into the surrounding gas, of which $2 M_\odot$ are metals. Numerically, this is done by using a kernel to deposit the feedback to the 32 nearest neighbours, similar to Hopkins et al. (2014). We assume one SN per $100 M_\odot$ stellar mass formed (Chabrier, 2003; Leitherer et al., 2014) and a delay time of 4 Myr, in line with recently observed feedback disruption times (Kruijssen et al., 2019a; Chevance et al., 2020a,b), before detonation.

The initial conditions resemble those of the AGORA disc (Kim et al., 2016), and were chosen from the parameter space surveyed in Gensior et al. (2020) (specifically, we adopt and modify runs B_M30_R3, B_M60_R2 and B_M90_R1 from that work; see Chapter 2, Table 2.1), to cover a range in different galactic potentials from disc-dominated galaxy to spheroidal. Table 4.1 lists all isolated galaxy simulations considered in this chapter.

²<https://grackle.readthedocs.io/>

All initial conditions were created according to the procedure detailed by Springel et al. (2005a). Each isolated galaxy is initialised in a dark matter halo with a Hernquist (1990) profile which has a concentration $c = 10$, a spin parameter $\lambda = 0.04$ and a circular velocity $v_{\text{circ}} = 180 \text{ km s}^{-1}$. The stellar component has a mass of $M_* \sim 4.71 \times 10^{10} M_{\odot}$ and is divided into a bulge and disc component. We also model the bulge with a Hernquist (1990) profile, while the disc is described by an exponential radial profile and a sech^2 profile in the vertical direction. The defining parameters of the bulge profile are varied between different initial conditions, from 30–90 per cent of the initial stellar mass for the bulge mass M_{b} and 1–3 kpc for the bulge scale radius R_{b} . To maximise the difference in gravitational potential between the three different options, we combine M_{b} and R_{b} to yield a compact, completely bulge-dominated galaxy ($M_{\text{b}} = 0.9M_*$, $R_{\text{b}} = 1 \text{ kpc}$), a disc-dominated galaxy ($M_{\text{b}} = 0.3M_*$, $R_{\text{b}} = 3 \text{ kpc}$) and one with an intermediate bulge component ($M_{\text{b}} = 0.6M_*$, $R_{\text{b}} = 2 \text{ kpc}$). The mass of stars in the disc is determined by $M_{\text{d}} = M_* - M_{\text{b}}$, its radial scale length is $R_{\text{d}} = 4.6 \text{ kpc}$, and its exponential scale height is $0.1R_{\text{d}}$. The gaseous component follows the same profile as the stellar disc. We vary the mass of gas in the disc for each set of initial conditions between $0.01\text{--}0.20M_*$. This is done to explore how the trends with gravitational potential seen for $f_{\text{gas}} \equiv M_{\text{gas}}/M_* = 0.05$ reported by Gensior et al. (2020) depend on the gas fraction, extending the suite into regimes where galaxies are more gas-poor or more gas-rich than the original sample (thereby smoothly connecting the properties of local early-type galaxies to those of high redshift galaxies, e.g. Geach et al. 2011; Tacconi et al. 2013). A mass resolution of $\sim 1 \times 10^4 M_{\odot}$ is used for the gas cells and stellar particles, while that of the dark matter is $1 \times 10^5 M_{\odot}$. We use adaptive gravitational softening (Price and Monaghan, 2007) to achieve optimum gravitational resolution, with minimum softening lengths of 12 and 26 pc for baryons and dark matter, respectively. This results in an average softening length of 25 pc for gas at a density of 10 cm^{-3} .

4.3 Results

4.3.1 Gas Dynamics

We first explore how the turbulent state of the gas is affected by the underlying gravitational potential and the gas fraction. The turbulent velocity dispersion directly influences the star formation rate via the virial parameter. Figure 4.1 shows the radial velocity dispersion profiles for gas meeting our density and temperature criteria for star formation. We measure the median and the 16th-to-84th percentiles in several snapshots to average over fluctuations due to cloud-scale evolutionary cycling (e.g. Kruijssen et al., 2018; Chevance et al., 2020b). To do so, we use snapshots from 300 Myr onward (offset from the start of the simulation to allow the galaxy to settle into equilibrium) until the end of the simulation at 1 Gyr. The snapshots are separated by 100 Myr, which is approximately a galactic dynamical time.

The panels in Figure 4.1 represent different gravitational potentials, with disc-dominated potential (runs B_M30_R3) on the left, intermediate bulges (runs B_M60_R2) in the middle, and the extremely bulge-dominated potential (runs B_M90_R1) on the right. In all simulations, the velocity dispersion increases towards the galactic centre. For all

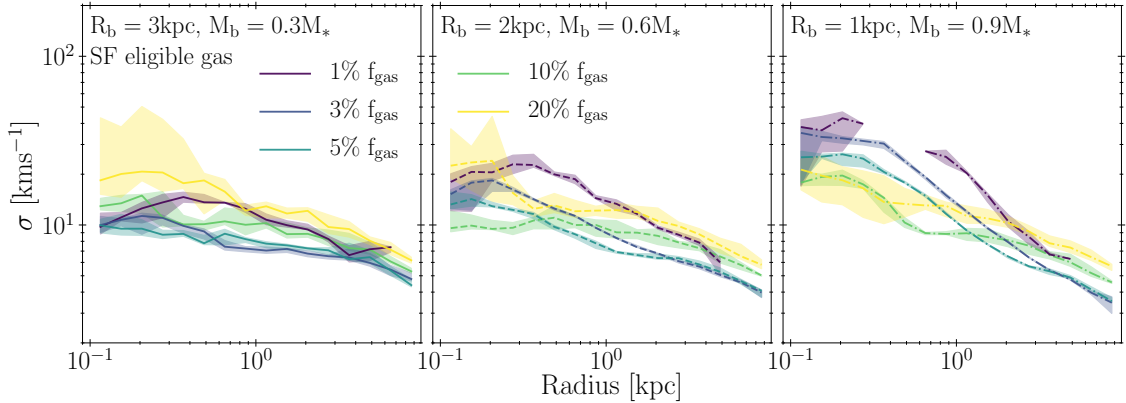


Figure 4.1: The effect of the gravitational potential and gas fractions on the velocity dispersion. Each panel shows the radial profile of the gas velocity dispersion for galaxies with gas-to-stellar mass ratios of 0.01–0.20, for the disc-dominated (left), intermediate bulge (middle) and completely bulge-dominated (right) potentials. Lines indicate the median over time, while the shaded regions indicate the 16th-to-84th percentile variation of the median over time.

gas-to-stellar mass ratios $f_{\text{gas}} \leq 0.10$, this increase is steeper for more prominent bulges. The runs with $f_{\text{gas}} = 0.20$ are the only exception, because their median velocity dispersion profiles are the same across all panels to within the snapshot-to-snapshot time variation. We thus identify a gas-to-stellar mass ratio threshold of $f_{\text{gas}} \sim 10$ per cent) above which the velocity dispersion of the gas disc is no longer affected by the underlying gravitational potential. Even in the run with the most compact bulge (B_M90_R1_fg20), the gas disc is sufficiently dense that its self-gravity dominates over the shear induced by the stellar potential.

All runs with a gas-to-stellar mass ratio of $f_{\text{gas}} = 0.01$ exhibit a similar velocity dispersion profile shape. The median velocity dispersion increases from the outskirts of the disc towards the centre of the galaxy³. As we demonstrate in Gensior et al. (2020) this radial trend signifies that the shearing motions in the underlying potential increase the velocity dispersion. It demonstrates that at the lowest gas fractions a minor bulge component is enough to affect the gas dynamics. Even for the disc-dominated potential (B_M30_R3_fg1), we find a modest increase in velocity dispersion, of ~ 0.3 dex across the full range of radii, whereas the bulge-dominated potential (B_M90_R1_fg1) induces

³The profile of B_M90_R1_fg1 contains a gap between 300–700 pc. This is a result of the star formation eligibility criteria that we apply. Although gas is present at all radii within the simulation, the shear induced by the potential prevents gas from fragmenting into dense clumps and instead smooths it into a featureless disc (Gensior et al., 2020). At $f_{\text{gas}} = 0.01$, this leads to the absence of star-formation eligible gas between 300–700 pc, because the shearing apart of overdensities leads to gas with densities below 1 cm^{-3} when so little gas is present. For a quantitative discussion of how these mechanisms affect the gas density distribution and the interstellar medium (ISM) structure in the simulations, we refer the interested reader to Appendix C.2.

a ~ 1 dex difference, sustaining median velocity dispersions of $\sim 40\text{--}50 \text{ km s}^{-1}$ at the galactic centre.

At intermediate gas-to-stellar mass ratios ($f_{\text{gas}} = 0.03\text{--}0.10$), the gas in the disc-dominated runs (B_M30_R3, left panel in Figure 4.1) has an approximately flat median velocity dispersion throughout the inner $\sim 5\text{kpc}$, which only declines slightly towards larger radii. This is equivalent to the profile found for a bulgeless galaxy by Gensior et al. (2020). Conversely, the most bulge-dominated simulations (B_M90_R1, right panel in Figure 4.1) all show the distinct increase in velocity dispersion towards the centre of the galaxy indicative of turbulent motions induced by the bulge. Also at these intermediate gas fractions, we find that the magnitude of the effect increases towards lower gas fractions. The velocity dispersion increases by $\sim \{0.9, 0.7\}$ dex within the inner $\{4, 3\}$ kpc in the runs with $f_{\text{gas}} = \{0.03, 0.05\}$, while the run with $f_{\text{gas}} = 0.10$ experiences a rise of 0.3 dex in the inner 700 pc. Under the influence of the intermediately bulge-dominated potential (B_M60_R2, middle panel in Figure 4.1), only runs with $f_{\text{gas}} \leq 0.05$ show an increase of the central velocity dispersion. This shows that the gas-to-stellar mass threshold below which the bulge enhances the gas velocity dispersion increases with the central stellar surface density.

At high gas-to-stellar mass ratios ($f_{\text{gas}} = 0.10\text{--}0.20$), the median velocity dispersion profiles are nearly insensitive to the gravitational potential. Interestingly, they also exhibit a larger time variation of the median velocity dispersion compared to those with $f_{\text{gas}} \leq 0.05$ for all gravitational potentials. This is related to the significantly higher SFR in these objects (also see Section 4.3.2). One might expect that a larger global SFR leads to less bursty star formation and thus less variation of the median velocity dispersion over time. However, within each radial bin, star formation is always bursty and thus a net high(er) SFR leads to a larger number of subsequent feedback events and more variation of the velocity dispersion. An additional difference compared to the profiles of the galaxies with $f_{\text{gas}} \leq 0.05$ is that they have slightly elevated velocity dispersions at large radii. A higher gas fraction leads to a more massive gas disc and will increase the mid-plane pressure, against which the gas needs to support itself with higher σ (e.g. Krumholz et al., 2018; Schrubba et al., 2019).

4.3.2 Star Formation

We now investigate how the integrated star formation activity of a galaxy is affected by the combination of its gas fraction and gravitational potential. In Figure 4.2, the global star formation activity of the simulated galaxies is compared to that of galaxies in the xCOLDGASS (Saintonge et al., 2017) and xGASS (Catinella et al., 2018) surveys. As in Gensior et al. (2020), we exclude the central 300 pc of our galaxies from the star formation analysis, because we do not model AGN feedback. This form of feedback would help to disperse gas that accumulates at the centre and reaches very high densities. While the simulations do not include AGN feedback, they also lack the gravitational resolution to accurately model the star formation activity at the very centre of the galaxy. The simulation results represent a global average taken between 300 Myr and 1 Gyr, when the galaxy has settled into equilibrium.

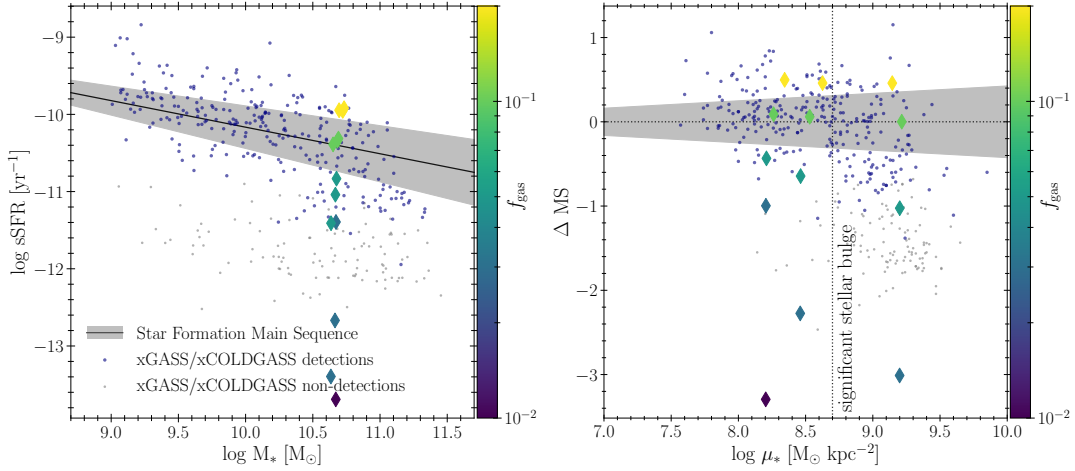


Figure 4.2: Comparison of the star formation activity of the simulated galaxies to the observed galaxy population in the xGASS Catinella et al. (2018) and xCOLDGASS Saintonge et al. (2017) surveys. Left: specific SFR (sSFR \equiv SFR/ M_*) as a function of stellar mass. The black line shows the star formation main sequence from Catinella et al. (2018), with the grey-shaded band indicating the 1σ scatter. Right: vertical offset from the star formation main sequence as a function of the stellar surface density (μ_*). In both panels, diamonds show the results from the simulations, colour coded by their gas-to-stellar mass ratio f_{gas} . Navy (grey) points show the detections (non-detections) of the xGASS (HI, Catinella et al., 2018) and xCOLDGASS (CO, Saintonge et al., 2017) surveys. The central 300pc of the simulations are excluded from the analysis (see the text).

The left panel of Figure 4.2 shows the specific SFR (sSFR \equiv SFR/ M_*) as a function of stellar mass, where the colour of the simulation points indicates their initial gas-to-stellar mass ratio f_{gas} . All simulated galaxies have a very similar stellar mass by construction; differences arise exclusively due to differences in SFR over the course of the simulation. To first order, the (s)SFR increases with the gas-to-stellar mass ratio, which directly follows from the well-known observation that $\text{SFR} \propto M_{\text{gas}}$ for star-forming main sequence galaxies (e.g. Kennicutt, 1998b; Bigiel et al., 2008; Leroy et al., 2013). Quantitatively, galaxies with gas-to-stellar mass ratios $f_{\text{gas}} > 0.05$ fall within the 1σ scatter around the xGASS and xCOLDGASS Catinella et al. (2018) star formation main sequence (SFMS, e.g. Noeske et al. 2007b; Peng et al. 2010). Galaxies with gas-to-stellar mass ratios $f_{\text{gas}} \leq 0.05$ tend to fall below the main sequence. While Figure 4.2 clearly demonstrates that the gas mass has a strong influence on the global SFR of a galaxy, we are mainly interested in trends with the gravitational potential. The left panel of Figure 4.2 shows that the spread in the sSFR of simulations with the same gas fraction increases towards galaxies with lower gas fractions, indicating a stronger impact of dynamical suppression. The most gas-rich simulations ($f_{\text{gas}} = 0.10\text{--}0.20$) exhibit a negligible range of ≤ 0.1 dex in sSFR, irrespective of the gravitational potential. By contrast, galaxies with intermediate

gas content ($f_{\text{gas}} = 0.03\text{--}0.05$) span a range in sSFR of ~ 2 and 0.6 dex, respectively, highlighting that the gravitational potential has a major impact on the sSFR (recall that Gensior et al. 2020 adopted $f_{\text{gas}} = 0.05$ in all simulations). In the most gas-poor systems ($f_{\text{gas}} = 0.01$), only the disc-dominated run B_M30_R3_fg1 forms a non-negligible amount of stars.⁴

To further quantify how the gravitational potential affects the position of a galaxy relative to the SFMS and to show how this position depends on the gas fraction, the right panel of Figure 4.2 shows the offset from the Catinella et al. (2018) SFMS as a function of the stellar surface density μ_* (defined as the mean surface density within the galaxy’s stellar half-mass radius) for all simulations. The stellar half-mass surface density traces both the bulge surface density and bulge-dominance. This panel clearly visualises the key trends that govern the SFMS offsets visible in the left panel. Galaxies with higher stellar surface densities generally fall further below the SFMS, but this trend becomes shallower at higher gas-to-stellar mass ratios, until it eventually vanishes altogether for $f_{\text{gas}} = 0.20$. In such gas-rich galaxies, the gas achieves densities high enough that it is self-gravitating and forms stars on a free-fall time-scale. For $f_{\text{gas}} = 0.10$, the simulations show a very slight decrease in star formation activity towards more bulge-dominated potentials, but the overall decrease is only ~ 0.1 dex. For lower gas fractions, the dynamical suppression of star formation going from disc-dominated to bulge-dominated potentials is much larger, and continues to steepen as the gas fraction decreases. This is a direct consequence of the behaviour seen in Figure 4.1 and described in Section 4.3.1, where we find that only galaxies with $f_{\text{gas}} < 0.05$ are sensitive to the shear induced by bulge-dominated potentials, and that this sensitivity increases towards lower gas fractions.

These results imply that a dominant spheroidal component in itself is not sufficient to quench a galaxy or maintain quiescence – only galaxies with gas-to-stellar mass ratios $f_{\text{gas}} \leq 0.05$ are found to show a significant relation between SFMS offset and stellar surface density. Dynamical suppression is rendered ineffective altogether in more gas-rich galaxies (as applies to the high-redshift galaxy population, to which gas-regulator models have been calibrated). In the next section, we derive analytical expressions for the stellar masses and redshifts at which dynamical suppression becomes important.

4.4 When the Elephant steps into the Bathtub: Predicting the Onset of Dynamical Suppression

Figure 4.2 highlights that the effectiveness of dynamical suppression exhibits a strong dependence on the gas fraction and a moderate (but important) dependence on the stellar

⁴To verify that our results are not caused by the absence of gas eligible for star formation in the inner 300–700 pc of B_M90_R1_fg1 (see the discussion of Figure 4.1), we ran an additional simulation with a density threshold of 0.1 cm^{-3} and a temperature ceiling of 10^4 K to define gas eligible for star formation. We also ran a simulation with the same star formation criteria as B_M90_R1_fg1, but a factor of three higher resolution. Neither of these additional simulations exhibit any significant differences in sSFR relative to B_M90_R1_fg1.

surface density. We quantify the effect on the sSFR by performing a multi-linear regression⁵ of the simulated data. This yields the following relation:

$$\begin{aligned} \log(\text{sSFR}_{\text{sim}}[\text{Gyr}^{-1}]) &= -1.79 + 4.00 \log\left(\frac{f_{\text{gas}}}{0.05}\right) \\ &\quad - 0.99 \log\left(\frac{\mu_*}{10^8 \text{ M}_\odot \text{ kpc}^{-2}}\right), \end{aligned} \quad (4.4.1)$$

for $8.0 < \log(\mu_*/\text{M}_\odot \text{ kpc}^{-2}) < 9.5$ and $0.01 \leq f_{\text{gas}} \leq 0.20$. By combining this fit with observed scaling relations describing the galaxy population, we can predict a minimum stellar mass as a function of redshift at which dynamical suppression will become effective.

First, we rewrite the right-hand side of equation 4.4.1 in terms of $\log M_*$ and z . The stellar surface density is given by $\mu_* = M_*/(2\pi R_e^2)$ and can be converted to solely depend on stellar mass and redshift by assuming a galaxy mass-radius-redshift relation. For this, we use:

$$R_e = 8.9 \text{ kpc} (1+z)^{-0.75} (M_*/5 \times 10^{10} \text{ M}_\odot)^{0.22}, \quad (4.4.2)$$

as obtained for late-type galaxies by van der Wel et al. (2014). Early-type galaxies are found to have smaller radii and larger stellar surface densities, which means that the mass-radius relation for late-type galaxies can indeed be used to derive the limiting case that we are interested in here. Secondly, we use the observed scaling of the gas fraction as a function of redshift and stellar mass (Tacconi et al., 2018) to eliminate f_{gas} from equation 4.4.1. This adds further justification to our choice of the late-type mass-radius relation, because the Tacconi et al. (2018) relation was derived for star-forming galaxies. We chose their best fit for a Speagle et al. (2014) SFMS, which gives:

$$\begin{aligned} \log\left(\frac{f_{\text{gas}}}{0.05}\right) &= 0.11 + 2.49 \log(1+z) + 0.52 \Delta\text{MS} \\ &\quad - 0.36 \log\left(\frac{M_*}{5 \times 10^{10} \text{ M}_\odot}\right), \end{aligned} \quad (4.4.3)$$

where ΔMS is the main sequence offset in dex.

We define ‘effective dynamical suppression’ as causing a SFMS offset of $\Delta\text{MS} = -0.5$ dex, which is expressed as a negative to reflect a suppression of star formation. The magnitude of the offset, 0.5 dex, is a compromise between the mass-dependent scatter about the main sequence and the maximum variation of 0.6 dex experienced by galaxies throughout their life on the SFMS (Catinella et al., 2018; Tacconi et al., 2018). As such, this definition means that galaxies need to be at least 1σ below the main sequence for dynamical suppression to be ‘important’. We keep ΔMS constant, because Speagle et al. (2014) find that the scatter around the SFMS varies little across cosmic time. Now, we can evaluate equation 4.4.1 at $\Delta\text{MS} = -0.5$ dex and write:

$$\begin{aligned} \log(\text{sSFR}_{\text{sim}}[\text{Gyr}^{-1}]) &= -2.39 + 8.48 \log(1+z) \\ &\quad - 1.99 \log\left(\frac{M_*}{5 \times 10^{10} \text{ M}_\odot}\right). \end{aligned} \quad (4.4.4)$$

⁵We discuss the validity of using this parameterisation in Appendix C.1.

Requiring $\Delta\text{MS} = -0.5$ dex as our minimum SFMS offset for equation 4.4.4 then allows us to define the condition:

$$-0.5 > \log(\text{sSFR}_{\text{sim}}[\text{Gyr}^{-1}]) - \log(\text{sSFR}_{\text{MS,obs}}[\text{Gyr}^{-1}]), \quad (4.4.5)$$

where we use the Speagle et al. (2014) SFMS to define $\log(\text{sSFR}_{\text{MS,obs}}[\text{Gyr}^{-1}])$ for self-consistency with the preceding derivation, specifically with the f_{gas} relation from Tacconi et al. (2018). Therefore, equation 4.4.5 becomes:

$$\begin{aligned} -0.5 > & -2.39 + 8.48 \log(1+z) - 1.99 \log\left(\frac{M_*}{5 \times 10^{10} \text{ M}_\odot}\right) \\ & -(-0.16 - 0.026t_c) \times \left(\log\left(\frac{M_*}{5 \times 10^{10} \text{ M}_\odot}\right) + 10.73\right) \\ & + (6.51 - 0.11t_c) - 9, \end{aligned} \quad (4.4.6)$$

for $9.0 < \log(M_*/\text{M}_\odot) < 11.7$, $8.0 < \log(\mu_*/\text{M}_\odot \text{ kpc}^{-2}) < 9.5$, and $0.01 \leq f_{\text{gas}} \leq 0.20$. If this condition is satisfied, dynamical suppression is predicted to drive galaxies off the SFMS. The t_c in this equation is the age of the universe in Gyr and can be written as a function of redshift (Tacconi et al., 2018):

$$\begin{aligned} \log t_c = & 1.143 - 1.026 \log(1+z) - 0.599 \log^2(1+z) \\ & + 0.528 \log^3(1+z), \end{aligned} \quad (4.4.7)$$

which assumes a flat Λ CDM universe with $\Omega_m = 0.3$ and $H_0 = 70 \text{ km s}^{-1} \text{ Mpc}^{-1}$.

Finally, we can reorder the condition of equation 4.4.6 to predict the minimum required stellar mass at a given redshift above which dynamical suppression becomes important:

$$\log\left(\frac{M_*}{5 \times 10^{10} \text{ M}_\odot}\right) > \frac{-2.66 + 8.48 \log(1+z) + 0.17t_c}{1.83 - 0.026t_c}, \quad (4.4.8)$$

where t_c is defined as a function of redshift according to equation 4.4.7. We find that the condition of equation 4.4.8 can be approximated to within < 1 per cent by a third-order polynomial fit, providing the minimum stellar mass as a function of redshift:

$$\log\left(\frac{M_*}{5 \times 10^{10} \text{ M}_\odot}\right) > -0.21 + 0.87z - 0.11z^2 + 0.0082z^3. \quad (4.4.9)$$

Expressed as a maximum redshift as a function of stellar mass, this equivalently becomes:

$$\begin{aligned} z < & 0.23 + 1.22 \log\left(\frac{M_*}{5 \times 10^{10} \text{ M}_\odot}\right) \\ & + 0.17 \log^2\left(\frac{M_*}{5 \times 10^{10} \text{ M}_\odot}\right) + 0.069 \log^3\left(\frac{M_*}{5 \times 10^{10} \text{ M}_\odot}\right). \end{aligned} \quad (4.4.10)$$

The prediction expressed equivalently in equations 4.4.8–4.4.10 is shown in Figure 4.3. The black line indicates the minimum stellar mass a galaxy must have at a given redshift (or, conversely, a maximum redshift at a given stellar mass) to experience dynamical suppression, as in equations 4.4.8 and 4.4.10. Galaxies residing below the line, in the grey-shaded area,

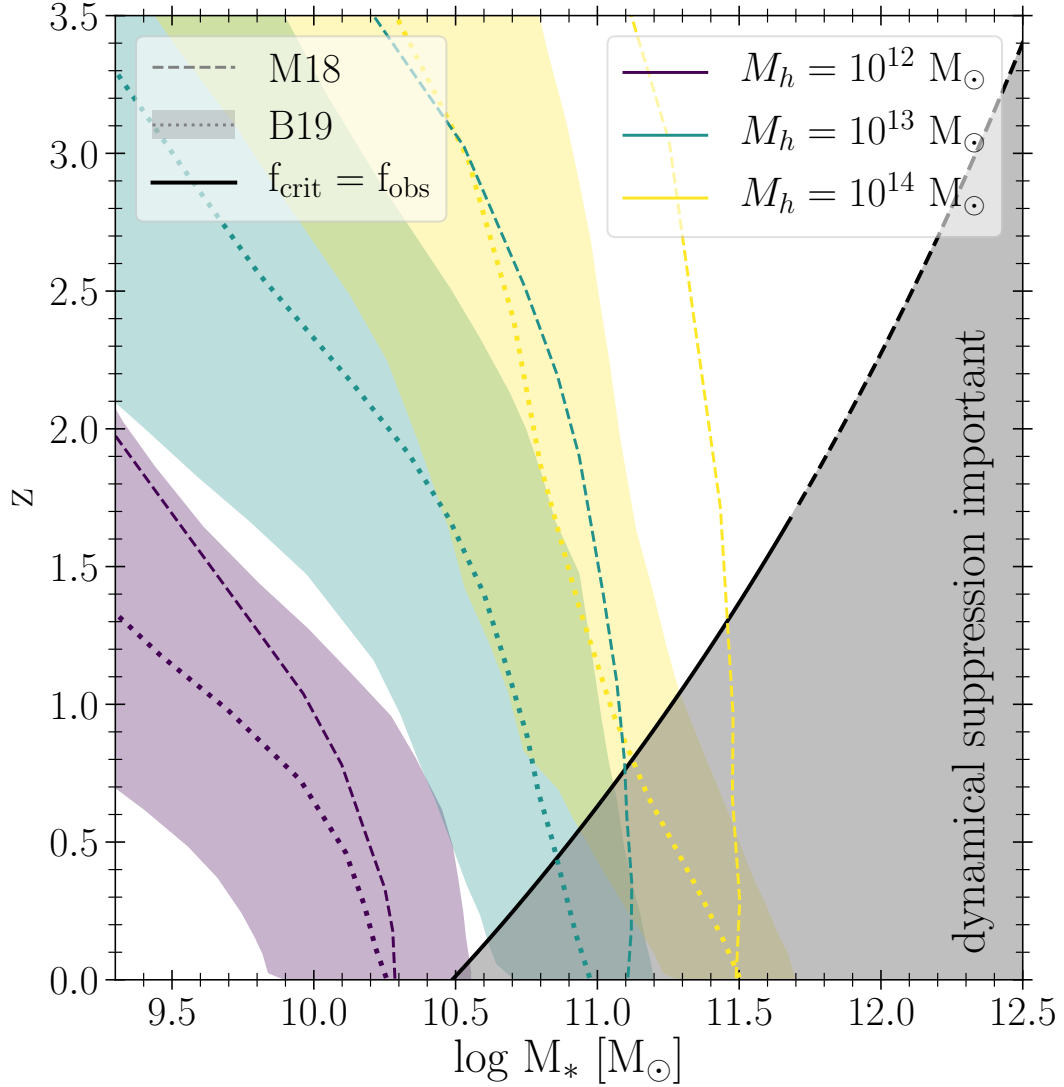


Figure 4.3: Redshift and stellar mass range for which galaxies are predicted to be affected by the dynamical suppression of star formation. The black line indicates where the typical observed gas fraction (Tacconi et al., 2018) and the gas fraction required for dynamical suppression are equal, as expressed in equation 4.4.8. Galaxies below the line (grey-shaded area) are predicted to experience dynamical suppression. Coloured lines show the stellar mass growth histories of galaxies with $z = 0$ stellar masses ranging from $1.8 \times 10^{10} M_\odot$ to $3 \times 10^{11} M_\odot$, as predicted by Moster et al. (2018) and Behroozi et al. (2019) (see the legend).

should typically fall below the SFMS as a result of dynamical suppression, even if it does not quench the galaxy completely. As the equation 4.4.3 has been derived for stellar masses $\log(M_*/M_\odot) \leq 11.7$ (Tacconi et al., 2018), the black line is an extrapolation at stellar masses above this limit (visualised by a dashed line).

In Figure 4.3, we show which galaxies are affected by dynamical suppression, and for how long this has been the case. To make this comparison, we adopt the stellar mass assembly histories from Moster et al. (2018) and Behroozi et al. (2019), who have used a combination of halo abundance matching and empirical constraints. Coloured lines in Figure 4.3 show the average assembly history, as predicted by the models of Moster et al. (2018) and Behroozi et al. (2019), for galaxies with a stellar mass at $z = 0$ in the range of $1.8 \times 10^{10} \leq M_*/M_\odot \leq 3 \times 10^{11}$, derived from halos with final masses of 10^{12} , 10^{13} , and $10^{14}M_\odot$. The figure shows that L_* galaxies like the Milky Way have typically been experiencing the onset of dynamical suppression since $z \leq 0.23$ (or up to 2.8 Gyr). By contrast, the most massive galaxies considered here ($M_* \sim 3 \times 10^{11} M_\odot$) are predicted to have experienced dynamically suppressed star formation since $z \leq 0.82$ (up to 6.9 Gyr ago) (Behroozi et al., 2019) or $z \leq 1.36$ (up to 8.8 Gyr ago) (Moster et al., 2018) depending on the stellar mass assembly history model.

In the Milky Way, there is evidence for the dynamical suppression of star formation in the bulge-dominated central 500 pc (Longmore et al., 2013; Kruijssen et al., 2014). For galaxies out to $z \sim 1$, there is indirect evidence supporting our prediction in terms of observed morphological trends. For instance, the transition from discs to spheroids dominating the stellar mass budgets of galaxies occurs at a stellar mass of $10^{10.5} M_\odot$ for the galaxy population at $z \sim 0.1$. Moreover, the average bulge-to-total ratio increases with increasing stellar mass (Thanjavur et al., 2016), such that the most massive galaxies tend to be bulge-dominated from $z \sim 1.5$ onward (Bundy et al., 2006, 2010; Buitrago et al., 2013). We predict that these galaxies are susceptible to the dynamical suppression of star formation.

4.5 Discussion

4.5.1 Summary

In this chapter, we have used a suite of 15 hydrodynamical simulations of isolated galaxies to investigate under which conditions galactic-dynamical processes can suppress star formation. The simulations span a variety of gravitational potentials (most prominently tracing different stellar surface densities or bulge-to-disc ratios) and gas-to-stellar mass ratios (in the range $f_{\text{gas}} = 0.01\text{--}0.20$). The simulations adopt a dynamics-dependent sub-grid star formation model, in which more super-virial gas clouds form stars less efficiently. The results are summarised as follows:

1. The dynamical suppression of star formation proceeds by the increase of the gas velocity dispersion by shear, rendering the gas supervirial. The bulge component of the simulated galaxies drives a central increase of the velocity dispersion most efficiently at high central stellar surface densities (i.e. high bulge-to-disc ratios) and low gas fractions. At the lowest

gas-to-stellar mass ratio ($f_{\text{gas}} = 0.01$), even the weakest bulge component considered in this work is sufficient to drive up the central velocity dispersion. At the highest gas-to-stellar mass ratio ($f_{\text{gas}} = 0.20$), the median velocity dispersion is insensitive to the gravitational potential.

2. The extent to which the SFR is dynamically suppressed depends on both the gas-to-stellar mass ratio (f_{gas}) and the stellar surface density (μ_*). For a given μ_* , we identify the critical f_{gas} above which dynamical suppression becomes ineffective, because the stellar spheroidal component no longer dominates the local gravitational potential. Conversely, the effect of dynamical suppression increases towards lower gas fractions, driving galaxy off the star formation main sequence (SFMS), into the population of quenched galaxies.
3. The gas-to-stellar mass ratio (or gas fraction) does not only act as a threshold for dynamical suppression, but also regulates its overall strength and dependence on stellar surface density. The lower the gas fraction, the steeper the anti-correlation between the SFR and stellar surface density – not only is the global (s)SFR more suppressed at lower gas fractions, but the amount of suppression compared to the SFMS becomes steeper.
4. We perform a multi-linear regression to quantify the relation between sSFR, μ_* , and f_{gas} . By combining this relation with the observed dependence of these quantities on galaxy mass and redshift (Tacconi et al., 2018), we can derive the subset of the galaxy population for which dynamical suppression is predicted to be effective. We find that the physics of star formation can be the rate-limiting step in the baryon cycle at high galaxy masses (equation 4.4.9) and low redshifts (equation 4.4.10; also see Figure 4.3).

4.5.2 Implications for Galaxy Evolution and Quenching

Our findings are in good agreement with recent observational results. Similarly to Tacconi et al. (2018), who relate the main sequence offset to gas fraction and stellar mass across redshift, nearby grand design spirals also exhibit a direct link between SFR, stellar surface density and gas fraction on 500 pc scales (Morselli et al., 2020). Surveys of the galaxy population at $z \sim 0$ additionally suggest that the offset from the SFMS is driven by a combination of (molecular) gas fraction and star formation efficiency (e.g. Zhang et al., 2019; Brownson et al., 2020; Piotrowska et al., 2020). This is consistent with our findings in Section 4.3.2, where we predict that the star formation efficiency decreases steeply with μ_* (and can thus be considered synonymous) at fixed gas fraction. Observations also reveal that the main sequence offset increases with bulge-to-disc ratio (Bluck et al. 2019; Cook et al. 2020 and references therein), which again agrees qualitatively with our prediction that high stellar surface densities lead to the dynamical suppression of star formation.

Numerically, our results are in agreement with (but considerably extend) previous simulations of similar systems (e.g. Martig et al., 2013; Semenov et al., 2016; Su et al., 2019; Kretschmer and Teyssier, 2020). Like ours, these simulations predict that gas dynamics influence star formation only in sufficiently gas-poor galaxies. Interestingly, Martig et al. (2009) find that star formation in their cosmological zoom-in simulation is dynamically

suppressed from $z \sim 0.8$ onward when the galaxy’s stellar mass exceeds $10^{11} M_{\odot}$, which is consistent with our prediction. While the quantitative agreement is likely a coincidence, the general qualitative agreement is encouraging and implies that it is crucial to take dynamical suppression into account when modelling the evolution of massive ($M_* > 3 \times 10^{10} M_{\odot}$) galaxies in the intermediate-to-low redshift universe. The analytical representations of our findings can be readily incorporated in gas regulator models, or as sub-grid models in semi-analytic models and hydrodynamic simulations.

While the suite of simulations presented here provides key insights into the dynamical suppression of star formation and its dependence on the host galaxy properties, they represent idealised numerical experiments that generate various follow-up questions. The simulations do not model gas inflow onto the galactic halo, nor do the initial conditions include a hot circumgalactic medium. How do more realistic boundary conditions affect the onset and extent of dynamical suppression? The models also do not include AGN feedback, which is a key agent for driving gas outflows and quenching galaxies. What is the interplay between AGN feedback and dynamical suppression? The SN feedback used in the simulations does expel some amount of gas from the disc, which later rains back down onto the galaxy. This provides some level of gas outflow and inflow, despite which dynamical suppression is found to regulate the SFR in an important part of galaxy mass-redshift space. There is reason to believe that the Padoan et al. (2012, 2017) model may somewhat overpredict the extent to which star formation is suppressed (Schruba et al., 2019), because the star formation efficiency carries a strong exponential dependence on the virial parameter. Further uncertainty on the predictions of Figure 4.3 may arise through the relations adopted to express the dependence of μ_* and f_{gas} on M_* , particularly due to using an observational f_{gas} relation that solely describes the molecular gas. While the cold ISM in high-redshift galaxies is mostly molecular, there is a transition at $z = 0.1\text{--}0.3$ below which atomic gas becomes the dominant component (Tacconi et al., 2018). This implies that we might overpredict the magnitude and onset of dynamical suppression at galaxy stellar masses $\log(M_*/M_{\odot}) \leq 10.75$ and redshifts $z \lesssim 0.3$. Nonetheless, this is a relatively small part of the mass range considered in Figure 4.3. The qualitative agreement of our simulations with both observational and numerical studies demonstrates that there is indeed a regime where dynamical suppression drives down the SFR in galaxies.

Our results do not imply that dynamical suppression is solely responsible for galaxy quenching, even in the grey-shaded area of galaxy mass-redshift space in Figure 4.3 where it is expected to act. On its own, the effectiveness of dynamical suppression has a simple dependence on galactic properties – the higher the gas fraction (or redshift) of a galaxy, the higher its stellar mass must be to have a gravitational potential deep enough to affect the gas motions and star formation. Therefore, dynamical suppression should act more effectively when combined with physical processes capable of preventing the accumulation of a massive gas reservoir. An example of such a process is halo quenching (Dekel and Birnboim, 2006; Davé et al., 2017), which halts the gas inflow from the cosmic web.⁶ Alternatively, the

⁶While halo quenching curtails the growth of the cold ISM from external accretion, the ISM of a galaxy will still be replenished through stellar mass loss from AGB stars. However, recent studies of the cold gas and dust in early-type galaxies show that stellar mass loss only contributes a small fraction to their cold

existence of a massive gas reservoir could be prevented by AGN feedback, by heating and expelling gas from the galaxy (e.g. Bower et al., 2006; Croton et al., 2006; Fabian, 2012; Donnari et al., 2019; Lacerda et al., 2020; Su et al., 2020). AGN feedback and dynamical suppression might be forming a symbiotic cycle – dynamical suppression requires some mechanism to deplete the galactic gas supply (a role plausibly fulfilled by AGN feedback), and once this is achieved, dynamical suppression will help preserve and build a quiescent gas disc at the centre of the galaxy, which is not consumed by star formation and therefore can feed the AGN again. Our simulations suggest that this nuanced picture, in which a combination of dynamical suppression and AGN feedback or halo quenching regulates the baryon cycle, is necessary to create the quiescent galaxy population (as been argued by a number of observational studies, see e.g. Lang et al., 2014; Hahn et al., 2017).

Ultimately, our prediction that the dynamical suppression of star formation should manifest itself at certain galaxy masses and redshifts (Figure 4.3) should be interpreted as evidence for a regime in which galaxy evolution is no longer solely determined by the balance between gas inflow and outflow. Recently, there have been attempts to add improved star formation physics to gas-regulator models. For instance, Belfiore et al. (2019) include an empirically-motivated star formation efficiency that changes as a function of galactic radius, whereas Tacchella et al. (2020) take into account molecular cloud lifetimes. Figure 4.3 acts as a guide to determine on which parts of parameter space future studies should focus, both in observational surveys of the galaxy population and through cosmological (zoom-in) simulations.

ISM (e.g. Davis et al., 2019; Kokusho et al., 2019). Therefore, the effectiveness of dynamical suppression will not be strongly affected by the mass loss of old stars.

Chapter 5

Conclusions

The scientific aim of this thesis was to understand the impact of the galactic gravitational potential on ISM properties (e.g. gas morphology, velocity dispersion) and star formation. In particular, quantifying the conditions in which star formation might be suppressed or quenched through the influence of a dominant spheroid. To do so, a sub-grid star formation model that goes beyond the constant star formation efficiency approaches and can be used in galaxy- and cosmology-scale simulations has been developed. Dynamical suppression has been studied using a large suite of isolated galaxy simulations to go beyond the phenomenology of the seminal morphological quenching paper (Martig et al., 2009).

In Section 5.1 and subsections I will summarise the content of the main chapters of this thesis. These will be placed in the context of the current status of the field in Section 5.2 and possibilities for future research will conclude the thesis in Section 5.3.

5.1 Summary

Chapter II: Heart of Darkness

Motivated by the observational evidence that the SFE per free-fall time varies both within and across galaxies (e.g. Murray, 2011; Utomo et al., 2018), we develop a new sub-grid star formation model for the moving-mesh code `AREPO` (Springel, 2010; Weinberger et al., 2020) that includes a variable ϵ_{ff} . The parametrisation of the star formation efficiency stems from empirical fits to high-resolution simulations of a molecular cloud in a turbulent box (Padoan et al., 2012, 2017) and introduces a dependence on the galactic dynamics via the virial parameter of the gas: $\epsilon_{\text{ff}} = 0.4 \exp(-1.6\alpha_{\text{vir}}^{0.5})$. The algorithm with which it is calculated effectively performs an on-the-fly cloud identification, by identifying an overdensity surrounding each gas cell. In this characteristic region, the velocity dispersion and subsequently the virial parameter are calculated. The algorithm is well converged across a decade in resolution and generic enough that any cloud-scale quantities can be calculated with it. In the limit of a disc-only gravitational potential (i.e. no additional shear through a bulge component), the dynamics-dependent efficiency converges to the constant efficiency case. However, in bulge-dominated potentials, there are noticeable

differences in the ISM morphology, global and radial SFR. Namely, where the ISM of the constant SFE galaxies shows the holes characteristic of SN feedback at all radii, that of the bulge-dominated galaxies remains in a smooth disc in the central region. Furthermore, the SFR is more centrally suppressed when modelled with the dynamics-dependent SFE, which results in a global SFR difference of 0.5 dex in the spheroid.

Equipped with the dynamics-dependent SFE, we then use ten isolated galaxy simulations to study the impact of the gravitational potential on star formation. All galaxies in the suite have identical initial stellar and gas masses ($M_{\text{gas}} = 0.05M_*$) and gas distribution, but morphologies ranging from disc galaxies to spheroids. We find that the presence of a spheroid drives turbulence and enhances the velocity dispersion, virial parameter and turbulent pressure of the gas towards the galactic centre. The effect becomes stronger the higher the central stellar surface density μ_* , i.e. the more compact and/or massive the bulge component. This quantifies the prediction of Martig et al. (2009): the shear from a dominant spheroid increases the velocity dispersion of the gas. Furthermore, we find that the shear-driven turbulence stabilises the gas reservoir: the ISM in the bulge-dominated galaxies forms a smooth, dense gas disc in the central region, spanning more than 4 kpc across in the spheroids case. Contrary to that, the ISM of the disc-dominated galaxies is clumpy, porous and sub-structured throughout the galaxy. Finally, gas turbulence impacts star formation within the galaxy and globally. The SFR of the galaxies is increasingly suppressed towards the galactic centre with increasing μ_* . The global SFR in the spheroid-dominated galaxies reduced by a factor of 5 compared to the bulge-less galaxy. Thus we find that morphological quenching is a viable mechanism to suppress the SFR in bulge-dominated, gas poor galaxies. We coin the term *dynamical suppression*, to highlight the importance of the galaxy dynamics in the process.

Chapter III: The WISDOM of Power Spectra

In this chapter, we use power spectra of the surface density to quantify the turbulence (e.g. Elmegreen and Scalo, 2004) in the central 2.25 kpc of the ten isolated galaxies modelled with a dynamics-dependent SFE introduced in Chapter 2. The power spectrum depends on the morphology of the gas (Koch et al., 2020). Its slope is expected to steepen in the absence of fragmentation (Renaud et al., 2013; Grisdale et al., 2017). If the smooth circumnuclear gas reservoirs result from the suppression of fragmentation through the shear-driven turbulence induced by a spheroid-dominated potential, we expect to see a clear trend between the power spectrum slope and μ_* .

Indeed, we see a strong correlation of increasing power spectrum slope with increasing central stellar surface density. The correlation has a mean Spearman rank coefficient of $0.86_{-0.07}^{+0.07}$ and is significant at the $p < 0.01$ level. This demonstrates that shear dynamically suppresses fragmentation in the centres of bulge-dominated galaxies. The trend between power spectrum slope and central stellar surface density might level off and oscillate shallowly around a constant power spectrum slope once $\log(\mu_*/M_\odot\text{kpc}^{-2}) \geq 8.75$. This might be physical in nature, the result of the limited numerical resolution and/or other systematic assumptions that mask a (shallower) steepening of the power spectra at very high central stellar surface densities. If physical, the flattening of the trend at

$\log(\mu_*/M_\odot\text{kpc}^{-2}) \geq 8.75$ would imply that there is a maximum extent to which shear can suppress fragmentation. The close correspondence of these power spectra slopes to two-dimensional Kolmogorov (1941) turbulence might indicate that sufficiently high shear drives incompressible turbulence in the plane of the galaxy.

To corroborate our findings, we apply the same analysis to ^{12}CO observations of twelve galaxies from the WISDOM project (e.g. Onishi et al., 2017), comprising a mix of late- and early-type galaxies with a range of μ_* . Contrary to the simulations, the WISDOM power spectra do not show any trend with the central stellar surface densities. Instead they are very scattered, with an average slope of 2.55. However, since the majority of the WISDOM sample has $\log(\mu_*/M_\odot\text{kpc}^{-2}) \geq 8.75$, this is in broad agreement with the simulations. This hints that the convergence of the simulations to a single power spectrum slope could be physical in nature. The large scatter of the observations is likely driven by physical processes (e.g. interactions with other galaxies, galactic environment) not captured in the isolated galaxy simulations. The only correlation we find for the power spectra of the WISDOM galaxies is between the power spectrum slope and the central *gas* surface density. This suggests that in the real Universe, the potential of the gas, rather than the stars, plays a more dominant role in the driving of galactic turbulence. However, since this trend has some dependence on the heterogeneity of the observations, confirmation from a more homogeneous data set is still required.

Chapter IV: The Elephant in the Bathtub

In this chapter, we consider the effect of dynamical suppression on quiescence for the wider galaxy population. Specifically, we investigate how the results presented in Chapter 2 are affected by varying the gas fraction of the simulated galaxies. Recent works (e.g. Brownson et al., 2020; Colombo et al., 2020; Piotrowska et al., 2020) have highlighted the importance of the combination of gas fraction and SFE in quenching galaxies. It has been indicated previously that dynamical suppression acts predominantly at low gas fractions (Martig et al., 2013; Kretschmer and Teyssier, 2020). We simulate the most disc- and bulge-dominated galaxies, as well as one intermediate case from the suite presented in Chapter 2, with initial gas-to-stellar mass ratios ranging from 1–20 per cent.

The effectiveness of dynamical suppression depends on how much and how effectively turbulence can be driven by the shear from the bulge component of the potential. We identify a critical gas-to-stellar mass ratio f_{gas} , above which self-gravity locally dominates over shear. The gas becomes indifferent to the underlying galactic gravitational potential: the velocity dispersion is set by stellar feedback at all radii and the SFR is no longer affected by the potential. Conversely, dynamical suppression becomes more effective, the lower the gas fraction. In this case, larger central turbulent velocity dispersions can be sustained and, at the lowest gas fraction considered, even the disc-dominated galaxy exhibits a moderate increase of velocity dispersion towards the galactic centre. The global SFR is more suppressed, while the anti-correlation between SFR and μ_* steepens, too, the more the gas fraction decreases. Therefore, f_{gas} controls both the overall strength of the dynamical suppression and its dependence on the central stellar surface density.

To extend these conclusions to the galaxy population at large, we perform a multi-

linear regression analysis of the data to quantify the effect of f_{gas} and μ_* on the sSFR. We then derive a prediction for the subset of the galaxy population affected by dynamical suppression by combining our regression result with empirical scaling relations for the evolution of the gas fraction (Tacconi et al., 2018), the sSFR (Speagle et al., 2014) and the galaxy radius (van der Wel et al., 2014) with galaxy mass and redshift. We find that dynamical suppression can effectively suppress star formation for high galaxy masses ($\log(M_*/M_\odot) \gtrsim 10.5$) at intermediate-to-low redshift ($z \lesssim 1.5$). The physics of star formation are therefore predicted to dominate the baryon cycle of galaxies at high galaxy stellar masses and intermediate-to-low redshifts by suppressing the conversion of gas to stars.

5.2 Discussion

As this thesis comes to a close one question remains: *what have we learned?* The research conducted over the past four years and summarised in Section 5.1 above can be recast into some overarching ideas that naturally lead to future research directions. They will be expanded upon below.

5.2.1 Galactic dynamics matter

Chapter 4 highlights that dynamical suppression requires low gas fractions in order to be effective. This is in good agreement with previous studies (Martig et al., 2009, 2013; Su et al., 2019; Kretschmer and Teyssier, 2020). This can be understood in terms of the cloud-scale physics: once clouds are dynamically decoupled from the galactic background and the local free-fall time falls below the shear timescale, collapse will proceed (e.g. Jeffreson and Kruijssen, 2018; Meidt et al., 2020). The higher the gas fraction, the larger the local density, making it easier for clouds to decouple from the dynamics. Conversely, larger local stellar densities can sustain larger gas fractions while star formation remains suppressed (as can be seen in e.g. Ellison et al., 2021b). Preceding the dynamical suppression of star formation is the suppression of gas fragmentation. The power spectrum analysis of Chapter 3 confirms that this is the result of shear-driven turbulence from the spheroid-dominated gravitational potential.

There is much observational evidence for quenching beginning ‘inside-out’, i.e. star formation is suppressed in the centres of galaxies even if globally they still fall on the SFMS or a SK relation (e.g. Longmore et al., 2013; Kruijssen et al., 2014 for the CMZ, Usero et al., 2015; Bigiel et al., 2016; Gallagher et al., 2018; Méndez-Abreu et al., 2019; Querejeta et al., 2019; Ellison et al., 2021b for external galaxies and Tacchella et al., 2018 for massive galaxies at $z \sim 2$). The central suppression of star formation becomes even more pronounced for galaxies below the SFMS (e.g. Belfiore et al., 2018; Ellison et al., 2018; Medling et al., 2018; Kalinova et al., 2021; Nelson et al., 2021). Dynamical suppression naturally leads to a stronger central suppression of star formation, because there the shear induced by a spheroidal component is the strongest. Figure 2.14 in Chapter 2 demonstrates that the central suppression of star formation can even occur in for disc-dominated galaxies

with low μ_* .

5.2.2 Dynamical suppression maintains quiescence but does not quench

The dependence of dynamical suppression on the local balance between gas and stellar potential has a strong implication for its ability to quench galaxies. No matter whether quenching happens ‘fast’ (< 1 Gyr, sometimes even < 250 - 500 Myr e.g. Schawinski et al., 2014) or ‘slow’ (~ 2 - 5 Gyr e.g. Hahn et al., 2017) it is unlikely that dynamical suppression causes the initial quenching. This is more obvious for the fast quenching route, which is commonly attributed to a (merger-induced) starburst that rapidly consumes gas and drives strong outflows (e.g. Veilleux et al., 2005), powered by AGN or stellar feedback. Slow quenching has previously been attributed to dynamical suppression (e.g. Hahn et al., 2017; Gobat et al., 2018; Kim et al., 2018; Belli et al., 2021). However, for dynamical suppression to act effectively, the gas reservoir of a galaxy must be replenished at a slower rate than star formation consumes it. Since dynamical suppression actively reduces the SFR, it necessitates a mechanism that prevents or drastically reduces gas cooling from the halo. It could be cosmological starvation (Feldmann and Mayer, 2015) that reduces gas accretion because the dark matter halo starves, halo quenching (e.g. Birnboim and Dekel, 2003; Dekel and Birnboim, 2006) or radio-mode AGN feedback (e.g. Best et al., 2005; Bower et al., 2006; Croton et al., 2006) which keep the halo hot.

Once any of these mechanisms inhibits cold gas accretion from the halo, a galaxy’s SFR can be dynamically suppressed. In this mode, dynamical suppression will likely be capable of keeping a galaxy quiescent across cosmic time to $z = 0$ in the face of stellar mass loss replenishing the ISM (since stellar mass loss only contributes a small fraction to the cold ISM of ETGs, see Davis et al., 2019; Kokusho et al., 2019). If a galaxy has been quenched for a sufficiently long time and the residual gas reservoir is depleted enough, even a gas-rich minor merger should not cause a rejuvenation of star formation. This would explain the observations of Davis et al. (2015) and van de Voort et al. (2018), who find that the SFR of ETGs at $z < 0.1$ remains very suppressed following a recent merger, while Belli et al. (2021) find that a merger rejuvenated a massive galaxy at $z \sim 1$.

Dynamical suppression is not redundant in the face of all the actual quenching mechanisms. Instead it is required to maintain quiescence in galaxies that retain (or re-acquire) a cold gas reservoir after quenching (e.g. Martig et al., 2013; Davis et al., 2014, 2015; French et al., 2015; Rowlands et al., 2015; Hahn et al., 2017; Suess et al., 2017; Gobat et al., 2018; van de Voort et al., 2018; Colombo et al., 2020; Belli et al., 2021; Williams et al., 2021).

5.2.3 Environmentally-dependent star formation models are important

Chapter 2 discusses in detail the different approaches taken to model star formation in galaxy-scale simulations. In many cases, a constant SFE in combination with density and temperature thresholds is assumed, calibrated against the SK relation. Yet we find in Chapter 2 that much of the dynamical SFR suppression is missed, and star formation takes place in spite of the suppression of fragmentation when using a constant SFE model. We need the more physically-motivated, dynamics-dependent sub-grid model to accurately

capture the effect of dynamical suppression. This finding is mirrored by Kretschmer and Teyssier (2020), whose cosmological zoom-in simulation only results in a quiescent ETG when using a dynamics-dependent SFE. Semenov et al. (2019) argue in the same vein. Their simulations of a LTG only match the observed, near linear-scaling of the molecular SK relation (e.g. Bigiel et al., 2008; Leroy et al., 2013) if a dependence on the virial parameter is included in the star formation model.

Cosmological simulations tend to have a very simplistic ISM and star formation model, where gas does not cool below 10^4 K and can form stars once it reaches densities of 0.1cm^{-3} . Comparing the radial sSFR profiles of green valley galaxies in the Evolution and Assembly of GaLaxies and their Environments (EAGLE; Crain et al., 2015; Schaye et al., 2015) and Illustris (Genel et al., 2014; Vogelsberger et al., 2014) with observations, Starkenburg et al. (2019) find that the simulations do not match the observations. Both cosmological simulations fail to reproduce the observed central suppression of sSFR, showing the opposite trend instead. Nelson et al. (2021) find that this discrepancy is somewhat mitigated with the improved AGN feedback in IllustrisTNG (Weinberger et al., 2018; Nelson et al., 2019). The radial sSFR profiles qualitatively match the behaviour of the observations. However, quantitatively, the sSFR is overpredicted in the inner regions of the galaxy. It is moderate for the SFMS galaxies, approximately a factor of 2 and only converges with the observations at galactocentric radii > 3 kpc. The difference is more drastic for the galaxies below the SFMS. There, the IllustrisTNG profile rises much more steeply, overpredicting the sSFR by up to ~ 0.6 dex and only converging with the observations at a radius of 5 kpc. SIMBA (Davé et al., 2019) is a cosmological simulation that actually has a cool ISM, H_2 -based star formation and halo quenching, in addition to sophisticated stellar and black hole feedback. Although it qualitatively predicts the centrally suppressed sSFR of green valley galaxies, it still overpredicts the sSFR by an order of magnitude (Appleby et al., 2020). Much work has been done on improving AGN feedback recipes for these cosmological simulations. However, these mismatches in the radial sSFR profiles, but also other star forming properties (e.g. Hahn et al., 2019; Iyer et al., 2020), highlight that (AGN) feedback on its own is not enough to match observations. Dynamical suppression naturally leads to the centrally suppressed sSFR of galaxies below the SFMS, but as Chapter 2 demonstrates, this is only truly visible when using a dynamics-dependent star formation sub-grid model.

5.3 Outlook

Following on from the key points highlighted in the discussion, particularly Section 5.2.3, the next step is to use environmentally-dependent SFEs in the star formation models of cosmological simulations. This we plan to do in the Empirically-Motivated Physics (EMP) simulations (Kruijssen et al. in preparation, Keller et al. in preparation). Because running a large cosmological volume at high baryonic resolution is very expensive, the first step towards this is through a suite of cosmological zoom-in simulations. The EMP-*Pathfinder* suite encompasses 25 galaxies drawn from the EAGLE (Schaye et al., 2015) volume, with Milky Way-masses ($M_{\text{halo}} \sim 10^{12} M_{\odot}$) at $z = 0$. Each galaxy is simulated twice, once with a constant SFE and once using the Gensior et al. (2020) environmentally-dependent SFE

introduced in Chapter 2 (Reina Campos, 2020, Reina-Campos et al. in preparation). With these simulations, I will study how the star forming properties of galaxies evolve across cosmic time and quantify how they contrast with predictions from traditional models. Key observables are global properties like galaxy masses, gas content, morphology, and star formation histories, but also gas properties, such as the sub-kpc ISM structure, velocity dispersion and virial parameters. With two realisations of the same galaxy, it will be possible to pinpoint the unique predictions of the cloud-scale SFE model. Furthermore, *EMP-Pathfinder* will be a first test for the prediction of Chapter 4: is the star formation activity dynamically suppressed below the SFMS in the more massive galaxies?

Another step is to use empirically-motivated sub-grid star formation models in simulations with AGN, as has recently been pioneered by Dubois et al. (2020). In Chapter 4 we speculate that dynamical suppression of fragmentation might act in symbiosis with AGN feedback, by building a large circumnuclear gas reservoir that could subsequently fuel the AGN (see also, e.g. Wada, 2004; Davies et al., 2007). Dedicated simulations will be able to determine if there is a symbiotic effect. Furthermore, specifically comparing cosmological (zoom-in) simulations with and without AGN will drive progress towards establishing whether bulge mass strongly correlates with quiescence due to the dynamical suppression of star formation, the presence of a SMBH, or a combination of both (e.g. Bluck et al., 2014, 2019). Density power spectra (and other turbulence statistics) of the gas in such cosmological zoom-in simulations will improve our understanding of what drives turbulence in galaxies. Potentially, they could reveal the underlying physical mechanism that causes the correlation between power spectrum slope and central gas surface density in the WISDOM galaxies found in Chapter 3.

Observationally, the future looks bright for improving our understanding of star formation and quenching. With upcoming observatories such as the James Webb Space Telescope and the Extremely Large Telescope it will be possible to obtain SFRs and star formation histories for a large number of galaxies across cosmic time. Observations of the star formation histories of such a wealth of galaxies will place strong constraints on quenching timescales and mechanisms. They can test if dynamical suppression does affect massive galaxies at low redshifts as predicted in Chapter 4. The *EMP-Pathfinder* and EMP galaxies are evolved self-consistently with an environmentally-dependent SFE that is calibrated on $z = 0$ star-forming clouds. Comparing results from these simulations to observations will pinpoint if cloud-scale star formation changes across cosmic time. In parallel, surveys such as PHANGS (Leroy et al., 2021b), which resolve gas on the GMC-scale in a large set of galaxies, will revolutionise our understanding of cloud-scale star formation and what drives the SFE. Thus, paving the way for empirically-motivated sub-grid models that are directly based on cloud-scale observations.

Concluding remarks

In this thesis, I have investigated the impact of the galactic gravitational potential on the interstellar medium and star formation activity of galaxies. This has demonstrated that shear induced by a dominant spheroidal component can drive sufficient turbulence to dynamically suppress first the fragmentation of gas into clouds and subsequently the star formation activity of the galaxy. Furthermore, I have shown that the dynamical suppression of star formation is a viable mechanism to keep massive galaxies with molecular gas reservoirs quiescent. However, dynamical suppression depends on initially reducing the cold gas fraction of a galaxy, if not keeping it low permanently, via a different quenching mechanism. This highlights that more work is required to fully understand what governs the star formation and quenching of galaxies.

Acknowledgements

It is a truth universally acknowledged,
that a young lady in possession of a
sharp mind must be in want of a PhD.

J. Austen, *PhD & Prejudice*

The first time I ever visited Heidelberg was a bit more than four years ago, for the PhD interviews. When I walked through town, my thoughts went something like »*I would really like to live here, I hope that I get offered a project I want to work on*« and the rest, as they say, is history. A massive thank you to my supervisor Diederik Kruijssen for offering me this chance and project. I have grown a lot, both scientifically and personally, over the past four years, and this would not have been possible in other circumstances. I am also deeply grateful to Ralf Klessen and Henrik Beuther for being on my thesis committee and refereeing this thesis, as well as to Anna Pasquali and Björn Malte Schäfer for being part of my examination committee. During my time in Heidelberg, I have been lucky to be part of the IMPRS-HD and the HGSFP. A lot of people are continuously working behind the scenes to make sure that PhD students can focus on their research, thesis writing, etc., always being available for (admin) help and having ones back. Thank you all for the stellar jobs you have done, the help and support over the years, and particularly the (unexpected) nuggets of kindness that manage to salvage even the worst and most stressful situations.

Sadly the plague prevented me from visiting you in person, Martin Bureau and Tim Davis, but it has nonetheless been a pleasure to collaborate with you and the WISDOM team. I have learned a lot from the two of you and for that I am incredibly grateful. Special thanks to Tim for always answering my I-do-not-understand-(ALMA)-observations questions so quickly and comprehensively; you made sure that I did not just hopelessly despair when faced with observational data. The MUSTANG group is also deserving of an enormous thanks, I am glad I got to embark on this science journey alongside you all (roughly in order of appearance): Alex Hygate, Dan Haydon, Marta Reina-Campos, Sarah Jeffreson, Mélanie Chevance, Jake Ward, Ben Keller, Sebastian Trujillo-Gomez, Maya Petkova, Jaeyeon Kim, Verena Fürnkranz, Andrew Winter, Louise Kluge and Leon Fordinal. Special shout-outs to Ben and Sebastian for being my office mates – I do not think I will ever miss the instant ramen concertos at 3pm, but I certainly remember them with fond nostalgia; to Maya for being a fellow dancer; to Marta for patiently showing me the ropes; and to Leon (and Louise) – supervising and advising you has been a pleasure,

with the additional bonus of teaching me a lot of things along the way.

Last, but most importantly, I would like to express my gratitude towards everyone outside of academia who has helped and supported me throughout this journey. Thank you to all the fabulous dancing associations and assorted people that have kept me sane and well-exercised throughout this PhD: the New Scotland old guard, the SchloB dancers and the SwingStep community. Many thanks to all my friends old and "new" – especially to Jet, for keeping me well stashed with Lemon Sherbets and PG Tips, but more importantly for being such a fabulous human being that is at most a call away; and to Tom and Helen for being there since the beginning. My eternal love and gratitude to my parents, siblings and my Reading family – I could not be here without you. Finally, Florian – instead of walking the other way when I spent our first date in the what-am-I-doing-with-my-life-and-why-did-I-think-a-PhD-was-a-good-idea funk, you stuck around and made my life all the better for it.

This thesis is dedicated to Ryan, the best host father one could wish for. My sleep rhythm could certainly have benefited from some of your late night interventions, and it saddens me greatly that you are no longer here to witness it, but I have made it – thank you for everything.

* * *

We thank Volker Springel for allowing us access to Arepo.

The authors acknowledge support by the High Performance and Cloud Computing Group at the Zentrum für Datenverarbeitung of the University of Tübingen, the state of Baden-Württemberg through bwHPC and the German Research Foundation (DFG) through grant no INST 37/935-1 FUGG.

This thesis makes use of the following ALMA data: ADS/JAO.ALMA #2013.1.00493.S #2015.1.00419.S #2015.1.00466.S #2015.1.00597.S #2016.1.00419.S #2016.1.00437.S #2016.2.00053.S #2017.1.00391.S #2017.1.00572.S #2017.1.00904.S #2017.1.00907.S. ALMA is a partnership of ESO (representing its member states), NSF (USA) and NINS (Japan), together with NRC (Canada), MOST and ASIAA (Taiwan), and KASI (Republic of Korea), in cooperation with the Republic of Chile. The Joint ALMA Observatory is operated by ESO, AUI/NRAO, and NAOJ.

This research has made use of the NASA/IPAC Extragalactic Database (NED), which is operated by the Jet Propulsion Laboratory, California Institute of Technology, under contract with the National Aeronautics and Space Administration.

This thesis has also made use of the HyperLeda database (<http://leda.univ-lyon1.fr>).

I gratefully acknowledge funding from the Deutsche Forschungsgemeinschaft (DFG, German Research Foundation) through an Emmy Noether Research grant (grant number KR4801/1-1), as well as from the European Research Council (ERC) under the European Union's Horizon 2020 research and innovation programme via the ERC Starting Grant MUSTANG (grant agreement number 714907), both held by Diederik Kruijssen.

Images from the World Wide Web

Figure 1.1. Image credit: STScI; downloaded from <https://hubblesite.org/contents/media/images/1999/34/890-Image.html> in April 2021. The image is in the public domain, as specified by the hubblesite's copyright policy.

Figure 1.3: The underlying image of M82 is from <https://apod.nasa.gov/apod/ap160221.html>, downloaded in April 2021. Image credit: NASA, ESA, The Hubble Heritage Team, (STScI/AURA); M.Mountain (STScI), P.Puxley (NSF), J. Gallagher (U. Wisconsin). As a NASA image, it is in the public domain as per the NASA media usage guidelines.

Bibliography

- Abadi, Mario G., Ben Moore, and Richard G. Bower (Oct. 1999). “Ram pressure stripping of spiral galaxies in clusters”. *MNRAS* 308.4, 947–954. arXiv: astro-ph/9903436 [astro-ph] (cit. on p. 11).
- Abramson, Louis E. et al. (Apr. 2014). “The Mass-independence of Specific Star Formation Rates in Galactic Disks”. *ApJ* 785.2, L36, L36. arXiv: 1402.7076 [astro-ph.GA] (cit. on p. 9).
- Agertz, Oscar and Andrey V. Kravtsov (May 2015). “On the Interplay between Star Formation and Feedback in Galaxy Formation Simulations”. *ApJ* 804.1, 18, 18. arXiv: 1404.2613 [astro-ph.GA] (cit. on p. 12).
- Agertz, Oscar et al. (June 2013). “Toward a Complete Accounting of Energy and Momentum from Stellar Feedback in Galaxy Formation Simulations”. *ApJ* 770.1, 25, 25. arXiv: 1210.4957 [astro-ph.CO] (cit. on pp. 14, 33, 43, 96).
- Alves, João, Marco Lombardi, and Charles J. Lada (Oct. 2017). “The shapes of column density PDFs. The importance of the last closed contour”. *A&A* 606, L2, L2. arXiv: 1707.02636 [astro-ph.GA] (cit. on p. 18).
- André, Ph. et al. (Apr. 2011). “Origin of the prestellar core mass function and link to the IMF - Herschel first results”. *Computational Star Formation*. Ed. by João. Alves et al. Vol. 270, 255–262 (cit. on p. 18).
- Appleby, Sarah et al. (June 2020). “The impact of quenching on galaxy profiles in the SIMBA simulation”. *MNRAS* 494.4, 6053–6071. arXiv: 1911.02041 [astro-ph.GA] (cit. on p. 118).
- Asplund, Martin et al. (Sept. 2009). “The Chemical Composition of the Sun”. *ARA&A* 47.1, 481–522. arXiv: 0909.0948 [astro-ph.SR] (cit. on p. 16).
- Aumer, Michael et al. (Oct. 2013). “Towards a more realistic population of bright spiral galaxies in cosmological simulations”. *MNRAS* 434.4, 3142–3164. arXiv: 1304.1559 [astro-ph.GA] (cit. on p. 12).
- Babyk, Iu. V. et al. (Dec. 2019). “Origins of Molecular Clouds in Early-type Galaxies”. *ApJ* 887.2, 149, 149. arXiv: 1810.11465 [astro-ph.GA] (cit. on p. 4).
- Bacchini, Cecilia et al. (Feb. 2019). “Volumetric star formation laws of disc galaxies”. *A&A* 622, A64, A64. arXiv: 1810.03616 [astro-ph.GA] (cit. on p. 6).
- Bacchini, Cecilia et al. (Dec. 2020). “The volumetric star formation law for nearby galaxies. Extension to dwarf galaxies and low-density regions”. *A&A* 644, A125, A125. arXiv: 2010.07948 [astro-ph.GA] (cit. on p. 6).

- Baggett, W. E., S. M. Baggett, and K. S. J. Anderson (Oct. 1998). “Bulge-Disk Decomposition of 659 Spiral and Lenticular Galaxy Brightness Profiles”. *AJ* 116.4, 1626–1642. arXiv: astro-ph/9807047 [astro-ph] (cit. on p. 74).
- Balbus, Steven A. and John F. Hawley (Jan. 1998). “Instability, turbulence, and enhanced transport in accretion disks”. *Reviews of Modern Physics* 70.1, 1–53 (cit. on p. 19).
- Baldry, Ivan K. et al. (Jan. 2004). “Quantifying the Bimodal Color-Magnitude Distribution of Galaxies”. *ApJ* 600.2, 681–694. arXiv: astro-ph/0309710 [astro-ph] (cit. on p. 3).
- Balogh, Michael L., Julio F. Navarro, and Simon L. Morris (Sept. 2000). “The Origin of Star Formation Gradients in Rich Galaxy Clusters”. *ApJ* 540.1, 113–121. arXiv: astro-ph/0004078 [astro-ph] (cit. on p. 11).
- Balogh, Michael L. et al. (Oct. 2001). “Revisiting the cosmic cooling crisis”. *MNRAS* 326.4, 1228–1234. arXiv: astro-ph/0104041 [astro-ph] (cit. on p. 4).
- Barnes, A. T. et al. (Aug. 2017). “Star formation rates and efficiencies in the Galactic Centre”. *MNRAS* 469.2, 2263–2285. arXiv: 1704.03572 [astro-ph.GA] (cit. on p. 22).
- Barnes, Joshua E. (Aug. 1988). “Encounters of Disk/Halo Galaxies”. *ApJ* 331, 699 (cit. on p. 4).
- Barro, Guillermo et al. (Mar. 2013). “CANDELS: The Progenitors of Compact Quiescent Galaxies at $z \sim 2$ ”. *ApJ* 765.2, 104, 104. arXiv: 1206.5000 [astro-ph.CO] (cit. on p. 97).
- Barro, Guillermo et al. (May 2017). “Structural and Star-forming Relations since $z \sim 3$: Connecting Compact Star-forming and Quiescent Galaxies”. *ApJ* 840.1, 47, 47. arXiv: 1509.00469 [astro-ph.GA] (cit. on p. 97).
- Begum, Ayesha, Jayaram N. Chengalur, and Somnath Bhardwaj (Oct. 2006). “Power spectrum of HI intensity fluctuations in DDO 210”. *MNRAS* 372.1, L33–L37. arXiv: astro-ph/0607367 [astro-ph] (cit. on p. 70).
- Behroozi, Peter et al. (Sept. 2019). “UNIVERSEMACHINE: The correlation between galaxy growth and dark matter halo assembly from $z = 0-10$ ”. *MNRAS* 488.3, 3143–3194. arXiv: 1806.07893 [astro-ph.GA] (cit. on pp. 108, 109).
- Belfiore, F. et al. (July 2019). “From ‘bathtub’ galaxy evolution models to metallicity gradients”. *MNRAS* 487.1, 456–474. arXiv: 1903.05105 [astro-ph.GA] (cit. on pp. 15, 112).
- Belfiore, Francesco et al. (July 2018). “SDSS IV MaNGA - sSFR profiles and the slow quenching of discs in green valley galaxies”. *MNRAS* 477.3, 3014–3029. arXiv: 1710.05034 [astro-ph.GA] (cit. on pp. 31, 32, 116).
- Belli, Sirio et al. (Mar. 2021). “The Diverse Molecular Gas Content of Massive Galaxies Undergoing Quenching at $z \sim 1$ ”. *ApJ* 909.1, L11, L11. arXiv: 2102.07881 [astro-ph.GA] (cit. on p. 117).
- Bertoldi, Frank and Christopher F. McKee (Aug. 1992). “Pressure-confined Clumps in Magnetized Molecular Clouds”. *ApJ* 395, 140 (cit. on pp. 19, 34).
- Best, P. N. et al. (Sept. 2005). “The host galaxies of radio-loud active galactic nuclei: mass dependences, gas cooling and active galactic nuclei feedback”. *MNRAS* 362.1, 25–40. arXiv: astro-ph/0506269 [astro-ph] (cit. on p. 117).

- Bigiel, F. et al. (Dec. 2008). “The Star Formation Law in Nearby Galaxies on Sub-Kpc Scales”. *AJ* 136.6, 2846–2871. arXiv: 0810.2541 [astro-ph] (cit. on pp. 5, 6, 18, 31, 33, 68, 75, 97, 104, 118).
- Bigiel, Frank et al. (May 2016). “The EMPIRE Survey: Systematic Variations in the Dense Gas Fraction and Star Formation Efficiency from Full-disk Mapping of M51”. *ApJ* 822.2, L26, L26. arXiv: 1604.05316 [astro-ph.GA] (cit. on pp. 7, 22, 26, 116).
- Binney, James and Scott Tremaine (2008). *Galactic Dynamics: Second Edition*. Princeton University Press (cit. on p. 20).
- Birnboim, Yuval and Avishai Dekel (Oct. 2003). “Virial shocks in galactic haloes?” *MNRAS* 345.1, 349–364. arXiv: astro-ph/0302161 [astro-ph] (cit. on pp. 11, 117).
- Bland-Hawthorn, Joss and Ortwin Gerhard (Sept. 2016). “The Galaxy in Context: Structural, Kinematic, and Integrated Properties”. *ARA&A* 54, 529–596. arXiv: 1602.07702 [astro-ph.GA] (cit. on p. 40).
- Blanton, Michael R. and John Moustakas (Sept. 2009). “Physical Properties and Environments of Nearby Galaxies”. *ARA&A* 47.1, 159–210. arXiv: 0908.3017 [astro-ph.GA] (cit. on p. 4).
- Blitz, Leo and Erik Rosolowsky (Oct. 2006). “The Role of Pressure in GMC Formation II: The H₂-Pressure Relation”. *ApJ* 650.2, 933–944. arXiv: astro-ph/0605035 [astro-ph] (cit. on p. 19).
- Block, David L. et al. (July 2010). “A Two-component Power Law Covering Nearly Four Orders of Magnitude in the Power Spectrum of Spitzer Far-infrared Emission from the Large Magellanic Cloud”. *ApJ* 718.1, L1–L6. arXiv: 1006.2080 [astro-ph.CO] (cit. on p. 69).
- Bluck, Asa F. L. et al. (June 2014). “Bulge mass is king: the dominant role of the bulge in determining the fraction of passive galaxies in the Sloan Digital Sky Survey”. *MNRAS* 441.1, 599–629. arXiv: 1403.5269 [astro-ph.GA] (cit. on pp. 12, 13, 119).
- Bluck, Asa F. L. et al. (May 2019). “What shapes a galaxy? - unraveling the role of mass, environment, and star formation in forming galactic structure”. *MNRAS* 485.1, 666–696. arXiv: 1902.01665 [astro-ph.GA] (cit. on pp. 12, 13, 110, 119).
- Bogdán, Ákos et al. (Nov. 2017). “Probing the Hot X-Ray Corona around the Massive Spiral Galaxy, NGC 6753, Using Deep XMM-Newton Observations”. *ApJ* 850.1, 98, 98. arXiv: 1710.07286 [astro-ph.GA] (cit. on p. 74).
- Bolatto, Alberto D., Mark Wolfire, and Adam K. Leroy (Aug. 2013). “The CO-to-H₂ Conversion Factor”. *ARA&A* 51.1, 207–268. arXiv: 1301.3498 [astro-ph.GA] (cit. on p. 5).
- Bolatto, Alberto D. et al. (Sept. 2017). “The EDGE-CALIFA Survey: Interferometric Observations of 126 Galaxies with CARMA”. *ApJ* 846.2, 159, 159. arXiv: 1704.02504 [astro-ph.GA] (cit. on p. 6).
- Bonazzola, S. et al. (Jan. 1987). “Jeans collapse in a turbulent medium”. *A&A* 172.1-2, 293–298 (cit. on p. 23).
- Bonnor, W. B. (Jan. 1956). “Boyle’s Law and gravitational instability”. *MNRAS* 116, 351 (cit. on p. 20).

- Bouché, N. et al. (Aug. 2010). “The Impact of Cold Gas Accretion Above a Mass Floor on Galaxy Scaling Relations”. *ApJ* 718.2, 1001–1018. arXiv: 0912.1858 [astro-ph.CO] (cit. on pp. 15, 96).
- Bournaud, Frédéric et al. (Dec. 2010). “ISM properties in hydrodynamic galaxy simulations: turbulence cascades, cloud formation, role of gravity and feedback”. *MNRAS* 409.3, 1088–1099. arXiv: 1007.2566 [astro-ph.CO] (cit. on pp. 81, 91).
- Bower, R. G. et al. (Aug. 2006). “Breaking the hierarchy of galaxy formation”. *MNRAS* 370.2, 645–655. arXiv: astro-ph/0511338 [astro-ph] (cit. on pp. 11, 97, 112, 117).
- Brammer, Gabriel B. et al. (Sept. 2011). “The Number Density and Mass Density of Star-forming and Quiescent Galaxies at $0.4 \leq z \leq 2.2$ ”. *ApJ* 739.1, 24, 24. arXiv: 1104.2595 [astro-ph.CO] (cit. on p. 3).
- Brownson, Simcha et al. (Nov. 2020). “What drives galaxy quenching? Resolving molecular gas and star formation in the green valley”. *MNRAS* 498.1, L66–L71. arXiv: 2007.02976 [astro-ph.GA] (cit. on pp. 110, 115).
- Brunt, C. M., M. H. Heyer, and M. -M. Mac Low (Sept. 2009). “Turbulent driving scales in molecular clouds”. *A&A* 504.3, 883–890. arXiv: 0910.0398 [astro-ph.GA] (cit. on p. 19).
- Buitrago, Fernando et al. (Jan. 2013). “Early-type galaxies have been the predominant morphological class for massive galaxies since only $z \sim 1$ ”. *MNRAS* 428.2, 1460–1478. arXiv: 1111.6993 [astro-ph.CO] (cit. on pp. 9, 109).
- Bundy, Kevin et al. (Nov. 2006). “The Mass Assembly History of Field Galaxies: Detection of an Evolving Mass Limit for Star-Forming Galaxies”. *ApJ* 651.1, 120–141. arXiv: astro-ph/0512465 [astro-ph] (cit. on pp. 9, 109).
- Bundy, Kevin et al. (Aug. 2010). “The Rise and Fall of Passive Disk Galaxies: Morphological Evolution Along the Red Sequence Revealed by COSMOS”. *ApJ* 719.2, 1969–1983. arXiv: 0912.1077 [astro-ph.CO] (cit. on pp. 9, 109).
- Burgers, J. M. (1939). “Mathematical examples illustrating relations occurring in the theory of turbulent fluid motion”. *Verhandelingen der Koninklijke Nederlandsche Akademie van Wetenschappen, Afdeling Natuurkunde* 17.2, 1–53 (cit. on pp. 17, 18, 69).
- Burkhart, Blakesley (Aug. 2018). “The Star Formation Rate in the Gravoturbulent Interstellar Medium”. *ApJ* 863.2, 118, 118. arXiv: 1801.05428 [astro-ph.GA] (cit. on pp. 24–26, 34).
- Burkhart, Blakesley and Philip Mocz (July 2019). “The Self-gravitating Gas Fraction and the Critical Density for Star Formation”. *ApJ* 879.2, 129, 129. arXiv: 1805.11104 [astro-ph.GA] (cit. on p. 26).
- Burkhart, Blakesley, Kye Stalpes, and David C. Collins (Jan. 2017). “The Razor’s Edge of Collapse: The Transition Point from Lognormal to Power-Law Distributions in Molecular Clouds”. *ApJ* 834.1, L1, L1. arXiv: 1609.04409 [astro-ph.GA] (cit. on pp. 17, 25, 26).
- Burkhart, Blakesley et al. (Jan. 2010). “Characterizing Magnetohydrodynamic Turbulence in the Small Magellanic Cloud”. *ApJ* 708.2, 1204–1220. arXiv: 0911.3652 [astro-ph.GA] (cit. on pp. 16, 26).

- Burkhart, Blakesley et al. (Oct. 2015). “The Lognormal Probability Distribution Function of the Perseus Molecular Cloud: A Comparison of HI and Dust”. *ApJ* 811.2, L28, L28. arXiv: 1509.02889 [astro-ph.GA] (cit. on p. 26).
- Caldú-Primo, Anahi et al. (Dec. 2013). “A High-dispersion Molecular Gas Component in Nearby Galaxies”. *AJ* 146.6, 150, 150. arXiv: 1309.6324 [astro-ph.CO] (cit. on pp. 17, 18).
- Caldwell, Spencer and Philip Chang (Mar. 2018). “The accelerating pace of star formation”. *MNRAS* 474.4, 4818–4823. arXiv: 1711.07512 [astro-ph.GA] (cit. on p. 25).
- Calzetti, Daniela (2013). “Star Formation Rate Indicators”. *Secular Evolution of Galaxies*. Ed. by Jesús Falcón-Barroso and Johan H. Knapen, 419 (cit. on p. 5).
- Cappellari, Michele et al. (May 2011a). “The ATLAS^{3D} project - I. A volume-limited sample of 260 nearby early-type galaxies: science goals and selection criteria”. *MNRAS* 413.2, 813–836. arXiv: 1012.1551 [astro-ph.CO] (cit. on p. 74).
- Cappellari, Michele et al. (Sept. 2011b). “The ATLAS^{3D} project - VII. A new look at the morphology of nearby galaxies: the kinematic morphology-density relation”. *MNRAS* 416.3, 1680–1696. arXiv: 1104.3545 [astro-ph.CO] (cit. on p. 2).
- Carnall, A. C. et al. (July 2020). “Timing the earliest quenching events with a robust sample of massive quiescent galaxies at $2 < z < 5$ ”. *MNRAS* 496.1, 695–707. arXiv: 2001.11975 [astro-ph.GA] (cit. on p. 10).
- Carroll, Bradley W. and Dale A. Ostlie (2006). *An introduction to modern astrophysics and cosmology*. Pearson, Addison-Wesely (cit. on p. 4).
- Catalán-Torrecilla, C. et al. (Oct. 2017). “Star Formation in the Local Universe from the CALIFA Sample. II. Activation and Quenching Mechanisms in Bulges, Bars, and Disks”. *ApJ* 848.2, 87, 87. arXiv: 1709.01035 [astro-ph.GA] (cit. on p. 9).
- Catinella, Barbara et al. (May 2018). “xGASS: total cold gas scaling relations and molecular-to-atomic gas ratios of galaxies in the local Universe”. *MNRAS* 476.1, 875–895. arXiv: 1802.02373 [astro-ph.GA] (cit. on pp. 32, 58, 59, 65, 103–106).
- Cen, Renyue and Jeremiah P. Ostriker (Nov. 1992). “Galaxy Formation and Physical Bias”. *ApJ* 399, L113 (cit. on p. 30).
- Ceverino, Daniel, Avishai Dekel, and Frederic Bournaud (June 2010). “High-redshift clumpy discs and bulges in cosmological simulations”. *MNRAS* 404.4, 2151–2169. arXiv: 0907.3271 [astro-ph.CO] (cit. on p. 13).
- Chabrier, Gilles (July 2003). “Galactic Stellar and Substellar Initial Mass Function”. *PASP* 115.809, 763–795. arXiv: astro-ph/0304382 [astro-ph] (cit. on pp. 38, 73, 100).
- Chevalier, R. A. and A. W. Clegg (Sept. 1985). “Wind from a starburst galaxy nucleus”. *Nature* 317.6032, 44–45 (cit. on pp. 12, 14).
- Chevance, Mélanie et al. (Oct. 2020a). “Pre-supernova feedback mechanisms drive the destruction of molecular clouds in nearby star-forming disc galaxies”. *arXiv e-prints*, arXiv:2010.13788, arXiv:2010.13788. arXiv: 2010.13788 [astro-ph.GA] (cit. on pp. 22, 73, 100).
- Chevance, Mélanie et al. (Apr. 2020b). “The lifecycle of molecular clouds in nearby star-forming disc galaxies”. *MNRAS* 493.2, 2872–2909. arXiv: 1911.03479 [astro-ph.GA] (cit. on pp. 18, 22, 33, 38, 73, 100, 101).

- Chevance, Mélanie et al. (Apr. 2020c). “The Molecular Cloud Lifecycle”. *Space Sci. Rev.* 216.4, 50, 50. arXiv: 2004.06113 [astro-ph.GA] (cit. on pp. 18–20, 22).
- Chisholm, John et al. (Oct. 2015). “Scaling Relations Between Warm Galactic Outflows and Their Host Galaxies”. *ApJ* 811.2, 149, 149. arXiv: 1412.2139 [astro-ph.GA] (cit. on p. 14).
- Cho, Jungyeon and A. Lazarian (Oct. 2003). “Compressible magnetohydrodynamic turbulence: mode coupling, scaling relations, anisotropy, viscosity-damped regime and astrophysical implications”. *MNRAS* 345.12, 325–339. arXiv: astro-ph/0301062 [astro-ph] (cit. on p. 18).
- Christensen, Charlotte et al. (Oct. 2012). “Implementing molecular hydrogen in hydrodynamic simulations of galaxy formation”. *MNRAS* 425.4, 3058–3076. arXiv: 1205.5567 [astro-ph.CO] (cit. on p. 33).
- Cioffi, Denis F., Christopher F. McKee, and Edmund Bertschinger (Nov. 1988). “Dynamics of Radiative Supernova Remnants”. *ApJ* 334, 252 (cit. on p. 38).
- Colbert, James W., John S. Mulchaey, and Ann I. Zabludoff (Feb. 2001). “The Optical and Near-Infrared Morphologies of Isolated Early-Type Galaxies”. *AJ* 121.2, 808–819. arXiv: astro-ph/0010534 [astro-ph] (cit. on p. 4).
- Collins, David C. et al. (May 2012). “The Two States of Star-forming Clouds”. *ApJ* 750.1, 13, 13. arXiv: 1202.2594 [astro-ph.SR] (cit. on pp. 17, 25).
- Colombo, D. et al. (Mar. 2019). “The integrated properties of the molecular clouds from the JCMT CO(3-2) High-Resolution Survey”. *MNRAS* 483.4, 4291–4340. arXiv: 1812.04688 [astro-ph.GA] (cit. on pp. 19, 20).
- Colombo, D. et al. (Dec. 2020). “The EDGE-CALIFA survey: exploring the role of molecular gas on galaxy star formation quenching”. *A&A* 644, A97, A97. arXiv: 2009.08383 [astro-ph.GA] (cit. on pp. 115, 117).
- Combes, F. et al. (Mar. 2012). “Dust and gas power spectrum in M 33 (HERM33ES)”. *A&A* 539, A67, A67. arXiv: 1201.2558 [astro-ph.CO] (cit. on pp. 69, 70, 91, 92).
- Combes, Françoise, Lisa M. Young, and Martin Bureau (June 2007). “Molecular gas and star formation in the SAURON early-type galaxies”. *MNRAS* 377.4, 1795–1807. arXiv: astro-ph/0703557 [astro-ph] (cit. on p. 4).
- Conselice, Christopher J. (Aug. 2014). “The Evolution of Galaxy Structure Over Cosmic Time”. *ARA&A* 52, 291–337. arXiv: 1403.2783 [astro-ph.GA] (cit. on p. 2).
- Cook, Robin H. W. et al. (Apr. 2020). “xGASS: the role of bulges along and across the local star-forming main sequence”. *MNRAS* 493.4, 5596–5605. arXiv: 2003.02464 [astro-ph.GA] (cit. on pp. 8–10, 110).
- Cox, Donald P. (Sept. 2005). “The Three-Phase Interstellar Medium Revisited”. *ARA&A* 43.1, 337–385 (cit. on p. 16).
- Crain, Robert A. et al. (June 2015). “The EAGLE simulations of galaxy formation: calibration of subgrid physics and model variations”. *MNRAS* 450.2, 1937–1961. arXiv: 1501.01311 [astro-ph.GA] (cit. on p. 118).
- Crocker, Alison et al. (Apr. 2012). “The ATLAS^{3D} project - XI. Dense molecular gas properties of CO-luminous early-type galaxies”. *MNRAS* 421.2, 1298–1314. arXiv: 1112.3641 [astro-ph.CO] (cit. on p. 7).

- Croton, Darren J. et al. (Jan. 2006). “The many lives of active galactic nuclei: cooling flows, black holes and the luminosities and colours of galaxies”. MNRAS 365.1, 11–28. arXiv: [astro-ph/0508046](#) [astro-ph] (cit. on pp. 11, 97, 112, 117).
- Crovisier, J. and J. M. Dickey (June 1983). “The spatial power spectrum of galactic neutral hydrogen from observations of the 21-cm emission line.” A&A 122, 282–296 (cit. on p. 69).
- Daddi, E. et al. (Nov. 2007). “Multiwavelength Study of Massive Galaxies at $z \sim 2$. I. Star Formation and Galaxy Growth”. ApJ 670.1, 156–172. arXiv: [0705.2831](#) [astro-ph] (cit. on p. 8).
- Dalla Vecchia, Claudio and Joop Schaye (Oct. 2012). “Simulating galactic outflows with thermal supernova feedback”. MNRAS 426.1, 140–158. arXiv: [1203.5667](#) [astro-ph.GA] (cit. on p. 38).
- Davé, Romeel, Kristian Finlator, and Benjamin D. Oppenheimer (Mar. 2012). “An analytic model for the evolution of the stellar, gas and metal content of galaxies”. MNRAS 421.1, 98–107. arXiv: [1108.0426](#) [astro-ph.CO] (cit. on p. 15).
- Davé, Romeel, Mika H. Rafieferantsoa, and Robert J. Thompson (Oct. 2017). “mufasa: the assembly of the red sequence”. MNRAS 471.2, 1671–1687. arXiv: [1704.01135](#) [astro-ph.GA] (cit. on pp. 11, 111).
- Davé, Romeel et al. (June 2019). “SIMBA: Cosmological simulations with black hole growth and feedback”. MNRAS 486.2, 2827–2849. arXiv: [1901.10203](#) [astro-ph.GA] (cit. on p. 118).
- Davies, R. I. et al. (Dec. 2007). “A Close Look at Star Formation around Active Galactic Nuclei”. ApJ 671.2, 1388–1412. arXiv: [0704.1374](#) [astro-ph] (cit. on p. 119).
- Davis, Timothy A., Nikki Zabel, and James M. Dawson (June 2020a). *KinMS: Three-dimensional kinematic modelling of arbitrary gas distributions*. ascl: 2006.003 (cit. on p. 73).
- Davis, Timothy A. et al. (Feb. 2013a). “A black-hole mass measurement from molecular gas kinematics in NGC4526”. Nature 494.7437, 328–330. arXiv: [1301.7184](#) [astro-ph.CO] (cit. on p. 73).
- Davis, Timothy A. et al. (Feb. 2013b). “The ATLAS^{3D} Project - XIV. The extent and kinematics of the molecular gas in early-type galaxies”. MNRAS 429.1, 534–555. arXiv: [1211.1011](#) [astro-ph.CO] (cit. on pp. 4, 166).
- Davis, Timothy A. et al. (Nov. 2014). “The ATLAS^{3D} Project - XXVIII. Dynamically driven star formation suppression in early-type galaxies”. MNRAS 444.4, 3427–3445. arXiv: [1403.4850](#) [astro-ph.GA] (cit. on pp. 6, 7, 12, 13, 15, 31, 43, 68, 97, 117).
- Davis, Timothy A. et al. (June 2015). “Molecular and atomic gas in dust lane early-type galaxies - I. Low star formation efficiencies in minor merger remnants”. MNRAS 449.4, 3503–3516. arXiv: [1503.05162](#) [astro-ph.GA] (cit. on pp. 15, 117).
- Davis, Timothy A. et al. (July 2017). “WISDOM Project - II. Molecular gas measurement of the supermassive black hole mass in NGC 4697”. MNRAS 468.4, 4675–4690. arXiv: [1703.05248](#) [astro-ph.GA] (cit. on p. 75).

- Davis, Timothy A. et al. (Jan. 2018). “WISDOM Project - III. Molecular gas measurement of the supermassive black hole mass in the barred lenticular galaxy NGC4429”. MNRAS 473.3, 3818–3834. arXiv: 1710.01488 [astro-ph.GA] (cit. on pp. 74, 75, 77).
- Davis, Timothy A. et al. (June 2019). “The MASSIVE survey - XI. What drives the molecular gas properties of early-type galaxies”. MNRAS 486.1, 1404–1423. arXiv: 1903.08884 [astro-ph.GA] (cit. on pp. 4, 31, 68, 112, 117).
- Davis, Timothy A. et al. (Aug. 2020b). “Revealing the intermediate-mass black hole at the heart of the dwarf galaxy NGC 404 with sub-parsec resolution ALMA observations”. MNRAS 496.4, 4061–4078. arXiv: 2007.05536 [astro-ph.GA] (cit. on pp. 74, 75).
- de los Reyes, Mithi A. C. and Jr. Kennicutt Robert C. (Feb. 2019). “Revisiting the Integrated Star Formation Law. I. Non-starbursting Galaxies”. ApJ 872.1, 16, 16. arXiv: 1901.01283 [astro-ph.GA] (cit. on pp. 5, 31, 68).
- Dekel, A. and J. Silk (Apr. 1986). “The Origin of Dwarf Galaxies, Cold Dark Matter, and Biased Galaxy Formation”. ApJ 303, 39 (cit. on p. 12).
- Dekel, A. et al. (Jan. 2009). “Cold streams in early massive hot haloes as the main mode of galaxy formation”. Nature 457.7228, 451–454. arXiv: 0808.0553 [astro-ph] (cit. on pp. 11, 14).
- Dekel, A. et al. (Oct. 2013). “Toy models for galaxy formation versus simulations”. MNRAS 435.2, 999–1019. arXiv: 1303.3009 [astro-ph.CO] (cit. on pp. 15, 96).
- Dekel, Avishai and Yuval Birnboim (May 2006). “Galaxy bimodality due to cold flows and shock heating”. MNRAS 368.1, 2–20. arXiv: astro-ph/0412300 [astro-ph] (cit. on pp. 11, 97, 111, 117).
- (Jan. 2008). “Gravitational quenching in massive galaxies and clusters by clumpy accretion”. MNRAS 383.1, 119–138. arXiv: 0707.1214 [astro-ph] (cit. on p. 11).
- Dekel, Avishai and Nir Mandelker (Nov. 2014). “An analytic solution for the minimal bathtub toy model: challenges in the star formation history of high-z galaxies”. MNRAS 444.3, 2071–2084. arXiv: 1402.2283 [astro-ph.CO] (cit. on pp. 15, 97).
- den Brok, J. S. et al. (July 2021). “New constraints on the $^{12}\text{CO}(2-1)/(1-0)$ line ratio across nearby disc galaxies”. MNRAS 504.3, 3221–3245. arXiv: 2103.10442 [astro-ph.GA] (cit. on p. 75).
- Di Matteo, Tiziana, Volker Springel, and Lars Hernquist (Feb. 2005). “Energy input from quasars regulates the growth and activity of black holes and their host galaxies”. Nature 433.7026, 604–607. arXiv: astro-ph/0502199 [astro-ph] (cit. on p. 11).
- Diemand, Jürg, Michael Kuhlen, and Piero Madau (Oct. 2007). “Formation and Evolution of Galaxy Dark Matter Halos and Their Substructure”. ApJ 667.2, 859–877. arXiv: astro-ph/0703337 [astro-ph] (cit. on p. 11).
- Dobbs, C. L. et al. (Jan. 2014). “Formation of Molecular Clouds and Global Conditions for Star Formation”. *Protostars and Planets VI*. Ed. by Henrik Beuther et al., 3. arXiv: 1312.3223 [astro-ph.GA] (cit. on p. 19).
- Donnari, Martina et al. (June 2019). “The star formation activity of IllustrisTNG galaxies: main sequence, UVJ diagram, quenched fractions, and systematics”. MNRAS 485.4, 4817–4840. arXiv: 1812.07584 [astro-ph.GA] (cit. on pp. 9, 10, 112).

- Draine, Bruce T. (2011). *Physics of the Interstellar and Intergalactic Medium*. Princeton University Press (cit. on p. 16).
- Dubois, Y. and R. Teyssier (Jan. 2008). “On the onset of galactic winds in quiescent star forming galaxies”. *A&A* 477.1, 79–94. arXiv: 0707.3376 [astro-ph] (cit. on p. 38).
- Dubois, Yohan et al. (Sept. 2020). “Introducing the NewHorizon simulation: galaxy properties with resolved internal dynamics across cosmic time”. *arXiv e-prints*, arXiv:2009.10578, arXiv:2009.10578. arXiv: 2009.10578 [astro-ph.GA] (cit. on p. 119).
- Dutta, Prasun et al. (Feb. 2008). “HI power spectrum of the spiral galaxy NGC628”. *MNRAS* 384.1, L34–L37. arXiv: 0711.1234 [astro-ph] (cit. on p. 70).
- (Sept. 2009a). “A study of interstellar medium of dwarf galaxies using HI power spectrum analysis”. *MNRAS* 398.2, 887–897. arXiv: 0905.1756 [astro-ph.GA] (cit. on pp. 69, 70, 84, 92).
- (July 2009b). “The scaleheight of NGC 1058 measured from its HI power spectrum”. *MNRAS* 397.1, L60–L63. arXiv: 0905.1450 [astro-ph.GA] (cit. on pp. 70, 77, 92).
- (June 2010). “Turbulence in the harassed galaxy NGC4254”. *MNRAS* 405.1, L102–L106. arXiv: 1004.1528 [astro-ph.GA] (cit. on p. 90).
- (Feb. 2013). “Probing interstellar turbulence in spiral galaxies using H I power spectrum analysis”. *New Ast.* 19, 89–98. arXiv: 1208.5386 [astro-ph.GA] (cit. on pp. 69, 70, 92).
- Ebert, R. (Jan. 1957). “Zur Instabilität kugelsymmetrischer Gasverteilungen. Mit 2 Textabbildungen”. *ZAp* 42, 263 (cit. on p. 20).
- Elbaz, D. et al. (June 2007). “The reversal of the star formation-density relation in the distant universe”. *A&A* 468.1, 33–48. arXiv: astro-ph/0703653 [astro-ph] (cit. on p. 8).
- Elbaz, D. et al. (Sept. 2011). “GOODS-Herschel: an infrared main sequence for star-forming galaxies”. *A&A* 533, A119, A119. arXiv: 1105.2537 [astro-ph.CO] (cit. on p. 8).
- Ellison, Sara L. et al. (Feb. 2018). “Star formation is boosted (and quenched) from the inside-out: radial star formation profiles from MaNGA”. *MNRAS* 474.2, 2039–2054. arXiv: 1711.00915 [astro-ph.GA] (cit. on p. 116).
- Ellison, Sara L. et al. (Mar. 2021a). “The ALMaQUEST Survey - V. The non-universality of kpc-scale star formation relations and the factors that drive them”. *MNRAS* 501.4, 4777–4797. arXiv: 2012.04771 [astro-ph.GA] (cit. on pp. 8, 9, 13).
- Ellison, Sara L. et al. (Mar. 2021b). “The ALMaQUEST survey - VI. The molecular gas main sequence of ‘retired’ regions in galaxies”. *MNRAS* 502.1, L6–L10. arXiv: 2012.04772 [astro-ph.GA] (cit. on p. 116).
- Elmegreen, B. G. (Aug. 1995). “An effective Q parameter for two-fluid instabilities in spiral galaxies”. *MNRAS* 275.4, 944–950 (cit. on p. 12).
- Elmegreen, Bruce G., Sungeun Kim, and Lister Staveley-Smith (Feb. 2001). “A Fractal Analysis of the H I Emission from the Large Magellanic Cloud”. *ApJ* 548.2, 749–769. arXiv: astro-ph/0010578 [astro-ph] (cit. on p. 69).
- Elmegreen, Bruce G. and John Scalo (Sept. 2004). “Interstellar Turbulence I: Observations and Processes”. *ARA&A* 42.1, 211–273. arXiv: astro-ph/0404451 [astro-ph] (cit. on pp. 16, 18, 26, 69, 114).

- Engargiola, G. et al. (Dec. 2003). “Giant Molecular Clouds in M33. I. BIMA All-Disk Survey”. *ApJS* 149.2, 343–363. arXiv: astro-ph/0308388 [astro-ph] (cit. on p. 18).
- Evans N. J., II and E. A. Lada (Jan. 1991). “Star Formation in Three Nearby Molecular Cloud Complexes”. *Fragmentation of Molecular Clouds and Star Formation*. Ed. by Edith Falgarone, F. Boulanger, and G. Duvert. Vol. 147, 293 (cit. on p. 21).
- Evans Neal J., II, Amanda Heiderman, and Nalin Vutisalchavakul (Feb. 2014). “Star Formation Relations in Nearby Molecular Clouds”. *ApJ* 782.2, 114, 114. arXiv: 1401.3287 [astro-ph.GA] (cit. on p. 21).
- Evans Neal J., II et al. (Apr. 2009). “The Spitzer c2d Legacy Results: Star-Formation Rates and Efficiencies; Evolution and Lifetimes”. *ApJS* 181.2, 321–350. arXiv: 0811.1059 [astro-ph] (cit. on p. 27).
- Event Horizon Telescope Collaboration et al. (Apr. 2019). “First M87 Event Horizon Telescope Results. I. The Shadow of the Supermassive Black Hole”. *ApJ* 875.1, L1, L1. arXiv: 1906.11238 [astro-ph.GA] (cit. on p. 2).
- Fabian, A. C. (Sept. 2012). “Observational Evidence of Active Galactic Nuclei Feedback”. *ARA&A* 50, 455–489. arXiv: 1204.4114 [astro-ph.CO] (cit. on pp. 14, 97, 112).
- Faesi, Christopher M., Charles J. Lada, and Jan Forbrich (Apr. 2018). “The ALMA View of GMCs in NGC 300: Physical Properties and Scaling Relations at 10 pc Resolution”. *ApJ* 857.1, 19, 19. arXiv: 1801.06238 [astro-ph.GA] (cit. on p. 60).
- Fall, S. M. and G. Efstathiou (Oct. 1980). “Formation and rotation of disc galaxies with haloes.” *MNRAS* 193, 189–206 (cit. on p. 4).
- Fang, Jerome J. et al. (May 2018). “Demographics of Star-forming Galaxies since $z \sim 2.5$. I. The UVJ Diagram in CANDELS”. *ApJ* 858.2, 100, 100. arXiv: 1710.05489 [astro-ph.GA] (cit. on p. 10).
- Farouki, R. and S. L. Shapiro (Jan. 1981). “Computer simulations of environmental influences on galaxy evolution in dense clusters. II - Rapid tidal encounters”. *ApJ* 243, 32–41 (cit. on p. 11).
- Federrath, C. et al. (Mar. 2010). “Comparing the statistics of interstellar turbulence in simulations and observations. Solenoidal versus compressive turbulence forcing”. *A&A* 512, A81, A81. arXiv: 0905.1060 [astro-ph.SR] (cit. on pp. 17, 23).
- Federrath, Christoph (Dec. 2013). “On the universality of supersonic turbulence”. *MNRAS* 436.2, 1245–1257. arXiv: 1306.3989 [astro-ph.SR] (cit. on pp. 18, 69).
- Federrath, Christoph and Ralf S. Klessen (Dec. 2012). “The Star Formation Rate of Turbulent Magnetized Clouds: Comparing Theory, Simulations, and Observations”. *ApJ* 761.2, 156, 156. arXiv: 1209.2856 [astro-ph.SR] (cit. on pp. 22–26, 34, 45).
- Federrath, Christoph, Ralf S. Klessen, and Wolfram Schmidt (Dec. 2008). “The Density Probability Distribution in Compressible Isothermal Turbulence: Solenoidal versus Compressive Forcing”. *ApJ* 688.2, L79. arXiv: 0808.0605 [astro-ph] (cit. on p. 17).
- Feldmann, Robert and Lucio Mayer (Jan. 2015). “The Argo simulation - I. Quenching of massive galaxies at high redshift as a result of cosmological starvation”. *MNRAS* 446.2, 1939–1956. arXiv: 1404.3212 [astro-ph.GA] (cit. on pp. 11, 117).

- Feldmann, Robert et al. (May 2016). “The formation of massive, quiescent galaxies at cosmic noon”. MNRAS 458.1, L14–L18. arXiv: 1601.04704 [astro-ph.GA] (cit. on p. 11).
- Ferrière, Katia M. (Oct. 2001). “The interstellar environment of our galaxy”. *Reviews of Modern Physics* 73.4, 1031–1066. arXiv: astro-ph/0106359 [astro-ph] (cit. on p. 16).
- Field, G. B., D. W. Goldsmith, and H. J. Habing (Mar. 1969). “Cosmic-Ray Heating of the Interstellar Gas”. ApJ 155, L149 (cit. on p. 16).
- Field, George B., Eric G. Blackman, and Eric R. Keto (Mar. 2008). “A model of cloud fragmentation”. MNRAS 385.1, 181–188 (cit. on p. 18).
- Finlator, Kristian and Romeel Davé (Apr. 2008). “The origin of the galaxy mass-metallicity relation and implications for galactic outflows”. MNRAS 385.4, 2181–2204. arXiv: 0704.3100 [astro-ph] (cit. on pp. 15, 96).
- Fleck Robert C., Jr. (Feb. 1996). “Scaling Relations for the Turbulent, Non-Self-gravitating, Neutral Component of the Interstellar Medium”. ApJ 458, 739 (cit. on p. 69).
- Fontana, A. et al. (July 2009). “The fraction of quiescent massive galaxies in the early Universe”. A&A 501.1, 15–20. arXiv: 0901.2898 [astro-ph.GA] (cit. on p. 10).
- Freedman, Wendy L. et al. (May 2001). “Final Results from the Hubble Space Telescope Key Project to Measure the Hubble Constant”. ApJ 553.1, 47–72. arXiv: astro-ph/0012376 [astro-ph] (cit. on p. 74).
- Freeman, Pamela et al. (June 2017). “The varying mass distribution of molecular clouds across M83”. MNRAS 468.2, 1769–1781. arXiv: 1702.07728 [astro-ph.GA] (cit. on p. 19).
- French, K. Decker et al. (Mar. 2015). “Discovery of Large Molecular Gas Reservoirs in Post-starburst Galaxies”. ApJ 801.1, 1, 1. arXiv: 1501.00983 [astro-ph.GA] (cit. on pp. 10, 15, 117).
- Freundlich, J. et al. (Feb. 2019). “PHIBSS2: survey design and $z = 0.5 - 0.8$ results. Molecular gas reservoirs during the winding-down of star formation”. A&A 622, A105, A105. arXiv: 1812.08180 [astro-ph.GA] (cit. on p. 13).
- Gallagher, Molly J. et al. (May 2018). “Dense Gas, Dynamical Equilibrium Pressure, and Star Formation in Nearby Star-forming Galaxies”. ApJ 858.2, 90, 90. arXiv: 1803.10785 [astro-ph.GA] (cit. on pp. 7, 22, 116).
- Gao, Yu and Philip M. Solomon (May 2004). “The Star Formation Rate and Dense Molecular Gas in Galaxies”. ApJ 606.1, 271–290. arXiv: astro-ph/0310339 [astro-ph] (cit. on pp. 6, 7).
- Geach, James E. et al. (Apr. 2011). “On the Evolution of the Molecular Gas Fraction of Star-Forming Galaxies”. ApJ 730.2, L19, L19. arXiv: 1102.3694 [astro-ph.CO] (cit. on pp. 4, 101).
- Geha, M. et al. (Sept. 2012). “A Stellar Mass Threshold for Quenching of Field Galaxies”. ApJ 757.1, 85, 85. arXiv: 1206.3573 [astro-ph.CO] (cit. on p. 2).
- Genel, Shy et al. (Nov. 2014). “Introducing the Illustris project: the evolution of galaxy populations across cosmic time”. MNRAS 445.1, 175–200. arXiv: 1405.3749 [astro-ph.CO] (cit. on p. 118).

- Genel, Shy et al. (Jan. 2019). “A Quantification of the Butterfly Effect in Cosmological Simulations and Implications for Galaxy Scaling Relations”. *ApJ* 871.1, 21, 21. arXiv: 1807.07084 [astro-ph.GA] (cit. on p. 64).
- Gensior, Jindra and J. M. Diederik Kruijssen (Jan. 2021). “The elephant in the bathtub: when the physics of star formation regulate the baryon cycle of galaxies”. *MNRAS* 500.2, 2000–2011. arXiv: 2011.01235 [astro-ph.GA] (cit. on pp. xi, 68, 69, 72, 86).
- Gensior, Jindra, J. M. Diederik Kruijssen, and Benjamin W. Keller (June 2020). “Heart of darkness: the influence of galactic dynamics on quenching star formation in galaxy spheroids”. *MNRAS* 495.1, 199–223. arXiv: 2002.01484 [astro-ph.GA] (cit. on pp. xi, 68–70, 72, 77, 80, 87, 93, 97–103, 105, 118, 172, 179).
- Genzel, R. et al. (Apr. 2014). “The SINS/zC-SINF Survey of $z \sim 2$ Galaxy Kinematics: Evidence for Gravitational Quenching”. *ApJ* 785.1, 75, 75. arXiv: 1310.3838 [astro-ph.CO] (cit. on pp. 13, 97).
- Girichidis, Philipp et al. (Feb. 2014). “On the Evolution of the Density Probability Density Function in Strongly Self-gravitating Systems”. *ApJ* 781.2, 91, 91. arXiv: 1310.4346 [astro-ph.GA] (cit. on pp. 17, 26).
- Gobat, R. et al. (Jan. 2018). “The unexpectedly large dust and gas content of quiescent galaxies at $z > 1.4$ ”. *Nature Astronomy* 2, 239–246. arXiv: 1703.02207 [astro-ph.GA] (cit. on pp. 13, 117).
- González Delgado, R. M. et al. (May 2016). “Star formation along the Hubble sequence. Radial structure of the star formation of CALIFA galaxies”. *A&A* 590, A44, A44. arXiv: 1603.00874 [astro-ph.GA] (cit. on p. 9).
- Governato, F. et al. (Jan. 2010). “Bulgeless dwarf galaxies and dark matter cores from supernova-driven outflows”. *Nature* 463.7278, 203–206. arXiv: 0911.2237 [astro-ph.CO] (cit. on p. 12).
- Green, D. A. (May 1993). “A power spectrum analysis of the angular scale of Galactic neutral hydrogen emission towards $L = 140$ deg, $B = 0$ deg”. *MNRAS* 262.2, 327–342 (cit. on p. 69).
- Grisdale, Kearn et al. (Apr. 2017). “The impact of stellar feedback on the density and velocity structure of the interstellar medium”. *MNRAS* 466.1, 1093–1110. arXiv: 1608.08639 [astro-ph.GA] (cit. on pp. 33, 69, 70, 77, 80, 81, 90–92, 114, 167, 169).
- Guedes, Javiera et al. (Dec. 2011). “Forming Realistic Late-type Spirals in a Λ CDM Universe: The Eris Simulation”. *ApJ* 742.2, 76, 76. arXiv: 1103.6030 [astro-ph.CO] (cit. on p. 12).
- Gunn, James E. and III Gott J. Richard (Aug. 1972). “On the Infall of Matter Into Clusters of Galaxies and Some Effects on Their Evolution”. *ApJ* 176, 1 (cit. on pp. 11, 97).
- Haardt, Francesco and Piero Madau (Feb. 2012). “Radiative Transfer in a Clumpy Universe. IV. New Synthesis Models of the Cosmic UV/X-Ray Background”. *ApJ* 746.2, 125, 125. arXiv: 1105.2039 [astro-ph.CO] (cit. on pp. 37, 72, 100).
- Hahn, ChangHoon, Jeremy L. Tinker, and Andrew Wetzel (May 2017). “Star Formation Quenching Timescale of Central Galaxies in a Hierarchical Universe”. *ApJ* 841.1, 6, 6. arXiv: 1609.04398 [astro-ph.GA] (cit. on pp. 112, 117).

- Hahn, ChangHoon et al. (Feb. 2019). “IQ-Collaboratory 1.1: The Star-forming Sequence of Simulated Central Galaxies”. *ApJ* 872.2, 160, 160. arXiv: 1809.01665 [astro-ph.GA] (cit. on p. 118).
- Haydon, Daniel T. et al. (Oct. 2020). “An uncertainty principle for star formation - III. The characteristic emission time-scales of star formation rate tracers”. *MNRAS* 498.1, 235–257. arXiv: 1810.10897 [astro-ph.GA] (cit. on p. 42).
- Heckman, Timothy M., Lee Armus, and George K. Miley (Dec. 1990). “On the Nature and Implications of Starburst-driven Galactic Superwinds”. *ApJS* 74, 833 (cit. on pp. 12, 14).
- Heckman, Timothy M. et al. (Aug. 2000). “Absorption-Line Probes of Gas and Dust in Galactic Superwinds”. *ApJS* 129.2, 493–516. arXiv: astro-ph/0002526 [astro-ph] (cit. on p. 14).
- Heiderman, Amanda et al. (Nov. 2010). “The Star Formation Rate and Gas Surface Density Relation in the Milky Way: Implications for Extragalactic Studies”. *ApJ* 723.2, 1019–1037. arXiv: 1009.1621 [astro-ph.GA] (cit. on p. 25).
- Hennebelle, P. et al. (Aug. 2008). “From the warm magnetized atomic medium to molecular clouds”. *A&A* 486.3, L43–L46. arXiv: 0805.1366 [astro-ph] (cit. on p. 17).
- Hennebelle, Patrick and Gilles Chabrier (Dec. 2011). “Analytical Star Formation Rate from Gravoturbulent Fragmentation”. *ApJ* 743.2, L29, L29. arXiv: 1110.0033 [astro-ph.GA] (cit. on pp. 23–25, 34).
- Hennebelle, Patrick and Edith Falgarone (Nov. 2012). “Turbulent molecular clouds”. *A&A Rev.* 20, 55, 55. arXiv: 1211.0637 [astro-ph.GA] (cit. on pp. 16, 18, 20, 26).
- Hernquist, Lars (June 1990). “An Analytical Model for Spherical Galaxies and Bulges”. *ApJ* 356, 359 (cit. on pp. 40, 72, 101).
- Heyer, Mark et al. (July 2009). “Re-Examining Larson’s Scaling Relationships in Galactic Molecular Clouds”. *ApJ* 699.2, 1092–1103. arXiv: 0809.1397 [astro-ph] (cit. on pp. 19, 20).
- Heyer, Mark H. and Christopher M. Brunt (Nov. 2004). “The Universality of Turbulence in Galactic Molecular Clouds”. *ApJ* 615.1, L45–L48. arXiv: astro-ph/0409420 [astro-ph] (cit. on p. 17).
- Holmberg, E. (Jan. 1958). “A photographic photometry of extragalactic nebulae.” *Meddelanden fran Lunds Astronomiska Observatorium Serie II* 136, 1 (cit. on p. 3).
- Hopkins, Philip F., Eliot Quataert, and Norman Murray (Oct. 2011). “Self-regulated star formation in galaxies via momentum input from massive stars”. *MNRAS* 417.2, 950–973. arXiv: 1101.4940 [astro-ph.CO] (cit. on pp. 14, 33, 96).
- Hopkins, Philip F. et al. (Aug. 2009). “The effects of gas on morphological transformation in mergers: implications for bulge and disc demographics”. *MNRAS* 397.2, 802–814. arXiv: 0901.4111 [astro-ph.CO] (cit. on p. 4).
- Hopkins, Philip F. et al. (Nov. 2014). “Galaxies on FIRE (Feedback In Realistic Environments): stellar feedback explains cosmologically inefficient star formation”. *MNRAS* 445.1, 581–603. arXiv: 1311.2073 [astro-ph.CO] (cit. on pp. 12, 37, 38, 72, 100).

- Hopkins, Philip F. et al. (Oct. 2018a). “FIRE-2 simulations: physics versus numerics in galaxy formation”. MNRAS 480.1, 800–863. arXiv: 1702.06148 [astro-ph.GA] (cit. on pp. 30, 33, 38, 61).
- Hopkins, Philip F. et al. (June 2018b). “How to model supernovae in simulations of star and galaxy formation”. MNRAS 477.2, 1578–1603. arXiv: 1707.07010 [astro-ph.GA] (cit. on p. 38).
- Huang, Mei-Ling and Guinevere Kauffmann (Sept. 2014). “The variation in molecular gas depletion time among nearby galaxies: what are the main parameter dependences?” MNRAS 443.2, 1329–1338. arXiv: 1404.7138 [astro-ph.GA] (cit. on p. 31).
- Hubble, E. P. (Dec. 1926). “Extragalactic nebulae.” ApJ 64, 321–369 (cit. on p. 2).
- (1936). *Realm of the Nebulae*. Yale University Press (cit. on p. 2).
- Huertas-Company, M. et al. (Aug. 2015). “The Morphologies of Massive Galaxies from $z \sim 3$ —Witnessing the Two Channels of Bulge Growth”. ApJ 809.1, 95, 95. arXiv: 1506.03084 [astro-ph.GA] (cit. on p. 97).
- Ianjamasimanana, R. et al. (Oct. 2012). “The Shapes of the H I Velocity Profiles of the THINGS Galaxies”. AJ 144.4, 96, 96. arXiv: 1207.5041 [astro-ph.CO] (cit. on p. 18).
- Iliadis, Christian (2007). *Nuclear Physics of Stars* (cit. on p. 15).
- Iyer, Kartheik G. et al. (Oct. 2020). “The diversity and variability of star formation histories in models of galaxy evolution”. MNRAS 498.1, 430–463. arXiv: 2007.07916 [astro-ph.GA] (cit. on pp. 9, 10, 118).
- Janowiecki, Steven et al. (Apr. 2020). “xGASS: cold gas content and quenching in galaxies below the star-forming main sequence”. MNRAS 493.2, 1982–1995. arXiv: 2001.06614 [astro-ph.GA] (cit. on pp. 8, 9, 13).
- Jeans, J. H. (Jan. 1902). “The Stability of a Spherical Nebula”. *Philosophical Transactions of the Royal Society of London Series A* 199, 1–53 (cit. on p. 20).
- Jefferson, Sarah M. R. and J. M. Diederik Kruijssen (May 2018). “A general theory for the lifetimes of giant molecular clouds under the influence of galactic dynamics”. MNRAS 476.3, 3688–3715. arXiv: 1803.01850 [astro-ph.GA] (cit. on p. 116).
- Jian, Hung-Yu et al. (Jan. 2018). “First results on the cluster galaxy population from the Subaru Hyper Suprime-Cam survey. I. The role of group or cluster environment in star formation quenching from $z = 0.2$ to 1.1 ”. PASJ 70, S23, S23. arXiv: 1704.06219 [astro-ph.GA] (cit. on p. 10).
- Jog, C. J. and P. M. Solomon (Jan. 1984a). “A galactic disk as a two-fluid system - Consequences for the critical stellar velocity dispersion and the formation of condensations in the gas”. ApJ 276, 127–134 (cit. on p. 13).
- (Jan. 1984b). “Two-fluid gravitational instabilities in a galactic disk”. ApJ 276, 114–126 (cit. on p. 12).
- Johansson, Peter H., Thorsten Naab, and Jeremiah P. Ostriker (May 2009). “Gravitational Heating Helps Make Massive Galaxies Red and Dead”. ApJ 697.1, L38–L43. arXiv: 0903.2840 [astro-ph.CO] (cit. on p. 11).
- Kainulainen, J. and C. Federrath (Nov. 2017). “Relationship between turbulence energy and density variance in the solar neighbourhood molecular clouds”. A&A 608, L3, L3. arXiv: 1711.01602 [astro-ph.GA] (cit. on pp. 16, 26).

- Kainulainen, J. and J. C. Tan (Jan. 2013). “High-dynamic-range extinction mapping of infrared dark clouds. Dependence of density variance with sonic Mach number in molecular clouds”. *A&A* 549, A53, A53. arXiv: 1210.8130 [astro-ph.GA] (cit. on pp. 16, 26).
- Kainulainen, J. et al. (Dec. 2009). “Probing the evolution of molecular cloud structure. From quiescence to birth”. *A&A* 508.3, L35–L38. arXiv: 0911.5648 [astro-ph.GA] (cit. on p. 18).
- Kainulainen, J. et al. (June 2011). “Probing the evolution of molecular cloud structure. II. From chaos to confinement”. *A&A* 530, A64, A64. arXiv: 1104.0678 [astro-ph.GA] (cit. on p. 18).
- Kalinova, V. et al. (Apr. 2021). “Star formation quenching stages of active and non-active galaxies”. *A&A* 648, A64, A64. arXiv: 2101.10019 [astro-ph.GA] (cit. on p. 116).
- Karachentsev, I. D. et al. (July 2002). “The very local Hubble flow”. *A&A* 389, 812–824. arXiv: astro-ph/0204507 [astro-ph] (cit. on p. 74).
- Karakas, Amanda I. and John C. Lattanzio (July 2014). “The Dawes Review 2: Nucleosynthesis and Stellar Yields of Low- and Intermediate-Mass Single Stars”. 31, e030, e030. arXiv: 1405.0062 [astro-ph.SR] (cit. on p. 15).
- Katz, Neal (June 1992). “Dissipational Galaxy Formation. II. Effects of Star Formation”. *ApJ* 391, 502 (cit. on pp. 30, 72, 99).
- Katz, Neal, David H. Weinberg, and Lars Hernquist (July 1996). “Cosmological Simulations with TreeSPH”. *ApJS* 105, 19. arXiv: astro-ph/9509107 [astro-ph] (cit. on p. 4).
- Katz, Neal and Simon D. M. White (Aug. 1993). “Hierarchical Galaxy Formation: Overmerging and the Formation of an X-Ray Cluster”. *ApJ* 412, 455 (cit. on p. 14).
- Katz, Neal et al. (2003). “How Do Galaxies Get Their Gas?” *The IGM/Galaxy Connection. The Distribution of Baryons at z=0*. Ed. by J. L. Rosenberg and M. E. Putman. Vol. 281, 185 (cit. on p. 14).
- Kauffmann, Guinevere et al. (May 2003). “The dependence of star formation history and internal structure on stellar mass for 10^5 low-redshift galaxies”. *MNRAS* 341.1, 54–69. arXiv: astro-ph/0205070 [astro-ph] (cit. on p. 4).
- Kauffmann, Jens et al. (July 2017). “The Galactic Center Molecular Cloud Survey. II. A lack of dense gas and cloud evolution along Galactic center orbits”. *A&A* 603, A90, A90. arXiv: 1610.03502 [astro-ph.GA] (cit. on p. 51).
- Kawamura, Akiko et al. (Sept. 2009). “The Second Survey of the Molecular Clouds in the Large Magellanic Cloud by NANTEN. II. Star Formation”. *ApJS* 184.1, 1–17. arXiv: 0908.1168 [astro-ph.CO] (cit. on p. 18).
- Keller, B. W., J. Wadsley, and H. M. P. Couchman (Dec. 2016). “Cosmological galaxy evolution with superbubble feedback - II. The limits of supernovae”. *MNRAS* 463.2, 1431–1445. arXiv: 1604.08244 [astro-ph.GA] (cit. on p. 12).
- Keller, B. W. et al. (Jan. 2019). “Chaos and variance in galaxy formation”. *MNRAS* 482.2, 2244–2261. arXiv: 1803.05445 [astro-ph.GA] (cit. on p. 64).
- Kennicutt Robert C., Jr. (Sept. 1989). “The Star Formation Law in Galactic Disks”. *ApJ* 344, 685 (cit. on pp. 5, 6).

- Kennicutt Robert C., Jr. (Jan. 1998a). “Star Formation in Galaxies Along the Hubble Sequence”. *ARA&A* 36, 189–232. arXiv: astro-ph/9807187 [astro-ph] (cit. on p. 5).
- (May 1998b). “The Global Schmidt Law in Star-forming Galaxies”. *ApJ* 498.2, 541–552. arXiv: astro-ph/9712213 [astro-ph] (cit. on pp. 5–7, 30, 31, 33, 68, 72, 96, 104).
- Kennicutt, Robert C. and Neal J. Evans (Sept. 2012). “Star Formation in the Milky Way and Nearby Galaxies”. *ARA&A* 50, 531–608. arXiv: 1204.3552 [astro-ph.GA] (cit. on pp. 5, 31, 42, 62).
- Kereš, Dušan et al. (Oct. 2005). “How do galaxies get their gas?” *MNRAS* 363.1, 2–28. arXiv: astro-ph/0407095 [astro-ph] (cit. on p. 11).
- Kereš, Dušan et al. (May 2009). “Galaxies in a simulated Λ CDM Universe - I. Cold mode and hot cores”. *MNRAS* 395.1, 160–179. arXiv: 0809.1430 [astro-ph] (cit. on p. 11).
- Khochfar, Sadegh and Jeremiah P. Ostriker (June 2008). “Adding Environmental Gas Physics to the Semianalytic Method for Galaxy Formation: Gravitational Heating”. *ApJ* 680.1, 54–69. arXiv: 0704.2418 [astro-ph] (cit. on p. 11).
- Khoperskov, S. et al. (Jan. 2018). “Bar quenching in gas-rich galaxies”. *A&A* 609, A60, A60. arXiv: 1709.03604 [astro-ph.GA] (cit. on p. 13).
- Kim, Ji-hoon et al. (Dec. 2016). “The AGORA High-resolution Galaxy Simulations Comparison Project. II. Isolated Disk Test”. *ApJ* 833.2, 202, 202. arXiv: 1610.03066 [astro-ph.GA] (cit. on pp. 33, 38, 100).
- Kim, Jaeyeon et al. (Mar. 2021a). “On the duration of the embedded phase of star formation”. *MNRAS*. arXiv: 2012.00019 [astro-ph.GA] (cit. on p. 22).
- Kim, Jeong-Gyu, Eve C. Ostriker, and Nina Filippova (Apr. 2021b). “Star Formation Efficiency and Dispersal of Giant Molecular Clouds with UV Radiation Feedback: Dependence on Gravitational Boundedness and Magnetic Fields”. *ApJ* 911.2, 128, 128. arXiv: 2011.07772 [astro-ph.GA] (cit. on pp. 21, 27, 28).
- Kim, Keunho et al. (Nov. 2018). “Galaxy Structure, Stellar Populations, and Star Formation Quenching at $0.6 \lesssim z \lesssim 1.2$ ”. *ApJ* 867.2, 118, 118. arXiv: 1810.01498 [astro-ph.GA] (cit. on pp. 13, 97, 117).
- Kimm, Taysun and Renyue Cen (June 2014). “Escape Fraction of Ionizing Photons during Reionization: Effects due to Supernova Feedback and Runaway OB Stars”. *ApJ* 788.2, 121, 121. arXiv: 1405.0552 [astro-ph.GA] (cit. on pp. 37, 72, 100).
- Kimm, Taysun et al. (Aug. 2015). “Towards simulating star formation in turbulent high- z galaxies with mechanical supernova feedback”. *MNRAS* 451.3, 2900–2921. arXiv: 1501.05655 [astro-ph.GA] (cit. on p. 38).
- Kimm, Taysun et al. (Apr. 2017). “Feedback-regulated star formation and escape of LyC photons from mini-haloes during reionization”. *MNRAS* 466.4, 4826–4846. arXiv: 1608.04762 [astro-ph.GA] (cit. on pp. 25, 34, 36).
- Klessen, R. S. and P. Hennebelle (Sept. 2010). “Accretion-driven turbulence as universal process: galaxies, molecular clouds, and protostellar disks”. *A&A* 520, A17, A17. arXiv: 0912.0288 [astro-ph.CO] (cit. on p. 18).
- Klessen, Ralf S., Fabian Heitsch, and Mordecai-Mark Mac Low (June 2000). “Gravitational Collapse in Turbulent Molecular Clouds. I. Gasdynamical Turbulence”. *ApJ* 535.2, 887–906. arXiv: astro-ph/9911068 [astro-ph] (cit. on p. 17).

- Knapp, Gillian R. et al. (June 1989). “Interstellar Matter in Early-Type Galaxies. I. IRAS Flux Densities”. *ApJS* 70, 329 (cit. on p. 4).
- Koch, Eric W. et al. (July 2019). “TURBUSTAT: Turbulence Statistics in Python”. *AJ* 158.1, 1, 1. arXiv: 1904.10484 [astro-ph.IM] (cit. on p. 77).
- Koch, Eric W. et al. (Feb. 2020). “Spatial power spectra of dust across the Local Group: No constraint on disc scale height”. *MNRAS* 492.2, 2663–2682. arXiv: 1912.09459 [astro-ph.GA] (cit. on pp. 69, 70, 77, 79, 86, 91–93, 114, 167).
- Kokusho, T. et al. (Feb. 2019). “Dust properties in the cold and hot gas phases of the ATLAS^{3D} early-type galaxies as revealed by AKARI”. *A&A* 622, A87, A87. arXiv: 1812.09468 [astro-ph.GA] (cit. on pp. 4, 112, 117).
- Kolmogorov, A. (Jan. 1941). “The Local Structure of Turbulence in Incompressible Viscous Fluid for Very Large Reynolds’ Numbers”. *Akademiia Nauk SSSR Doklady* 30, 301–305 (cit. on pp. 17, 18, 69, 81, 93, 115).
- Kormendy, John and Luis C. Ho (Aug. 2013). “Coevolution (Or Not) of Supermassive Black Holes and Host Galaxies”. *ARA&A* 51.1, 511–653. arXiv: 1304.7762 [astro-ph.CO] (cit. on p. 12).
- Kormendy, John and Douglas Richstone (Jan. 1995). “Inward Bound—The Search For Supermassive Black Holes In Galactic Nuclei”. *ARA&A* 33, 581 (cit. on p. 2).
- Kretschmer, Michael and Romain Teyssier (Feb. 2020). “Forming early-type galaxies without AGN feedback: a combination of merger-driven outflows and inefficient star formation”. *MNRAS* 492.1, 1385–1398. arXiv: 1906.11836 [astro-ph.GA] (cit. on pp. 25, 32, 34, 62, 68, 72, 98, 110, 115, 116, 118).
- Krips, M. et al. (Oct. 2010). “Molecular gas in SAURON early-type galaxies: detection of ¹³CO and HCN emission”. *MNRAS* 407.4, 2261–2268. arXiv: 1005.5642 [astro-ph.GA] (cit. on p. 7).
- Kritsuk, Alexei G., Christoph T. Lee, and Michael L. Norman (Dec. 2013). “A supersonic turbulence origin of Larson’s laws”. *MNRAS* 436.4, 3247–3261. arXiv: 1309.5926 [astro-ph.GA] (cit. on p. 20).
- Kritsuk, Alexei G. and Michael L. Norman (Apr. 2002). “Thermal Instability-induced Interstellar Turbulence”. *ApJ* 569.2, L127–L131. arXiv: astro-ph/0112437 [astro-ph] (cit. on p. 19).
- Kritsuk, Alexei G., Michael L. Norman, and Rick Wagner (Jan. 2011). “On the Density Distribution in Star-forming Interstellar Clouds”. *ApJ* 727.1, L20, L20. arXiv: 1007.2950 [astro-ph.GA] (cit. on p. 17).
- Kritsuk, Alexei G. et al. (Aug. 2007). “The Statistics of Supersonic Isothermal Turbulence”. *ApJ* 665.1, 416–431. arXiv: 0704.3851 [astro-ph] (cit. on p. 17).
- Kruijssen, J. M. Diederik and Steven N. Longmore (Nov. 2013). “Comparing molecular gas across cosmic time-scales: the Milky Way as both a typical spiral galaxy and a high-redshift galaxy analogue”. *MNRAS* 435.3, 2598–2603. arXiv: 1309.0505 [astro-ph.CO] (cit. on p. 60).
- (Apr. 2014). “An uncertainty principle for star formation - I. Why galactic star formation relations break down below a certain spatial scale”. *MNRAS* 439.4, 3239–3252. arXiv: 1401.4459 [astro-ph.GA] (cit. on pp. 21, 41).

- Kruijssen, J. M. Diederik et al. (June 2014). “What controls star formation in the central 500 pc of the Galaxy?” MNRAS 440.4, 3370–3391. arXiv: 1303.6286 [astro-ph.GA] (cit. on pp. 7, 31, 51, 68, 109, 116).
- Kruijssen, J. M. Diederik et al. (Sept. 2018). “An uncertainty principle for star formation - II. A new method for characterizing the cloud-scale physics of star formation and feedback across cosmic history”. MNRAS 479.2, 1866–1952. arXiv: 1805.00012 [astro-ph.GA] (cit. on pp. 21, 44, 101).
- Kruijssen, J. M. Diederik et al. (May 2019a). “Fast and inefficient star formation due to short-lived molecular clouds and rapid feedback”. Nature 569.7757, 519–522. arXiv: 1905.08801 [astro-ph.GA] (cit. on pp. 38, 73, 100).
- (May 2019b). “Fast and inefficient star formation due to short-lived molecular clouds and rapid feedback”. Nature 569.7757, 519–522. arXiv: 1905.08801 [astro-ph.GA] (cit. on pp. 46, 64).
- Krumholz, Mark R. (June 2014). “The big problems in star formation: The star formation rate, stellar clustering, and the initial mass function”. Phys. Rep. 539, 49–134. arXiv: 1402.0867 [astro-ph.GA] (cit. on pp. 1, 20).
- Krumholz, Mark R., Adam K. Leroy, and Christopher F. McKee (Apr. 2011). “Which Phase of the Interstellar Medium Correlates with the Star Formation Rate?” ApJ 731.1, 25, 25. arXiv: 1101.1296 [astro-ph.CO] (cit. on p. 16).
- Krumholz, Mark R. and Christopher F. McKee (Sept. 2005). “A General Theory of Turbulence-regulated Star Formation, from Spirals to Ultraluminous Infrared Galaxies”. ApJ 630.1, 250–268. arXiv: astro-ph/0505177 [astro-ph] (cit. on pp. 23–27, 33).
- Krumholz, Mark R., Christopher F. McKee, and Joss Bland-Hawthorn (Aug. 2019). “Star Clusters Across Cosmic Time”. ARA&A 57, 227–303. arXiv: 1812.01615 [astro-ph.GA] (cit. on p. 22).
- Krumholz, Mark R. and Jonathan C. Tan (Jan. 2007). “Slow Star Formation in Dense Gas: Evidence and Implications”. ApJ 654.1, 304–315. arXiv: astro-ph/0606277 [astro-ph] (cit. on p. 27).
- Krumholz, Mark R. et al. (June 2018). “A unified model for galactic discs: star formation, turbulence driving, and mass transport”. MNRAS 477.2, 2716–2740. arXiv: 1706.00106 [astro-ph.GA] (cit. on pp. 18, 19, 26, 44, 80, 103).
- Lacerda, Eduardo A. D. et al. (Mar. 2020). “Galaxies hosting an active galactic nucleus: a view from the CALIFA survey”. MNRAS 492.3, 3073–3090. arXiv: 2001.00099 [astro-ph.GA] (cit. on pp. 97, 112).
- Lada, Charles J., Marco Lombardi, and João F. Alves (Nov. 2010). “On the Star Formation Rates in Molecular Clouds”. ApJ 724.1, 687–693. arXiv: 1009.2985 [astro-ph.GA] (cit. on pp. 6, 25).
- Lada, Charles J. et al. (Feb. 2012). “Star Formation Rates in Molecular Clouds and the Nature of the Extragalactic Scaling Relations”. ApJ 745.2, 190, 190. arXiv: 1112.4466 [astro-ph.GA] (cit. on pp. 6, 26).
- Landau, L. D. and E. M. Lifshitz (1987). *Fluid Mechanics* (cit. on p. 17).
- Lang, Philipp et al. (June 2014). “Bulge Growth and Quenching since $z = 2.5$ in CANDELS/3D-HST”. ApJ 788.1, 11, 11. arXiv: 1402.0866 [astro-ph.GA] (cit. on p. 112).

- Larson, R. B. (Mar. 1981). “Turbulence and star formation in molecular clouds.” *MNRAS* 194, 809–826 (cit. on pp. 17, 19).
- Larson, R. B., B. M. Tinsley, and C. N. Caldwell (May 1980). “The evolution of disk galaxies and the origin of S0 galaxies”. *ApJ* 237, 692–707 (cit. on pp. 11, 97).
- Lazarian, A. and D. Pogosyan (July 2000). “Velocity Modification of H I Power Spectrum”. *ApJ* 537.2, 720–748. arXiv: astro-ph/9901241 [astro-ph] (cit. on p. 69).
- Lee, Eve J., Marc-Antoine Miville-Deschênes, and Norman W. Murray (Dec. 2016). “Observational Evidence of Dynamic Star Formation Rate in Milky Way Giant Molecular Clouds”. *ApJ* 833.2, 229, 229. arXiv: 1608.05415 [astro-ph.GA] (cit. on pp. 21, 25, 27).
- Lee, Nicholas et al. (Mar. 2015). “A Turnover in the Galaxy Main Sequence of Star Formation at $M_* \sim 10^{10} M_\odot$ for Redshifts $z < 1.3$ ”. *ApJ* 801.2, 80, 80. arXiv: 1501.01080 [astro-ph.GA] (cit. on pp. 8, 17).
- Leitherer, Claus et al. (May 2014). “The Effects of Stellar Rotation. II. A Comprehensive Set of Starburst99 Models”. *ApJS* 212.1, 14, 14. arXiv: 1403.5444 [astro-ph.GA] (cit. on pp. 38, 73, 100).
- Lequeux, J. et al. (Dec. 1979). “Reprint of 1979A&A....80..155L. Chemical composition and evolution of irregular and blue compact galaxies.” *A&A* 500, 145–156 (cit. on p. 97).
- Leroy, Adam K. et al. (Dec. 2008). “The Star Formation Efficiency in Nearby Galaxies: Measuring Where Gas Forms Stars Effectively”. *AJ* 136.6, 2782–2845. arXiv: 0810.2556 [astro-ph] (cit. on pp. 6, 12).
- Leroy, Adam K. et al. (Aug. 2013). “Molecular Gas and Star Formation in nearby Disk Galaxies”. *AJ* 146.2, 19, 19. arXiv: 1301.2328 [astro-ph.CO] (cit. on pp. 5, 6, 33, 42, 96, 104, 118).
- Leroy, Adam K. et al. (Nov. 2016). “A Portrait of Cold Gas in Galaxies at 60 pc Resolution and a Simple Method to Test Hypotheses That Link Small-scale ISM Structure to Galaxy-scale Processes”. *ApJ* 831.1, 16, 16. arXiv: 1606.07077 [astro-ph.GA] (cit. on p. 60).
- Leroy, Adam K. et al. (Sept. 2017). “Cloud-scale ISM Structure and Star Formation in M51”. *ApJ* 846.1, 71, 71. arXiv: 1706.08540 [astro-ph.GA] (cit. on pp. 20, 22, 27).
- Leroy, Adam K. et al. (Oct. 2019). “A $z = 0$ Multiwavelength Galaxy Synthesis. I. A WISE and GALEX Atlas of Local Galaxies”. *ApJS* 244.2, 24, 24. arXiv: 1910.13470 [astro-ph.GA] (cit. on pp. 74, 75).
- Leroy, Adam K. et al. (Apr. 2021a). “PHANGS-ALMA Data Processing and Pipeline”. *arXiv e-prints*, arXiv:2104.07665, arXiv:2104.07665. arXiv: 2104.07665 [astro-ph.IM] (cit. on p. 69).
- Leroy, Adam K. et al. (Apr. 2021b). “PHANGS-ALMA: Arcsecond CO(2-1) Imaging of Nearby Star-Forming Galaxies”. *arXiv e-prints*, arXiv:2104.07739, arXiv:2104.07739. arXiv: 2104.07739 [astro-ph.GA] (cit. on pp. 19, 69, 119).
- Leslie, Sarah K. et al. (Aug. 2020). “The VLA-COSMOS 3 GHz Large Project: Evolution of Specific Star Formation Rates out to $z \sim 5$ ”. *ApJ* 899.1, 58, 58. arXiv: 2006.13937 [astro-ph.GA] (cit. on pp. 8, 9).

- Lilly, Simon J. et al. (Aug. 2013). “Gas Regulation of Galaxies: The Evolution of the Cosmic Specific Star Formation Rate, the Metallicity-Mass-Star-formation Rate Relation, and the Stellar Content of Halos”. *ApJ* 772.2, 119, 119. arXiv: 1303.5059 [astro-ph.CO] (cit. on pp. 15, 96).
- Lin, Lihwai et al. (Nov. 2020). “ALMaQUEST. IV. The ALMA-MaNGA QUEnching and STar Formation (ALMaQUEST) Survey”. *ApJ* 903.2, 145, 145. arXiv: 2010.01751 [astro-ph.GA] (cit. on p. 8).
- Liu, Michael C., James R. Graham, and Stéphane Charlot (Jan. 2002). “Surface Brightness Fluctuations of Fornax Cluster Galaxies: Calibration of Infrared Surface Brightness Fluctuations and Evidence for Recent Star Formation”. *ApJ* 564.1, 216–233. arXiv: astro-ph/0107357 [astro-ph] (cit. on p. 74).
- Lombardi, Marco, João Alves, and Charles J. Lada (Apr. 2015). “Molecular clouds have power-law probability distribution functions”. *A&A* 576, L1, L1. arXiv: 1502.03859 [astro-ph.SR] (cit. on p. 18).
- Longmore, S. N. et al. (Feb. 2013). “Variations in the Galactic star formation rate and density thresholds for star formation”. *MNRAS* 429.2, 987–1000. arXiv: 1208.4256 [astro-ph.GA] (cit. on pp. 7, 31, 43, 59, 68, 109, 116).
- Low, C. and D. Lynden-Bell (Aug. 1976). “The minimum Jeans mass or when fragmentation must stop.” *MNRAS* 176, 367–390 (cit. on p. 20).
- Lynden-Bell, D. (Aug. 1969). “Galactic Nuclei as Collapsed Old Quasars”. *Nature* 223.5207, 690–694 (cit. on p. 2).
- Ma, Chung-Pei et al. (Nov. 2014). “The MASSIVE Survey. I. A Volume-limited Integral-field Spectroscopic Study of the Most Massive Early-type Galaxies within 108 Mpc”. *ApJ* 795.2, 158, 158. arXiv: 1407.1054 [astro-ph.GA] (cit. on p. 74).
- Mac Low, Mordecai-Mark (Oct. 1999). “The Energy Dissipation Rate of Supersonic, Magneto-hydrodynamic Turbulence in Molecular Clouds”. *ApJ* 524.1, 169–178. arXiv: astro-ph/9809177 [astro-ph] (cit. on p. 18).
- Mac Low, Mordecai-Mark and Ralf S. Klessen (Jan. 2004). “Control of star formation by supersonic turbulence”. *Reviews of Modern Physics* 76.1, 125–194. arXiv: astro-ph/0301093 [astro-ph] (cit. on pp. 18, 23, 26).
- Mac Low, Mordecai-Mark et al. (Mar. 1998). “Kinetic Energy Decay Rates of Supersonic and Super-Alfvénic Turbulence in Star-Forming Clouds”. *Phys. Rev. Lett.* 80.13, 2754–2757. arXiv: astro-ph/9712013 [astro-ph] (cit. on p. 18).
- Madau, Piero and Mark Dickinson (Aug. 2014). “Cosmic Star-Formation History”. *ARA&A* 52, 415–486. arXiv: 1403.0007 [astro-ph.CO] (cit. on p. 8).
- Magdis, G. E. et al. (Jan. 2010). “On the stellar masses of IRAC detected Lyman Break Galaxies at $z \sim 3$ ”. *MNRAS* 401.3, 1521–1531. arXiv: 0909.3950 [astro-ph.CO] (cit. on p. 8).
- Magorrian, John et al. (June 1998). “The Demography of Massive Dark Objects in Galaxy Centers”. *AJ* 115.6, 2285–2305. arXiv: astro-ph/9708072 [astro-ph] (cit. on p. 12).
- Malkan, Matthew A., Varoujan Gorjian, and Raymond Tam (July 1998). “A Hubble Space Telescope Imaging Survey of Nearby Active Galactic Nuclei”. *ApJS* 117.1, 25–88. arXiv: astro-ph/9803123 [astro-ph] (cit. on p. 74).

- Man, Allison and Sirio Belli (Sept. 2018). “Star formation quenching in massive galaxies”. *Nature Astronomy* 2, 695–697. arXiv: 1809.00722 [astro-ph.GA] (cit. on pp. 9, 10).
- Mannucci, F. et al. (Nov. 2010). “A fundamental relation between mass, star formation rate and metallicity in local and high-redshift galaxies”. *MNRAS* 408.4, 2115–2127. arXiv: 1005.0006 [astro-ph.CO] (cit. on p. 97).
- Maragkoudakis, A. et al. (Apr. 2017). “The sub-galactic and nuclear main sequences for local star-forming galaxies”. *MNRAS* 466.1, 1192–1204. arXiv: 1611.10085 [astro-ph.GA] (cit. on p. 9).
- Marino, A. et al. (Feb. 2011). “Nearby early-type galaxies with ionized gas: the UV emission from GALEX observations”. *MNRAS* 411.1, 311–331. arXiv: 1009.1931 [astro-ph.CO] (cit. on p. 74).
- Martig, Marie et al. (Dec. 2009). “Morphological Quenching of Star Formation: Making Early-Type Galaxies Red”. *ApJ* 707.1, 250–267. arXiv: 0905.4669 [astro-ph.CO] (cit. on pp. 4, 12, 13, 18, 19, 31, 68, 97, 98, 110, 113, 114, 116).
- Martig, Marie et al. (July 2013). “The ATLAS^{3D} project - XXII. Low-efficiency star formation in early-type galaxies: hydrodynamic models and observations”. *MNRAS* 432.3, 1914–1927. arXiv: 1212.2288 [astro-ph.CO] (cit. on pp. 7, 13, 32, 62, 68, 69, 86, 97, 98, 110, 115–117).
- Martin, P. G. et al. (Aug. 2015). “GHIGLS: H I Mapping at Intermediate Galactic Latitude Using the Green Bank Telescope”. *ApJ* 809.2, 153, 153. arXiv: 1504.07723 [astro-ph.GA] (cit. on p. 69).
- Matzner, Christopher D. (Feb. 2002). “On the Role of Massive Stars in the Support and Destruction of Giant Molecular Clouds”. *ApJ* 566.1, 302–314. arXiv: astro-ph/0110278 [astro-ph] (cit. on p. 18).
- Matzner, Christopher D. and Christopher F. McKee (Dec. 2000). “Efficiencies of Low-Mass Star and Star Cluster Formation”. *ApJ* 545.1, 364–378. arXiv: astro-ph/0007383 [astro-ph] (cit. on p. 23).
- McBride, James, Onsi Fakhouri, and Chung-Pei Ma (Oct. 2009). “Mass accretion rates and histories of dark matter haloes”. *MNRAS* 398.4, 1858–1868. arXiv: 0902.3659 [astro-ph.CO] (cit. on p. 11).
- McCarthy, I. G. et al. (Apr. 2011). “Gas expulsion by quasar-driven winds as a solution to the overcooling problem in galaxy groups and clusters”. *MNRAS* 412.3, 1965–1984. arXiv: 1008.4799 [astro-ph.CO] (cit. on p. 11).
- McGee, Sean L. et al. (May 2011). “The Dawn of the Red: star formation histories of group galaxies over the past 5 billion years”. *MNRAS* 413.2, 996–1012. arXiv: 1012.2388 [astro-ph.CO] (cit. on p. 10).
- McKee, C. F. and J. P. Ostriker (Nov. 1977). “A theory of the interstellar medium: three components regulated by supernova explosions in an inhomogeneous substrate.” *ApJ* 218, 148–169 (cit. on p. 16).
- McKee, Christopher F. and Eve C. Ostriker (Sept. 2007). “Theory of Star Formation”. *ARA&A* 45.1, 565–687. arXiv: 0707.3514 [astro-ph] (cit. on pp. 1, 16, 18, 20).

- McMullin, J. P. et al. (Oct. 2007). “CASA Architecture and Applications”. *Astronomical Data Analysis Software and Systems XVI*. Ed. by R. A. Shaw, F. Hill, and D. J. Bell. Vol. 376. Astronomical Society of the Pacific Conference Series, 127 (cit. on p. 75).
- Medling, Anne M. et al. (Apr. 2018). “The SAMI Galaxy Survey: spatially resolving the main sequence of star formation”. *MNRAS* 475.4, 5194–5214. arXiv: 1801.04283 [astro-ph.GA] (cit. on pp. 9, 116).
- Meidt, Sharon E. et al. (June 2015). “Short GMC Lifetimes: An Observational Estimate with the PdBI Arcsecond Whirlpool Survey (PAWS)”. *ApJ* 806.1, 72, 72. arXiv: 1504.04528 [astro-ph.GA] (cit. on p. 18).
- Meidt, Sharon E. et al. (Feb. 2018). “A Model for the Onset of Self-gravitation and Star Formation in Molecular Gas Governed by Galactic Forces. I. Cloud-scale Gas Motions”. *ApJ* 854.2, 100, 100. arXiv: 1712.06364 [astro-ph.GA] (cit. on pp. 18, 26).
- Meidt, Sharon E. et al. (Apr. 2020). “A Model for the Onset of Self-gravitation and Star Formation in Molecular Gas Governed by Galactic Forces. II. The Bottleneck to Collapse Set by Cloud-Environment Decoupling”. *ApJ* 892.2, 73, 73. arXiv: 2001.07459 [astro-ph.GA] (cit. on pp. 26, 116).
- Méndez-Abreu, J., S. F. Sánchez, and A. de Lorenzo-Cáceres (Sept. 2019). “Star formation in CALIFA early-type galaxies: a matter of discs”. *MNRAS* 488.1, L80–L84. arXiv: 1906.10759 [astro-ph.GA] (cit. on pp. 13, 32, 43, 60, 116).
- Mestel, L. and Jr. Spitzer L. (Jan. 1956). “Star formation in magnetic dust clouds”. *MNRAS* 116, 503 (cit. on p. 18).
- Mihos, J. Christopher and Lars Hernquist (June 1996). “Gasdynamics and Starbursts in Major Mergers”. *ApJ* 464, 641. arXiv: astro-ph/9512099 [astro-ph] (cit. on p. 4).
- Miville-Deschênes, M. -A. et al. (Nov. 2003). “High resolution 21 cm mapping of the Ursa Major Galactic cirrus: Power spectra of the high-latitude H I gas”. *A&A* 411, 109–121. arXiv: astro-ph/0306570 [astro-ph] (cit. on p. 69).
- Miville-Deschênes, M. -A. et al. (July 2010). “Herschel-SPIRE observations of the Polaris flare: Structure of the diffuse interstellar medium at the sub-parsec scale”. *A&A* 518, L104, L104. arXiv: 1005.2746 [astro-ph.GA] (cit. on pp. 69, 92).
- Miville-Deschênes, Marc-Antoine, Norman Murray, and Eve J. Lee (Jan. 2017). “Physical Properties of Molecular Clouds for the Entire Milky Way Disk”. *ApJ* 834.1, 57, 57. arXiv: 1610.05918 [astro-ph.GA] (cit. on p. 19).
- Mo, H. J., Shude Mao, and Simon D. M. White (Apr. 1998). “The formation of galactic discs”. *MNRAS* 295.2, 319–336. arXiv: astro-ph/9707093 [astro-ph] (cit. on p. 4).
- Mo, Houjun, Frank C. van den Bosch, and Simon White (2010). *Galaxy Formation and Evolution*. Cambridge University Press (cit. on p. 2).
- Mocz, Philip and Blakesley Burkhart (Oct. 2019). “A Markov Model for Non-lognormal Density Distributions in Compressive Isothermal Turbulence”. *ApJ* 884.2, L35, L35. arXiv: 1908.00544 [astro-ph.GA] (cit. on p. 26).
- Molina, F. Z. et al. (July 2012). “The density variance-Mach number relation in supersonic turbulence - I. Isothermal, magnetized gas”. *MNRAS* 423.3, 2680–2689 (cit. on p. 17).
- Monaghan, J. J. (Jan. 1992). “Smoothed particle hydrodynamics.” *ARA&A* 30, 543–574 (cit. on p. 37).

- Moore, Ben et al. (Feb. 1996). “Galaxy harassment and the evolution of clusters of galaxies”. *Nature* 379.6566, 613–616. arXiv: astro-ph/9510034 [astro-ph] (cit. on pp. 11, 97).
- Morselli, L. et al. (Jan. 2017). “Bulges and discs in the local Universe. Linking the galaxy structure to star formation activity”. *A&A* 597, A97, A97. arXiv: 1607.07675 [astro-ph.GA] (cit. on p. 10).
- Morselli, L. et al. (Aug. 2020). “A panchromatic spatially resolved analysis of nearby galaxies - II. The main sequence - gas relation at sub-kpc scale in grand-design spirals”. *MNRAS* 496.4, 4606–4623. arXiv: 2003.02861 [astro-ph.GA] (cit. on p. 110).
- Moster, Benjamin P., Thorsten Naab, and Simon D. M. White (June 2018). “EMERGE - an empirical model for the formation of galaxies since $z \sim 10$ ”. *MNRAS* 477.2, 1822–1852. arXiv: 1705.05373 [astro-ph.GA] (cit. on pp. 108, 109).
- Mouschovias, T. Ch. and Jr. Spitzer L. (Dec. 1976). “Note on the collapse of magnetic interstellar clouds.” *ApJ* 210, 326 (cit. on p. 22).
- Muñoz Marín, Víctor M. et al. (Aug. 2007). “An Atlas of the Circumnuclear Regions of 75 Seyfert Galaxies in the Near-Ultraviolet with the Hubble Space Telescope Advanced Camera for Surveys”. *AJ* 134.2, 648–667. arXiv: 0704.3617 [astro-ph] (cit. on p. 74).
- Murray, Norman (Mar. 2011). “Star Formation Efficiencies and Lifetimes of Giant Molecular Clouds in the Milky Way”. *ApJ* 729.2, 133, 133. arXiv: 1007.3270 [astro-ph.GA] (cit. on pp. 21, 22, 27, 113).
- Muzzin, Adam et al. (Nov. 2013). “The Evolution of the Stellar Mass Functions of Star-forming and Quiescent Galaxies to $z = 4$ from the COSMOS/UltraVISTA Survey”. *ApJ* 777.1, 18, 18. arXiv: 1303.4409 [astro-ph.CO] (cit. on p. 3).
- Myers, P. C. et al. (Feb. 1986). “Molecular Clouds and Star Formation in the Inner Galaxy: A Comparison of CO, H ii, and Far-Infrared Surveys”. *ApJ* 301, 398 (cit. on p. 21).
- Naab, Thorsten and Jeremiah P. Ostriker (Aug. 2017). “Theoretical Challenges in Galaxy Formation”. *ARA&A* 55.1, 59–109. arXiv: 1612.06891 [astro-ph.GA] (cit. on p. 4).
- Nakamura, Fumitaka and Zhi-Yun Li (June 2007). “Protostellar Turbulence Driven by Collimated Outflows”. *ApJ* 662.1, 395–412. arXiv: astro-ph/0703152 [astro-ph] (cit. on p. 19).
- Nandakumar, Meera and Prasun Dutta (Aug. 2020). “Evidence of large-scale energy cascade in the spiral galaxy NGC 5236”. *MNRAS* 496.2, 1803–1810. arXiv: 2006.04575 [astro-ph.GA] (cit. on p. 69).
- Navarro, J. F. and S. D. M. White (Nov. 1993). “Simulations of Dissipative Galaxy Formation in Hierarchically Clustering Universes - Part One - Tests of the Code”. *MNRAS* 265, 271 (cit. on p. 33).
- Nelson, Dylan et al. (Dec. 2019). “First results from the TNG50 simulation: galactic outflows driven by supernovae and black hole feedback”. *MNRAS* 490.3, 3234–3261. arXiv: 1902.05554 [astro-ph.GA] (cit. on p. 118).
- Nelson, Erica J. et al. (Jan. 2021). “Spatially Resolved Star Formation and Inside-out Quenching in the TNG50 Simulation and 3D-HST Observations”. *arXiv e-prints*, arXiv:2101.12212, arXiv:2101.12212. arXiv: 2101.12212 [astro-ph.GA] (cit. on pp. 116, 118).

- Nickerson, Sarah, Romain Teyssier, and Joakim Rosdahl (Mar. 2019). “Towards the complete census of molecular hydrogen in a simulated disc galaxy”. *MNRAS* 484.1, 1238–1256. arXiv: 1809.01657 [astro-ph.GA] (cit. on p. 33).
- Noeske, K. G. et al. (May 2007a). “Star Formation in AEGIS Field Galaxies since $z=1.1$: Staged Galaxy Formation and a Model of Mass-dependent Gas Exhaustion”. *ApJ* 660.1, L47–L50. arXiv: astro-ph/0703056 [astro-ph] (cit. on p. 9).
- Noeske, K. G. et al. (May 2007b). “Star Formation in AEGIS Field Galaxies since $z=1.1$: The Dominance of Gradually Declining Star Formation, and the Main Sequence of Star-forming Galaxies”. *ApJ* 660.1, L43–L46. arXiv: astro-ph/0701924 [astro-ph] (cit. on pp. 8, 59, 96, 104).
- Norman, Colin A. and Andrea Ferrara (Aug. 1996). “The Turbulent Interstellar Medium: Generalizing to a Scale-dependent Phase Continuum”. *ApJ* 467, 280. arXiv: astro-ph/9602146 [astro-ph] (cit. on p. 18).
- North, Eve V. et al. (Nov. 2019). “WISDOM project - V. Resolving molecular gas in Keplerian rotation around the supermassive black hole in NGC 0383”. *MNRAS* 490.1, 319–330. arXiv: 1909.05884 [astro-ph.GA] (cit. on pp. 60, 61, 69, 74, 75, 90).
- North, Eve V. et al. (Mar. 2021). “WISDOM project - VIII. Multi-scale feedback cycles in the brightest cluster galaxy NGC 0708”. *MNRAS*. arXiv: 2103.08988 [astro-ph.GA] (cit. on p. 75).
- Núñez-Castiñeyra, A. et al. (Jan. 2021). “Cosmological simulations of the same spiral galaxy: the impact of baryonic physics”. *MNRAS* 501.1, 62–77. arXiv: 2004.06008 [astro-ph.GA] (cit. on p. 25).
- Ochsendorf, Bram B. et al. (June 2017). “What Sets the Massive Star Formation Rates and Efficiencies of Giant Molecular Clouds?” *ApJ* 841.2, 109, 109. arXiv: 1704.06965 [astro-ph.GA] (cit. on p. 22).
- Ocvirk, P., C. Pichon, and R. Teyssier (Nov. 2008). “Bimodal gas accretion in the Horizon-MareNostrum galaxy formation simulation”. *MNRAS* 390.4, 1326–1338. arXiv: 0803.4506 [astro-ph] (cit. on p. 11).
- Onishi, Kyoko et al. (July 2017). “WISDOM project - I. Black hole mass measurement using molecular gas kinematics in NGC 3665”. *MNRAS* 468.4, 4663–4674. arXiv: 1703.05247 [astro-ph.GA] (cit. on pp. 70, 77, 93, 115).
- Oosterloo, Tom et al. (Dec. 2010). “Early-type galaxies in different environments: an HI view”. *MNRAS* 409.2, 500–514. arXiv: 1007.2059 [astro-ph.CO] (cit. on p. 4).
- Oppenheimer, Benjamin D. and Romeel Davé (June 2008). “Mass, metal, and energy feedback in cosmological simulations”. *MNRAS* 387.2, 577–600. arXiv: 0712.1827 [astro-ph] (cit. on p. 14).
- Ostriker, Eve C., James M. Stone, and Charles F. Gammie (Jan. 2001). “Density, Velocity, and Magnetic Field Structure in Turbulent Molecular Cloud Models”. *ApJ* 546.2, 980–1005. arXiv: astro-ph/0008454 [astro-ph] (cit. on p. 17).
- Pacifici, Camilla et al. (June 2016). “Timing the Evolution of Quiescent and Star-forming Local Galaxies”. *ApJ* 824.1, 45, 45. arXiv: 1604.02460 [astro-ph.GA] (cit. on p. 10).

- Padoan, Paolo, Troels Haugbølle, and Åke Nordlund (Nov. 2012). “A Simple Law of Star Formation”. *ApJ* 759.2, L27, L27. arXiv: 1208.3758 [astro-ph.GA] (cit. on pp. 27, 34, 45, 51, 62, 64, 72, 99, 111, 113).
- Padoan, Paolo and Åke Nordlund (Mar. 2011). “The Star Formation Rate of Supersonic Magnetohydrodynamic Turbulence”. *ApJ* 730.1, 40, 40. arXiv: 0907.0248 [astro-ph.GA] (cit. on pp. 22–24, 26, 34).
- Padoan, Paolo, Åke Nordlund, and Bernard J. T. Jones (June 1997). “The universality of the stellar initial mass function”. *MNRAS* 288.1, 145–152. arXiv: astro-ph/9703110 [astro-ph] (cit. on p. 17).
- Padoan, Paolo et al. (May 2017). “Supernova Driving. IV. The Star-formation Rate of Molecular Clouds”. *ApJ* 840.1, 48, 48. arXiv: 1702.07270 [astro-ph.GA] (cit. on pp. 27, 34, 45, 72, 99, 111, 113).
- Palla, Francesco and Steven W. Stahler (Sept. 2000). “Accelerating Star Formation in Clusters and Associations”. *ApJ* 540.1, 255–270 (cit. on p. 25).
- Pan, Hsi-An et al. (Feb. 2018). “SDSS IV MaNGA: Dependence of Global and Spatially Resolved SFR-M_{*} Relations on Galaxy Properties”. *ApJ* 854.2, 159, 159. arXiv: 1801.04446 [astro-ph.GA] (cit. on p. 9).
- Pannella, M. et al. (June 2009). “Star Formation and Dust Obscuration at $z \approx 2$: Galaxies at the Dawn of Downsizing”. *ApJ* 698.2, L116–L120. arXiv: 0905.1674 [astro-ph.CO] (cit. on p. 8).
- Peng, Ying-jie and Roberto Maiolino (Oct. 2014). “From haloes to Galaxies - I. The dynamics of the gas regulator model and the implied cosmic sSFR history”. *MNRAS* 443.4, 3643–3664. arXiv: 1402.5964 [astro-ph.CO] (cit. on pp. 15, 97).
- Peng, Ying-jie et al. (Sept. 2010). “Mass and Environment as Drivers of Galaxy Evolution in SDSS and zCOSMOS and the Origin of the Schechter Function”. *ApJ* 721.1, 193–221. arXiv: 1003.4747 [astro-ph.CO] (cit. on pp. 8, 10, 59, 96, 104).
- Peng, Ying-jie et al. (Sept. 2012). “Mass and Environment as Drivers of Galaxy Evolution. II. The Quenching of Satellite Galaxies as the Origin of Environmental Effects”. *ApJ* 757.1, 4, 4. arXiv: 1106.2546 [astro-ph.CO] (cit. on p. 10).
- Péroux, Céline and J. Christopher Howk (Aug. 2020). “The Cosmic Baryon and Metal Cycles”. *ARA&A* 58, 363–406. arXiv: 2011.01935 [astro-ph.GA] (cit. on p. 14).
- Pilkington, K. et al. (Nov. 2011). “The cold gas content of bulgeless dwarf galaxies”. *MNRAS* 417.4, 2891–2898. arXiv: 1107.2922 [astro-ph.CO] (cit. on p. 91).
- Pillepich, Annalisa et al. (Jan. 2018). “Simulating galaxy formation with the IllustrisTNG model”. *MNRAS* 473.3, 4077–4106. arXiv: 1703.02970 [astro-ph.GA] (cit. on pp. 12, 33).
- Pingel, N. M. et al. (Apr. 2018). “Multi-phase Turbulence Density Power Spectra in the Perseus Molecular Cloud”. *ApJ* 856.2, 136, 136. arXiv: 1802.10092 [astro-ph.GA] (cit. on pp. 69, 92).
- Piotrowska, Joanna M. et al. (Feb. 2020). “Towards a deeper understanding of the physics driving galaxy quenching - inferring trends in the gas content via extinction”. *MNRAS* 492.1, L6–L11. arXiv: 1911.06693 [astro-ph.GA] (cit. on pp. 110, 115).

- Popesso, P. et al. (Mar. 2019). “The main sequence of star-forming galaxies - I. The local relation and its bending”. MNRAS 483.3, 3213–3226. arXiv: 1812.07057 [astro-ph.GA] (cit. on pp. 8, 9).
- Price, D. J. and J. J. Monaghan (Feb. 2007). “An energy-conserving formalism for adaptive gravitational force softening in smoothed particle hydrodynamics and N-body codes”. MNRAS 374.4, 1347–1358. arXiv: astro-ph/0610872 [astro-ph] (cit. on pp. 37, 63, 72, 101).
- Querejeta, M. et al. (May 2019). “Dense gas is not enough: environmental variations in the star formation efficiency of dense molecular gas at 100 pc scales in M 51”. A&A 625, A19, A19. arXiv: 1902.10437 [astro-ph.GA] (cit. on pp. 7, 22, 116).
- Reina Campos, Marta (2020). *Formation and evolution of globular clusters in a cosmological context*. Heidelberg. URL: <http://archiv.ub.uni-heidelberg.de/volltextserver/29004/> (cit. on p. 119).
- Renaud, F. et al. (Dec. 2013). “A sub-parsec resolution simulation of the Milky Way: global structure of the interstellar medium and properties of molecular clouds”. MNRAS 436.2, 1836–1851. arXiv: 1307.5639 [astro-ph.GA] (cit. on pp. 69, 91, 114).
- Renzini, Alvio and Ying-jie Peng (Mar. 2015). “An Objective Definition for the Main Sequence of Star-forming Galaxies”. ApJ 801.2, L29, L29. arXiv: 1502.01027 [astro-ph.GA] (cit. on p. 8).
- Roberts, Morton S. and M. P. Haynes (Jan. 1994). “Physical Parameters along the Hubble Sequence”. ARA&A 32, 115–152 (cit. on pp. 3, 4).
- Roberts, W. W. (Oct. 1969). “Large-Scale Shock Formation in Spiral Galaxies and its Implications on Star Formation”. ApJ 158, 123 (cit. on p. 18).
- Robertson, Brant et al. (May 2004). “Disk Galaxy Formation in a Λ Cold Dark Matter Universe”. ApJ 606.1, 32–45. arXiv: astro-ph/0401252 [astro-ph] (cit. on p. 4).
- Robertson, Brant et al. (July 2006). “A Merger-driven Scenario for Cosmological Disk Galaxy Formation”. ApJ 645.2, 986–1000. arXiv: astro-ph/0503369 [astro-ph] (cit. on p. 4).
- Robertson, Brant E. and Andrey V. Kravtsov (June 2008). “Molecular Hydrogen and Global Star Formation Relations in Galaxies”. ApJ 680.2, 1083–1111. arXiv: 0710.2102 [astro-ph] (cit. on p. 33).
- Rodighiero, G. et al. (July 2010). “The first Herschel view of the mass-SFR link in high- z galaxies”. A&A 518, L25, L25. arXiv: 1005.1089 [astro-ph.CO] (cit. on p. 8).
- Rodighiero, G. et al. (Oct. 2011). “The Lesser Role of Starbursts in Star Formation at $z = 2$ ”. ApJ 739.2, L40, L40. arXiv: 1108.0933 [astro-ph.CO] (cit. on pp. 8, 15).
- Rodighiero, G. et al. (Feb. 2015). “Relationship between Star Formation Rate and Black Hole Accretion At $Z = 2$: the Different Contributions in Quiescent, Normal, and Starburst Galaxies”. ApJ 800.1, L10, L10. arXiv: 1501.04634 [astro-ph.GA] (cit. on p. 15).
- Romeo, Alessandro B., Andreas Burkert, and Oscar Agertz (Sept. 2010). “A Toomre-like stability criterion for the clumpy and turbulent interstellar medium”. MNRAS 407.2, 1223–1230. arXiv: 1001.4732 [astro-ph.CO] (cit. on p. 92).

- Rosdahl, Joakim et al. (Apr. 2017). “Snap, crackle, pop: sub-grid supernova feedback in AMR simulations of disc galaxies”. *MNRAS* 466.1, 11–33. arXiv: 1609.01296 [astro-ph.GA] (cit. on p. 38).
- Rosdahl, Joakim et al. (Sept. 2018). “The SPHINX cosmological simulations of the first billion years: the impact of binary stars on reionization”. *MNRAS* 479.1, 994–1016. arXiv: 1801.07259 [astro-ph.GA] (cit. on p. 34).
- Roškar, Rok et al. (Nov. 2014). “A systematic look at the effects of radiative feedback on disc galaxy formation”. *MNRAS* 444.3, 2837–2853. arXiv: 1308.6321 [astro-ph.CO] (cit. on p. 12).
- Rosolowsky, E. et al. (Dec. 2003). “Giant Molecular Clouds in M33. II. High-Resolution Observations”. *ApJ* 599.1, 258–274. arXiv: astro-ph/0307322 [astro-ph] (cit. on p. 19).
- Rowlands, K. et al. (Mar. 2015). “The evolution of the cold interstellar medium in galaxies following a starburst”. *MNRAS* 448.1, 258–279. arXiv: 1412.6090 [astro-ph.GA] (cit. on pp. 10, 12, 15, 117).
- Saintonge, Amelie et al. (Oct. 2016). “Molecular and atomic gas along and across the main sequence of star-forming galaxies”. *MNRAS* 462.2, 1749–1756. arXiv: 1607.05289 [astro-ph.GA] (cit. on pp. 8, 9).
- Saintonge, Amélie et al. (July 2011). “COLD GASS, an IRAM legacy survey of molecular gas in massive galaxies - II. The non-universality of the molecular gas depletion time-scale”. *MNRAS* 415.1, 61–76. arXiv: 1104.0019 [astro-ph.CO] (cit. on pp. 6, 13).
- Saintonge, Amélie et al. (Oct. 2012). “The Impact of Interactions, Bars, Bulges, and Active Galactic Nuclei on Star Formation Efficiency in Local Massive Galaxies”. *ApJ* 758.2, 73, 73. arXiv: 1209.0476 [astro-ph.CO] (cit. on pp. 6, 31).
- Saintonge, Amélie et al. (Dec. 2017). “xCOLD GASS: The Complete IRAM 30 m Legacy Survey of Molecular Gas for Galaxy Evolution Studies”. *ApJS* 233.2, 22, 22. arXiv: 1710.02157 [astro-ph.GA] (cit. on pp. 4, 32, 40, 58, 59, 65, 72, 103, 104).
- Sanders, D. B. et al. (Feb. 1988). “Ultraluminous Infrared Galaxies and the Origin of Quasars”. *ApJ* 325, 74 (cit. on p. 11).
- Scalo, John et al. (Sept. 1998). “On the Probability Density Function of Galactic Gas. I. Numerical Simulations and the Significance of the Polytropic Index”. *ApJ* 504.2, 835–853. arXiv: astro-ph/9710075 [astro-ph] (cit. on p. 17).
- Schawinski, Kevin et al. (May 2014). “The green valley is a red herring: Galaxy Zoo reveals two evolutionary pathways towards quenching of star formation in early- and late-type galaxies”. *MNRAS* 440.1, 889–907. arXiv: 1402.4814 [astro-ph.GA] (cit. on pp. 11, 117).
- Schaye, Joop et al. (Jan. 2015). “The EAGLE project: simulating the evolution and assembly of galaxies and their environments”. *MNRAS* 446.1, 521–554. arXiv: 1407.7040 [astro-ph.GA] (cit. on pp. 12, 118).
- Schiminovich, David et al. (Dec. 2007). “The UV-Optical Color Magnitude Diagram. II. Physical Properties and Morphological Evolution On and Off of a Star-forming Sequence”. *ApJS* 173.2, 315–341. arXiv: 0711.4823 [astro-ph] (cit. on p. 8).

- Schmidt, Maarten (Mar. 1959). “The Rate of Star Formation.” *ApJ* 129, 243 (cit. on pp. 5, 30).
- Schommer, R. A. and G. D. Bothun (May 1983). “Very red, yet HI rich galaxies.” *AJ* 88, 577–582 (cit. on p. 6).
- Schreiber, C. et al. (Mar. 2015). “The Herschel view of the dominant mode of galaxy growth from $z = 4$ to the present day”. *A&A* 575, A74, A74. arXiv: 1409.5433 [[astro-ph.GA](#)] (cit. on pp. 8, 9).
- Schruba, Andreas, J. M. Diederik Kruijssen, and Adam K. Leroy (Sept. 2019). “How Galactic Environment Affects the Dynamical State of Molecular Clouds and Their Star Formation Efficiency”. *ApJ* 883.1, 2, 2. arXiv: 1908.04306 [[astro-ph.GA](#)] (cit. on pp. 18, 20, 27, 33, 47, 51, 60, 103, 111).
- Schruba, Andreas et al. (Aug. 2011). “A Molecular Star Formation Law in the Atomic-gas-dominated Regime in Nearby Galaxies”. *AJ* 142.2, 37, 37. arXiv: 1105.4605 [[astro-ph.CO](#)] (cit. on pp. 5, 6).
- Semenov, Vadim A., Andrey V. Kravtsov, and Nickolay Y. Gnedin (Aug. 2016). “Nonuniversal Star Formation Efficiency in Turbulent ISM”. *ApJ* 826.2, 200, 200. arXiv: 1512.03101 [[astro-ph.GA](#)] (cit. on pp. 27, 34, 35, 62, 72, 110).
- (Aug. 2017). “The Physical Origin of Long Gas Depletion Times in Galaxies”. *ApJ* 845.2, 133, 133. arXiv: 1704.04239 [[astro-ph.GA](#)] (cit. on pp. 22, 62).
- (July 2018). “How Galaxies Form Stars: The Connection between Local and Global Star Formation in Galaxy Simulations”. *ApJ* 861.1, 4, 4. arXiv: 1803.00007 [[astro-ph.GA](#)] (cit. on pp. 22, 62).
- (Jan. 2019). “What Sets the Slope of the Molecular Kennicutt-Schmidt Relation?” *ApJ* 870.2, 79, 79. arXiv: 1809.07328 [[astro-ph.GA](#)] (cit. on p. 118).
- Serra, Paolo et al. (May 2012). “The ATLAS^{3D} project - XIII. Mass and morphology of H I in early-type galaxies as a function of environment”. *MNRAS* 422.3, 1835–1862. arXiv: 1111.4241 [[astro-ph.CO](#)] (cit. on p. 92).
- Sérsic, J. L. (Feb. 1963). “Influence of the atmospheric and instrumental dispersion on the brightness distribution in a galaxy”. *Boletín de la Asociación Argentina de Astronomía La Plata Argentina* 6, 41–43 (cit. on p. 8).
- Seth, Anil C. et al. (May 2010). “The NGC 404 Nucleus: Star Cluster and Possible Intermediate-mass Black Hole”. *ApJ* 714.1, 713–731. arXiv: 1003.0680 [[astro-ph.CO](#)] (cit. on p. 74).
- Shapiro, Paul R. and George B. Field (May 1976). “Consequences of a New Hot Component of the Interstellar Medium”. *ApJ* 205, 762–765 (cit. on p. 14).
- Shen, Sijing et al. (Sept. 2014). “The Baryon Cycle of Dwarf Galaxies: Dark, Bursty, Gas-rich Polluters”. *ApJ* 792.2, 99, 99. arXiv: 1308.4131 [[astro-ph.CO](#)] (cit. on p. 12).
- Shu, Frank H., Fred C. Adams, and Susana Lizano (Jan. 1987). “Star formation in molecular clouds: observation and theory.” *ARA&A* 25, 23–81 (cit. on p. 22).
- Skrutskie, M. F. et al. (Feb. 2006). “The Two Micron All Sky Survey (2MASS)”. *AJ* 131.2, 1163–1183 (cit. on pp. 74, 75).

- Slyz, Adrienne D. et al. (Jan. 2005). “Towards simulating star formation in the interstellar medium”. MNRAS 356.2, 737–752. arXiv: astro-ph/0411383 [astro-ph] (cit. on p. 17).
- Smircina, A. et al. (Mar. 2018). “After the Fall: The Dust and Gas in E+A Post-starburst Galaxies”. ApJ 855.1, 51, 51. arXiv: 1802.04798 [astro-ph.GA] (cit. on pp. 10, 13).
- Smith, Britton D. et al. (Apr. 2017). “GRACKLE: a chemistry and cooling library for astrophysics”. MNRAS 466.2, 2217–2234. arXiv: 1610.09591 [astro-ph.CO] (cit. on pp. 37, 72, 100).
- Smith, Mark D. et al. (May 2019). “WISDOM project - IV. A molecular gas dynamical measurement of the supermassive black hole mass in NGC 524”. MNRAS 485.3, 4359–4374. arXiv: 1903.03124 [astro-ph.GA] (cit. on pp. 74, 75, 77).
- Smith, Mark D. et al. (Mar. 2021). “WISDOM project - VII. Molecular gas measurement of the supermassive black hole mass in the elliptical galaxy NGC 7052”. MNRAS. arXiv: 2103.08920 [astro-ph.GA] (cit. on p. 75).
- Sobolev, V. V. (1960). *Moving envelopes of stars* (cit. on p. 35).
- Solomon, P. M. et al. (Aug. 1987). “Mass, Luminosity, and Line Width Relations of Galactic Molecular Clouds”. ApJ 319, 730 (cit. on pp. 17, 19).
- Somerville, Rachel S. and Romeel Davé (Aug. 2015). “Physical Models of Galaxy Formation in a Cosmological Framework”. ARA&A 53, 51–113. arXiv: 1412.2712 [astro-ph.GA] (cit. on p. 4).
- Speagle, J. S. et al. (Oct. 2014). “A Highly Consistent Framework for the Evolution of the Star-Forming “Main Sequence” from $z \sim 0-6$ ”. ApJS 214.2, 15, 15. arXiv: 1405.2041 [astro-ph.GA] (cit. on pp. 8, 106, 107, 116, 177, 178).
- Spitzer, Lyman (1978). *Physical processes in the interstellar medium* (cit. on p. 21).
- Springel, Volker (Jan. 2010). “E pur si muove: Galilean-invariant cosmological hydrodynamical simulations on a moving mesh”. MNRAS 401.2, 791–851. arXiv: 0901.4107 [astro-ph.CO] (cit. on pp. 34, 36, 72, 99, 113).
- Springel, Volker, Tiziana Di Matteo, and Lars Hernquist (Aug. 2005a). “Modelling feedback from stars and black holes in galaxy mergers”. MNRAS 361.3, 776–794. arXiv: astro-ph/0411108 [astro-ph] (cit. on pp. 38, 101).
- Springel, Volker and Lars Hernquist (Feb. 2003). “Cosmological smoothed particle hydrodynamics simulations: a hybrid multiphase model for star formation”. MNRAS 339.2, 289–311. arXiv: astro-ph/0206393 [astro-ph] (cit. on p. 33).
- Springel, Volker et al. (June 2005b). “Simulations of the formation, evolution and clustering of galaxies and quasars”. Nature 435.7042, 629–636. arXiv: astro-ph/0504097 [astro-ph] (cit. on pp. 2, 12).
- Stanimirovic, S. et al. (Jan. 1999). “The large-scale HI structure of the Small Magellanic Cloud”. MNRAS 302.3, 417–436 (cit. on pp. 69, 70, 90).
- Starkenbug, Tjitske K., Stephanie Tonnesen, and Claire Kopenhafer (Apr. 2019). “What Is Inside Matters: Simulated Green Valley Galaxies Have too Centrally Concentrated Star Formation”. ApJ 874.2, L17, L17. arXiv: 1812.01017 [astro-ph.GA] (cit. on p. 118).

- Stinson, G. S. et al. (Jan. 2013). “Making Galaxies In a Cosmological Context: the need for early stellar feedback”. MNRAS 428.1, 129–140. arXiv: 1208.0002 [astro-ph.CO] (cit. on p. 12).
- Stinson, Greg et al. (Dec. 2006). “Star formation and feedback in smoothed particle hydrodynamic simulations - I. Isolated galaxies”. MNRAS 373.3, 1074–1090. arXiv: astro-ph/0602350 [astro-ph] (cit. on p. 33).
- Stone, James M., Eve C. Ostriker, and Charles F. Gammie (Nov. 1998). “Dissipation in Compressible Magnetohydrodynamic Turbulence”. ApJ 508.1, L99–L102. arXiv: astro-ph/9809357 [astro-ph] (cit. on p. 18).
- Straatman, Caroline M. S. et al. (Mar. 2014). “A Substantial Population of Massive Quiescent Galaxies at $z \sim 4$ from ZFOURGE”. ApJ 783.1, L14, L14. arXiv: 1312.4952 [astro-ph.GA] (cit. on p. 11).
- Stutzki, J. et al. (Aug. 1998). “On the fractal structure of molecular clouds”. A&A 336, 697–720 (cit. on p. 69).
- Su, Kung-Yi et al. (Aug. 2019). “The failure of stellar feedback, magnetic fields, conduction, and morphological quenching in maintaining red galaxies”. MNRAS 487.3, 4393–4408. arXiv: 1809.09120 [astro-ph.GA] (cit. on pp. 13, 32, 61, 98, 110, 116).
- Su, Kung-Yi et al. (Jan. 2020). “Cosmic rays or turbulence can suppress cooling flows (where thermal heating or momentum injection fail)”. MNRAS 491.1, 1190–1212. arXiv: 1812.03997 [astro-ph.GA] (cit. on p. 112).
- Suess, Katherine A. et al. (Sept. 2017). “Massive Quenched Galaxies at $z \sim 0.7$ Retain Large Molecular Gas Reservoirs”. ApJ 846.2, L14, L14. arXiv: 1708.03337 [astro-ph.GA] (cit. on pp. 10, 12, 13, 15, 68, 97, 98, 117).
- Sun, Jiayi et al. (June 2018). “Cloud-scale Molecular Gas Properties in 15 Nearby Galaxies”. ApJ 860.2, 172, 172. arXiv: 1805.00937 [astro-ph.GA] (cit. on pp. 18, 20, 51, 60).
- Sun, Jiayi et al. (Apr. 2020a). “Dynamical Equilibrium in the Molecular ISM in 28 Nearby Star-forming Galaxies”. ApJ 892.2, 148, 148. arXiv: 2002.08964 [astro-ph.GA] (cit. on pp. 20, 60).
- Sun, Jiayi et al. (Sept. 2020b). “Molecular Gas Properties on Cloud Scales across the Local Star-forming Galaxy Population”. ApJ 901.1, L8, L8. arXiv: 2009.01842 [astro-ph.GA] (cit. on pp. 18, 20).
- Sweatman, Martin B. and Alistair Coombs (May 2018). “Decoding European Palaeolithic art: Extremely ancient knowledge of precession of the equinoxes”. *arXiv e-prints*, arXiv:1806.00046, arXiv:1806.00046. arXiv: 1806.00046 [physics.hist-ph] (cit. on p. 1).
- Swift, Jonathan J. and William J. Welch (Jan. 2008). “A Case Study of Low-Mass Star Formation”. ApJS 174.1, 202–222. arXiv: 0706.2206 [astro-ph] (cit. on p. 69).
- Tacchella, S. et al. (May 2018). “Dust Attenuation, Bulge Formation, and Inside-out Quenching of Star Formation in Star-forming Main Sequence Galaxies at $z \sim 2$ ”. ApJ 859.1, 56, 56. arXiv: 1704.00733 [astro-ph.GA] (cit. on p. 116).
- Tacchella, Sandro, John C. Forbes, and Neven Caplar (Sept. 2020). “Stochastic modelling of star-formation histories II: star-formation variability from molecular clouds and gas inflow”. MNRAS 497.1, 698–725. arXiv: 2006.09382 [astro-ph.GA] (cit. on pp. 15, 112).

- Tacconi, L. J. et al. (May 2013). “Phibss: Molecular Gas Content and Scaling Relations in $z \sim 1-3$ Massive, Main-sequence Star-forming Galaxies”. *ApJ* 768.1, 74, 74. arXiv: 1211.5743 [astro-ph.CO] (cit. on pp. 4, 101).
- Tacconi, L. J. et al. (Feb. 2018). “PHIBSS: Unified Scaling Relations of Gas Depletion Time and Molecular Gas Fractions”. *ApJ* 853.2, 179, 179. arXiv: 1702.01140 [astro-ph.GA] (cit. on pp. 4, 106–111, 116).
- Tacconi, Linda J., Reinhard Genzel, and Amiel Sternberg (Aug. 2020). “The Evolution of the Star-Forming Interstellar Medium Across Cosmic Time”. *ARA&A* 58, 157–203. arXiv: 2003.06245 [astro-ph.GA] (cit. on p. 4).
- Tamburro, D. et al. (May 2009). “What is Driving the H I Velocity Dispersion?” *AJ* 137.5, 4424–4435. arXiv: 0903.0183 [astro-ph.GA] (cit. on p. 18).
- Thanjavur, Karun et al. (June 2016). “Stellar mass functions of galaxies, discs and spheroids at $z \sim 0.1$ ”. *MNRAS* 459.1, 44–69. arXiv: 1602.08674 [astro-ph.GA] (cit. on p. 109).
- Thilker, David A. et al. (May 2010). “NGC 404: A Rejuvenated Lenticular Galaxy on a Merger-induced, Blueward Excursion Into the Green Valley”. *ApJ* 714.1, L171–L175. arXiv: 1003.4985 [astro-ph.CO] (cit. on p. 74).
- Tielens, A. G. G. M. (2005). *The Physics and Chemistry of the Interstellar Medium*. Cambridge University Press (cit. on p. 16).
- Tomczak, Adam R. et al. (Feb. 2016). “The SFR- M^* Relation and Empirical Star-Formation Histories from ZFOURGE* at $0.5 < z < 4$ ”. *ApJ* 817.2, 118, 118. arXiv: 1510.06072 [astro-ph.GA] (cit. on p. 8).
- Tonry, John L. et al. (Jan. 2001). “The SBF Survey of Galaxy Distances. IV. SBF Magnitudes, Colors, and Distances”. *ApJ* 546.2, 681–693. arXiv: astro-ph/0011223 [astro-ph] (cit. on p. 74).
- Toomre, A. (May 1964). “On the gravitational stability of a disk of stars.” *ApJ* 139, 1217–1238 (cit. on pp. 12, 31, 97).
- Toomre, Alar (Jan. 1977). “Mergers and Some Consequences”. *Evolution of Galaxies and Stellar Populations*. Ed. by Beatrice M. Tinsley and D. Campbell Larson Richard B. Gehret, 401 (cit. on p. 4).
- Toomre, Alar and Juri Toomre (Dec. 1972). “Galactic Bridges and Tails”. *ApJ* 178, 623–666 (cit. on p. 2).
- Trebitsch, Maxime et al. (Sept. 2017). “Fluctuating feedback-regulated escape fraction of ionizing radiation in low-mass, high-redshift galaxies”. *MNRAS* 470.1, 224–239. arXiv: 1705.00941 [astro-ph.GA] (cit. on pp. 25, 34, 62, 98).
- Tremonti, Christy A. et al. (Oct. 2004). “The Origin of the Mass-Metallicity Relation: Insights from 53,000 Star-forming Galaxies in the Sloan Digital Sky Survey”. *ApJ* 613.2, 898–913. arXiv: astro-ph/0405537 [astro-ph] (cit. on p. 97).
- Tumlinson, J. et al. (Nov. 2011). “The Large, Oxygen-Rich Halos of Star-Forming Galaxies Are a Major Reservoir of Galactic Metals”. *Science* 334.6058, 948. arXiv: 1111.3980 [astro-ph.CO] (cit. on p. 14).
- Usero, Antonio et al. (Oct. 2015). “Variations in the Star Formation Efficiency of the Dense Molecular Gas across the Disks of Star-forming Galaxies”. *AJ* 150.4, 115, 115. arXiv: 1506.00703 [astro-ph.GA] (cit. on pp. 7, 26, 116).

- Utomo, Dyas et al. (July 2018). “Star Formation Efficiency per Free-fall Time in nearby Galaxies”. *ApJ* 861.2, L18, L18. arXiv: 1806.11121 [astro-ph.GA] (cit. on pp. 22, 33, 113).
- van de Voort, Freeke et al. (May 2018). “An ALMA view of star formation efficiency suppression in early-type galaxies after gas-rich minor mergers”. *MNRAS* 476.1, 122–132. arXiv: 1801.08140 [astro-ph.GA] (cit. on pp. 6, 15, 117).
- van den Bergh, S. (June 1976). “A new classification system for galaxies.” *ApJ* 206, 883–887 (cit. on p. 2).
- van der Wel, A. et al. (Sept. 2014). “Geometry of Star-forming Galaxies from SDSS, 3D-HST, and CANDELS”. *ApJ* 792.1, L6, L6. arXiv: 1407.4233 [astro-ph.GA] (cit. on pp. 106, 116).
- van Zee, Liese and Jessica Bryant (Nov. 1999). “Neutral Gas Distribution and Kinematics of the Nearly Face-on Spiral Galaxy NGC 1232”. *AJ* 118.5, 2172–2183. arXiv: astro-ph/9907278 [astro-ph] (cit. on p. 18).
- Vazquez-Semadeni, Enrique (Mar. 1994). “Hierarchical Structure in Nearly Pressureless Flows as a Consequence of Self-similar Statistics”. *ApJ* 423, 681 (cit. on p. 17).
- Vázquez-Semadeni, E., J. Ballesteros-Paredes, and R. S. Klessen (Mar. 2003). “A Holistic Scenario of Turbulent Molecular Cloud Evolution and Control of the Star Formation Efficiency: First Tests”. *ApJ* 585.2, L131–L134. arXiv: astro-ph/0301546 [astro-ph] (cit. on p. 23).
- Vázquez-Semadeni, Enrique, Adriana Gazol, and John Scalo (Sept. 2000). “Is Thermal Instability Significant in Turbulent Galactic Gas?” *ApJ* 540.1, 271–285. arXiv: astro-ph/0001027 [astro-ph] (cit. on p. 19).
- Veilleux, Sylvain, Gerald Cecil, and Joss Bland-Hawthorn (Sept. 2005). “Galactic Winds”. *ARA&A* 43.1, 769–826. arXiv: astro-ph/0504435 [astro-ph] (cit. on pp. 12, 14, 117).
- Vogelsberger, Mark et al. (Oct. 2014). “Introducing the Illustris Project: simulating the coevolution of dark and visible matter in the Universe”. *MNRAS* 444.2, 1518–1547. arXiv: 1405.2921 [astro-ph.CO] (cit. on pp. 11, 118).
- Vutisalchavakul, Nalin, II Evans Neal J., and Mark Heyer (Nov. 2016). “Star Formation Relations in the Milky Way”. *ApJ* 831.1, 73, 73. arXiv: 1607.06518 [astro-ph.SR] (cit. on pp. 21, 27).
- Wada, Keiichi (Jan. 2004). “Fueling Gas to the Central Region of Galaxies”. *Coevolution of Black Holes and Galaxies*. Ed. by Luis C. Ho, 186. arXiv: astro-ph/0308134 [astro-ph] (cit. on p. 119).
- (Mar. 2008). “Instabilities of Spiral Shocks. II. A Quasi-Steady State in the Multiphase Inhomogeneous ISM”. *ApJ* 675.1, 188–193. arXiv: 0710.0407 [astro-ph] (cit. on p. 18).
- Walker, A. P. et al. (June 2014). “The role of feedback in shaping the structure of the interstellar medium”. *MNRAS* 441.1, 525–531. arXiv: 1403.0488 [astro-ph.GA] (cit. on pp. 70, 80, 91–93).
- Wang, Peng et al. (Jan. 2010). “Outflow Feedback Regulated Massive Star Formation in Parsec-Scale Cluster-Forming Clumps”. *ApJ* 709.1, 27–41. arXiv: 0908.4129 [astro-ph.SR] (cit. on p. 19).

- Weinberger, Rainer, Volker Springel, and Rüdiger Pakmor (June 2020). “The AREPO Public Code Release”. *ApJS* 248.2, 32, 32. arXiv: 1909.04667 [astro-ph.IM] (cit. on pp. 72, 113).
- Weinberger, Rainer et al. (Sept. 2018). “Supermassive black holes and their feedback effects in the IllustrisTNG simulation”. *MNRAS* 479.3, 4056–4072. arXiv: 1710.04659 [astro-ph.GA] (cit. on p. 118).
- Welch, Gary A., Leslie J. Sage, and Lisa M. Young (Dec. 2010). “The Cool Interstellar Medium in Elliptical Galaxies. II. Gas Content in the Volume-limited Sample and Results from the Combined Elliptical and Lenticular Surveys”. *ApJ* 725.1, 100–114. arXiv: 1009.5259 [astro-ph.CO] (cit. on p. 4).
- Wetzel, Andrew R., Jeremy L. Tinker, and Charlie Conroy (July 2012). “Galaxy evolution in groups and clusters: star formation rates, red sequence fractions and the persistent bimodality”. *MNRAS* 424.1, 232–243. arXiv: 1107.5311 [astro-ph.CO] (cit. on p. 10).
- Wetzel, Andrew R. et al. (June 2013). “Galaxy evolution in groups and clusters: satellite star formation histories and quenching time-scales in a hierarchical Universe”. *MNRAS* 432.1, 336–358. arXiv: 1206.3571 [astro-ph.CO] (cit. on p. 10).
- Whitaker, Katherine E. et al. (July 2011). “The NEWFIRM Medium-band Survey: Photometric Catalogs, Redshifts, and the Bimodal Color Distribution of Galaxies out to $z \sim 3$ ”. *ApJ* 735.2, 86, 86. arXiv: 1105.4609 [astro-ph.CO] (cit. on pp. 3, 10).
- Whitaker, Katherine E. et al. (Aug. 2012). “The Star Formation Mass Sequence Out to $z = 2.5$ ”. *ApJ* 754.2, L29, L29. arXiv: 1205.0547 [astro-ph.CO] (cit. on p. 8).
- Whitaker, Katherine E. et al. (Nov. 2014). “Constraining the Low-mass Slope of the Star Formation Sequence at $0.5 < z < 2.5$ ”. *ApJ* 795.2, 104, 104. arXiv: 1407.1843 [astro-ph.GA] (cit. on p. 8).
- White, S. D. M. and M. J. Rees (May 1978). “Core condensation in heavy halos: a two-stage theory for galaxy formation and clustering.” *MNRAS* 183, 341–358 (cit. on p. 2).
- Wild, Vivienne et al. (May 2009). “Post-starburst galaxies: more than just an interesting curiosity”. *MNRAS* 395.1, 144–159. arXiv: 0810.5122 [astro-ph] (cit. on p. 10).
- Wild, Vivienne et al. (Nov. 2016). “The evolution of post-starburst galaxies from $z=2$ to 0.5”. *MNRAS* 463.1, 832–844. arXiv: 1608.00588 [astro-ph.GA] (cit. on p. 10).
- Willett, Kyle W., Bruce G. Elmegreen, and Deidre A. Hunter (May 2005). “Power Spectra in V band and $H\alpha$ of Nine Irregular Galaxies”. *AJ* 129.5, 2186–2196. arXiv: astro-ph/0503295 [astro-ph] (cit. on pp. 70, 77).
- Williams, Christina C. et al. (Feb. 2021). “ALMA Measures Rapidly Depleted Molecular Gas Reservoirs in Massive Quiescent Galaxies at $z \sim 1.5$ ”. *ApJ* 908.1, 54, 54. arXiv: 2012.01433 [astro-ph.GA] (cit. on pp. 68, 117).
- Williams, J. P., L. Blitz, and C. F. McKee (May 2000). “The Structure and Evolution of Molecular Clouds: from Clumps to Cores to the IMF”. *Protostars and Planets IV*. Ed. by V. Mannings, A. P. Boss, and S. S. Russell, 97. arXiv: astro-ph/9902246 [astro-ph] (cit. on p. 20).
- Williams, Jonathan P., Eugene J. de Geus, and Leo Blitz (June 1994). “Determining Structure in Molecular Clouds”. *ApJ* 428, 693 (cit. on p. 19).

- Williams, Rik J. et al. (Feb. 2009). “Detection of Quiescent Galaxies in a Bicolor Sequence from $Z = 0-2$ ”. *ApJ* 691.2, 1879–1895. arXiv: 0806.0625 [astro-ph] (cit. on p. 10).
- Wilson, Christine D. et al. (Sept. 2019). “The Kennicutt-Schmidt Law and Gas Scale Height in Luminous and Ultraluminous Infrared Galaxies”. *ApJ* 882.1, 5, 5. arXiv: 1907.05432 [astro-ph.GA] (cit. on p. 84).
- Wolf, Max (July 1908). “Die Klassifizierung der kleinen Nebelflecken”. *Publikationen des Astrophysikalischen Instituts Koenigstuhl-Heidelberg* 3, 109–112 (cit. on p. 2).
- Wong, Tony and Leo Blitz (Apr. 2002). “The Relationship between Gas Content and Star Formation in Molecule-rich Spiral Galaxies”. *ApJ* 569.1, 157–183. arXiv: astro-ph/0112204 [astro-ph] (cit. on pp. 4, 5, 12, 16, 33).
- Wu, Jingwen et al. (June 2010). “The Properties of Massive, Dense Clumps: Mapping Surveys of HCN and CS”. *ApJS* 188.2, 313–357. arXiv: 1004.0398 [astro-ph.GA] (cit. on p. 6).
- Wuyts, Stijn et al. (Dec. 2011). “Galaxy Structure and Mode of Star Formation in the SFR-Mass Plane from $z \sim 2.5$ to $z \sim 0.1$ ”. *ApJ* 742.2, 96, 96. arXiv: 1107.0317 [astro-ph.CO] (cit. on pp. 8, 9, 97).
- Yesuf, Hassen M. and Luis C. Ho (Sept. 2020). “Some Die Filthy Rich: The Diverse Molecular Gas Contents of Post-starburst Galaxies Probed by Dust Absorption”. *ApJ* 900.2, 107, 107. arXiv: 2007.14004 [astro-ph.GA] (cit. on p. 10).
- Yim, Kijeong et al. (Dec. 2014). “The Interstellar Medium and Star Formation in Edge-On Galaxies. II. NGC 4157, 4565, and 5907”. *AJ* 148.6, 127, 127. arXiv: 1408.5905 [astro-ph.GA] (cit. on p. 84).
- Yıldız, M. K. et al. (Apr. 2020). “Cold gas and dust: Hunting spiral-like structures in early-type galaxies”. *A&A* 636, A8, A8. arXiv: 2001.08087 [astro-ph.GA] (cit. on p. 4).
- Young, Lisa M. et al. (June 2011). “The ATLAS^{3D} project - IV. The molecular gas content of early-type galaxies”. *MNRAS* 414.2, 940–967. arXiv: 1102.4633 [astro-ph.CO] (cit. on pp. 4, 31, 40, 68, 72).
- Zhang, Chengpeng et al. (Oct. 2019). “Nearly all Massive Quiescent Disk Galaxies Have a Surprisingly Large Atomic Gas Reservoir”. *ApJ* 884.2, L52, L52. arXiv: 1910.02093 [astro-ph.GA] (cit. on p. 110).
- Zhang, Hong-Xin, Deidre A. Hunter, and Bruce G. Elmegreen (July 2012). “H I Power Spectra and the Turbulent Interstellar Medium of Dwarf Irregular Galaxies”. *ApJ* 754.1, 29, 29. arXiv: 1205.3793 [astro-ph.CO] (cit. on pp. 69, 70, 92, 93).
- Zweibel, E. G. and K. Josafatsson (July 1983). “Hydromagnetic wave dissipation in molecular clouds”. *ApJ* 270, 511–518 (cit. on p. 18).

Appendix A

Appendix: Heart of Darkness

This appendix contains supplementary material for Chapter 2. Specifically, we test the convergence of the cloud-scale parameter estimation in Appendix A.1 and the robustness of the dynamics-dependent SFE model results to changes in the star formation thresholds in Appendix A.2.

A.1 Resolution Test

The dynamics-dependent sub-grid star formation model includes a weak dependence on the (number of) neighbouring gas cells during the initial tree-walk. Therefore, we simulate the fiducial initial conditions at both higher and lower resolution (runs B_M60_R2_hres and B_M60_R2_lres respectively) to test the convergence of the star formation model over a decade in resolution. The virial parameter is the crucial quantity for which the effect of resolution has to be determined, because it sets the SFE. In Figure A.1, we show the time-averaged median virial parameter as a function of the galactocentric radius. It shows that the virial parameter follows the same radial trends despite the different mass resolution. With feedback also being affected by resolution, some offsets and slight variation in profile shape are expected. We therefore consider the convergence expressed by Figure A.1 to be satisfactory.

Figure A.2 shows the cumulative distribution of the virial parameter of all gas cells. This figure illustrates that, despite the order of magnitude difference in resolution, there is very little difference between the distribution of virial parameters in the three simulations. The median of the high-resolution run is slightly higher compared to the other two, but due to the relatively modest dependence of the SFE on the virial parameter (see equation 2.2.1), this only makes a difference of a few percent in SFE, demonstrating good convergence. This is further corroborated by Figure A.3, which shows the cumulative distributions of the virial parameters from which stars *actually* formed in the three simulations. While the median values vary between 1.3 and 2.9 from the highest to the lowest resolution, this is an acceptable difference considering the factor-of-10 difference in resolution.

Combining the above tests, we conclude that our star formation model reaches satisfactory convergence at the $10^4 M_{\odot}$ resolution that we have used in this study.

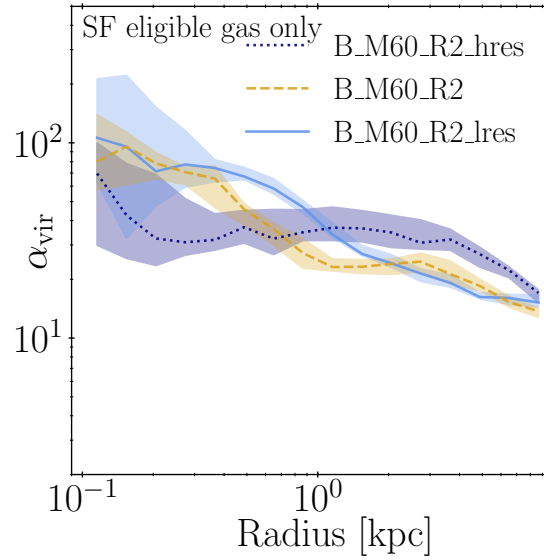


Figure A.1: Time-averaged radial profiles of the virial parameter, shown for three simulations of the fiducial bulge galaxy spanning a decade in numerical resolution. All profiles follow a similar trend, but differences persist. These differences result from stellar feedback having a slightly different effect at different resolutions.

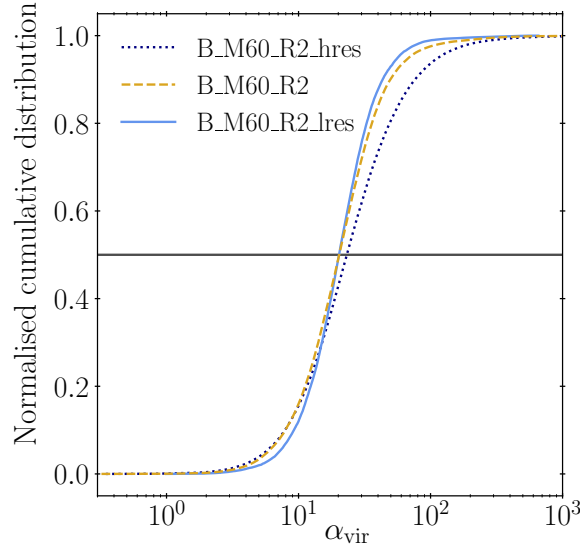


Figure A.2: Normalised cumulative distribution of the virial parameter for the different resolutions tested, as indicated by the legend. The horizontal black line indicates the median of each distribution.

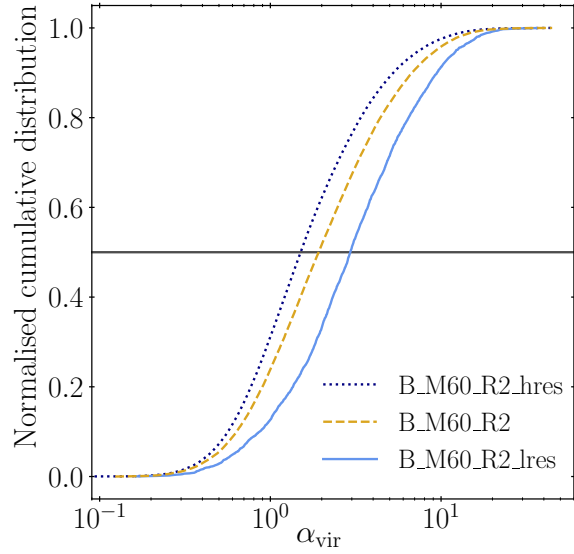


Figure A.3: Normalised cumulative distribution of the virial parameter with which stars formed, comparing the three simulations with different resolutions, as indicated by the legend. The horizontal black line indicates the median of each distribution. The median α_{vir} with which stars form lies between $\alpha_{\text{vir}} = 1.3$ for B_M60_R2_hres and $\alpha_{\text{vir}} = 2.9$ for B_M60_R2_lres.

A.2 Choice of Star Formation Thresholds

To ascertain the robustness of our sub-grid star formation model, and to ensure that our results are not influenced by the choices of thresholds determining which gas cells are eligible for star formation, we simulate the fiducial bulge galaxy with a range of different density and temperature thresholds for star formation. These thresholds are listed in Table A.1, and include both a higher and lower density threshold by an order of magnitude, as well as a temperature threshold that is higher by a factor of 50.

For the gas that is eligible for star formation, Figure A.4 shows that the gas virial parameters change considerably when using a different density threshold. Higher-density gas is more likely to be self-gravitating and thus have a lower virial parameter. Similarly, including more diffuse gas in the median will push the α_{vir} to higher values. Similar differences are shown in Figure A.5, which shows the normalised cumulative distributions of the virial parameter in the different simulations.

However, the gas with low virial parameters at which stars form most efficiently represents only a small fraction of the total mass. As a result, the differences in the virial parameter, which mostly manifest themselves at high α_{vir} , do not strongly affect the global SFR. This is demonstrated by Figure A.6, where only the virial parameter in simulation B_M60_R2_hDT shows a small offset, whereas the other three runs agree excellently.

Finally, Figure A.7 shows the star formation relation, generated in the same way as those

Name	Density threshold [cm^{-3}]	Temperature threshold [K]
B_M60_R2	1	1×10^3
B_M60_R2_IDT	0.1	1×10^3
B_M60_R2_hDT	10	1×10^3
B_M60_R2_hTT	1	5×10^4

Table A.1: Summary of simulations run to test the influence of star formation thresholds on the dynamics-dependent sub-grid star formation model. All simulations are those of the fiducial bulge ($R_b = 2$ kpc and $M_b = 0.6M_*$). We only vary the listed threshold parameters.

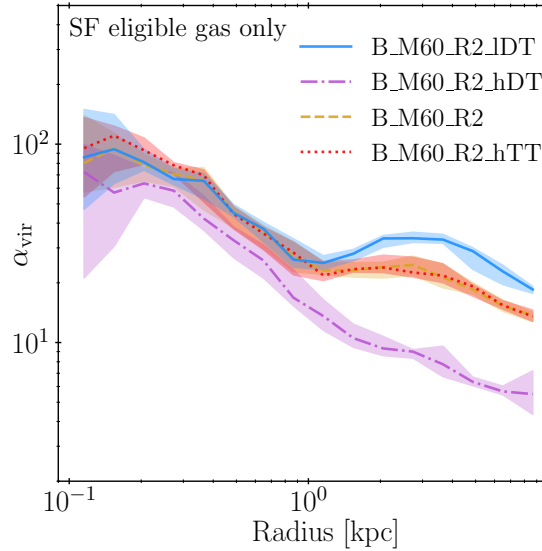


Figure A.4: Time-averaged radial profiles of the virial parameter, comparing simulations with different star formation thresholds, as detailed in Table A.1.

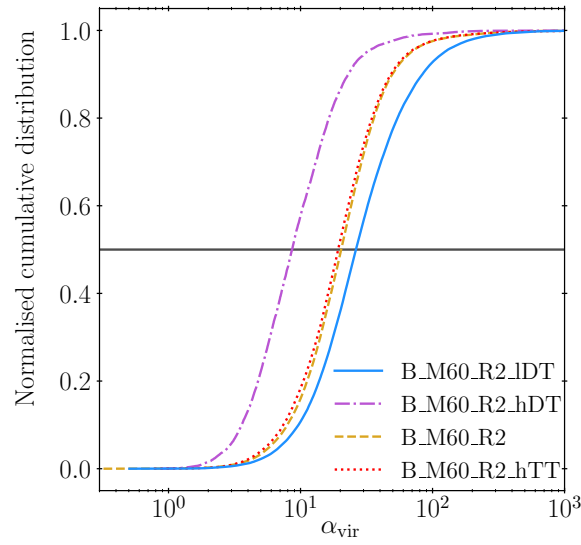


Figure A.5: Normalised cumulative distribution of α_{vir} , comparing simulations with different star formation thresholds, as detailed in Table A.1.

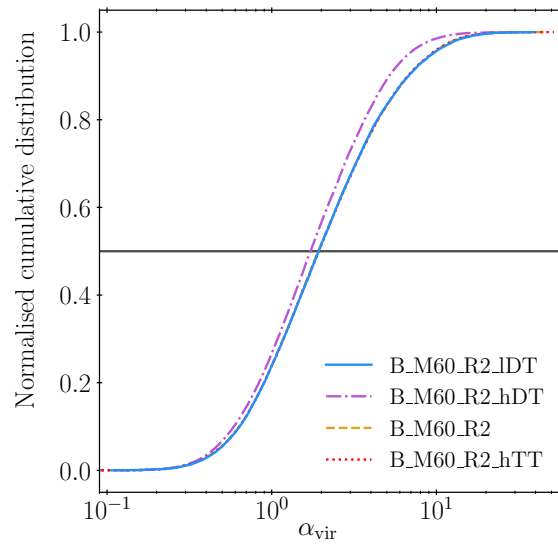


Figure A.6: Normalised cumulative distribution of α_{vir} with which stars have formed after 1 Gyr, comparing simulations with different star formation thresholds, as detailed in Table A.1.

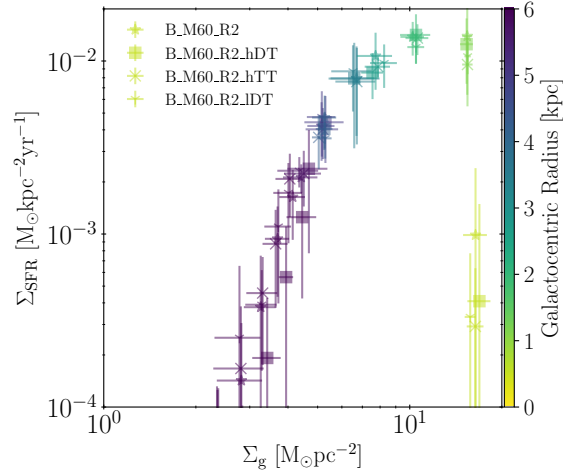


Figure A.7: SFR surface density as a function of gas surface density, comparing simulations with different star formation thresholds, as detailed in Table A.1. The colour coding indicates the galactocentric radius.

discussed in Section 2.4.1 and Section 2.5.5. All simulations are quantitatively consistent with the fiducial simulation B_M60_R2. For all of them, the Σ_{SFR} flattens towards the centre of the galaxy with increasing Σ_{g} , with a pronounced suppression in the central radial bin. Any differences agree to within the uncertainties implied by the time variability of the SFR. The insensitivity of the star formation relation to the density and temperature thresholds used is a result of the fact that our dynamics-dependent star formation model self-consistently selects self-gravitating overdensities by increasing their SFE. Irrespectively of the thresholds set, stars form at the roughly same rate, with a median $\alpha_{\text{vir}} \sim 1.9$, and follow the same star formation relation.

We conclude that the density and temperature thresholds for star formation used elsewhere in the literature, and which originally have been tuned to work for a constant ϵ_{ff} , can also be used with our model. They do not affect our conclusions regarding the influence of the gravitational potential on the SFR of galaxies. As our tests demonstrate, our sub-grid star formation model could also be used without any threshold at all, even if this would imply an increase in computational expense.

Appendix B

Appendix: WISDOM of Power Spectra

This appendix contains supplementary material for Chapter 3. In Appendix B.1 and Appendix B.2 we test how various choices in generating the mock observations of the simulations affect the measured power spectra. Appendix B.3 presents some additional simulations with $\log(\mu_*/M_\odot \text{kpc}^{-2}) > 8.85$ and Appendix B.4 lists all correlation.

B.1 KinMS

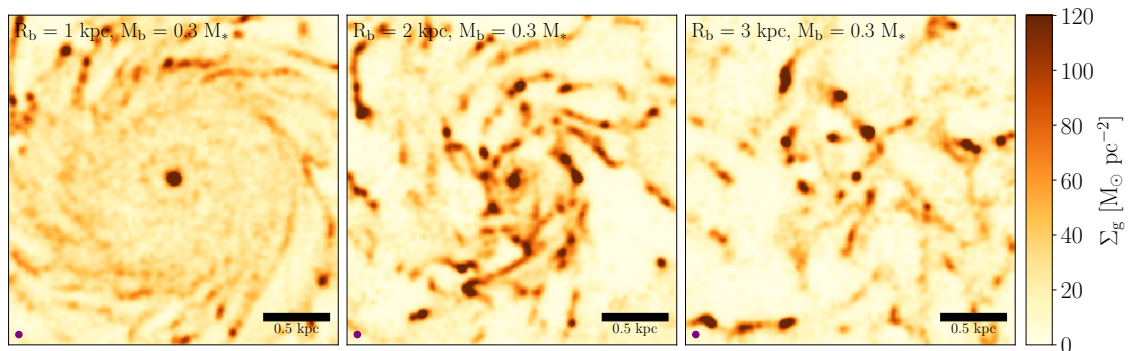


Figure B.1: Gas surface density maps generated using the `KinMS` tool, exemplary shown for the three galaxies with a bulge mass of $0.3M_*$ (left column of Figure 3.1), 600 Myr after the start of the simulations. The map has an extent of 2.25 kpc a side and the purple circle in the bottom left corner indicates the size of the beam. There is good agreement between the `AREPO` generated surface density projections and the `KinMS` maps, although the mock observations with `KinMS` tend to wash out smaller structures.

The `KinMS` tool is capable of creating mock interferometric observations from an underlying particle distribution. It can mimic observational effects such as beam smearing and

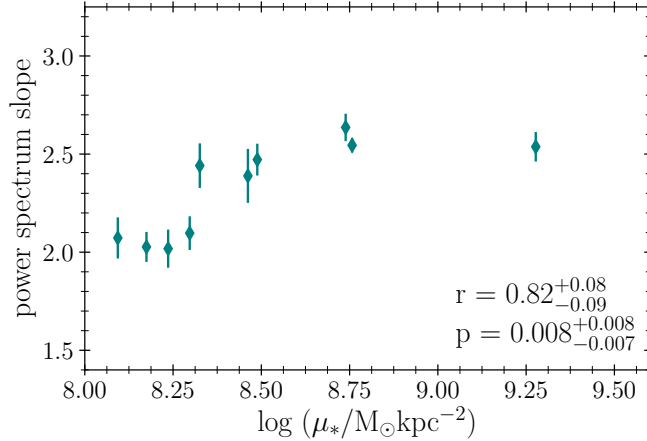


Figure B.2: Slopes of the power spectra obtained from the `KinMS` gas maps as a function of central stellar surface density (μ_*). Although the dynamic range in slopes is smaller compared to Figure 3.4, the strong correlation between power spectrum slope and central stellar surface densities persists.

velocity binning (Davis et al., 2013b), that do not get taken into account when computing surface densities using `AREPO`'s ray tracing. Although `KinMS` can mock an asymmetric beam at a position angle and incline the gas distribution, we restrict ourselves to the simple test case of using a symmetric beam with a FWHM of 43.3 pc and a map of 0° inclination here. This is done to better match the simulation results presented in Section 3.3.1, but we will explore the impact of inclination and beam size on the power spectrum in Appendix B.2.

We pass `KinMS` the position and mass of the gas cells, as well as the rotation curve for each simulated galaxy. The final maps have a velocity resolution of 10 km s^{-1} , a bandwidth of $\approx 1000 \text{ km s}^{-1}$ and a pixel size of 11 pc (corresponding to resolving the beam with ~ 4 pixels). Like the `AREPO` surface density projections, we generate mock observations for 8 snapshots from 300 Myr to 1 Gyr. As an example, Figure B.1 shows the maps for the three galaxies whose bulge contains 30 per cent of the initial stellar mass at 600 Myr. Overall there is good agreement between the `AREPO` (left column of Figure 3.1) and the `KinMS` maps shown here.

Figure B.2 shows the power spectrum slopes of the `KinMS` moment zero maps as a function of central stellar surface densities of the corresponding simulations. Qualitatively we find the same trend of steepening power spectrum slope with increasing central stellar surface density as for the surface density projections (Figure 3.4). The Spearman rank coefficient of $r = 0.82^{+0.08}_{-0.09}$ with $p = 0.008^{+0.008}_{-0.007}$ indicates a strong and probable correlation, which agrees with the one found in Section 3.3.1 within the uncertainties. Qualitatively there is a difference in power spectrum slope for the galaxies with $\log(\mu_*/M_\odot \text{kpc}^{-2}) \leq 8.35$. Although they show the same behaviour quantitatively, the `KinMS` power spectra of these galaxies have consistently steeper slopes, ranging from 2.01 to 2.09, than their surface

density projection counterparts which vary between 1.77 to 1.89. This is a result of the `KinMS` beam that smooths out some of the small scale structure, thereby steepening the slope. We have confirmed that we can reproduce the steeper slopes of the low μ_* galaxies to within their uncertainty using our original `AREPO` ray-tracing map and convolving it with the `KinMS` beam kernel. Since both methods yield qualitatively the same results, we use the `AREPO` surface density projection convolved with a Gaussian kernel, which stays truer to the underlying gas distribution.

B.2 Parameter Tests

This appendix details a number of test we have performed on the simulations and the surface density maps obtained from them. Below we will discuss in detail how the FWHM of the Gaussian kernel used to smooth the map prior to obtaining the power spectra (Section B.2.1), the inclination gas distribution (Section B.2.2), clipping the surface density map at a threshold (Section B.2.3) and our choice of masking the centre (Section B.2.4 affect the slope of the power spectra and the correlation between slope and central stellar surface density we find for the simulations.

B.2.1 Beam Size

For the main analysis of Chapter 3 we smooth the ray-tracing surface density projections generated with `AREPO` with a Gaussian kernel that has a FWHM of 43.3 pc, equivalent to the geometric mean of the NGC 0383 beam. However, the beam can affect the shape of the power spectrum up to a few times the FWHM (e.g. Grisdale et al., 2017; Koch et al., 2020). We only consider spatial scales in excess of $3 \times \text{FWHM}/\sqrt{8 \log 2}$, which should somewhat

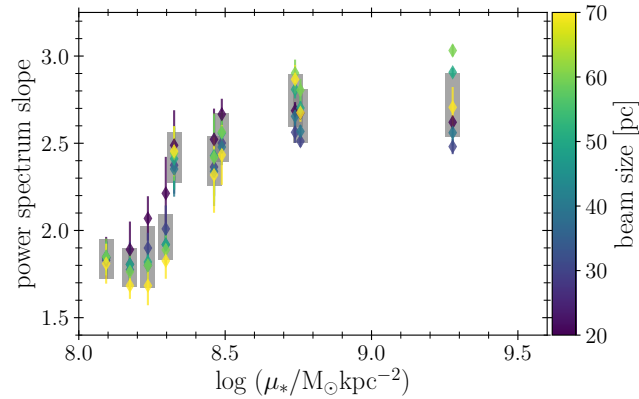


Figure B.3: Time-averaged power spectrum slope of the simulations as a function of their central stellar surface density (μ_*). Points are colour-coded by the size of the beam (FWHM of the Gaussian kernel) with which the map was smoothed prior to computing the power spectrum. The error bars indicate the standard deviation of the slope over time and the shading indicates the average error on the slope fit.

mitigate this effect. Nonetheless, we test the robustness of our results to changes in beam size here. To do so, we vary the FWHM of the Gaussian smoothing kernel we apply on our original surface density projection from 20×20 to 70×70 pc². We subsequently re-grid the map such that the beam is always resolved by approximately 4 pixels. When computing the power spectrum we account for the difference in beam size by adjusting the lower spatial limit of the fit accordingly.

Figure B.3 shows the time-averaged power spectrum slopes as a function of the central stellar surface density, colour-coded by the beam size. The error bars denote the standard deviation of the power spectrum slope over time, while the grey shaded region indicates the average uncertainty on the fit. There is some variation in power spectrum slope with changing beam size, however excepting the most bulge-dominated galaxy this only occurs over a range in slope that is comparable to the error on the fit. There is no clear pattern of how the beam size affects the power spectrum slope. The power spectra of galaxies with $\log(\mu_*/M_\odot \text{kpc}^{-2}) \leq 8.3$ and a more sub-structured ISM appear to become shallower when the beam size is increased. For the other galaxies, there is no longer a monotonic trend of the slope with beam size and in each case the points scatter differently. Tendentially the power spectra of galaxies with $\log(\mu_*/M_\odot \text{kpc}^{-2}) > 8.7$ steepen with increasing beam size. This is likely caused by smoothing out more of the smallest (invisible) density fluctuations, making the gas discs even smoother.

We list the Spearman rank correlation coefficients and the probability for each data set to be statistically significant in Table B.1. At all beam sizes considered here, the correlation between the power spectrum slopes and central stellar surface density remains strong and statistically significant. In short, although there is some quantitative variation of the power spectrum shape that depends on the beam size, this discrepancy is only of order the error on the fit. Qualitatively, there is good agreement between all the power spectra.

Beam size [pc]	Spearman r	p-value
20	$0.82^{+0.09}_{-0.08}$	$0.009^{+0.008}_{-0.007}$
30	$0.82^{+0.09}_{-0.09}$	$0.008^{+0.008}_{-0.008}$
40	$0.86^{+0.06}_{-0.07}$	$0.004^{+0.004}_{-0.001}$
50	$0.91^{+0.05}_{-0.04}$	$0.001^{+0.001}_{-0.000}$
60	$0.92^{+0.04}_{-0.05}$	$0.001^{+0.001}_{-0.000}$
70	$0.86^{+0.05}_{-0.05}$	$0.003^{+0.003}_{-0.002}$

Table B.1: Spearman rank coefficients and p-values for the correlation between power spectrum slope and central stellar surface density of the simulated galaxies, when using different beam sizes in the Gaussian smoothing kernel applied to the surface density maps.

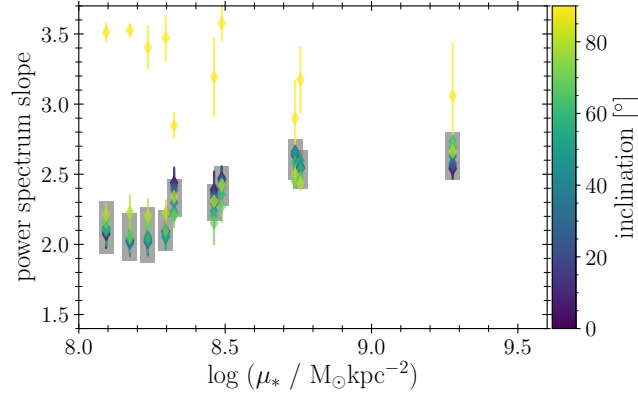


Figure B.4: Time-averaged power spectrum slope of the simulations as a function of their central stellar surface density (μ_*). Points are colour-coded by the inclination of the map from which the power spectrum was computed. The errorbars indicate the standard deviation of the slope over time, while the grey patches show the average error on the power spectrum slope fit.

B.2.2 Inclination

Another important quantity to consider is the inclination of the surface density map on which the power spectrum is computed. Our default for the simulations is a face-on projection, but the WISDOM observations have inclinations ranging from 20 to 70°. We use `KinMS` to produce surface density maps at inclinations ranging from 0 to 90° and otherwise using the set-up described in Appendix B.1. We show the resultant time-averaged power spectral indices as a function of central stellar surface density in Figure B.4. Each point is colour-coded by the inclination of the map from which it was produced, error bars on the points indicate the standard deviation of the slope over time and the grey-shaded patch indicates the average error on the fit. There is some variation in slope as a function of inclination, but for inclinations below 90° the slopes are often in agreement within the variation over time, and always within the error on the fit. Qualitatively, the correlation of steeper power spectra with increasing μ_* is preserved at the $p < 0.01$ level for inclinations below 70°. It persists with a lower Spearman rank coefficient (although still within the 16th-to-84th percentile variation) at the $p < 0.05$ interval for inclinations of 70 and 80°, as shown in Table B.2. The power spectra are only significantly affected at an inclination of 90°. When the galaxy is viewed edge-on all power spectra are very steep. This affects the disc-dominated galaxies with a more sub-structured ISM more than the bulge-dominated ones. In the $\log(\mu_*/M_\odot \text{kpc}^{-2}) \leq 8.3$ galaxies some steepening occurs already at inclinations $\gtrsim 70^\circ$. Thus, caution is advised when considering power spectra of galaxies whose gas reservoirs have inclinations above 70°, but below that the expected variation of the power spectrum slope are small. This is in good agreement with Grisdale et al. (2017) who find that inclining their galaxies to 40° mostly affects the total power in the power spectrum and the shape below the beam scale.

Inclination [°]	Spearman r	p-value
0	$0.82^{+0.08}_{-0.08}$	$0.007^{+0.007}_{-0.006}$
10	$0.83^{+0.08}_{-0.08}$	$0.007^{+0.007}_{-0.006}$
20	$0.84^{+0.08}_{-0.08}$	$0.006^{+0.006}_{-0.005}$
30	$0.84^{+0.07}_{-0.06}$	$0.005^{+0.005}_{-0.004}$
40	$0.87^{+0.05}_{-0.05}$	$0.002^{+0.002}_{-0.002}$
50	$0.87^{+0.06}_{-0.06}$	$0.003^{+0.003}_{-0.002}$
60	$0.86^{+0.09}_{-0.08}$	$0.005^{+0.005}_{-0.004}$
70	$0.76^{+0.12}_{-0.13}$	$0.026^{+0.026}_{-0.022}$
80	$0.78^{+0.11}_{-0.11}$	$0.020^{+0.020}_{-0.013}$
90	$-0.43^{+0.19}_{-0.21}$	$0.261^{+0.208}_{-0.261}$

Table B.2: Spearman rank coefficients and p-values for the correlation between power spectrum slope and central stellar surface density of the simulated galaxies, when inclining the maps of the simulated galaxies by the angle specified in column 1.

B.2.3 Surface Density Threshold

In contrast to the CO observations, the surface density projections for the galaxy include all (cold) gas within the simulation because we do not use a sufficiently sophisticated chemical

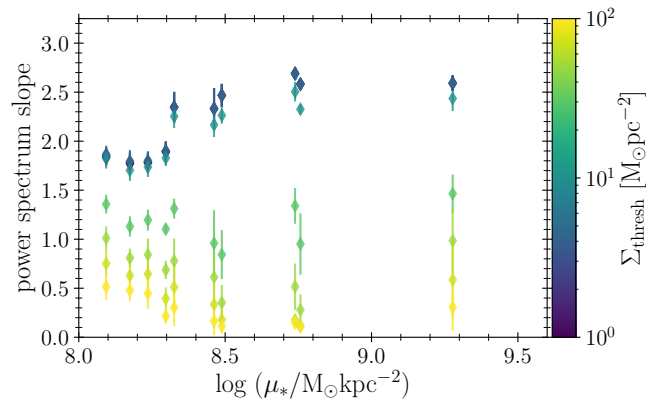


Figure B.5: Time-averaged power spectrum slope of the simulations as a function of their central stellar surface density (μ_*). Points are colour-coded by the surface density threshold imposed on the map from which the power spectrum was computed. The errorbars indicate the standard deviation of the slope over time.

Σ_{thresh} [$M_{\odot}\text{pc}^{-2}$]	Spearman r	p-value
0	$0.86^{+0.06}_{-0.05}$	$0.004^{+0.003}_{-0.001}$
1	$0.86^{+0.06}_{-0.05}$	$0.003^{+0.003}_{-0.002}$
3	$0.86^{+0.06}_{-0.06}$	$0.004^{+0.003}_{-0.002}$
5	$0.86^{+0.06}_{-0.06}$	$0.004^{+0.003}_{-0.003}$
10	$0.84^{+0.07}_{-0.08}$	$0.006^{+0.006}_{-0.003}$
30	$-0.01^{+0.22}_{-0.22}$	$0.651^{+0.285}_{-0.256}$
50	$-0.44^{+0.25}_{-0.20}$	$0.281^{+0.252}_{-0.230}$
70	$-0.57^{+0.25}_{-0.24}$	$0.159^{+0.155}_{-0.159}$
100	$-0.58^{+0.22}_{-0.23}$	$0.148^{+0.141}_{-0.148}$

Table B.3: Spearman rank coefficients and p-values for the correlation between power spectrum slope and central stellar surface density of the simulated galaxies, when restricting the analysis to maps with surface densities exceeding those listed in column 1.

model that models molecular gas or tracks CO specifically. Here we test the effect the effect of clipping our surface density maps at specific thresholds on the power spectrum slope. After obtaining the AREPO-generated surface density map, we set all surface density values below our threshold to NaN. We test thresholds up to $100 M_{\odot}\text{pc}^{-2}$ and show this as the coloured points in the time-averaged power spectrum slopes as a function of central stellar surface density plot in Figure B.5. For $\Sigma_{\text{thresh}} \leq 10 M_{\odot}\text{pc}^{-2}$ the power spectra remain largely unaffected, the slopes agreeing within the standard deviation over time, or within the error on the fit. Notable differences start to appear for $\Sigma_{\text{thresh}} \geq 30 M_{\odot}\text{pc}^{-2}$, the green and yellow diamonds in Figure B.5. The power spectra become much shallower for all galaxies. This is the result of focussing on smaller and smaller, (very) high density peaks. These are preferentially found in the more disc-dominated galaxies, which already have a clumpier ISM with starker density contrasts. Therefore, the differences in power spectrum slope are larger for the bulge-dominated galaxies. However, it is clear that these high surface density thresholds are somewhat unphysical for our simulations, as what remains left is a noise map in essence. As before, we show the Spearman rank coefficient for a correlation between β and μ_* with different thresholds in Table B.3. In summary, our results remain robust even when introducing a reasonable threshold that would mimic molecular gas more closely, such as $\sim 10 M_{\odot}\text{pc}^{-2}$.

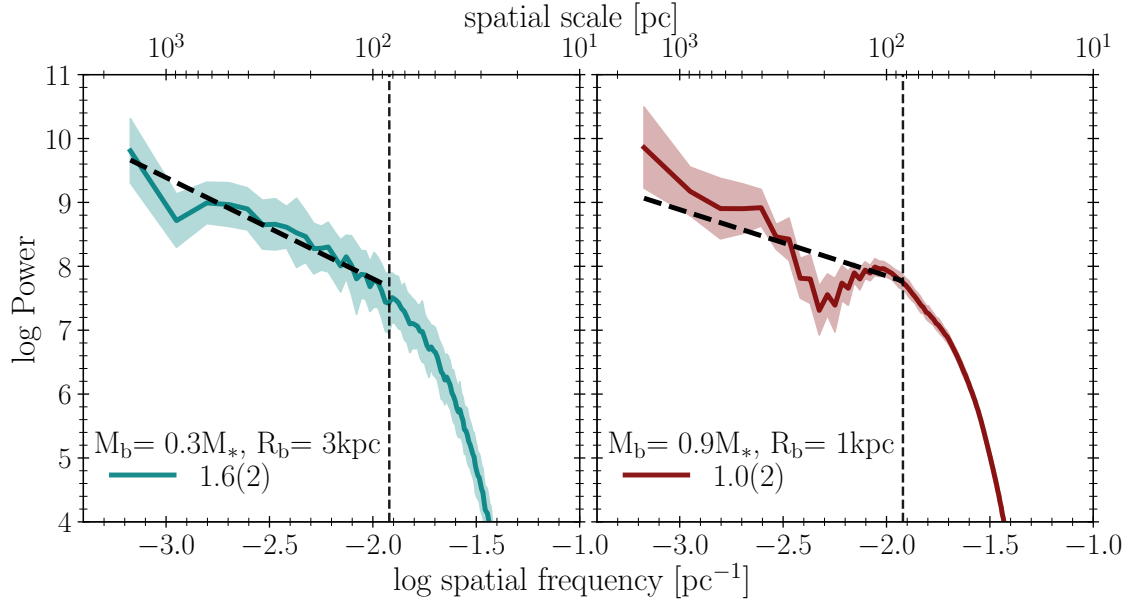


Figure B.6: Power spectra of the most disc- and bulge-dominated galaxies B_M30_R3 B_M90_R1 without masking the centre. The power spectrum of B_M90_R1 is clearly dominated by the very dense attenuation of gas at the centre of the galaxy on scales up to 200 pc, while the power spectrum of B_M30_R3 is very similar to the centre masked one.

B.2.4 Centre Masking

Lastly, we discuss the effect masking the centres has on the power spectrum slopes we measure. Figure B.6 gives an example of how extreme the effect of the very dense central region in the bulge-dominated galaxies is, by contrasting it with the power spectrum of an unmasked disc-dominated galaxy. In the B_M90_R1 spectrum there is a bump followed by an order of magnitude drop in power on the spatial scales associated with the central region that make fitting the power spectrum with any kind of power law impossible. This central attenuation of gas is a consequence of the star formation rate suppression in the galactic centre and the lack of feedback from active galactic nuclei and therefore unphysical (see also the discussion in Gensior et al. 2020). To avoid contamination in the power spectrum from this bright centre we mask it using the Cosine Bell Window function of `astropy`.

We show the evolution of the power spectrum slope as a function of the masking parameter α in Figure B.7. The disc-dominated galaxies with a sub-structured ISM are not strongly affected by the centre masking until $\alpha > 0.5$ is reached, but even then there is only moderate steepening. The bulge-dominated galaxies show a lot more variation. At $\alpha < 0.1$ slopes are shallow and change dramatically between the data points because the central region is not completely masked. This trend of variation due to the very dominant central region continues for the more bulge dominated galaxies until $\alpha \sim 0.25$ and only equilibrate somewhat afterwards. The slopes of the more bulge-dominated galaxies also increase with

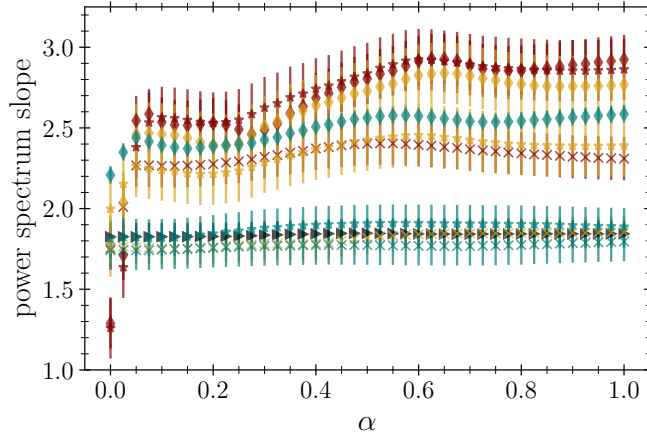


Figure B.7: Power spectrum slope for all simulations (exemplary at 600 Myr) as a function of the masking parameter α that determines the width of the Cosine Bell window used to mask the centre of simulations and observations alike.

Name	M_b [$10^{10}M_\odot$]	R_b [kpc]	$\log(\mu_*/M_\odot\text{kpc}^{-2})$
B_M75_R1	3.50	1	9.01
B_M90_R1p5	4.24	1.5	8.96
B_M100_R1	4.67	1	9.43
B_M100_R2	4.67	2	8.86

Table B.4: Initial conditions of the additional simulations. We only vary the listed parameters.

increasing α , however for those where the change is drastic, the errors on the fit are very large. We choose our masking parameter from the region where all power spectrum slopes have reached a temporary equilibrium, i.e. where the central region of the bulge-dominated galaxies no longer dominates the power spectrum fit, and thus settle on $\alpha = 0.35$. The corresponding masking parameter for the observations is calculated as:

$$\alpha_{\text{obs}} = \frac{16b_{\text{avg}}(n_{\text{pix}} - 1)}{l_{\text{pix}}}, \quad (\text{B.2.1})$$

where b_{avg} is the geometric beam average, n_{pix} the number of pixels along one side of the map and l_{pix} the size of a pixel in pc.

B.3 Additional Simulations

To test whether the power spectrum slope approaches a constant value at high central stellar surface density, we perform four additional simulations with $\log \mu_*$ values ranging from 8.86 to 9.43. These additional initial conditions are generated following the procedure

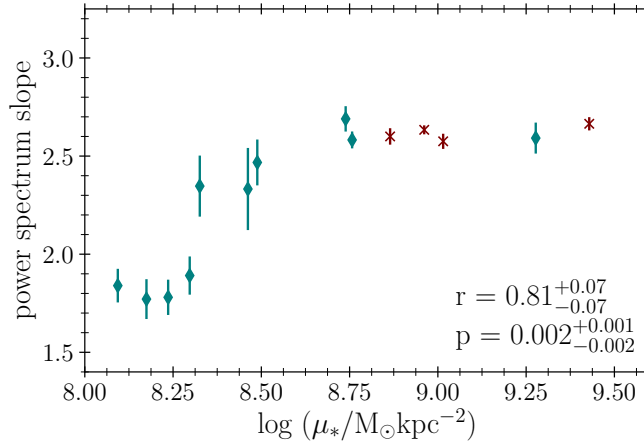


Figure B.8: Power spectrum slopes (β) of all simulations as a function of central stellar surface density (μ_*). For easier visibility, the additional simulations discussed in this appendix are highlighted in maroon and displayed as crosses. The strong correlation between β and μ_* persists.

outlined in Section 2.3.2. Table B.4 lists the different bulge masses and scale radii that result in galaxies with μ_* values in the range we want to investigate.

In Figure B.8 the power spectrum slope is plotted against the central stellar surface density of both the original simulations discussed in Chapter 3, and the additional simulations, highlighted by maroon crosses. Although weaker than the original correlation, with $r = 0.81^{+0.07}_{-0.07}$ and $p = 0.002^{+0.001}_{-0.002}$ the correlation between β and μ_* still holds at a statistically significant level. Indeed, the Monte Carlo simulations indicate that the correlation found with the additional simulations is stronger, and the Spearman rank values agree within the 16th/84th percentile uncertainties. The three additional simulations with central stellar surface densities between $8.8 < \log \mu_* < 9.25$ have a slope comparable to the runs B_M90_R2 and B_M90_R1 immediately bracketing them. Only run B_M100_R1 exhibits a slightly steeper slope, which still falls within the variation over time of run B_M90_R1. For all additional simulations, the variation in power spectrum slope over time is minimal.

The slopes of the additional simulations do indicate that the trend of steeper power spectrum slopes with increasing central stellar surface density becomes much shallower, if not approaching a constant value at $\log \mu_* \geq 8.75$. This implies that the central gas reservoir in these galaxies reaches a "maximum smoothness" without any fragmentation or substructure, that there is a limit to how much shear can affect and tear apart the gas. There are two possible explanations for observing this behaviour: It is either a physical limit, or a numerical resolution effect. The latter could be caused by our relatively low resolution of $\sim 1 \times 10^4 M_\odot$ per gas particle, making it difficult to resolve objects comparable to smaller giant molecular clouds properly. However, testing whether this is a numerical effect requires additional simulations at a much higher resolution, which are beyond the

scope of the current study. Therefore, it will remain unclear whether the flattening of the $\beta - \mu_*$ trend is physical or numerical in origin.

It should also be noted following Appendix B.2.1, that even the choice of beam size affects if we see a flattening. At beam sizes of 20 and 30 pc (around the average gravitational resolution of 25 pc), the trend between β and μ_* is less pronounced, whereas it becomes stronger (and does not approach a constant slope) for beam sizes of 50 and 60 pc. We also test the behaviour of the power spectrum using surface density maps that are 4.5 kpc a side. This is marginally larger than the diameter of the smooth gas reservoir in the most bulge-dominated galaxy. Although the power spectrum slopes become shallower on average, the trend between power spectrum slopes and central stellar surface densities is preserved and the slopes continuously increase with μ_* . This highlights further how sensitive power spectrum slopes in general, and the flattening effect in particular, are to parameter choices.

B.4 WISDOM Power Spectrum Slope (non-)Correlations

We summarise our search for correlations between the power spectrum slopes of the WISDOM galaxies and various properties in Table B.5. For each quantity we show the mean Spearman rank coefficient and p-value and indicate their 16th and 84th percentiles from 1000 Monte Carlo simulations, performed to account for the uncertainty on each power spectrum fit. In addition to showing the correlation probability for the entire sample, we also show it for the sub-samples of ETGs and Spirals. We test for correlation with: μ_{gas} , the central gas surface density; M_{gas} , the gas mass; R_{gas} , the half-light radius of the gas; the star formation rate (SFR); the specific star formation rate (sSFR); R_{CO}/R_e , the ratio of gas-to-stellar half-light radii; f_{gas} , the gas-to-stellar mass ratio; μ_{gas}/μ_* , the gas-to-stellar central surface density ratio; μ_* , the central stellar surface density; M_* , the stellar mass of the galaxy; Σ_{min} , the sensitivity of the observations; l_{min} , the smallest scale of the power law fit; $l_{\text{max}}-l_{\text{min}}$, the extent of the power law fit, and the geometric average of the beam (beam).

Property	all galaxies		ETGs		Spirals	
	Spearman r	p-value	Spearman r	p-value	Spearman r	p-value
μ_{gas}	$0.65^{+0.16}_{-0.17}$	$0.06^{+0.06}_{-0.06}$	$0.59^{+0.24}_{-0.26}$	$0.22^{+0.26}_{-0.04}$	$0.69^{+0.21}_{-0.19}$	$0.22^{+0.17}_{-0.19}$
M_{gas}	$0.29^{+0.15}_{-0.14}$	$0.40^{+0.25}_{-0.24}$	$-0.08^{+0.30}_{-0.27}$	$0.67^{+0.27}_{-0.01}$	$0.58^{+0.22}_{-0.28}$	$0.33^{+0.29}_{-0.23}$
R_{gas}	$0.09^{+0.16}_{-0.16}$	$0.66^{+0.24}_{-0.24}$	$-0.27^{+0.27}_{-0.34}$	$0.58^{+0.36}_{-0.51}$	$0.38^{+0.32}_{-0.38}$	$0.49^{+0.39}_{-0.30}$
SFR	$0.19^{+0.13}_{-0.13}$	$0.58^{+0.26}_{-0.24}$	$-0.37^{+0.22}_{-0.18}$	$0.48^{+0.31}_{-0.31}$	$0.12^{+0.28}_{-0.32}$	$0.67^{+0.20}_{-0.16}$
sSFR	$0.37^{+0.13}_{-0.13}$	$0.30^{+0.18}_{-0.18}$	$-0.28^{+0.19}_{-0.26}$	$0.58^{+0.29}_{-0.04}$	$0.34^{+0.36}_{-0.44}$	$0.50^{+0.37}_{-0.31}$
$R_{\text{gas}}/R_{\text{e}}$	$-0.01^{+0.13}_{-0.13}$	$0.76^{+0.17}_{-0.19}$	$-0.54^{+0.14}_{-0.18}$	$0.24^{+0.14}_{-0.69}$	$0.49^{+0.31}_{-0.31}$	$0.40^{+0.22}_{-0.30}$
f_{gas}	$0.27^{+0.12}_{-0.13}$	$0.43^{+0.24}_{-0.22}$	$-0.30^{+0.23}_{-0.20}$	$0.51^{+0.30}_{-0.17}$	$0.71^{+0.19}_{-0.21}$	$0.21^{+0.18}_{-0.17}$
μ_{gas}/μ_{*}	$0.51^{+0.12}_{-0.11}$	$0.11^{+0.08}_{-0.08}$	$0.52^{+0.16}_{-0.16}$	$0.26^{+0.17}_{-0.02}$	$0.28^{+0.22}_{-0.18}$	$0.64^{+0.23}_{-0.25}$
μ_{*}	$-0.10^{+0.18}_{-0.18}$	$0.64^{+0.26}_{-0.26}$	$0.10^{+0.15}_{-0.17}$	$0.71^{+0.23}_{-0.11}$	$0.07^{+0.23}_{-0.37}$	$0.72^{+0.15}_{-0.22}$
M_{*}	$-0.24^{+0.19}_{-0.20}$	$0.48^{+0.34}_{-0.32}$	$0.07^{+0.25}_{-0.29}$	$0.63^{+0.25}_{-0.09}$	$-0.54^{+0.24}_{-0.36}$	$0.37^{+0.26}_{-0.33}$
Σ_{min}	$0.49^{+0.16}_{-0.17}$	$0.16^{+0.15}_{-0.14}$	$0.46^{+0.22}_{-0.21}$	$0.33^{+0.21}_{-0.06}$	$0.46^{+0.24}_{-0.36}$	$0.45^{+0.42}_{-0.27}$
l_{min}	$-0.01^{+0.16}_{-0.16}$	$0.71^{+0.21}_{-0.22}$	$-0.12^{+0.23}_{-0.31}$	$0.68^{+0.26}_{-0.37}$	$0.06^{+0.24}_{-0.36}$	$0.74^{+0.26}_{-0.23}$
$l_{\text{max}}-l_{\text{min}}$	$0.14^{+0.16}_{-0.16}$	$0.61^{+0.29}_{-0.27}$	$-0.29^{+0.29}_{-0.32}$	$0.56^{+0.38}_{-0.46}$	$0.51^{+0.29}_{-0.21}$	$0.38^{+0.24}_{-0.28}$
beam	$-0.01^{+0.16}_{-0.17}$	$0.71^{+0.20}_{-0.21}$	$-0.13^{+0.24}_{-0.34}$	$0.66^{+0.28}_{-0.42}$	$0.08^{+0.22}_{-0.28}$	$0.73^{+0.14}_{-0.23}$

Table B.5: Mean Spearman rank correlation coefficient with 16th and 84th percentiles and probability for non-correlation between the slopes of the WISDOM power spectra and assorted properties. These have been estimated from 1000 Monte-Carlo simulations of the data, to take into account uncertainty on the power law fit. We show the correlation coefficient and p-values for the entire sample and the sub-sets of early- and late-type galaxies.

Appendix C

Appendix: Elephant in the Bathtub

This appendix contains supplementary material for Chapter 4. We first demonstrate the validity of using a multi-linear regression to fit the sSFR dependence on μ_* and f_{gas} in Appendix C.1. Then we discuss the density distribution of the gas in Appendix C.2.

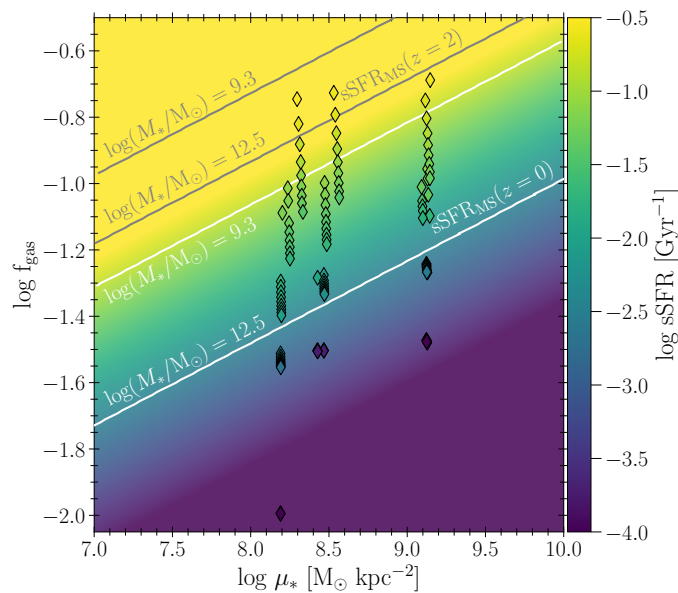


Figure C.1: Gas-to-stellar mass ratio f_{gas} and stellar surface density (μ_*) plane, coloured by the specific SFR (sSFR \equiv SFR/ M_*) predicted by the multi-linear regression of equation 4.4.1. Diamonds show results from the simulations at different times between 0.3–1 Gyr, colour-coded by their current sSFR. The grey and white lines indicate the expected range in sSFR between stellar masses $2 \times 10^9 M_\odot \leq M_* \leq 3 \times 10^{12} M_\odot$ for galaxies on the Speagle et al. (2014) SFMS at redshift 2 and 0 respectively. The good agreement between the colours of the data points and the background demonstrates that the multi-linear regression provides a satisfactory description of the simulations.

C.1 Validation of the Multi-linear Regression

Figure C.1 compares the sSFR measured in the simulations to the prediction from the multi-linear regression of equation 4.4.1, for a range of gas-to-stellar mass ratios and stellar surface densities. The comparison between the colour of the diamonds and the background shading shows good agreement between the two, within the boundaries set by the grey and white lines, which demarcate the range in sSFR expected from galaxies on the Speagle et al. (2014) SFMS with stellar masses $2 \times 10^9 M_\odot \leq M_* \leq 3 \times 10^{12} M_\odot$. We require agreement between the simulation data-points and the fit in the part of $f_{\text{gas}} - \mu_*$ parameter space encased by the lines, because this is the mass range considered in our prediction for the importance of dynamical suppression on the galaxy population. The grey lines denote values for the main sequence sSFR at $z = 2$, while the white lines show the sSFR for $z = 0$ galaxies. Consequently, the assessment of the quality of the fit should be restricted to points above the $\log M_* = 3 \times 10^{12} M_\odot$, $z = 0$ white line. Figure C.1 shows excellent agreement between linear model and simulations in this part of parameter space. Across the entire model grid, only a few points show a lower sSFR compared to the multi-linear regression fit, likely because our sub-grid star formation model might overestimate the suppression of star formation somewhat in part of parameter space (see discussion in Section 4.5.2). However, these points fall below the bottom white line, i.e. outside of our region of relevance, and thus do not influence our conclusion that a multi-linear parametrisation of the sSFR is an appropriate fit to the simulated data.

C.2 Gas Density Distributions

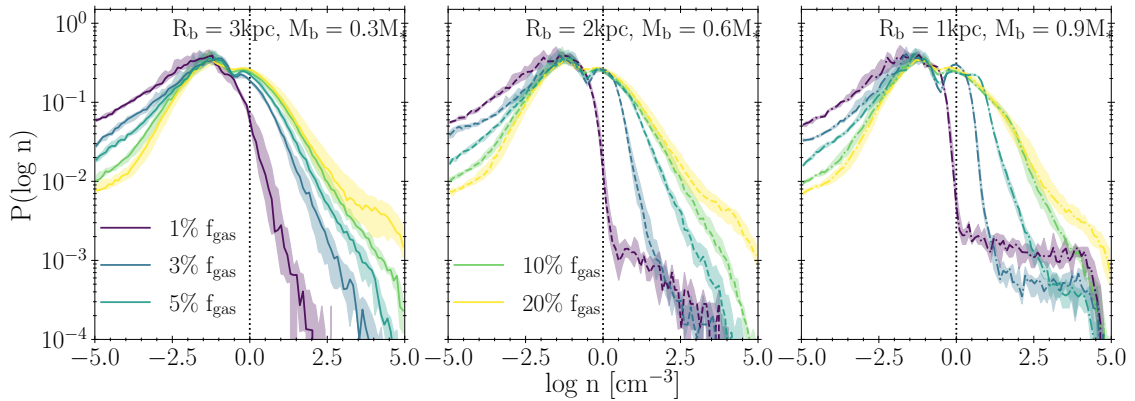


Figure C.2: Gas volume density distributions of the simulated galaxies. Each panel shows the probability density function (PDF) of the gas for galaxies with gas-to-stellar mass ratios of 0.01–0.20, for the disc-dominated (left), intermediate bulge (middle) and bulge-dominated (right) potentials. Lines indicate the median over time, while the shaded regions indicate the 16th-to-84th percentile variation over time. The vertical black dotted line indicates the minimum density threshold for star formation, which is $n_{\text{min}} = 1 \text{ cm}^{-3}$.

The probability density function (PDF) for all gas within the simulations is shown in Figure C.2, for the complete set of different stellar density profiles and gas-to-stellar mass ratio. The main difference in the gas distribution between the different gas fractions lies in the high-density tail of the PDF. The higher the gas-to-stellar mass ratio, the more gas is present at high densities. This difference between galaxies with different gas-to-stellar mass fractions increases the more spheroid-dominated the gravitational potential is. It is caused by shear, which inhibits the fragmentation of gas into smaller, denser clouds at low gas-to-stellar mass ratios (see also Figure C.3). Despite these differences at low gas-to-stellar mass ratios, the mass-weighted fractions of gas above the star formation threshold for the runs with $f_{\text{gas}} = 0.05\text{--}0.20$ only differ by a couple of per cent or less. The sharp drop of the gas PDF just below the density threshold for star formation seen for runs B_M60_R2_fg1 and B_M90_R1_fg1 might suggest a numerical bias in the sSFR of these galaxies, related to the choice of threshold density. To address this, we performed two (re-)simulations of B_M90_R1_fg1 (one with a density threshold of $n_{\text{min}} = 0.1 \text{ cm}^{-3}$ and one with higher resolution), which show that the SFRs presented in Chapter 4 are not affected by the threshold choice and resolution.

Figure C.3 shows a projection of the gas surface density for each simulated galaxy. Gensior et al. (2020) found that the shear induced by a dominant spheroidal component can suppress fragmentation in the ISM of the galaxy, creating a smooth circumnuclear gas disc. The extent of the disc depends on the bulge strength, i.e. the higher the central stellar surface density, the larger disc. Figure C.3 demonstrates that with $f_{\text{gas}} \leq 3$ per cent even the disc-dominated galaxies show signs of this process, even if the central gas reservoir is marginally disturbed. The more gas dominates the local gravitational potential at higher gas-to-stellar mass ratios, the lower the impact of the stellar potential. As shear becomes insufficient in suppressing fragmentation, star formation and stellar feedback proceed. These processes together lead to an increasingly more substructured ISM. At a gas-to-stellar mass ratio of 20 per cent, the most bulge-dominated potential barely hosts a central gas disc. Figure C.3 illustrates that, similarly to the dynamical suppression of star formation, the extent and existence of the smooth central gas disc also depends on both the gas-to-stellar mass ratio and the underlying gravitational potential.

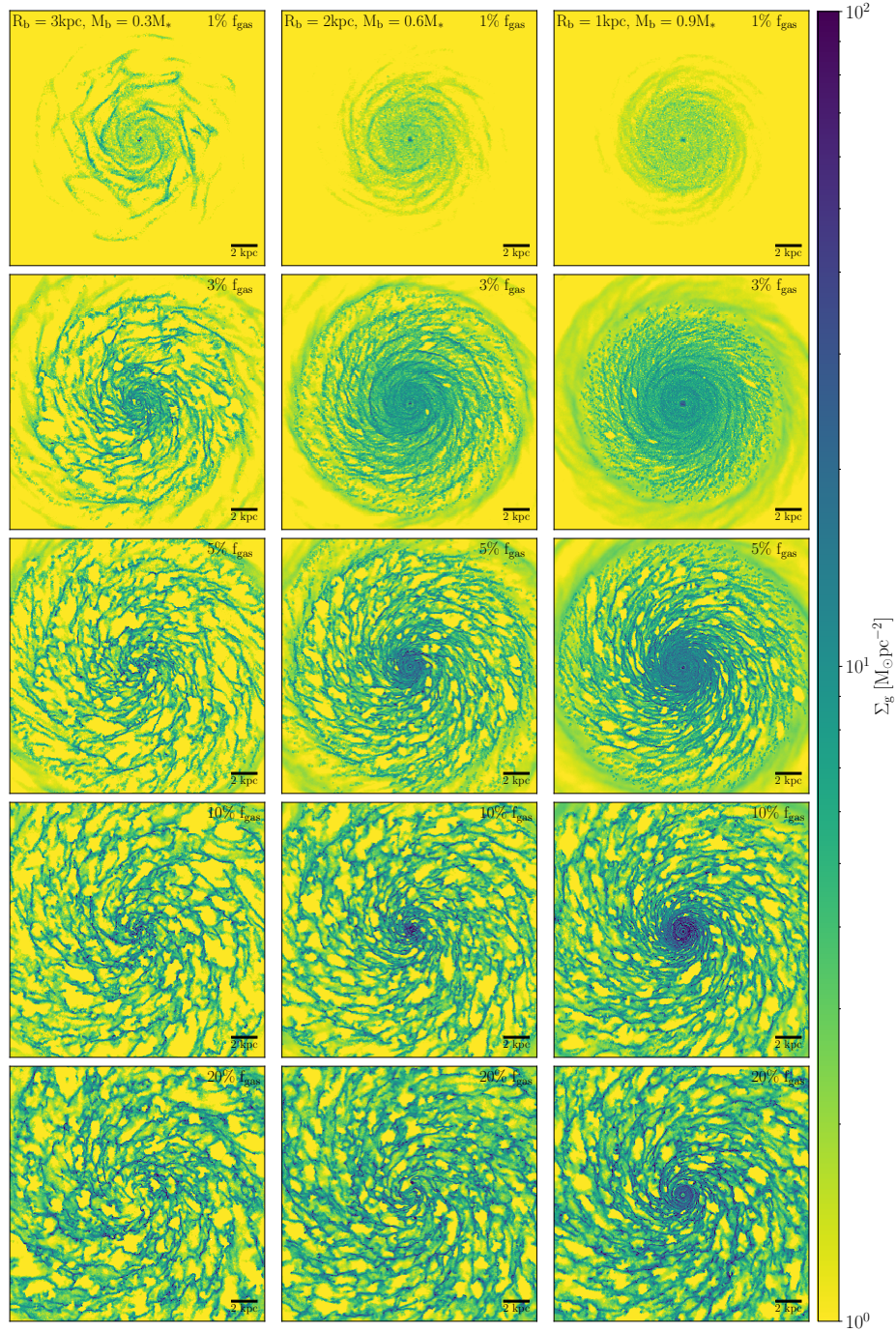


Figure C.3: Surface density projection of the gas component in the simulated galaxies. The columns indicate the distinct gravitational potentials, with disc-dominated on the left, intermediate bulge in the middle and bulge-dominated on the right. The gas-to-stellar mass ratio increases from 1 per cent in the top row to 20 per cent in the bottom row. The maps are shown at 900 Myr after the start of the each simulation and measure 20 kpc on a side. At low gas-to-stellar mass ratios, we find ubiquitous smooth nuclear gas discs, which arise from the dynamical suppression of fragmentation. At $f_{\text{gas}} \geq 10$ per cent, the ISM is predominantly substructured, due to gravitational instability and stellar feedback. At such a high gas fraction, even the completely bulge-dominated potential only hosts a very small central disc.